

Production of Direct Photons and Neutral Pions in Relativistic Au+Au Collisions

Tadaaki Isobe



A Dissertation Submitted in
Partial Fulfillment of the Requirements for
the Degree of Doctor of Science at
April, 2007

*Department of Physics
Graduate School of Science
University of Tokyo
7-3-1 Hongo, Bunkyo-ku, Tokyo 113-0033, JAPAN*

Abstract

In modern particle physics, a standard model to describe the dynamics of elementary particles, quarks, leptons and gauge bosons, has been developed. Quantum ChromoDynamics (QCD) is known as the theory to describe behaviors of strong interaction among quarks and gluons. There are two kinds of important features in the QCD: “color confinement” and “asymptotic freedom”. Ordinarily quarks and gluons, which have a degree of freedom of color, are confined in hadrons as a color-singlet state. On the other hand, the strong coupling constant (α_s) decreases at a large momentum transfer in high energy reaction, or in the environment of extremely high temperature or density. Thus, as the temperature or density of many-body system of hadrons are increased, a normal nuclear state is expected to transit into a new state of matter where quarks and gluons become color de-confined. The new state of matter is called “Quark Gluon Plasma” (QGP).

Such an extreme state of matter is expected to be formed in ultra-relativistic heavy ion collisions. Many heavy ion experiments have been carried out to find the signature of the state for a long time. Recently, Au+Au collisions whose center of mass energy per nucleon ($\sqrt{s_{NN}}$) is 200 GeV have been performed at Relativistic Heavy Ion Collider (RHIC) in Brookhaven National Laboratory (BNL), USA. In this thesis, the measurements of neutral pions and direct photons in the relativistic Au+Au collisions using RHIC-PHENIX spectrometer are reported. Neutral pions and direct photons are measured up to high transverse momentum (p_T) of 20 GeV/ c at mid-rapidity. From the comparison with the p+p data measured at the same experiment, the nuclear modifications on the neutral pion and direct photon production in Au+Au collisions are studied.

In the most central collisions, the suppression of neutral pion production at high- p_T has been observed, compared to the yield in p+p collision at same \sqrt{s} scaled by the number of underlying nucleon-nucleon collisions in Au+Au. The suppression is very strong by a factor of ~ 5 , and is almost constant from $p_T \sim 1$ GeV/ c up to $p_T \sim 20$ GeV/ c . In contrast, the direct photon yields in Au+Au collisions are in good agreement with the scaled p+p data.

Since most of high- p_T direct photons originate from initial hard-scattering processes and do not interact with the matter strongly, the agreement between measurement and the scaled p+p data of the direct photon yield suggests the initial hard-scattering probability is not reduced in the Au+Au collisions. It supports that point-like scaling, and binary scaling of high- p_T hadron production relative to p+p collisions is well represented by the Monte Carlo calculation which employs Glauber model. Therefore, the strong suppression of neutral pion production can be understood as due to the interaction of hard scattered partons in the created dense matter.

The suppression is interpreted as the consequence of parton energy loss through gluon bremsstrahlung in the created dense matter. Based on the comparison of neutral pion suppression pattern with a theoretical calculation by I. Vitev who employs GLV energy loss formalism, the effective gluon density (dN_{eff}^g/dy) of the dense matter produced in $\sqrt{s_{NN}} = 200$ GeV Au+Au collisions are estimated quantitatively to be about 1300^{+300}_{-100} . On the assumption of the formation of gluon dominated plasma with the formation time of 0.6 fm, it corresponds to the energy density of 18 GeV/fm³.

Contents

List of Figures	viii
List of Tables	x
1 Introduction	1
1.1 Quark Gluon Plasma and Relativistic Heavy Ion Collisions	2
1.2 Hard Scatterings as The Probes of Extreme State of Matter	2
1.3 Scope of This Thesis	4
2 Physics Background	7
2.1 Energy density of the Quark Gluon Plasma	7
2.2 Relativistic Heavy Ion Collisions	8
2.2.1 Space Time Evolution	9
2.2.2 Model for Heavy Ion Collision	11
2.3 Hard Scatterings and Jet Quenching	12
2.3.1 High- p_T Hadron Production in p+p Collision	13
2.3.2 High- p_T Direct Photon Production in p+p Collision	14
2.3.3 Nuclear Modification Factor	17
2.3.4 Parton Energy Loss	18
2.3.5 Initial State Effect	21
Cronin Effect	21
Nuclear Shadowing	22
2.3.6 Earlier Results on High- p_T Particle Production	24
2.4 Direct Photons from QGP	26
2.4.1 Thermal Photon from QGP	27
2.4.2 Thermal Photon from Hadron Gas	27
2.4.3 Direct Photon from the Interaction of Hard Scattering Partons in QGP .	28
2.4.4 Earlier Results on Direct Photon Production	29
2.5 Aim of This Study	30
3 Experimental Setup	31
3.1 The Relativistic Heavy Ion Collider	31
3.2 The PHENIX Experiment	31
3.2.1 Beam Detectors	32

3.2.2	PHENIX Central Arms	33
	Tracking System	35
	Particle Identification	37
	Calorimetry	38
3.2.3	PHENIX Muon Arms	38
3.2.4	PHENIX Data Acquisition System	39
3.3	The Electromagnetic Calorimeter	40
3.3.1	Lead-Scintillator Calorimeter	42
	Calibration and Monitoring System	42
3.3.2	Test Beam Performance of PbSc Calorimeter	43
	Energy Linearity and Resolution	43
	Position Resolution	45
3.3.3	Lead-Glass Calorimeter	46
3.3.4	Calorimeter Front-End Electronics	47
4	Run Conditions	51
4.1	Beam Conditions	51
4.2	Trigger Conditions	51
5	Data Analysis	55
5.1	Outline	55
5.2	Simulation Procedure	55
5.3	Measurement of the Event Characteristics	57
5.3.1	Minimum Bias Trigger Definition and Efficiency	57
5.3.2	Centrality Determination	57
5.3.3	The Glauber Model	58
5.3.4	Measurement of Reaction Plane	61
5.3.5	Criteria of Good Run Selection	62
5.4	Photon Measurement with PbSc-EMCal	63
5.4.1	Clustering Algorithm	64
	Reconstruction of Hit Position	65
	Reconstruction of Energy	65
	Correction on the Energy of Photons	67
5.4.2	Calibration of Energy Scale	68
5.4.3	Method of Photon Identification	70
5.5	Analysis for Neutral Pion Measurement	74
5.5.1	Extraction of Neutral Pion Signal	75
	Procedure	75
	Background Subtraction	75
5.5.2	Estimation of Neutral Pion Efficiency	77
	Geometrical Acceptance of $\gamma\gamma$ Pairs from π^0	77
	Estimation of Detection Efficiency with Embedding	77
	Simulation Study for π^0 Merging Effect	81
	Contribution from Off-Vertex π^0 s	83

	Bin-Shift Correction	84
5.5.3	Systematic Errors on Neutral Pion Measurement	86
	Peak Extraction	86
	Energy Scale	88
	Particle Identification Efficiency	89
	π^0 Merging Correction	89
	Conversion Correction	90
5.6	Analysis for Direct Photon Measurement	90
5.6.1	Measurement of Inclusive Photon Spectra	91
	Scanning of Real Data to Get Raw Inclusive Photon Spectra	91
	Geometrical Acceptance Correction	91
	Background from Hadrons	91
	Embedding Study for Photon Measurement	93
	Unfolding of the Effect of Energy Smearing	95
	Correction for γ Conversion	98
	Off-Vertex Photon	98
	Bin-Shift Correction	98
5.6.2	Direct Photon Yields	100
	Background from Decays of Hadrons	100
	π^0 Merging Effect on Background Photons	104
	$N_{\text{meas}}^\gamma(p_T)/N_{\text{meas}}^{\pi^0}(p_T)$ and Direct photon Excess Ratio	107
5.6.3	Systematic Errors on Direct Photon Measurement	109
	Correction for Hadron Contamination	110
	Correction for π^0 Merging Effect	110
	Conversion Correction	112
	$N^\eta(p_T)/N^{\pi^0}(p_T)$ Ratio	112
	Error Propagation to Direct Photon Spectrum	113
5.7	Parameterization of Cross-Section in p+p Collisions	116
5.7.1	Parameterization of Neutral Pion Cross-Section in $\sqrt{s} = 200$ GeV p+p Collisions	116
5.7.2	Parameterization of Direct Photon Cross-Section in $\sqrt{s} = 200$ GeV p+p Collisions	117
5.7.3	Propagation of the Error on p+p Cross-Section	118
6	Results	121
6.1	Results on Neutral Pion Production in $\sqrt{s_{\text{NN}}} = 200$ GeV Au+Au Collisions . . .	121
6.2	Results on Direct γ Production in $\sqrt{s_{\text{NN}}} = 200$ GeV Au+Au Collisions . . .	121
7	Discussions	127
7.1	Discussions on Neutral Pion Production in $\sqrt{s_{\text{NN}}} = 200$ GeV Au+Au Collisions	127
7.2	Comparisons with Theoretical Models	129
7.2.1	Comparison with <i>Higher Twist</i> approach	130
7.2.2	Comparison with GLV formalism	131
7.2.3	Comparison of Direct γ R _{AA} with Theoretical Models	134

7.2.4 Extraction of Bulk Matter Property based on $\pi^0 R_{AA}$	136
7.3 Comparison of $\pi^0 R_{AA}$ with single electron R_{AA}	140
8 Conclusion	143
Acknowledgment	145
A Kinematic Variables	147
B Functions to fit p_T spectrum	149
C Fits to data with Correlated Systematic Errors	151
D Centrality Information	155
D.1 Boundary of Centrality	155
D.2 Glauber Table	156
E Neutral Pion Data Tables	157
E.1 Neutral Pion Invariant Yield	157
E.2 Neutral Pion Nuclear Modification Factor	163
F Direct Photon Data Tables	169
F.1 Direct γ Excess Ratio	169
F.2 Direct Photon Invariant Yield	175
F.3 Direct Photon Nuclear Modification Factor	181
G Summary of Systematic Error	185
G.1 Factorized systematic error on π^0 invariant yield	185
G.2 Factorized systematic error on direct photon excess ratio	186
G.3 Factorized systematic error on direct photon invariant yield	187
H $\gamma\gamma$ Invariant Mass Distribution	189
H.1 Central 0-10 %	189
H.2 Central 80-92 %	193
I Information of the analysis	197
I.1 List of Analyzed Runs	197
I.2 Excluded EMCAL Modules	199

List of Figures

1.1	Phase diagram of hadronic matter.	3
1.2	Cartoon of Hard scatterings as a probe of dense matter	4
2.1	Lattice QCD results for the energy density divided by T^4 .	8
2.2	Space-time picture of a nucleus-nucleus collision.	9
2.3	Space-time picture of a nucleus-nucleus collision.	10
2.4	A sketch of the colliding nuclei before and after collision.	11
2.5	The diagram of calculation for hard scattering	13
2.6	Parton distribution function by the CTEQ group as a function of x	14
2.7	π^0 cross section in $\sqrt{s} = 200$ GeV p+p Collisions	15
2.8	Feynman diagrams of photon production processes.	16
2.9	Direct photon cross section in $\sqrt{s} = 200$ GeV p+p collisions	17
2.10	Fraction of the LO and NLO direct photon contribution in p+p $\sqrt{s} = 200$ GeV collisions	18
2.11	Schematics of jet-quenching effect in Heavy Ion Collision.	19
2.12	The expected inclusive p_T distribution of π^0 and nuclear modification factor of charged particle with parton energy loss in QGP.	20
2.13	Cronin effect as a function of p_T expressed as $R_{W/B}$	22
2.14	A phenomenological curve and some experimental data for shadowing effect.	23
2.15	Nuclear modification factor for π^0 production at SPS and ISR	24
2.16	Nuclear modification factor of π^0 in $\sqrt{s_{NN}} = 200$ GeV Au+Au collisions.	25
2.17	Nuclear modification factor of η in $\sqrt{s_{NN}} = 200$ GeV Au+Au collisions.	25
2.18	Direct photon spectrum in $\sqrt{s_{NN}} = 200$ GeV Au+Au collisions	26
2.19	Theoretical calculation of photon emission spectra from central Au+Au collisions at RHIC energy.	28
2.20	Schematics of the direct photon production through the interaction of hard scattering partons in dense matter and its expected yield in Au+Au collisions.	29
3.1	The RHIC Complex	33
3.2	The PHENIX Complex	34
3.3	PHENIX Coordinate	35
3.4	Some pictures of BBC.	36
3.5	BBC Timing Resolution.	36
3.6	Mechanical design of the production tungsten modules.	38

3.7	Vertex distribution measured by PHENIX inner detector	39
3.8	block diagram of DAQ	41
3.9	The PbSc Complex	43
3.10	The PbSc-EMCal calibration overview	44
3.11	Energy Linearity of PbSc	45
3.12	Energy Resolution of PbSc	46
3.13	Position resolution of PbSc	47
3.14	The PbGl Supermodule	48
3.15	Block diagram of the energy and timing measurement circuits for EMCal	49
3.16	AMU sampling diagram	50
4.1	Integrated luminosity in Year-4 Au+Au run at $\sqrt{s_{\text{NN}}} = 200$ GeV	52
4.2	z -vertex distribution	53
5.1	Simulation Procedure	56
5.2	Centrality determination in PHENIX	58
5.3	Viewing of the collision region.	59
5.4	The result of Glauber calculation	60
5.5	Systematic Uncertainty of the Centrality Definition	61
5.6	Schematic view of the strong elliptic flow at RHIC	62
5.7	Centrality distribution	63
5.8	Demonstration of the cluster splitting	64
5.9	Event display of the deposited energy on EMCal sector	66
5.10	An example of energy fraction from a electromagnetic cluster	67
5.11	The systematic error on π^0 and photon yield	69
5.12	Result of Tower by Tower Energy Correction	70
5.13	Run by Run energy scale dependence	71
5.14	Tower dependence of the energy scale	72
5.15	The PHENIX Complex	73
5.16	Measured energy with respect to input energy for each hadrons and electrons .	74
5.17	Sample output of π^0 peak	76
5.18	Number of events for each centrality	77
5.19	Raw spectra of neutral pion	78
5.20	Geometrical Acceptance of π^0	79
5.21	π^0 mass peak comparing with simulation	80
5.22	Comparison of π^0 peak mean between real and simulation	81
5.23	Comparison of π^0 peak width between real and simulation	82
5.24	π^0 detection efficiency	83
5.25	Distance of two clusters on the EMCal	84
5.26	π^0 merging probability as a function of $\pi^0 p_T$ and energy asymmetry	84
5.27	Comparison of π^0 merging probability with test beam result	85
5.28	Merging probability of embedded π^0 as a function of $\pi^0 p_T$	86
5.29	Ratio of reconstructed secondary π^0 s	87
5.30	Off-vertex π^0 from K_S^0	87

5.31 Ratio of corrected π^0 yield between different mass window cut.	88
5.32 Ratio of corrected π^0 yield between different cut	89
5.33 Systematic error for π^0 merging correction	90
5.34 Raw energy spectra measured with PbSc	92
5.35 Acceptance for single photons in PbSc.	93
5.36 Input hadron spectra for the estimation of hadron contamination.	94
5.37 Estimation of the Hadron contamination as a function of measured p_T	94
5.38 Detection efficiency of single photons	95
5.39 Energy smearing function of photon	96
5.40 Procedure of unfolding of the spectra	97
5.41 The ratio of re-smeared photon spectrum and original spectrum.	97
5.42 Smearing function of converted photons and non-converted photons	99
5.43 Source of off-vertex photon contribution	99
5.44 π^0 fitting for background calculation	101
5.45 Photon background from decays of hadrons	103
5.46 γ contribution from K_S^0	104
5.47 Survival ratio of the cluster where two photons from a π^0 end up in a same cluster	105
5.48 Probability of merged cluster which pass $\chi^2 < 3$ cut	106
5.49 $N_{\text{bkgd}}^\gamma(p_T)/N_{\text{fit}}^{\pi^0}(p_T)$ for each merging condition.	107
5.50 $N_{\text{meas}}^\gamma(p_T)/N_{\text{meas}}^{\pi^0}(p_T)$ (red) comparing with $N_{\text{bkgd}}^\gamma(p_T)/N_{\text{fit}}^{\pi^0}(p_T)$ (blue) in the case of $\chi^2 < 3$ cut.	108
5.51 $N_{\text{meas}}^\gamma(p_T)/N_{\text{meas}}^{\pi^0}(p_T)$ (red) comparing with $N_{\text{bkgd}}^\gamma(p_T)/N_{\text{fit}}^{\pi^0}(p_T)$ (blue) in the case of Stochastic cut 2.	108
5.52 Ratio of fully corrected inclusive photon spectra	111
5.53 correlation of energy smearing of merged π^0 clusters and input $p_T(\pi^0)$	112
5.54 Comparison of $N_{\text{meas}}^\gamma(p_T)/N_{\text{meas}}^{\pi^0}(p_T)$ (with and without shower shape cut)	113
5.55 Direct photon excess ratio for each particle identification and centrality.	114
5.56 $N^\eta(p_T)/N^{\pi^0}(p_T)$ ratio in p+p, d+Au, and Au+Au minimum bias and three centrality classes (0 – 20 %, 20 – 60 %, 60 – 92 %).	115
5.57 Parameterization of the neutral pion cross-section in $\sqrt{s} = 200$ GeV p+p collisions.	116
5.58 Parameterization of the direct photon cross-section in $\sqrt{s} = 200$ GeV p+p collisions.	117
5.59 Propagated error on p+p cross-section	118
 6.1 Neutral pion invariant yields as a function of p_T for nine centrality selections and minimum bias Au+Au collisions at $\sqrt{s_{\text{NN}}} = 200$ GeV.	122
6.2 Neutral pion nuclear modification factor as a function of p_T for each centrality in Au+Au collisions at $\sqrt{s_{\text{NN}}} = 200$ GeV.	123
6.3 Direct photon invariant yields as a function of p_T for nine centrality selections and minimum bias Au+Au collisions at $\sqrt{s_{\text{NN}}} = 200$ GeV.	124
6.4 Direct photon invariant yields as a function of p_T for nine centrality selections and minimum bias Au+Au collisions at $\sqrt{s_{\text{NN}}} = 200$ GeV.	125

6.5	Direct photon nuclear modification factor as a function of p_T for each centrality in Au+Au collisions at $\sqrt{s_{NN}} = 200$ GeV.	126
7.1	Direct photon and $\pi^0 R_{AA}$ as a function of number of participants	128
7.2	Comparison of Direct photon R_{AA} with the calculation which takes isospin effect into account.	129
7.3	Comparison of $\pi^0 R_{AA}$ with theoretical calculation by Higher Twist Approach. .	132
7.4	high- p_T $\pi^0 R_{AA}$ as a function of N_{part}	134
7.5	Comparison of direct photon R_{AA} with theoretical calculations	135
7.6	Comparison of Direct photon R_{AA} with the calculation which takes jet-quenching effect and isospin effect into account.	137
7.7	Comparison of Direct photon R_{AA} with the calculation which takes all of effect into account.	137
7.8	Likelihood function ratio as a function of energy loss parameter in Higher Twist formalism.	138
7.9	Likelihood function ratio as a function of energy loss parameter in GLV formalism.	139
7.10	Comparison of the $\pi^0 R_{AA}$ with single electron R_{AA}	141
G.1	Factorized systematic error on π^0 invariant yield	185
G.2	Factorized systematic error on direct photon excess ratio	186
G.3	Factorized systematic error on direct photon excess ratio (I)	187
G.4	Factorized systematic error on direct photon excess ratio (II)	188
H.1	$\gamma\gamma$ invariant mass spectra in 0-10 % central (I)	189
H.2	$\gamma\gamma$ invariant mass spectra in 0-10 % central (II)	190
H.3	$\gamma\gamma$ invariant mass spectra in 0-10 % central (III)	191
H.4	$\gamma\gamma$ invariant mass spectra in 0-10 % central (IV)	192
H.5	$\gamma\gamma$ invariant mass spectra in 0-10 % central (V)	193
H.6	$\gamma\gamma$ invariant mass spectra in 80-92 % central (I)	193
H.7	$\gamma\gamma$ invariant mass spectra in 80-92 % central (II)	194
H.8	$\gamma\gamma$ invariant mass spectra in 80-92 % central (III)	195
H.9	$\gamma\gamma$ invariant mass spectra in 80-92 % central (IV)	196
I.1	Map of excluded EMCAL towers for π^0 /photon analysis	199

List of Tables

1.1	Summary of Quark quantum numbers	2
3.1	Parameters and performance for RHIC heavy ion run	32
3.2	Summary of the PHENIX detectors.	37
3.3	Summary of the EMCal subsystem.	42
4.1	Typical Beam Conditions for the 100GeV/u Au	51
5.1	Run by Run energy scale correction	70
5.2	Systematic Error of π^0 invariant yield	88
5.3	Conversion probability due to the material in front of EMCal	98
5.4	Dominant sources of background photons from hadron	102
5.5	The photon yield coming from each sources.	106
5.6	Systematic errors on the inclusive photon invariant yields	109
5.7	Systematic errors on the direct photon excess double ratio	109
5.8	Systematic errors on the direct photon yield.	110
D.1	Boundary of Centrality in $\sqrt{s_{NN}} = 200$ GeV Au+Au collisions.	155
D.2	Glauber Calculation for $\sqrt{s_{NN}} = 200$ GeV Au+Au	156
E.1	π^0 Invariant Yield in $\sqrt{s_{NN}} = 200$ GeV Au+Au Collisions (0-10 % Central).	157
E.2	π^0 Invariant Yield in $\sqrt{s_{NN}} = 200$ GeV Au+Au Collisions (10-20 % Central).	158
E.3	π^0 Invariant Yield in $\sqrt{s_{NN}} = 200$ GeV Au+Au Collisions (20-30 % Central).	158
E.4	π^0 Invariant Yield in $\sqrt{s_{NN}} = 200$ GeV Au+Au Collisions (30-40 % Central).	159
E.5	π^0 Invariant Yield in $\sqrt{s_{NN}} = 200$ GeV Au+Au Collisions (40-50 % Central).	159
E.6	π^0 Invariant Yield in $\sqrt{s_{NN}} = 200$ GeV Au+Au Collisions (50-60 % Central).	160
E.7	π^0 Invariant Yield in $\sqrt{s_{NN}} = 200$ GeV Au+Au Collisions (60-70 % Central).	160
E.8	π^0 Invariant Yield in $\sqrt{s_{NN}} = 200$ GeV Au+Au Collisions (70-80 % Central).	161
E.9	π^0 Invariant Yield in $\sqrt{s_{NN}} = 200$ GeV Au+Au Collisions (80-92 % Central).	161
E.10	π^0 Invariant Yield in $\sqrt{s_{NN}} = 200$ GeV Au+Au Collisions (Minimum Bias).	162
E.11	$\pi^0 R_{AA}$ in $\sqrt{s_{NN}} = 200$ GeV Au+Au Collisions (0-10 % Central).	163
E.12	$\pi^0 R_{AA}$ in $\sqrt{s_{NN}} = 200$ GeV Au+Au Collisions (10-20 % Central).	164
E.13	$\pi^0 R_{AA}$ in $\sqrt{s_{NN}} = 200$ GeV Au+Au Collisions (20-30 % Central).	164
E.14	$\pi^0 R_{AA}$ in $\sqrt{s_{NN}} = 200$ GeV Au+Au Collisions (30-40 % Central).	165
E.15	$\pi^0 R_{AA}$ in $\sqrt{s_{NN}} = 200$ GeV Au+Au Collisions (40-50 % Central).	165

E.16 $\pi^0 R_{AA}$ in $\sqrt{s_{NN}} = 200$ GeV Au+Au Collisions (50-60 % Central).	166
E.17 $\pi^0 R_{AA}$ in $\sqrt{s_{NN}} = 200$ GeV Au+Au Collisions (60-70 % Central).	166
E.18 $\pi^0 R_{AA}$ in $\sqrt{s_{NN}} = 200$ GeV Au+Au Collisions (70-80 % Central).	167
E.19 $\pi^0 R_{AA}$ in $\sqrt{s_{NN}} = 200$ GeV Au+Au Collisions (80-92 % Central).	167
E.20 $\pi^0 R_{AA}$ in $\sqrt{s_{NN}} = 200$ GeV Au+Au Collisions (Minimum Bias).	168
F.1 Direct γ Excess Ratio in $\sqrt{s_{NN}} = 200$ GeV Au+Au Collisions (0-10 % Central).	169
F.2 Direct γ Excess Ratio in $\sqrt{s_{NN}} = 200$ GeV Au+Au Collisions (10-20 % Central).	170
F.3 Direct γ Excess Ratio in $\sqrt{s_{NN}} = 200$ GeV Au+Au Collisions (20-30 % Central).	170
F.4 Direct γ Excess Ratio in $\sqrt{s_{NN}} = 200$ GeV Au+Au Collisions (30-40 % Central).	171
F.5 Direct γ Excess Ratio in $\sqrt{s_{NN}} = 200$ GeV Au+Au Collisions (40-50 % Central).	171
F.6 Direct γ Excess Ratio in $\sqrt{s_{NN}} = 200$ GeV Au+Au Collisions (50-60 % Central).	172
F.7 Direct γ Excess Ratio in $\sqrt{s_{NN}} = 200$ GeV Au+Au Collisions (60-70 % Central).	172
F.8 Direct γ Excess Ratio in $\sqrt{s_{NN}} = 200$ GeV Au+Au Collisions (70-80 % Central).	173
F.9 Direct γ Excess Ratio in $\sqrt{s_{NN}} = 200$ GeV Au+Au Collisions (80-92 % Central).	173
F.10 Direct γ Excess Ratio in $\sqrt{s_{NN}} = 200$ GeV Au+Au Collisions (Minimum Bias).	174
F.11 Direct γ Invariant Yield in $\sqrt{s_{NN}} = 200$ GeV Au+Au Collisions (0-10 % Central).	175
F.12 Direct γ Invariant Yield in $\sqrt{s_{NN}} = 200$ GeV Au+Au Collisions (10-20 % Central).	176
F.13 Direct γ Invariant Yield in $\sqrt{s_{NN}} = 200$ GeV Au+Au Collisions (20-30 % Central).	176
F.14 Direct γ Invariant Yield in $\sqrt{s_{NN}} = 200$ GeV Au+Au Collisions (30-40 % Central).	177
F.15 Direct γ Invariant Yield in $\sqrt{s_{NN}} = 200$ GeV Au+Au Collisions (40-50 % Central).	177
F.16 Direct γ Invariant Yield in $\sqrt{s_{NN}} = 200$ GeV Au+Au Collisions (50-60 % Central).	178
F.17 Direct γ Invariant Yield in $\sqrt{s_{NN}} = 200$ GeV Au+Au Collisions (60-70 % Central).	178
F.18 Direct γ Invariant Yield in $\sqrt{s_{NN}} = 200$ GeV Au+Au Collisions (70-80 % Central).	179
F.19 Direct γ Invariant Yield in $\sqrt{s_{NN}} = 200$ GeV Au+Au Collisions (80-92 % Central).	179
F.20 Direct γ Invariant Yield in $\sqrt{s_{NN}} = 200$ GeV Au+Au Collisions (Minimum Bias).	180
F.21 Direct γR_{AA} in $\sqrt{s_{NN}} = 200$ GeV Au+Au Collisions (0-10 % Central).	181
F.22 Direct γR_{AA} in $\sqrt{s_{NN}} = 200$ GeV Au+Au Collisions (10-20 % Central).	181
F.23 Direct γR_{AA} in $\sqrt{s_{NN}} = 200$ GeV Au+Au Collisions (20-30 % Central).	182
F.24 Direct γR_{AA} in $\sqrt{s_{NN}} = 200$ GeV Au+Au Collisions (30-40 % Central).	182
F.25 Direct γR_{AA} in $\sqrt{s_{NN}} = 200$ GeV Au+Au Collisions (40-50 % Central).	182
F.26 Direct γR_{AA} in $\sqrt{s_{NN}} = 200$ GeV Au+Au Collisions (50-60 % Central).	183
F.27 Direct γR_{AA} in $\sqrt{s_{NN}} = 200$ GeV Au+Au Collisions (60-70 % Central).	183
F.28 Direct γR_{AA} in $\sqrt{s_{NN}} = 200$ GeV Au+Au Collisions (70-80 % Central).	183
F.29 Direct γR_{AA} in $\sqrt{s_{NN}} = 200$ GeV Au+Au Collisions (80-92 % Central).	184
F.30 Direct γR_{AA} in $\sqrt{s_{NN}} = 200$ GeV Au+Au Collisions (Minimum Bias).	184
I.1 Runlist 1 Au+Au	197
I.2 Runlist 2 Au+Au	198

Chapter 1

Introduction

Standard Model is a theory which describes three of the four known fundamental interactions (electromagnetic, strong and weak) between the elementary particles that make up all matter. For instance, nucleons are composed of quarks and gluons, which are elemental particles described by the Standard Model. Table 1.1 gives a list of the six flavors of quarks that have been observed. As the underlying theory of the interaction of quarks and gluons, Quantum ChromoDynamics (QCD), a local $SU(3)$ gauge theory, has been developed, and the theory is recognized as the correct theory for the strong force. One of the important features in the QCD is *color confinement*: quarks and gluons have a degree of freedom of color, and they are confined in hadrons as a color-singlet state. The interesting observation indicating quark constituent is the discovery of bound states formed from heavy quark-antiquark pairs, such as J/ψ ($c\bar{c}$) and Υ ($b\bar{b}$). In the 1970s, a massive $c\bar{c}$ meson state, J/ψ , was observed in e^+e^- collisions at Stanford Linear Accelerator Center (SLAC) using the e^+e^- collider, Stanford Positron-Electron Asymmetric Rings (SPEAR) [76]. This state was also observed in collisions of 28 GeV protons on a beryllium (Be) target using alternating gradient synchrotron (AGS) at Brookhaven National Laboratory (BNL) [74].

Even prior to the discovery of J/ψ , the property of nuclear matter at density and temperature extremes was of the great interest [110, 178, 177]. Especially it was proposed that new state of nuclear matter could be associated with a corresponding change in the structure of the vacuum. The phenomena of quark confinement is a consequence of the nonperturbative structure of the vacuum. The vacuum structure is modified at high temperatures and/or densities, suggesting that quarks and gluons under such conditions would be deconfined. The idea of quark deconfinement was also proposed early in the development of QCD. The reduction of the coupling constant at small distances, this property is so-called *asymptotic freedom*, indicated that the dense nuclear matter at the center of neutron stars would consist of deconfined quarks and gluons [111]. The first detailed examination of the high-temperature state was given by E.V. Shuryak in 1980 [200], and is also notable for proposing the phrase Quark Gluon Plasma (QGP) to describe the deconfined state.

Flavor	Q	J	I	I_z	B	S	C	B^*	T
up	$\frac{2}{3}$	$\frac{1}{2}$	$\frac{1}{2}$	$\frac{1}{2}$	$\frac{1}{3}$	0	0	0	0
down	$-\frac{1}{3}$	$\frac{1}{2}$	$\frac{1}{2}$	$-\frac{1}{2}$	$\frac{1}{3}$	0	0	0	0
strange	$-\frac{1}{3}$	$\frac{1}{2}$	0	0	$\frac{1}{3}$	-1	0	0	0
charm	$\frac{2}{3}$	$\frac{1}{2}$	0	0	$\frac{1}{3}$	0	1	0	0
bottom	$-\frac{1}{3}$	$\frac{1}{2}$	0	0	$\frac{1}{3}$	0	0	-1	0
top	$\frac{2}{3}$	$\frac{1}{2}$	0	0	$\frac{1}{3}$	0	0	0	1

Table 1.1: Summary of quark quantum numbers. “Q” is electric charge. “J” is spin. “I” is isospin. “ I_z ” is third component of isospin. “B” is baryon number. “S” is strangeness. “C” is charm quantum number. “ B^* ” is bottom quantum number. “T” is top quantum number.

1.1 Quark Gluon Plasma and Relativistic Heavy Ion Collisions

When the QGP is formed, quarks and gluons are deconfined. Such a state of matter is considered to have existed in the early universe, a few μs after the “Big Bang”. As the universe expands and cools down, the distance between partons (quarks and gluons) grows. The binding force between partons increases, and a phase transition eventually happens, when partons are combined with each other, and confined in colorless hadrons.

The phase diagram of hadronic matter including the QGP is schematically drawn as shown in Fig. 1.1. The horizontal axis is baryon density in the unit of density of normal nuclear matter: $\sim 0.15 \text{ GeV/fm}^3$ ($= 2.7 \times 10^{14} \text{ g/cm}^3$) and vertical axis is temperature. The diagram illustrate that the QGP exist at very high temperature and/or high baryon density conditions. The phases of QCD and the precise locations of critical lines and points are under study.

One of the ways to create the QGP is thought to use relativistic nucleus-nucleus collisions. In the case of nucleus-nucleus collisions with lower energy, provided at CERN-SPS and/or BNL-AGS, lower temperature but high baryon density could be achieved. In the head-on nucleus-nucleus collisions such as Au+Au with $\sqrt{s_{\text{NN}}} \geq O(10\text{-}100 \text{ GeV})$, where $\sqrt{s_{\text{NN}}}$ is center of mass energy per nucleon, a high energy and density matter could be produced (but low in baryon density). The Relativistic Heavy Ion Collider at BNL can collide Au nucleus at $\sqrt{s_{\text{NN}}} = 200 \text{ GeV}$, and it can provide with such situation.

1.2 Hard Scatterings as The Probes of Extreme State of Matter

Due to the complication of various processes after the heavy ion collisions, it is difficult to measure the signature of QGP directly. One of the possible probes is hadrons with large transverse momentum (p_T). Such hadrons are mainly the leading particles from the fragmentation

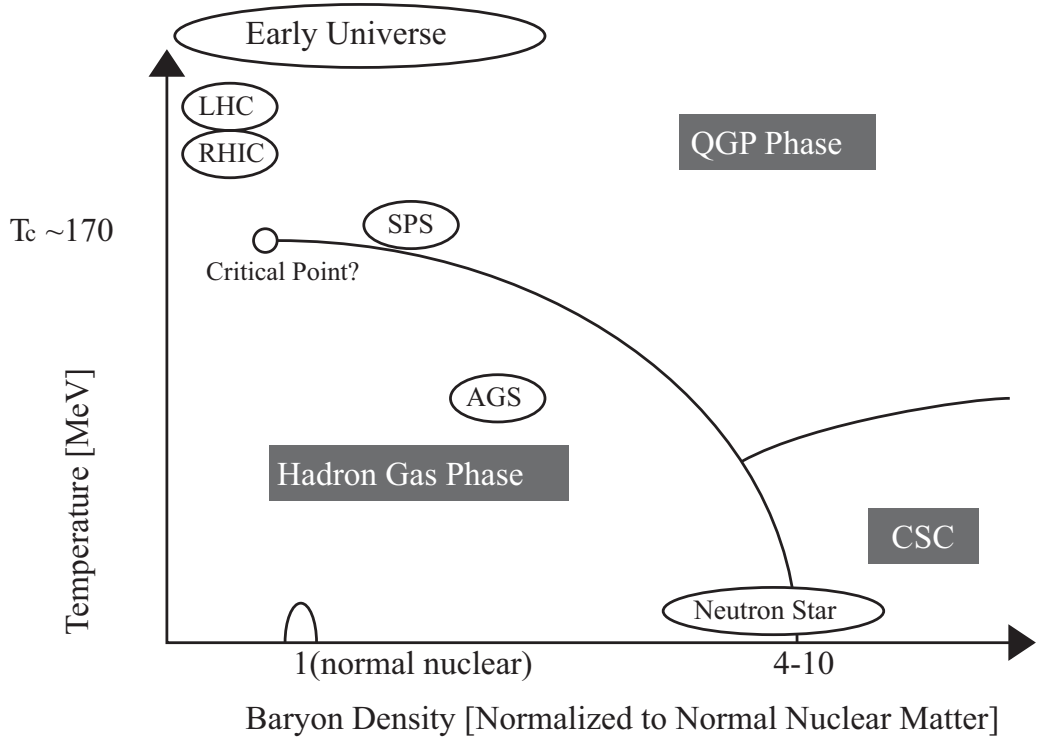


Figure 1.1: Phase diagram of hadronic matter. The emerging picture of the transition from hadronic to quark matter is illustrated.

of quarks and gluons, scattered with a large momentum transfer Q^2 . Hadron production can be estimated from nucleon-nucleon collisions if nuclear medium effects are absent. The production cross section of high- p_T hadrons is well reproduced by the calculation which uses three factorized processes: initial distribution of partons in the colliding species, the elementary parton-parton cross section and the fragmentation process of partons into hadrons. Since hard parton scatterings have small cross sections, one can regard the nuclei as an incoherent superposition of partons (“point-like scaling”). This can be approximated by modeling the nucleus-nucleus collision as a sum of independent nucleon-nucleon collisions (“binary scaling”), as illustrated in Fig. 1.2 (a). The difference between the measurement and the expectation may attribute to the created medium as shown in Fig. 1.2 (b). It has been predicted that the hard scattered partons lose their energy during passing through the high dense medium. Energy loss of the jet parton is primary due to gluon radiation, as similar to the electromagnetic bremsstrahlung radiation [150].

Direct photons are also a powerful probe to investigate the created matters during relativistic heavy ion collisions, since photons do not interact strongly once produced and thus can directly carry out information of the states of matter as shown in Fig. 1.2 (c). Photons in heavy ion collisions are expected to contain many contribution, hard scattering from the initial state and thermal radiation from the QGP. The hard scattering direct photons provide the confirmation of point-like scaling, and binary scaling of high- p_T hadron production in nucleus-nucleus collisions. In addition, the yield of photons provides an excellent input to theoretical predictions because photons have small ambiguity arising from uncertainties on hadronization process.

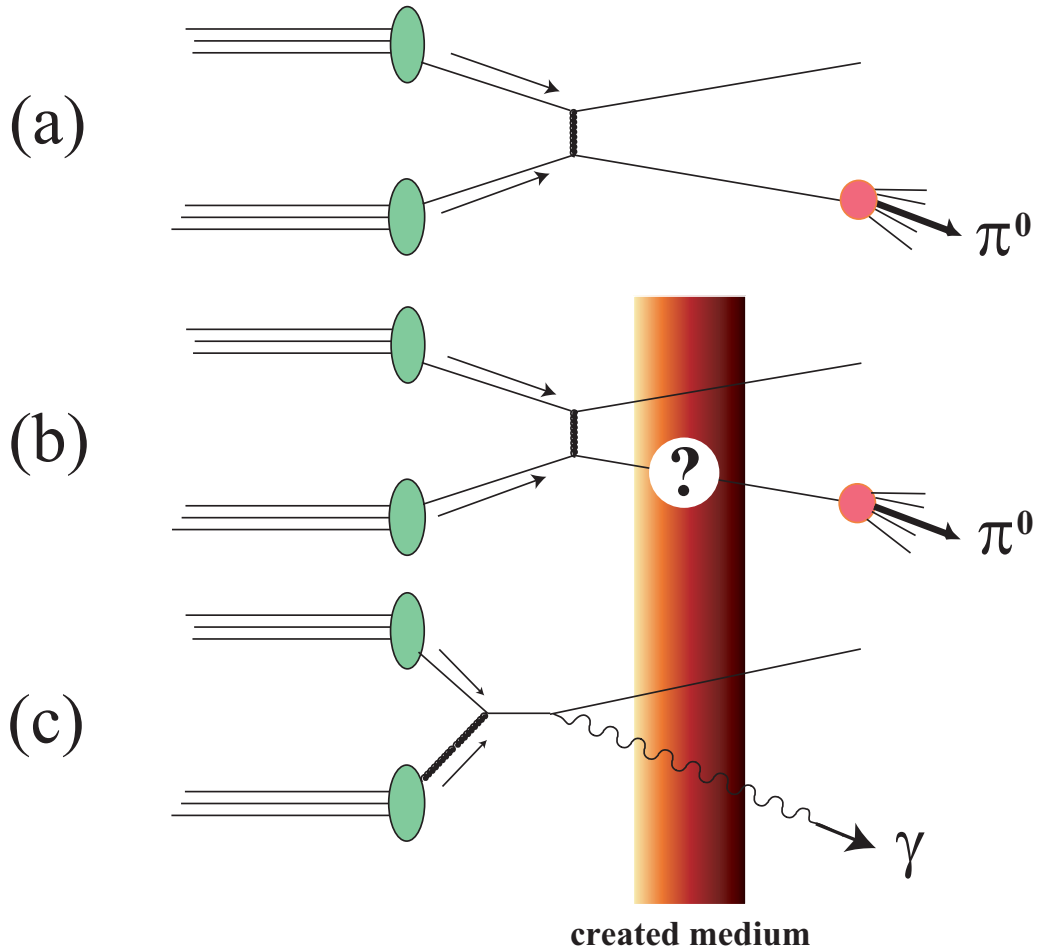


Figure 1.2: Sketch of Hard scatterings as a probe of dense matter.

While it is predicted that QGP exist at extremely high temperature and/or high density conditions, which might be achieved by relativistic heavy ion collisions, nobody finds the signature of QGP and knows its critical temperature and/or density. In order to study the property of created matter in $\sqrt{s_{NN}} = 200$ GeV Au+Au collision, neutral pions are measured as the hard probes, and direct photons are measured as the penetrating probes. Particularly, the study of high- p_T neutral pion and high- p_T direct photon provides the different measurement with similar systematics in terms of the hard production processes that would give more detailed insight in the states.

1.3 Scope of This Thesis

chapter 2 The physics background about the Quark Gluon Plasma, production of such extreme matter using relativistic heavy ion collisions, and measurement of high- p_T π^0 s and direct photons as probes of the created matter will be described.

chapter 3 The RHIC-PHENIX Experiment will be described in this chapter. Since EMCAL detector is used mainly in this analysis, the characteristics of EMCAL will be described in detail.

chapter 4 The beam condition, luminosity conditions and the trigger condition in 2004 (Year-4) Au+Au runs are explained.

chapter 5 The analysis of the neutral pion and the direct photon production will be explained.

chapter 6 The results of neutral pion and direct photon measurements are described.

chapter 7 Based on the results of neutral pion and direct photon measurements, the properties of bulk matter produced at RHIC will be discussed.

chapter 8 Conclude this thesis.

Chapter 2

Physics Background

In this chapter, the expected properties of QGP, and experimental approach to study the new deconfined phase will be described at first. Then, observables and probes to study the new matter will be mentioned. Mainly, the motivations for the measurement of π^0 and direct photons will be discussed.

2.1 Energy density of the Quark Gluon Plasma

The “Quark Gluon Plasma” (QGP) is a state where quarks and gluons are deconfined. In the thermal equilibrium, each bosonic degree of freedom contributes $(\pi^2/30) \cdot T^4$ to the energy density in the limit of massless non-interacting particles (“Stefan-Boltzmann” limit). And each fermionic degree of freedom contributes 7/8 of this value (due to the difference between the Fermi-Dirac statistics and the Bose-Einstein statistics). The corresponding limits of the energy density (ϵ_{SB}) is:

$$\epsilon_{SB} = \left(\frac{7}{8} d_{\text{quark}} + d_{\text{gluon}} \right) \frac{\pi^2}{30} T^4, \quad (2.1)$$

where d_{quark} and d_{gluon} stand for the degree of freedom of quarks and gluons, respectively. For the case of 2 (or 3) active flavor quark-gluon plasma, the energy density ($\epsilon_{SB}^{2(3)}$) is:

$$\epsilon_{SB}^{2(3)} = \left(2_f (\text{or } 3_f) \cdot 2_s \cdot 2_q \cdot 3_c \cdot \frac{7}{8} + 2_s \cdot 8_c \right) \frac{\pi^2}{30} T^4 \quad (2.2)$$

$$= 37 (\text{or } 47.5) \frac{\pi^2}{30} T^4. \quad (2.3)$$

In the Eq. 2.2, the degree of freedom for quark (the flavor, spin, quark/antiquark and color factors) and that for gluons (spin and color factors) are indicated as the sub indices.

According to the detailed calculation from the Lattice QCD, a phase transformation to QGP is expected to occur at a critical temperature $T_C \sim 170$ MeV [168], which corresponds to an energy density of $\epsilon_c \sim 1.2$ GeV/fm³. Figure 2.1 shows the result from Lattice QCD calculation

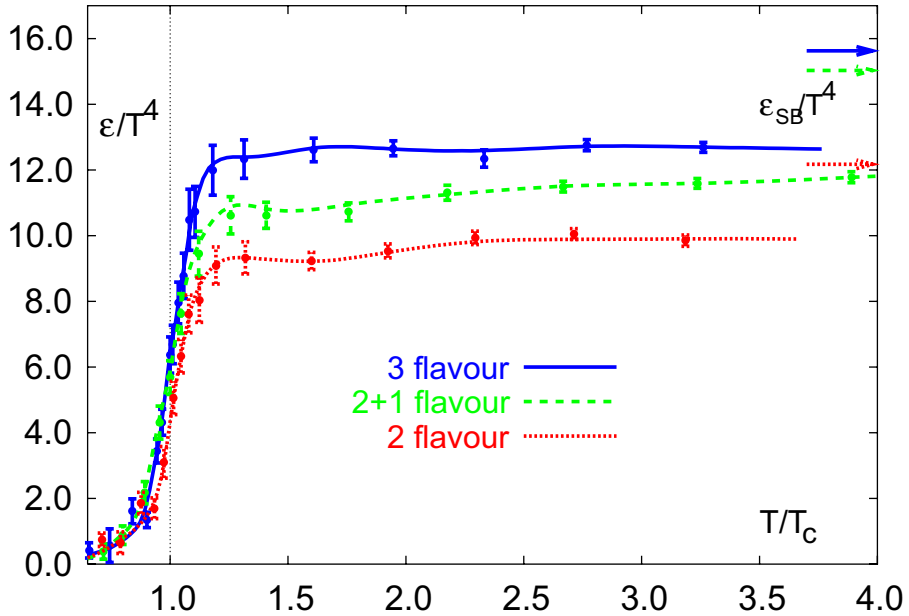


Figure 2.1: Lattice QCD results [168] for the energy density (ϵ) divided by T^4 , which is degree of freedom as known from Eq. 2.1), as a function of the temperature scaled by the critical temperature T_C . The arrows on the right side indicate the values for the Stefan-Boltzmann limit.

on the energy density as a function of temperature [167]. If the temperature is higher than the critical temperature (T_C), the phase would transit into a new phase, and the degree of freedom ($\propto \epsilon/T^4$) would be increased. The Stefan-Boltzmann limit of the energy density from Eq. 2.3 is also shown in Fig. 2.1. It is not reached even for temperatures four times larger than the critical temperature, indicating that interaction between quarks and gluons are still not negligible at these temperatures.

2.2 Relativistic Heavy Ion Collisions

The formation of QGP and its phase transition to hadronic matter are expected to be realized in the laboratory by colliding high energy heavy ions. Energy is deposited in the overlap region of the two colliding nuclei, and is spent to produce quark-antiquark pairs and gluons which potentially form a QGP.

The early investigations in a fixed-target experiments at the BNL AGS (c. 1987 – 1995) and the CERN SPS (c. 1987 – recent) have not give the answer for the existence of QGP. The heavy ion program started with the commissioning of BNL Relativistic Heavy Ion Collider (RHIC), a dedicated facility for the study of nuclear collisions at ultra-relativistic energies [99]. The RHIC accelerator and its four experiments [16, 7, 84, 9] were successfully commissioned in the summer of 2000. After that, the experiments have acquired data for Au+Au collisions at various energies (center of mass energy per nucleon, $\sqrt{s_{NN}} = 62.4, 130$, and 200 GeV), for p+p at same \sqrt{s} , and for d+Au collisions ($\sqrt{s_{NN}} = 200$ GeV/c).

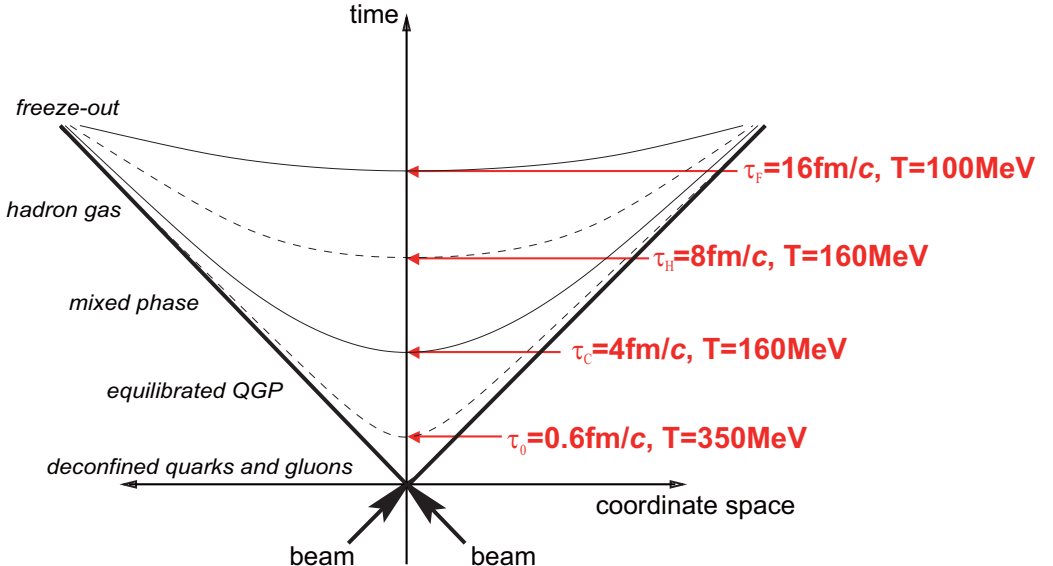


Figure 2.2: Space-time picture of a nucleus-nucleus collision. The times and temperatures for different phases are taken from [173].

2.2.1 Space Time Evolution

Relativistic heavy ion collision is a complicated process, because various phases are expected to exist intricately through initial collision to a final cold hadronic phase. J.D. Bjorken illustrated a scenario to describe the space-time evolution of the heavy ion collisions [103]. He estimated the initial energy density from the scenario.

Figure 2.2 shows the space-time picture of evolution of the matter created in ultra-relativistic heavy ion collisions at RHIC with the longitudinal coordinate z and the time coordinate t . At $t = 0$, free partons are produced by a collision between the two nuclei. These partons are mainly gluons. The system is initially not in thermal equilibrium, and the dynamics may be described by a cascade of colliding partons. The subsequent multiple parton scattering brings the matter to local equilibrium. If the deposited energy is large enough and exceeds the critical energy density, QGP might be formed, at the proper time $t = \tau_0$. If the QGP is formed, the system would evolve like fluid, expand and cool down. At $t = \tau_C$, the system will reach the critical temperature between QGP and ordinary hadrons, and after mixed phase, the system consists of the ordinary hadrons interacting with each other at $t = \tau_H$. At $t = \tau_F$, the each hadrons do not interact and produced particles are moving away.

The achieved energy density at the formation time (τ_0) can be estimated as follows. In the relativistic heavy ion collisions, nuclei look like pancakes due to the Lorentz contraction ($\gamma \sim 106$ at $\sqrt{s_{NN}} = 200$ GeV) in the c.m.s. of the collision. Once a relativistic heavy ion collision occurs, the two colliding pancakes pass through each other, and many inelastic nucleon-nucleon collisions occur in a very short time. Then, a large amount of energy is deposited in a small region of space as shown in Fig. 2.3. For a cylindrical region with longitudinal thickness $2d$ and the overlap area S ($S = \pi r^2$) at $t = \tau_0$, the energy E in the cylindrical region is estimated as:

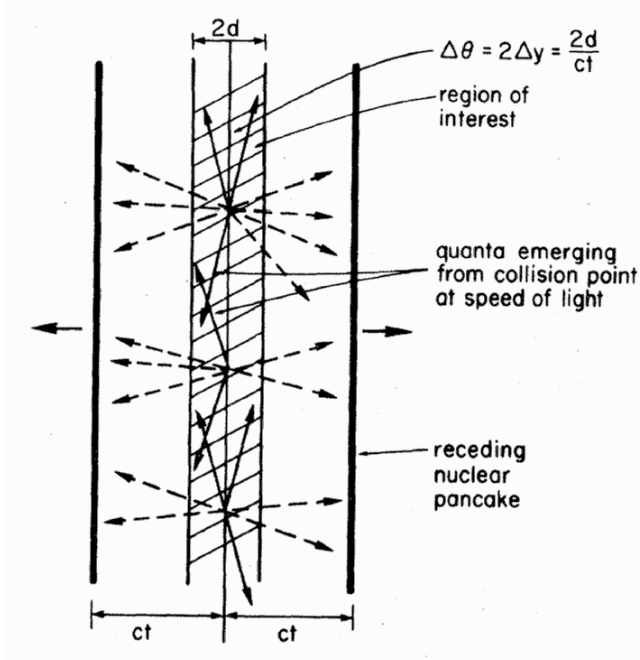


Figure 2.3: Figure from Bjorken [103] illustrating the geometry of initially produced particles at a time t after the overlap of the incoming nuclei.

$$E = \frac{d\langle E \rangle}{dy} \Delta y \quad (2.4)$$

$$= \frac{d\langle E \rangle}{dy} \frac{2d}{\tau_0}. \quad (2.5)$$

where $\langle E \rangle$ is the mean energy, and y is the rapidity as defined at Appendix A. Then, with the relation of $d\langle E_T \rangle / dy|_{y=0} \approx d\langle E \rangle / dy|_{y=0}$ (no longitudinal velocity at $y = 0$), and $r = r_0 \cdot N^{1/3}$ (nucleon radii), the energy density is estimated as:

$$\epsilon_{bj} = \frac{E}{2dS} \quad (2.6)$$

$$= \frac{1}{S} \frac{d\langle E \rangle}{dy} \frac{1}{\tau_0}, \quad (2.7)$$

$$= \frac{1}{\tau_0 \pi r_0^2 N^{2/3}} \frac{d\langle E \rangle}{dy}, \quad (2.8)$$

$$\approx \frac{1}{\tau_0 \pi r_0^2 N^{2/3}} \frac{d\langle E_T \rangle}{dy} \Big|_{y=0}, \quad (2.9)$$

$$= \frac{\langle E_T \rangle}{\tau_0 \pi r_0^2 N^{2/3}} \frac{dN}{dy} \Big|_{y=0}. \quad (2.10)$$

In the equation, τ_0 is the typical formation time as shown in Fig. 2.2, r_0 is the constant term for nucleon radii, N is the number of participating nucleons, $\langle E_T \rangle$ is the mean transverse energy and

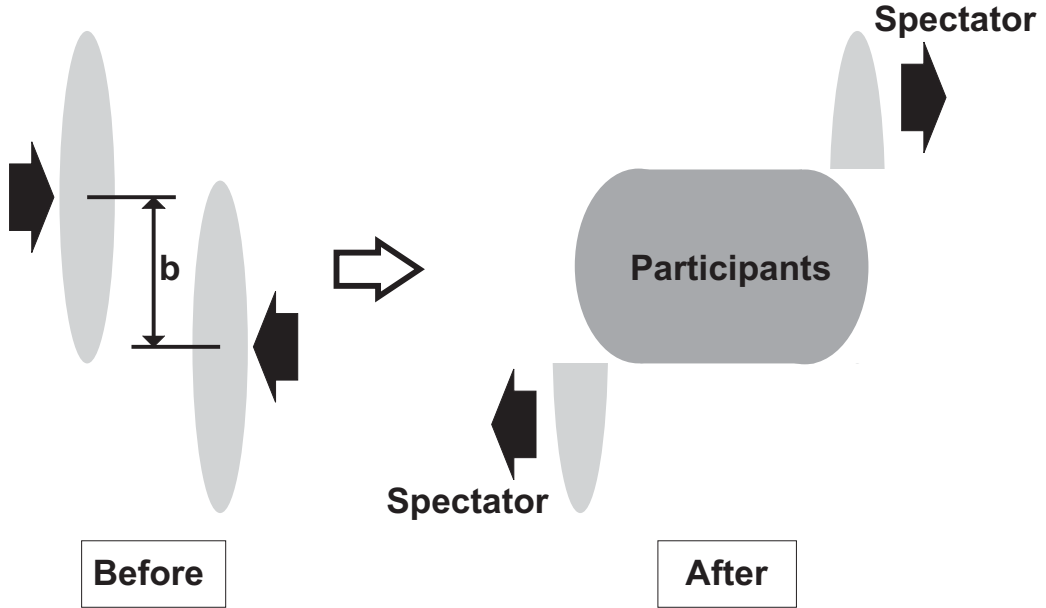


Figure 2.4: A sketch of the colliding nuclei before and after collision. They approach each other with impact parameter b before collision. After the collision, the system consists of two components: participants and spectators.

dN/dy is the rapidity density of the multiplicity. Also it is assumed as $d\langle E_T \rangle /dy = \langle E_T \rangle \cdot dN/dy$ in Eq. 2.10.

If we use $\tau_0 = 1 \text{ fm}/c$ and $r_0 = 1.18 \text{ fm}$ in the head-on nucleus-nucleus collision, the Bjorken energy density is estimated accordingly as $\sim 1.5 \text{ GeV}/\text{fm}^3$ in Au+Au collisions at AGS ($\sqrt{s_{NN}} = 5 \text{ GeV}$) [44] and $\sim 2.9 \text{ GeV}/\text{fm}^3$ in Pb+Pb collisions at SPS ($\sqrt{s_{NN}} = 17.2 \text{ GeV}$) [54] and $\sim 5 \text{ GeV}/\text{fm}^3$ in Au+Au collisions at RHIC ($\sqrt{s_{NN}} = 200 \text{ GeV}$) [12, 100]. These estimated energy densities exceed the critical density, which is $\sim 1 \text{ GeV}/\text{fm}^3$ [168]. However, this estimation is too simple. One of the issues which should be considered is the center of mass “crossing times” for AGS Au+Au and SPS Pb+Pb collisions. The crossing times which can be equated as $2r/\gamma$ are $5.3 \text{ fm}/c$ and $1.6 \text{ fm}/c$ for AGS and SPS, respectively, and these values violate the assumption for Eq. 2.4: two colliding pancakes are assumed to pass through each other (i.e. $\tau_0 > 2r/\gamma$).

2.2.2 Model for Heavy Ion Collision

In relativistic heavy ion collisions, a nucleus can be seen as an object composed of independent nucleons approximately. In this simple view, the Lorentz-contracted nucleus interacts only in the region of geometrical overlap, which is parameterized by the impact parameter “ b ” as shown in Fig. 2.4. The nucleons involved in the collisions are called *participants*, and the other nucleons unaffected by the collisions are called *spectators*.

In order to characterize the relativistic heavy ion collisions and to study the nuclear phenomena in the collisions systematically, a parameter, called *centrality*, is used. The parameter is expressed as percentile of the total cross section. For example, “10 % central collision” means

“most central 10 % fraction of the total cross section”.

For each centrality, the geometric parameters of nucleus-nucleus collisions, such as number of participants $\langle N_{part} \rangle$, number of collision $\langle N_{coll} \rangle$, nuclear overlapping function T_{AA} , and impact parameter $\langle b \rangle$, are estimated with the Glauber model [135, 198]. The model provides a quantitative consideration of the geometrical configuration of the nuclei when they collide, and basically describe the nucleus-nucleus interaction in terms of elementary nucleon-nucleon interaction σ_{NN} . A nucleon is assumed to travel on a straight line, independent of how many interacts with other nucleons.

The nucleon distribution inside the nucleus is assumed to be described by the Woods-Saxon density profile:

$$\rho(r) = \frac{\rho_0}{1 + e^{\frac{r-R}{a}}}, \quad (2.11)$$

with

$$R = (1.12A^{1/3} - 0.86A^{-1/3}) [\text{fm}] \quad (2.12)$$

$$\rho_0 = 0.169 [\text{fm}^3] \quad (2.13)$$

$$a = 0.54 [\text{fm}]. \quad (2.14)$$

2.3 Hard Scatterings and Jet Quenching

As illustrated in Fig. 2.2, the space-time expansion of the system after the heavy ion collisions is complicated. One can observe the superposition of particles from multiple phase, and it is hard to measure the observables from created matter directly. Then, experiments have to rely on the indirect observables that are sensitive to the formed state of matter. For example, observation of J/ψ suppression, chiral symmetry restoration, strangeness enhancement, thermal emission and so on are proposed as the signature of QGP formation [236, 96].

As one of the probes into the heavy ion collision, high- p_T hadrons produced by hard scattering are considered. Since hard scattering is point like (distance scale of $1/p_T \leq 0.1$ fm), the cross section of high- p_T hadrons in relativistic heavy ion collisions can be same as that in p+p collisions after multiplied by the number of collisions. If there is a difference between the measurement and the expectation from p+p collision, it can be attributed to the effect of the matter passed by, and give us the information of created matter. In contrast, photon does not interact strongly and photon is useful as a penetrating probe of created matter*, thus high- p_T direct photon from hard scattering would be useful for the confirmation of scaling by the number of collisions.

In the following sections, the theoretical approach to represent the high- p_T hadron and direct photon production in p+p collisions will be described. Then, the expected effects in the

*Photon mean free path (λ_γ) in QGP is briefly given by $\lambda_\gamma = \lambda_q/C_{EM}$, where $C_{EM} = 4\pi\alpha \langle e_q^2 \rangle \approx 0.09 \cdot (5/9) = 0.05$ (i.e. λ_γ is ~ 20 times larger than λ_q). Using the quark cross section in QGP, 5 mb [155], the photon mean free path is given by $\lambda_\gamma = 20 \cdot 1/n_q \sigma = 10$ (fm), where $n_q = 10$ (fm $^{-3}$).

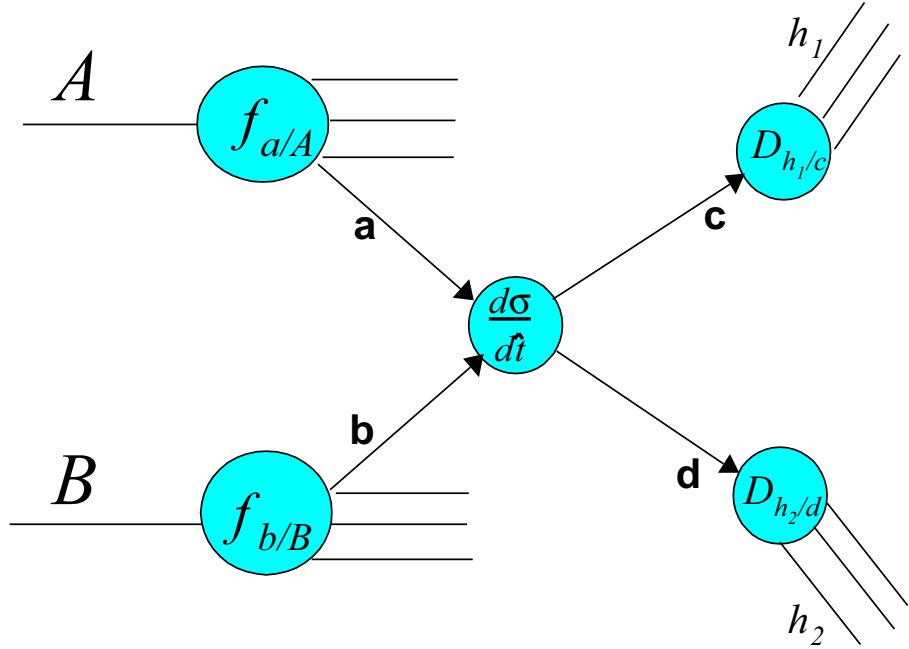


Figure 2.5: The diagram of calculation for hard scattering.

heavy ion collisions are introduced, and earlier results on the high- p_T particle production in heavy ion collisions will be reviewed.

2.3.1 High- p_T Hadron Production in p+p Collision

One of the interesting features of QCD is asymptotic freedom [140] due to the “anti-screening” feature of the QCD vacuum. The coupling strength decreases with the increase of momentum transfer squared (Q^2) of an interaction. One consequence is that interactions with Q^2 larger than a few GeV 2 can be calculated using the perturbation method, so-called “pQCD”. The high- p_T hadron cross section in nucleon-nucleon scattering is described in pQCD as the convolution of partonic reactions $ab \rightarrow cd$ with density functions as shown on Fig. 2.5:

$$\sigma^{AB \rightarrow hX} = \sum_{abcd} \int dx_a dx_b dz_c \cdot f_{a/A}(x_a, Q^2) \cdot f_{b/B}(x_b, Q^2) \cdot \sigma(ab \rightarrow cd) \cdot D_{h/cd}^0(z_{cd}, Q^2), \quad (2.15)$$

where $f_{a/A}(x_a, Q^2)(f_{b/B}(x_b, Q^2))$ is the parton distribution function (PDF) of the “a” (“b”) parton in the hadron “A” (“B”), $D_{h/cd}^0(z_{cd}, Q^2)$ is fragmentation function (FF) from the “c” (or “d”) parton to the hadron, and x (z) is the momentum fraction of the initial parton (final hadron) in the initial hadron (final parton). $\sigma(ab \rightarrow cd)$ represents the parton-parton cross section. It should be noted that only parton-parton scattering term in Eq. 2.15 (i.e. $\sigma(ab \rightarrow cd)$) is perturbatively computable, and other terms (PDF and FF) are parameterizations based upon the experimental data.

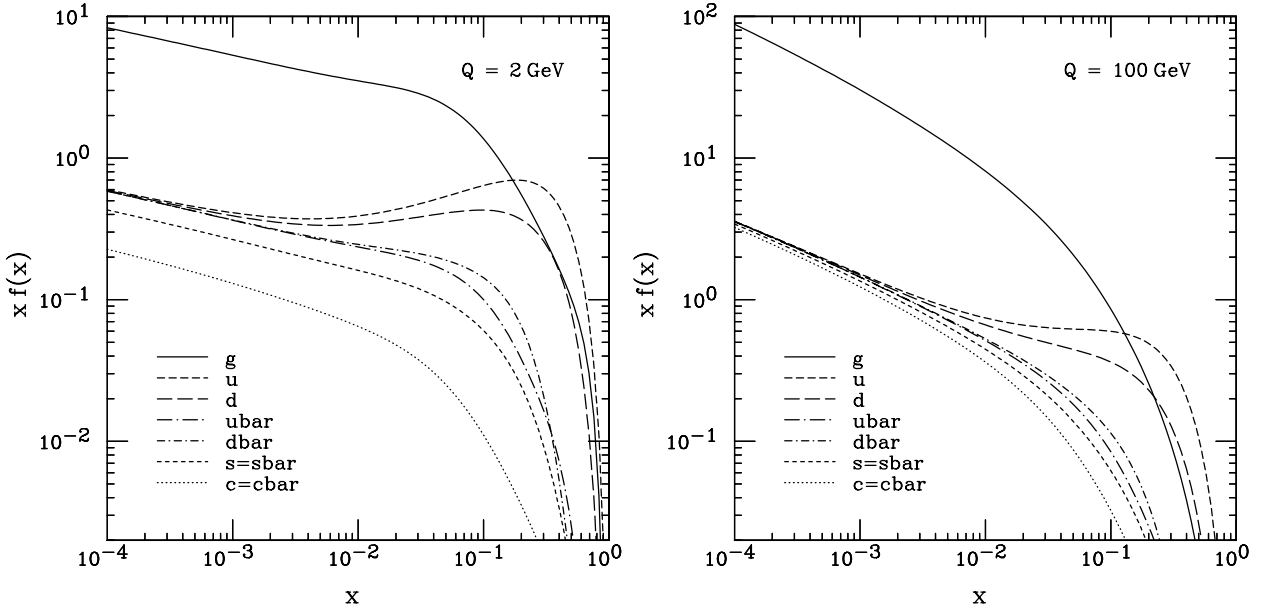


Figure 2.6: Parton distribution function by the CTEQ group as a function of x at $Q = 2$ and 100 GeV [192].

Since PDF can not be obtained by pQCD (because of the inherent non-perturbative effect in a QCD binding state), the function is obtained as parameterization by some theoretical groups using measured nuclear structure function $F_2(x, Q^2)$ [136, 205]. The proton structure function is measured by lepton deep inelastic scattering (DIS) in many experiments (e.g. at SLAC [232] and DESY [45, 120]). For example, CTEQ group provides the parameterized PDF as shown in Fig. 2.6 [192].

The fragmentation function, $D_{h/p}^0(z, Q^2)$, has been determined using the processes of $e^+ + e^- \rightarrow \gamma$ or $Z \rightarrow h + X$ in $\sqrt{s} \sim 3 - 183$ GeV lepton pair collisions [106, 46, 108, 56, 4, 6].

The next-to-leading order (NLO) pQCD calculations succeed in describing high- p_T particle production in high-energy nucleon-nucleon collisions [59, 2]. Figure 2.7 shows the π^0 spectra measured by PHENIX in p+p collisions at $\sqrt{s} = 200$ GeV [23], together with a NLO pQCD calculation [80, 163, 172, 175]. These calculations are consistent with the data, indicating that the particle production at high- p_T is dominated by the fragmentation of hard-scattered partons and the production rate is well reproduced.

2.3.2 High- p_T Direct Photon Production in p+p Collision

Direct photon is useful as a penetrating probe of created matter at RHIC. Direct photons in this study mean photons not originating from hadronic decays, such as $\pi^0, \eta \rightarrow \gamma\gamma$.

At high energy and high momentum transfer, the process of direct photon production can be described by pQCD as well. Three parton-parton subprocesses are expect to dominate at NLO: Compton scattering ($g+q \rightarrow \gamma+q$, “a” in Fig. 2.8), annihilation ($q+\bar{q} \rightarrow \gamma+g$, “b” in Fig. 2.8), and bremsstrahlung emission of photons from the quarks undergoing hard scattering (“c” in Fig. 2.8). The nucleon-nucleon direct photon cross section in NLO pQCD calculation is

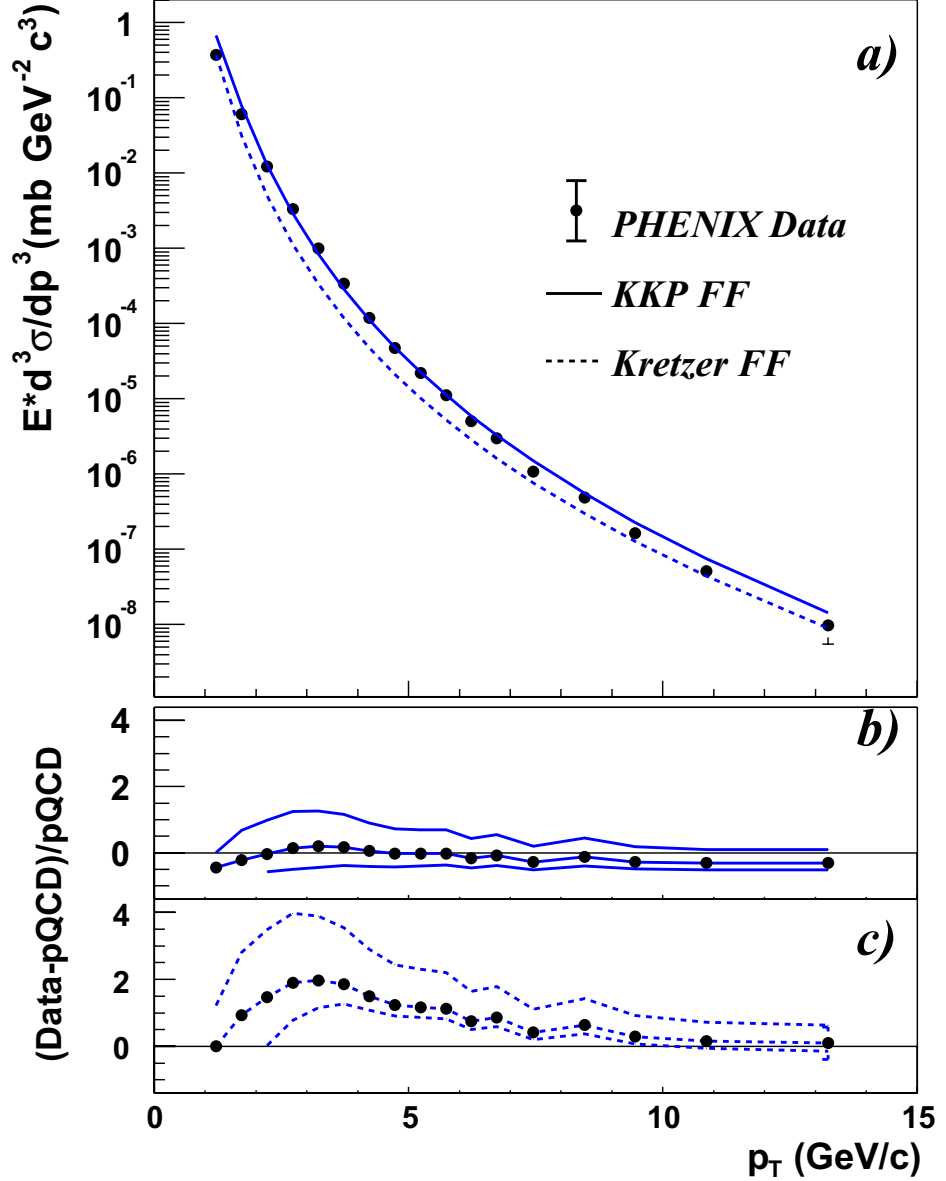


Figure 2.7: π^0 cross section in $\sqrt{s} = 200$ GeV p+p Collisions, together with NLO pQCD predictions from Vogelsang [80, 163]. a) The invariant differential cross section for inclusive π^0 production (points) and the results from NLO pQCD calculations with equal renormalization and factorization scales of p_T using the “Kniehl-Kramer-Pötter” (solid line) and “Kretzer” (dashed line) sets of fragmentation functions. b,c) The relative difference between the data and the theory using KKP [172] (b) and Kretzer [175] (c) fragmentation functions with scales of $p_T/2$ (lower curve), p_T , and $2p_T$ (upper curve). In all figures, the normalization error of 9.6 % is not shown [23].

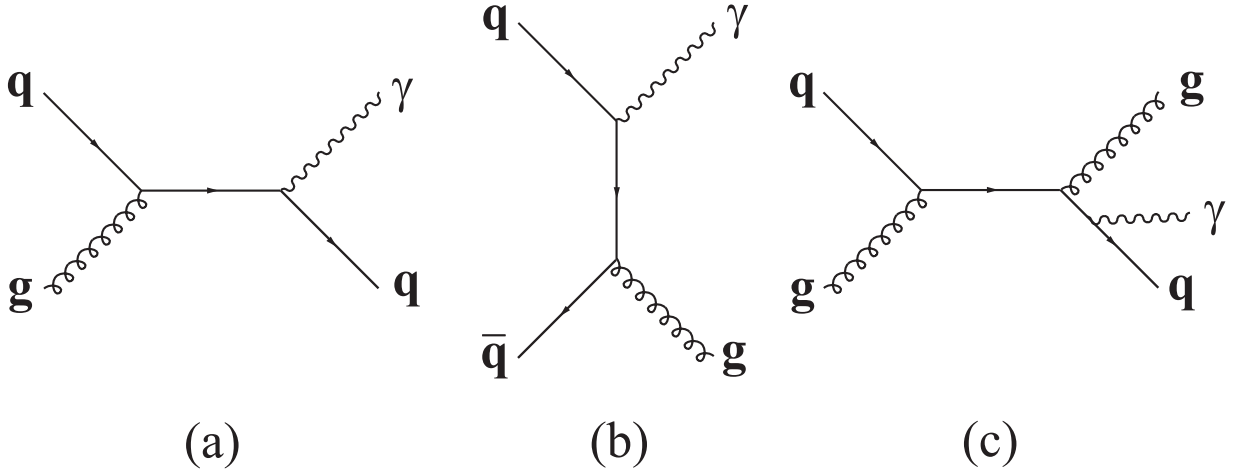


Figure 2.8: Feynman diagrams of the main production processes for direct photons in initial hard scatterings as well as in a thermalized quark-gluon plasma phase: (a) quark-gluon Compton scattering of order α_s , (b) quark-antiquark annihilation of order α_s , (c) bremsstrahlung of order α_s^2 .

the sum over prompt photon contribution (Compton + annihilation) and fragmentation photon contribution from bremsstrahlung process:

$$\sigma^{AB \rightarrow \gamma X} = \sigma_{prompt}^{AB \rightarrow \gamma X} + \sigma_{fragmentation}^{AB \rightarrow \gamma X} \quad (2.16)$$

$$= \sum_{abcd} \int dx_a dx_b dz_c \cdot f_{a/A}(x_a, Q^2) \cdot f_{b/B}(x_b, Q^2) \cdot (\sigma(ab \rightarrow \gamma) + D_{\gamma/cd}^0(z_{cd}, Q^2) \cdot \sigma(ab \rightarrow cd)), \quad (2.17)$$

where each density functions are same as in Eq. 2.15. While the production rate of the fragmentation photons is smaller than that of the prompt photons by a factor of α_s , the contribution from fragmentation photon is not negligible and expected to be about 30 % at high- p_T region as shown in left figure of Fig. 2.10.

Cross sections of direct photons at mid-rapidity production in p+p collisions at $\sqrt{s} = 200$ GeV are reported for transverse momenta of $3 < p_T < 16$ GeV/c as shown in Fig. 2.9 [39]. In addition, a numerical calculation of NLO pQCD predictions [138, 139, 77, 78, 88, 87] is shown. The annihilation process is expected to be suppressed in p+p collisions, due to the lower probability density of \bar{q} versus g in the proton. NLO pQCD describes the data well for $p_T > 5$ GeV/c, where the uncertainties of the measurement and theory are comparable.

The fragmentation photon from bremsstrahlung processes will produce photons in the vicinity of parton jets. Therefore, a requirement that the photon be isolated from parton jet activity can reduce the contribution. The right figure in Fig. 2.10 presents the results of the isolation cut for photons by RHIC-PHENIX [39]. Closed circles show the fraction of isolated direct photons to all direct photons. Isolated photons are selected with less than 10 % additional energy within a cone of radius $\Delta r = \sqrt{(\Delta\eta)^2 + (\Delta\phi)^2} = 0.5$ around the candidate photon direction. The curves are predictions from NLO pQCD, with the parton distribution and fragmentation

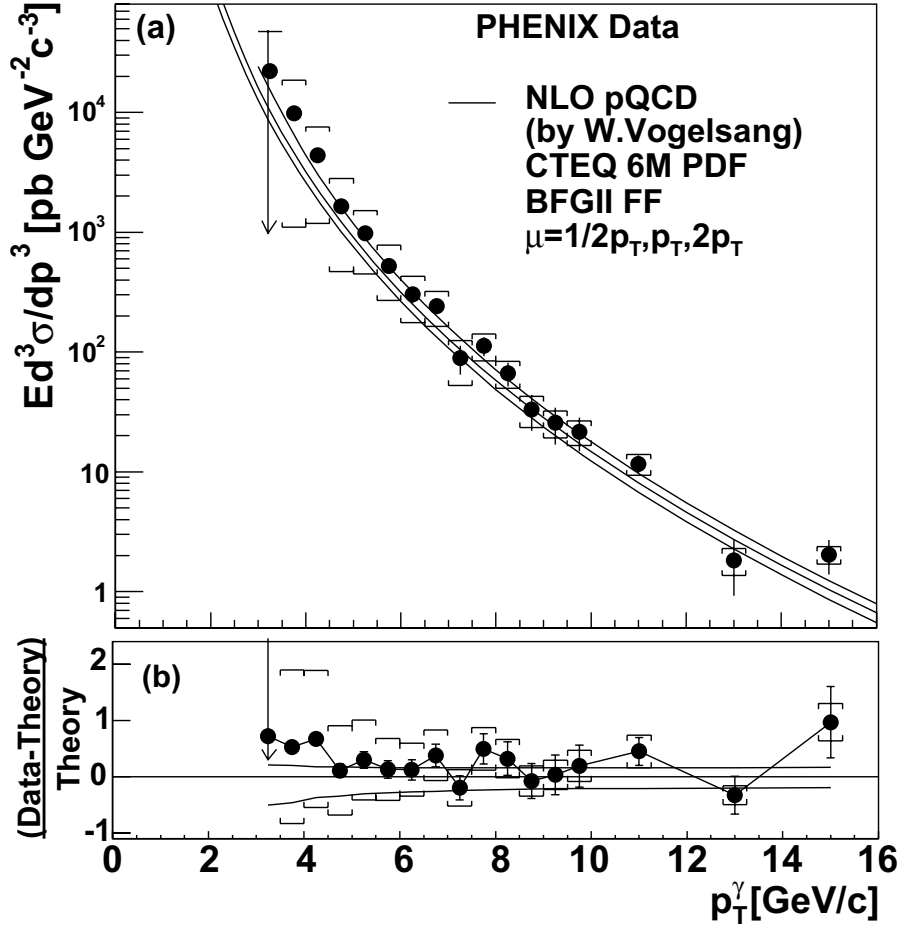


Figure 2.9: Direct photon cross section in $\sqrt{s} = 200$ GeV p+p collisions. (a) Direct photon spectra with NLO pQCD calculations for three factorization scales, μ . In the calculation, CTEQ 6M PDF [192] and the BFGII parton to photon FF [105] are used. Brackets around data points show systematic errors. (b) Comparison to the NLO pQCD calculation for $\mu = p_T$, with upper and lower curves for $\mu = p_T/2$ and $2p_T$.

functions same as in Fig. 2.9. The observed ratio is $\sim 90\%$ for $p_T > 7$ GeV/c and it is well described by pQCD. An additional loss of $\sim 15\%$ ($p_T = 3$ GeV/c) to less than 5% (for $p_T > 10$ GeV/c) due to the underlying event is estimated by a PYTHIA [201] simulation. The open circles show the ratio of isolated photons from π^0 decays to all photons from π^0 decays. This indicates significantly less isolation than in the direct photon sample.

2.3.3 Nuclear Modification Factor

The amount of nuclear effect can be quantified using a nuclear modification factor (R_{AA}). R_{AA} is the ratio between the measured yield and the expected yield from the p+p result, and is defined as

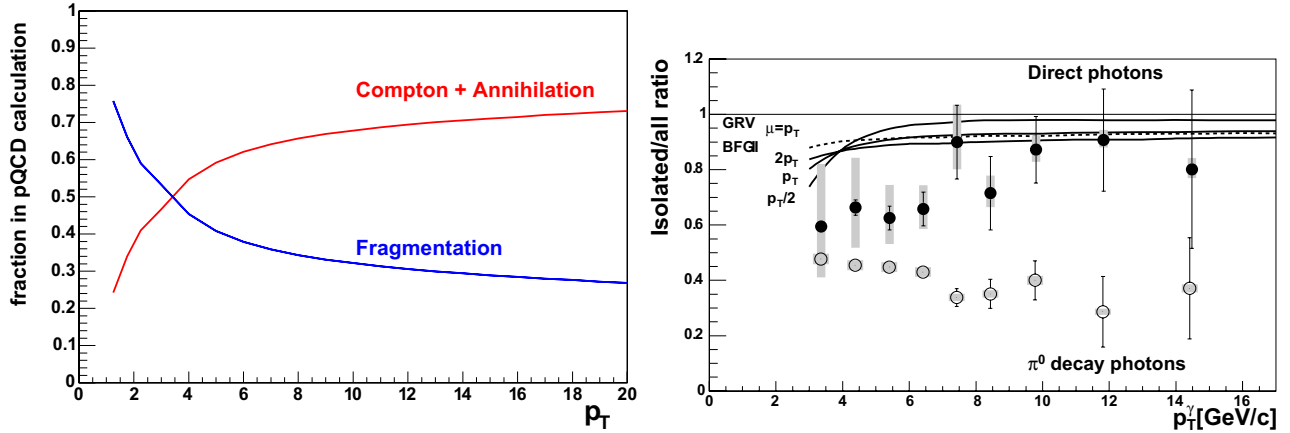


Figure 2.10: Left: Fraction of the direct photon contribution from LO (Compton and annihilation) processes and NLO (fragmentation of hard scattered partons) processes in $\sqrt{s} = 200$ GeV p+p collisions by pQCD as a function of p_T . Right: Closed circles: Ratio of isolated direct photons to all direct photons from the π^0 -tagging method. The statistical uncertainties are shown as black error bars and the systematic uncertainties are plotted as shaded bars. The solid and dashed curves are NLO pQCD calculations with three theory scales for BFGII [105] and one scale for GRV [137] parton to photon fragmentation functions. Open circles: Ratio of isolated photons from π^0 decays to all photons from π^0 decays.

$$R_{AA}(p_T) = \frac{d^2N_{AA}/dp_T d\eta}{T_{AA}(b)d^2\sigma_{NN}/dp_T d\eta}, \quad (2.18)$$

where the numerator is the invariant yield in unit rapidity and the denominator is the cross-section in the p+p collisions scaled with thickness function ($T_{AA}(b)$) in nucleus-nucleus collisions. $T_{AA}(b)$ is Glauber scaling factor, which is defined as:

$$T_{AA}(b) = \int d^2\mathbf{r} T_A(\mathbf{r}) T_A(\mathbf{r} - \mathbf{b}), \quad (2.19)$$

where

$$T_A(r) = \int dz \rho_A(\mathbf{r}, z). \quad (2.20)$$

And the average number of binary nucleon-nucleon collisions ($\langle N_{coll} \rangle$) at an impact parameter b is given by $T_{AA}(b) = \langle N_{coll}(b) \rangle / \sigma_{NN}$, where σ_{NN} is the total inelastic cross section. If a hard-scattered parton penetrates the bulk matter without any nuclear effects, the R_{AA} is unity.

2.3.4 Parton Energy Loss

An energetic charged particle passing through matter loses its energy due to collisions with electrons and nuclei via electromagnetic interactions. There are two main sources of energy loss: the collisional source and the radiative source (bremsstrahlung).

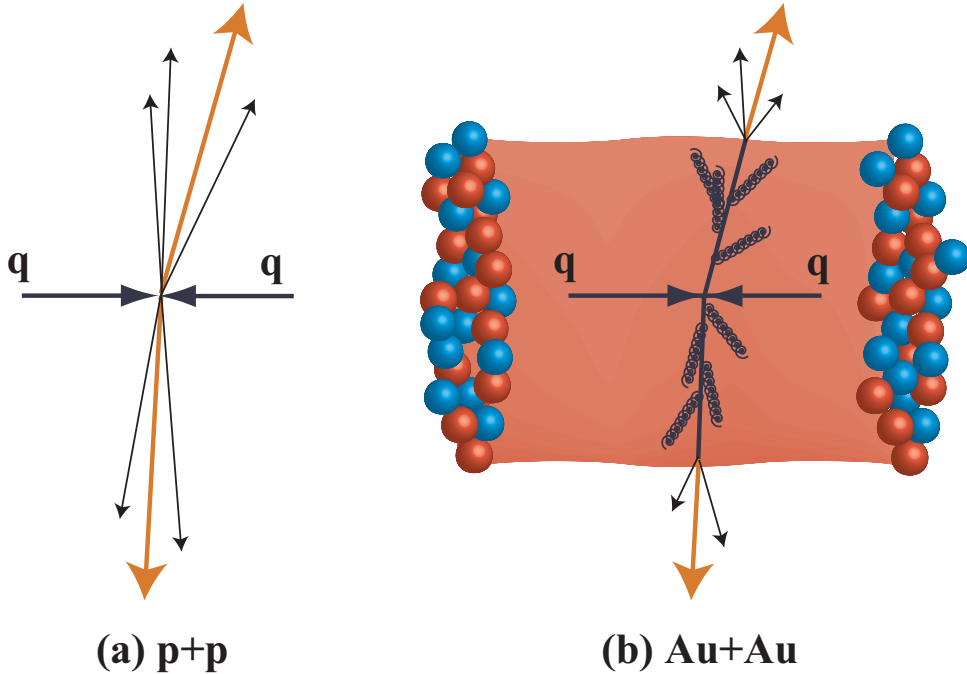


Figure 2.11: Schematic view of jet-quenching effect in central relativistic heavy ion collision. Jet partons generated by nucleon-nucleon collisions traverse the created dense medium, and lose its energy by gluon bremsstrahlung.

As well as charged particles lose their energy in charged medium, colored partons would lose their energy in colored medium. When an energetic parton propagates through a colored medium, it is predicted to lose its energy due to the interaction with other partons via strong interaction. In the relativistic heavy ion collisions, extremely dense matter is expected to be produced, and the energy loss effect would be stronger. In 1982, it was considered that energetic parton might lose its energy by the elastic scatterings with other partons in QGP [102, 148]. Ten years later, it was turned out that the energy loss by radiating soft gluons would be dominant effect rather than the elastic scatterings [228, 220]. As illustrated in Fig. 2.11, the hard scattered partons passing through the dense matter radiate the gluons by the interaction with soft partons in the matter. As the consequence of parton energy loss, the yield of jets are expected to be suppressed in the extreme state of the matter, such as QGP. This phenomena is named *jet quenching*.

The left panel in Fig. 2.12 shows the expected inclusive p_T spectra of π^0 and direct photon with and without constant parton energy loss ($dE/dx = 1 \text{ GeV/fm}$), where a large amount of suppression for π^0 is seen, while the suppression is not seen for direct photon [221].

The theoretical treatment of the energy loss is complicated by the fact that one has to consider destructive interference effects of the emitted gluons if the formation time of the gluon is large compared to its mean free path in the medium [150]. Analogous to the case in electromagnetic interaction where the interaction probability of photon bremsstrahlung is smaller for higher density medium than low density medium [183], which is called Landau-Pomeranchuk-Migdal (LPM) effect, the gluon radiation would be smaller for higher density

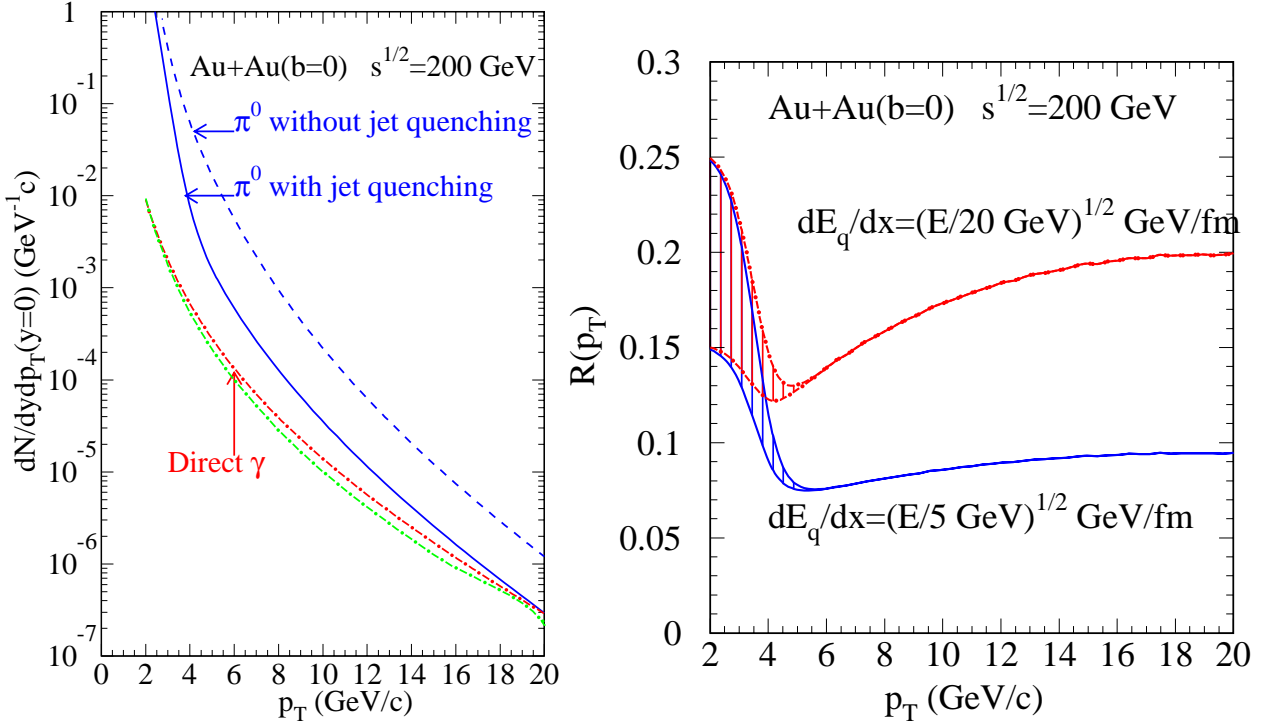


Figure 2.12: Left: The expected inclusive p_T spectra of π^0 with (solid) and without (dashed) parton energy loss compared to that of direct photons (dot-dashed) in central Au+Au collisions at $\sqrt{s_{\text{NN}}} = 200$ GeV by X.N. Wang. The constant energy loss, $dE/dx = 1$ GeV/fm, and mean free path of $\lambda_q = 1$ fm are assumed. Right: The expected nuclear modification factor of charged particle in central Au+Au collisions at $\sqrt{s_{\text{NN}}} = 200$ GeV by X.N. Wang. Energy-dependent energy loss, $dE/dx = \sqrt{E/E_0}$, and mean free pass $\lambda_q = 1$ fm are assumed. Both figures are referred from [221].

colored medium. R. Baier et al. had developed the theoretical calculation which takes LPM effect into account [92, 90, 91]. They expressed the energy loss of a hard scattered parton as:

$$\frac{dE}{dx} \propto -N_c \alpha_s \sqrt{E \frac{\mu^2}{\lambda}} \ln \frac{E}{\lambda \mu^2} \quad (\text{for } L > L_{cr}), \quad (2.21)$$

where $N_c = 3$, E is parton energy, μ^2 is the Debye screening mass for the effective parton scattering, λ is parton's mean free path in the medium, and $L_{cr} = \sqrt{\lambda E / \mu^2}$. For an energetic parton with $L_{cr} > L$, the energy loss becomes almost independent of the parton energy:

$$\frac{dE}{dx} = -\frac{N_c \alpha_s}{8} \Delta p_T^2 = \frac{N_c \alpha_s}{8} \delta p_T^2 \frac{L}{\lambda}, \quad (2.22)$$

where δp_T^2 is the transverse momentum kick the parton acquires per scattering. It means that dE/dx is proportional to the total length of traveling.

Since L_{cr} involves the two unknown parameters, λ and μ^2 , it is difficult to determine if L is larger than L_{cr} and which formalism is more realistic for the system of dense matter produced

in heavy ion collisions. X.N. Wang instead studied the phenomenological consequences in the single inclusive particle spectrum. He assumed that the energy loss is proportional to $\sqrt{E/E_0}$, where the factor E_0 is taken to be $20 \text{ fm}^2/\text{GeV}$ or $5 \text{ fm}^2/\text{GeV}$, and quark mean free path λ_q is 1 fm [229]. The right panel of Fig. 2.12 shows the expected R_{AA} of charged particle with parton energy loss, indicating the strong suppression by a factor of ~ 10 .

Additionally, the expansion of the system in a heavy ion collision leads to a rapid decrease of the color charge density. (Static medium is assumed for the calculation shown in Fig. 2.12.) This expansion should be taken into account. The proper time dependence of color charge density can be obtained as $\rho(\tau) \propto T(\tau)^3 \propto \tau^{-1}$ from the Landau hydrodynamical model [151] on the assumption of a longitudinally expanding of fireball [103]. The recent calculation takes the expansion into account, where the color charge density $\rho(\tau)$ is assumed to decrease as a function of proper time τ [215]:

$$\rho(\tau) = \frac{\tau_0}{\tau} \rho(\tau_0), \quad (2.23)$$

$$\text{where } \rho(\tau_0) = \frac{1}{\tau_0 \pi R^2} \frac{dN^g}{dy}. \quad (2.24)$$

The theoretical studies of the effects of parton energy loss in dense matter had been carried out. And it is found that the hadron spectra at high- p_T in relativistic heavy ion collisions is quite sensitive to how the energetic partons interact with the dense medium and lose their energy before they fragment into hadrons, leading to the suppression of high- p_T particles. Furthermore, the suppression factor as a function of p_T is sensitive to the energy dependence of the parton energy loss. The nonlinear length dependence of the energy loss leads to stronger suppression as suggested by R. Baier et al. [89]. If the energy loss “ dE/dx ” is constant value, the suppression should be small at high- p_T . The precise measurement of high- p_T hadrons makes it possible to constrain the energy loss mechanism, which gives the information for understanding the created matter.

2.3.5 Initial State Effect

As mentioned in Sec. 2.3.4, the parton energy loss can cause the jet quenching. However, it is also possible that other effects would affect the high- p_T hadron production. These effects should be taken into account before concluding the parton energy loss as the final state effect[†] and extracting the property of created matter. Therefore, it is important to understand these initial state effects[‡] present in nucleus-nucleus collisions. Followings are known initial state effects.

Cronin Effect

It was observed by J.W. Cronin et al. in 1974 that the cross section does not simply scale with the number of target nucleons A in a $p+A$ collision [112]. The cross section in $p+A$ collisions for a given p_T is parameterized as:

[†]“final state effect” means “effect owing to the matter created by relativistic nucleus-nucleus collision”.

[‡]“initial state effect” means “effect owing to the normal nuclear matter”.

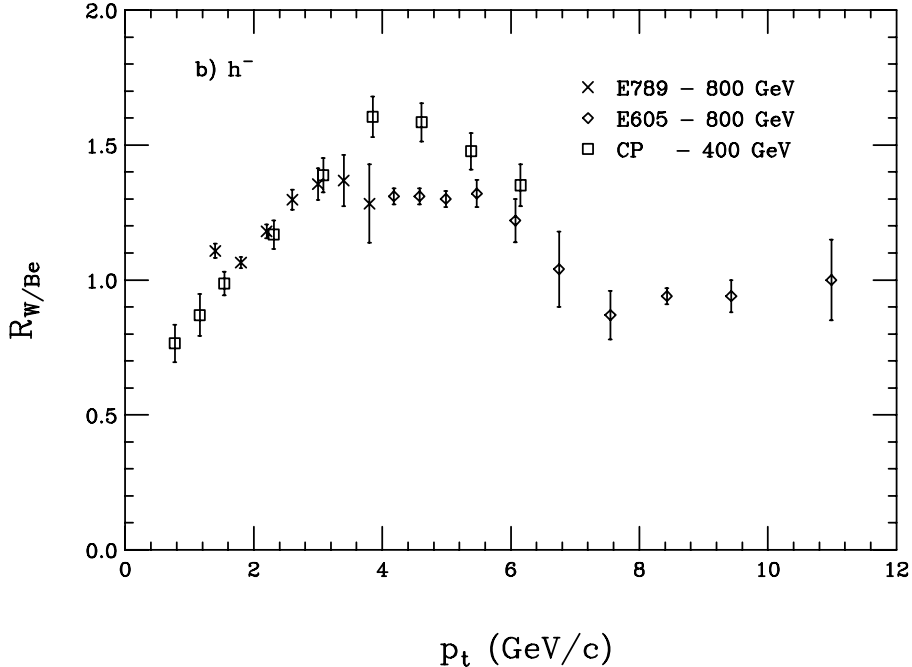


Figure 2.13: Cronin effect at fixed target energies expressed as $R_{W/B}$, which is the ratio of the point-like scaled cross sections in $p+W$ and $p+Be$ collisions as a function of p_T .

$$E \frac{d^3\sigma}{dp^3}(p_T, A) = E \frac{d^3\sigma}{dp^3}(p_T, 1) \cdot A^{\alpha(p_T)}. \quad (2.25)$$

As shown in Fig. 2.13, α becomes greater than 1 for the p_T region of $p_T \geq 1 \text{ GeV}/c$. Enhancement of particle production compared to the expectation from $p+p$ reactions is observed. The enhancement is explained as the multiple scattering of the incident partons while passing through the nucleus A before the collision [176, 179], which smears the axis of the hard scattering relative to the axis of the incident beam. Thus, this effect is also called as “ k_T smearing”, where k_T is the partonic transverse momentum.

The k_T in $p+p$ collisions at $\sqrt{s} = 200 \text{ GeV}$ has been measured by RHIC-PHENIX experiment using the method of two-particle azimuthal correlations [35], which worked well at ISR energies ($\sqrt{s} \leq 63 \text{ GeV}$) [61, 113, 189]. The extracted value, $\sqrt{\langle k_T^2 \rangle} = 2.68 \pm 0.35 \text{ GeV}/c$, is comparable with previous lower \sqrt{s} measurements.

Nuclear Shadowing

It was discovered by the EMC group in 1982 that the structure function $F_2(x, Q^2)$ per nucleon in iron differs significantly from that of a free nucleon [75].

For the comparison of nuclear structure functions, deuterium is often used as the reference, as it is a weak coupling system and represents an isospin-averaged nuclear structure function. The initial state nuclear effects are quantified as the ratio of the parton structure functions, $F_2^A(x, Q^2)/F_2^D(x, Q^2)$. Figure 2.14 shows a collection of data for different nuclei [69]. Shadowing

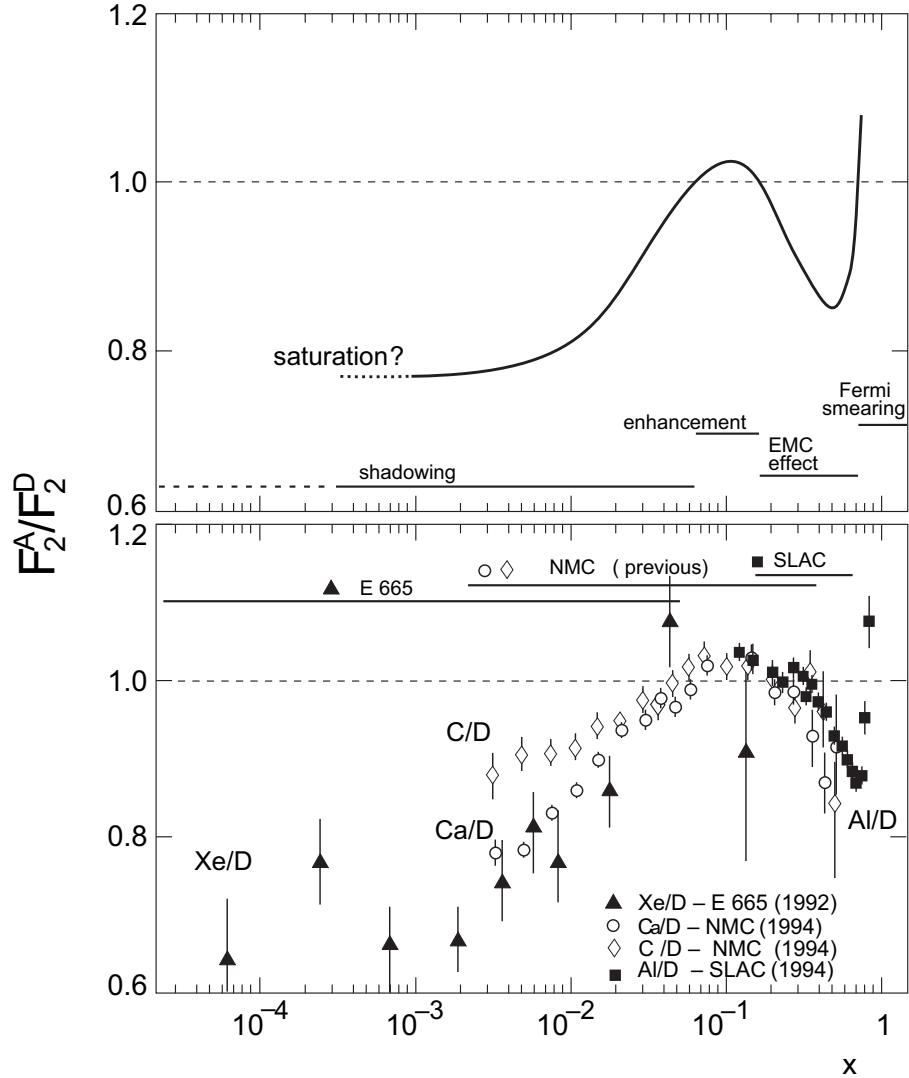


Figure 2.14: A phenomenological curve and some experimental data for nuclear effect on structure function, F_2^A/F_2^D , from [69].

$F_2^A(x, Q^2)/F_2^D(x, Q^2) \leq 1$ at $x \leq 0.1$, anti-shadowing $F_2^A(x, Q^2)/F_2^D(x, Q^2) \geq 1$ at $0.1 \leq x \leq 0.3$, EMC effect $F_2^A(x, Q^2)/F_2^D(x, Q^2) \leq 1$ at $0.3 \leq x \leq 0.7$, and Fermi motion at $x \leq 0.7$ are seen.

The relevant x -region of the scattered parton can be estimated by the p_T of the leading hadron. At mid- p_T rapidity region,

$$x \sim \frac{2p_T}{\sqrt{s_{NN}}}. \quad (2.26)$$

The p_T region ($1 < p_T < 20$ GeV/c) of hadrons measured in the mid-rapidity at RHIC is corresponding to the region ($0.01 < x < 0.2$) where nuclear shadowing should be considered.

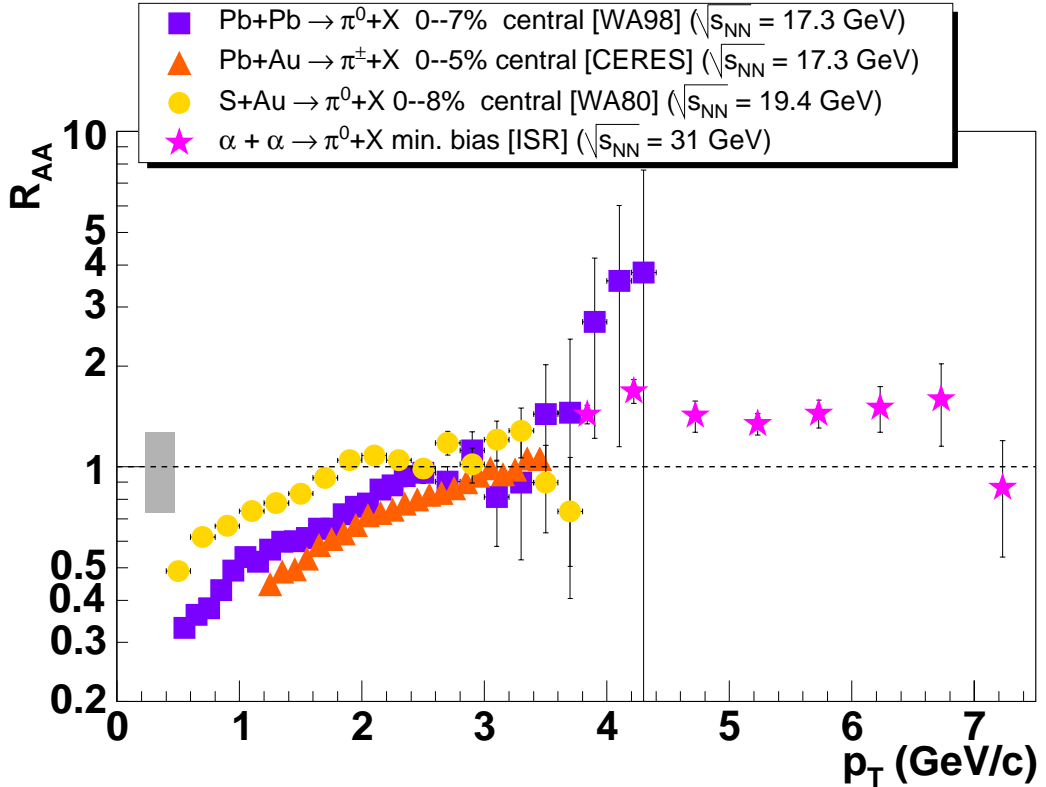


Figure 2.15: Nuclear modification factors for pion production at the CERN-SPS in central Pb+Pb [43], Pb+Au [202], and S+Au [53] reactions at $\sqrt{s_{NN}} \approx 20$ GeV, and for π^0 production at the CERN-ISR in minimum-bias $\alpha+\alpha$ reactions at $\sqrt{s_{NN}} = 31$ GeV [62]. The R_{AA} from SPS are obtained using the p+p parametrization proposed in ref. [117]. The shaded band around $R_{AA} = 1$ represents the overall fractional uncertainty of the SPS data (including in quadrature the 25 % uncertainty of the p+p reference and the 10 % error of the Glauber calculation of $\langle N_{coll} \rangle$). There is an additional overall uncertainty of ± 15 % for the CERES data not shown in the plot [202].

2.3.6 Earlier Results on High- p_T Particle Production

Pion production in the heavy ion collisions were measured in S+S and S+Au at $E_{lab} = 200A$ GeV ($\sqrt{s_{NN}} = 19.4$ GeV) by WA80 [53], in Pb+Au at $E_{lab} = 158A$ GeV by CERES [202], and in Pb+Pb at $E_{lab} = 158A$ GeV ($\sqrt{s_{NN}} = 17.3$ GeV) by WA98 [40, 43]. Figure 2.15 shows the pion R_{AA} in nucleus-nucleus collisions at $\sqrt{s_{NN}} \leq 31$ GeV. The results showed that the hadron suppression was not observed at SPS energy. On contrary, The pion yield in heavy ion collisions was larger at high- p_T region, which was interpreted as the consequence of Cronin effect. Based upon the difference between the measurement and theoretical expectation where initial state effects are taken into account, X.N. Wang estimated the energy loss of hard scattered partons as $dE/dx < 0.02$ GeV/fm on the assumption of no modification on FF [222].

In the contrast to the pion enhancement at SPS, the early results from the RHIC showed the suppressed yield of moderately high- p_T hadrons in central Au+Au collisions at $\sqrt{s_{NN}} = 200$ GeV with respect to the binary scaled p+p collisions. Figure 2.16 [14, 27] shows the R_{AA}

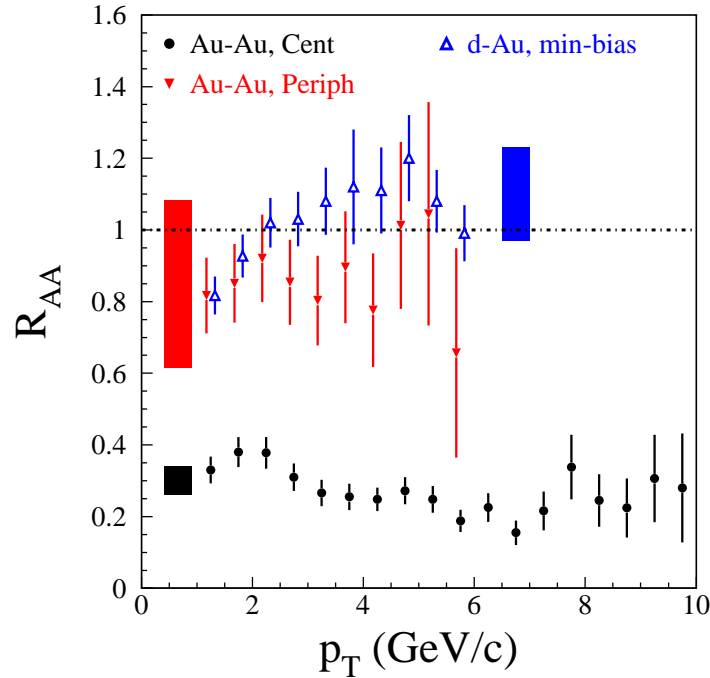


Figure 2.16: Nuclear modification factor of π^0 in the central and peripheral $\sqrt{s_{\text{NN}}} = 200$ GeV Au+Au collisions against that in d+Au collisions at same $\sqrt{s_{\text{NN}}}$ measured by RHIC-PHENIX experiment. The band around the data points indicate the normalization uncertainty.

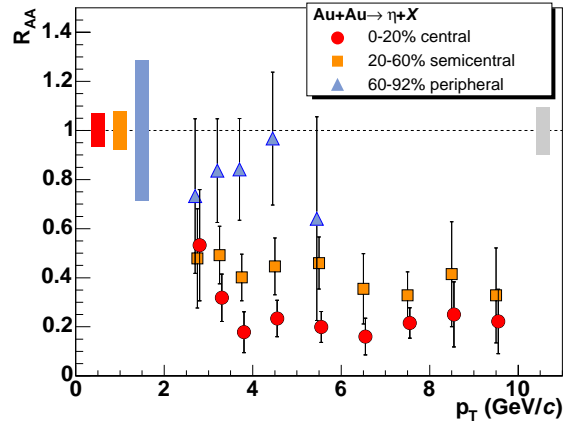


Figure 2.17: Nuclear modification factor of η in $\sqrt{s_{\text{NN}}} = 200$ GeV Au+Au collisions for each centrality. The suppression pattern of η meson is similar with that of π^0 .

of π^0 in central and peripheral Au+Au collisions against with R_{AA} in minimum bias d+Au collisions at $\sqrt{s_{\text{NN}}} = 200$ GeV. The yield in central Au+Au collisions are strongly suppressed. Since the π^0 yield is not suppressed in d+Au collisions [20, 19], the strong suppression is not likely to be due to the initial state effects, such as nuclear shadowing and Cronin effect, which should be present both in d+Au and Au+Au collisions. This observation has triggered extensive theoretical studies on its origin [215, 95, 223, 170, 133]. Most of these studies are based on the prediction [148, 228, 93] that multiple gluon radiations are induced from the scattered fast partons in extremely dense matter, effectively leading to a suppression of high- p_T hadronic fragmentation products (“jet quenching”).

Inclusive p_T spectra of η mesons and charged hadrons have been also measured up to ~ 10 GeV/c at mid-rapidity by the PHENIX experiment in p+p, d+Au and Au+Au collisions at $\sqrt{s_{\text{NN}}} = 200$ GeV [21, 28, 34, 19, 38]. Figure 2.17 shows the R_{AA} of η meson as a function of p_T for each centrality selection. The η yields are significantly suppressed compared to p+p yields scaled by the corresponding number of nucleon-nucleon collisions. The magnitude of the η suppression, and its dependence on centrality and p_T , is similar with that of π^0 suppression.

The measurement of high- p_T direct photons in Au+Au collisions at RHIC energy was reported by RHIC-PHENIX experiment [31]. Figure 2.18 shows the direct photon spectra in

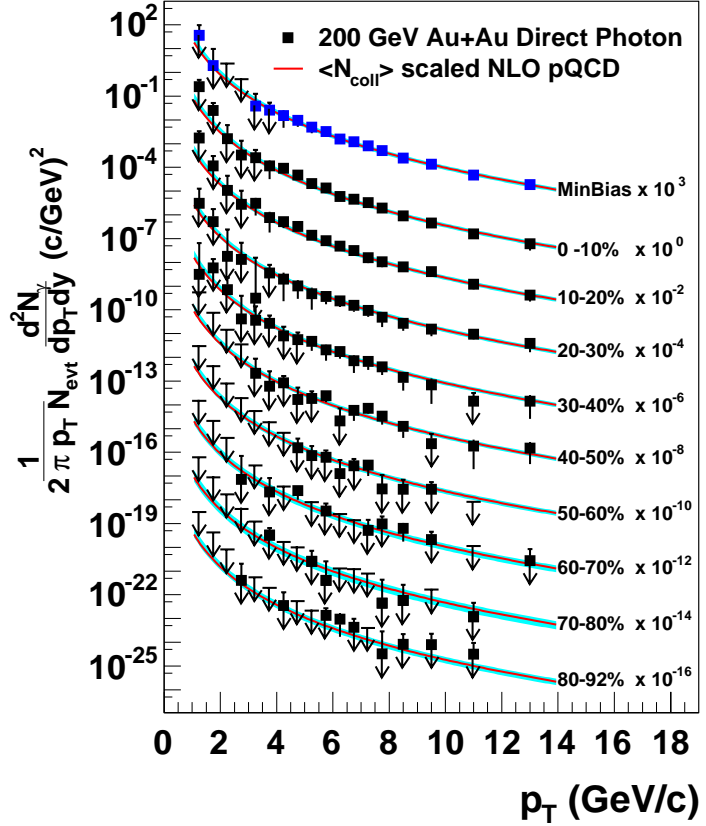


Figure 2.18: Direct photon invariant yields measured by RHIC-PHENIX experiment as a function of transverse momentum for 9 centrality selections and minimum bias Au+Au collisions at $\sqrt{s_{NN}} = 200$ GeV [31]. The vertical error bar on each point indicates the total error. Arrows indicate measurements consistent with zero yield with the tail of the arrow indicating the 90 % confidence level upper limit. The solid curves are binary scaled NLO pQCD predictions.

$\sqrt{s_{NN}} = 200$ GeV Au+Au collisions for each centrality. Each results are compared with binary scaled NLO pQCD calculation, which is same as in Fig. 2.9, and the result is consistent with expectation.

2.4 Direct Photons from QGP

While the direct photons are usually further classified into prompt photons produced in early hard scatterings, there are other photons which are not from hadronic decay. The second class of direct photon at RHIC is thermal photon. In advance of RHIC experiments, it was proposed that electromagnetic radiation would be a useful signature of QGP. In 1976, Feinberg suggested that a large amount of photon production would be a distinct feature of highly excited hadronic matter [129]. Models of QGP radiation have been refined after the proposal of thermal photon

emission, and it was claimed that finally observed direct photons are interesting because they can carry information of QGP directly through its complicated space-time evolution [199, 182].

If the appropriate degrees of freedom in the medium are hadrons, then direct photons can be produced through interactions such as $\pi + \rho \rightarrow \pi + \gamma$. Such state would be formed when the QGP expands and cool down, so this photons will be observed in addition to the thermal emission from QGP.

All above photons cannot be separated experimentally, but it is expected that the p_T spectra are different. At medium- p_T ($p_T = 1 - 5 \text{ GeV}/c$), the thermal signal has the largest contribution to the total direct photon yield, while hard scattering photons dominate at high- p_T . In the following section, a short theoretical overview of each process will be given.

2.4.1 Thermal Photon from QGP

A QGP emits photons, as does every thermal source, and the mean free path of photons in the QGP is large and so the photons are likely to survive. The techniques to calculate the emission of direct photons from a thermalized QGP is an exercise in thermal field theory, which has been used since 1950s [181]. For simplicity, the net baryon density is assumed to be zero in the QGP so that the quark distribution $f_q(E)$ and the antiquark distribution $f_{\bar{q}}(E)$ are same. The thermal emission rate of photons with momentum p can be derived by following equation both perturbatively [231, 182] and nonperturbatively [132]:

$$E_\gamma \frac{dR}{d^3 p_\gamma} = \frac{-2}{(2\pi)^3} \text{Im} \Pi_\mu^{R,\mu} \frac{1}{e^{E/T} - 1}, \quad (2.27)$$

where $\Pi_\mu^{R,\mu}$ is the retarded photon self-energy at finite T .

2.4.2 Thermal Photon from Hadron Gas

There was a presumption that a QGP produces a larger photon radiation than a hadron gas at the same temperature. Because the quarks in a QGP are massless, and they are able to interact strongly, it can be expected that there would be a lot of charges being scattered and so a large amount of electromagnetic radiation. However, it was turned out that hadron gas and QGP would produce very similar spectra of radiated photons at relevant temperatures ($\sim 200 \text{ MeV}$).

The computation technique for calculating thermal radiation from a hot hadron gas is the same as in thermal field theory [166]. The difference is that π s, η s, and the ρ mesons are treated as the constituted hadrons instead of quarks and gluons. For example, following hadronic processes are included for the calculation:



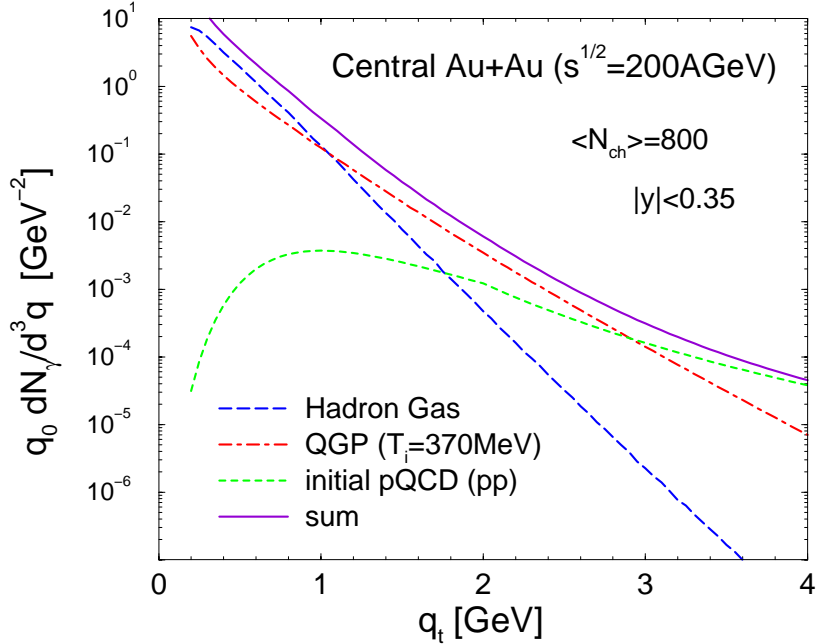


Figure 2.19: Theoretical calculation of photon emission spectra from central Au+Au collisions at RHIC energy by S. Turbide [212]. Short-dashed line: pQCD photons from hard scattering. Dashed-dotted line: thermal QGP radiation. Long-dashed line: thermal hadron gas emission. Solid line: total direct photon yield.

Reasonably state-of-the-art calculations for radiation from a thermal hadron gas were presented by S. Turbide et al. [213, 207]. The calculation assumes a temperature of 370 MeV and a formation time of 1/3 fm, and includes all processes listed above and uses a massive Yang-Mills model of hadron interactions. Figure 2.19 shows the result of theoretical calculation of photon emission spectra from central Au+Au collisions at RHIC energy [212]. The thermal photon spectra from a hadron gas are similar to that from a QGP at the same temperature, and the thermal radiation from QGP is dominant at $1 \leq p_T \leq 3$ GeV/c.

2.4.3 Direct Photon from the Interaction of Hard Scattering Partons in QGP

In addition to the direct photon from QGP, hadron gas, and initial hard scattering, it has been predicted by R.J. Fries et al. that there is another source of direct photons originating from the passage of the produced high-energy quark jets through the QGP (so-called “jet-photon conversion”) [131, 130]. A fast quark passing through the plasma will produce photons by Compton scattering with the thermal gluons ($q + g \rightarrow q + \gamma$) and annihilation with the thermal antiquarks ($q + \bar{q} \rightarrow \gamma + g$) as shown in Fig. 2.20. This process is higher-order in α_s compared with photons from initial hard scatterings, but it is not a sub-leading contribution, since it corresponds to double scattering, which is enhanced by the size of the system.

The p_T distribution of direct photon invariant yield is calculated by R.J. Fries et al. as shown in the right panel of Fig. 2.20. It is turned out that this source is at least comparable in

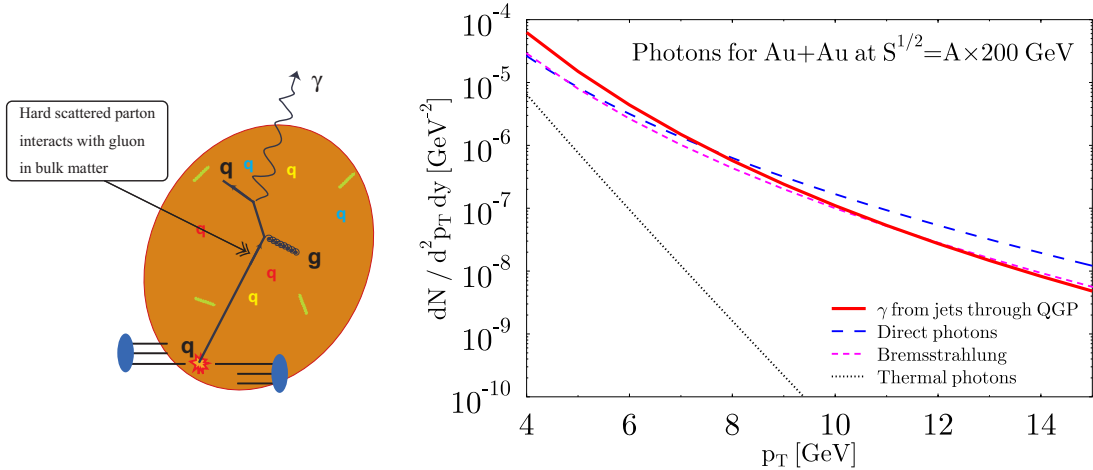


Figure 2.20: Left: Schematics of the direct photon production through the interaction of hard scattering partons in dense matter. Right: The invariant yield of direct photons at mid-rapidity for central 200 GeV Au+Au collisions given by R.J. Fries et al.. The photons from jets interacting with the medium (red solid line), direct hard photons (blue long dashed), bremsstrahlung photons as fragment of hard scattered partons (magenta short dashed), and thermal photons (black dotted) are shown.

strength to the other direct photon sources and even dominates in the range $p_T < 6 \text{ GeV}/c$ for Au+Au collisions at RHIC.

B.G. Zakharov also predicted that multiple scattering of fast quarks which undergo in the QGP may enhance photon radiation due to the induced photon emission ($q \rightarrow q\gamma$) [238].

2.4.4 Earlier Results on Direct Photon Production

The measurements of direct photon in p+p collisions were carried out by various experiments: UA6 [203, 94], WA70 [104], NA24 [180] at CERN-SPS, R110 [63], R806 [60] at CERN-ISR, and E706 [64] at FNAL-Tevatron. And direct photon in p+ \bar{p} collisions was measured by UA6 [203, 94] at CERN-SPS, UA1 [52], UA2 [57] at CERN-Sp \bar{p} S, and CDF [3], D0 [1] at FNAL-Tevatron. Direct photon data are reviewed in [216, 79, 191].

Measurement of direct photons in relativistic heavy ion collisions is challenging because there is a large amount of background from decay of neutral mesons such as π^0 and η . Even at RHIC energy, it is estimated that the signal-to-noise ratio would be $\sim 10\%$ at the p_T range of 2 – 4 GeV/c , where thermal photon is expected to be dominant. The experimental challenge for the measurement of direct photon in heavy ion collision was started at the CERN-SPS era. The HELIOS/NA34, WA80, and CERES/NA45 experiment investigated direct photon production from p, O and S beams at 200 AGeV ($\sqrt{s_{NN}} = 19 \text{ GeV}$) on C, Pt, Au and W targets [47, 55, 98]. They set the upper limits on the direct photon spectrum for O+Au collisions at 90 % confidence level (C.L.). The WA98 experiment descended from WA80 carried out the same program of measuring photons π^0 's and η 's in fixed target $^{208}\text{Pb} + ^{208}\text{Pb}$ collisions at 160 AGeV/c ($\sqrt{s_{NN}} = 17 \text{ GeV}$) using a highly-segmented lead-glass calorimeter. An excess of direct photon signal was observed in the range of $2.0 < p_T < 3.5 \text{ GeV}/c$ [41, 41]. This is the first experiment ever

in heavy ion collisions, a direct photon p_T spectrum was measured. Theoretical calculation based on the photon measurement supports that the high temperature of 200 – 330 MeV is formed at SPS energy [161, 134, 51, 124]. Especially, Srivastava and Sinha varied the initial thermalization time τ_0 and found a good fit to the data with a short $\tau_0 = 0.2 \text{ fm}/c$ for an initial QGP phase with a correspondingly high temperature of 335 MeV [206]. But the thermalization time is doubtful, because the crossing times of Pb+Pb is about $1.6 \text{ fm}/c$, as mentioned in Sec. 2.2.1, which contradict with the thermalization time. The understanding of the hadron gas dynamics is considered as crucial point for the interpretations of the low- p_T enhanced yield and the dynamics are under investigation [195, 50, 204].

2.5 Aim of This Study

With the motivation based upon the physics background of relativistic heavy ion collisions described in previous sections, the π^0 and direct photon p_T spectra are measured precisely with ten times larger statistics than previous measurement. Using the p+p reference data in spite of NLO pQCD calculation, which was used for previous study, the R_{AAS} of π^0 and direct photon are obtained, and will give us the confirmation of sign of strong suppression in high- p_T π^0 and no suppression in high- p_T direct photon. Based upon the comparison between the R_{AA} of π^0 and direct photon, one can constrain what the modification on high- p_T π^0 attribute to.

The high quality data make it possible to evaluate the theoretical expectation, and the evaluation gives us the information to understand the detail mechanism of energy loss, which was not understood with the previous data. In addition, quantitative evaluation of the properties, such as energy density, of created bulk matter produced by relativistic heavy ion collisions is carried out.

While it is hard to measure low- p_T direct photon due to the large background, the observation of the thermal photon which is expected to be dominant at low- p_T is the direct signature of the equilibrium state, and it is worth to try to measure the low- p_T direct photon.

Chapter 3

Experimental Setup

The Relativistic Heavy Ion Collider (RHIC) [154] was proposed in 1983 initially and built in the Brookhaven National Laboratory (BNL) in the United States of America. The Pioneering High Energy Nuclear Interaction eXperiment (PHENIX) for heavy ion physics at RHIC has started in the early summer of 2000.

3.1 The Relativistic Heavy Ion Collider

One of the aims of the RHIC is to study the nuclear matter under extreme conditions. The RHIC is designed to accelerate heavy ion at the maximum energy per nucleon of 100 GeV. Heavy ions are produced at the source and transported through Tandem-Van-de-Graaff. They are accelerated in the three synchrotrons: the booster accelerator, the Alternating Gradient Synchrotron (AGS) to 9 GeV for Au ions, and RHIC ring to the maximum energy. The RHIC ring has the total length of 3.8 km with the maximum bunch of 120 and the designed luminosity is $2 \times 10^{26} \text{ cm}^{-2}\text{s}^{-2}$ for Au ions. The some parameters and achieved performance for RHIC heavy ion run is summarized in Tab. 3.1. The RHIC collides two beams of gold ions head-on when they're traveling at nearly the 99.95 % speed of light. Figure 3.1 shows a schematic layout of RHIC accelerator complex.

RHIC is designed to study also the spin structure of the nucleon. The designed luminosity for polarized protons is $2 \times 10^{32} \text{ cm}^{-2}\text{s}^{-2}$, and the maximum energy is 250 GeV.

3.2 The PHENIX Experiment

The PHENIX [16] is a large spectrometer located in one of the 6 intersection points of the RHIC. Figure 3.2 shows the PHENIX spectrometer setup viewed from beam and side direction. In this thesis, the coordinate of the PHENIX spectrometer is defined as shown in Fig. 3.3. The beam axis is along with the z-axis, and the pseudo-rapidity is determined with θ as defined at Appendix A. In the central region, there are two spectrometers located back to back in ϕ . The pseudo-rapidity coverage of the central spectrometers is ± 0.35 . In the forward region, there are two muon spectrometers which have pseudo-rapidity coverage of $\pm(1.2 - 2.4)$, and beam detectors located at forward rapidity region. The each spectrometers are composed of

Injection Energy	$\gamma = 10.25$ ($p = 9.5$ GeV/c/nucleon)
Storage Energy	$\gamma = 107.4$ ($p = 100.0$ GeV/c/nucleon)
Bunch intensity	1.0×10^9 Au ions/bunch
Number of bunches	56 filled bunches
Transverse emittance	$15\pi \mu\text{m}$ (normalized, 95 %)
Longitudinal emittance	0.3 eVs/nucleon/bunch
Interaction diamond length (r.m.s.)	20 cm
Crossing angle, nominal (maximum)	0 (< 1.7) mrad
Bunch length	15 cm
Bunch radius	0.2 mm ($\beta^* = 1$)
Luminosity life time	3 hour

Table 3.1: Parameters and performance for RHIC heavy ion run

the detector subsystems, whose coverage and features are summarized in Tab. 3.2 As the focus of this study is the measurement of direct photons and neutral pions with the Electromagnetic Calorimeter (EMCal) in the central arms, the subsystem will be explained in detail, after the overview of the PHENIX detectors will be mentioned briefly.

3.2.1 Beam Detectors

There are 2 types of beam detectors used for event trigger, and used to measure the beam property, such as the luminosity and centrality [58]. The one is Beam Beam Counters (BBC) and the another is Zero Degree Calorimeters (ZDC).

The BBCs are two arrays of 64 Cherenkov counters, each of which is located 1.44 m north and south respectively from the nominal collision point. Each covers the pseudo-rapidity of 3.0 – 3.9. Pictures in Fig. 3.4 show (a) one counter, (b) an array, (c) BBC mounted. Each counter is composed of 3 cm thick quartz as a Cherenkov radiator equipped with 64 1-inch diameter mesh-dynode photomultiplier tube (Hamamatsu R6178). The BBC is designed to measure the number of charged particles produced by the collisions, the collision vertex and the start time for the time-of-flight system. The BBC plays an important role for the centrality determination in combination with ZDC. Due to the limited acceptance coverage, the 93 % and 50 % of the inelastic collisions can be triggered for Au+Au and p+p collisions at $\sqrt{s_{\text{NN}}} = 200$ GeV, respectively.

ZDCs are positioned at each of the four RHIC experiments [18]. The detector is hadron calorimeter designed to measure the number of neutrons from the collision. Figure 3.6 shows the cross-section of ZDC, which consists of three modules, 27 layers of Tungsten alloy plates, optical fibers and a photo-multiplier tube (PMT: Hamamatsu R329-2). The thickness corresponds to 2 hadronic interaction length. The energy resolution of ZDC was obtained to be $\sigma_E/E = 218\%/\sqrt{E} (\text{GeV})$ from beam test experiment. ZDCs are located at 18.25 m north and south from nominal collision vertex, and both ZDCs are at just the upstream of the last bending magnet of the RHIC system. Most of the charged particles are swept out from the acceptance. This detector allows a common event characterization for monitoring of the collider

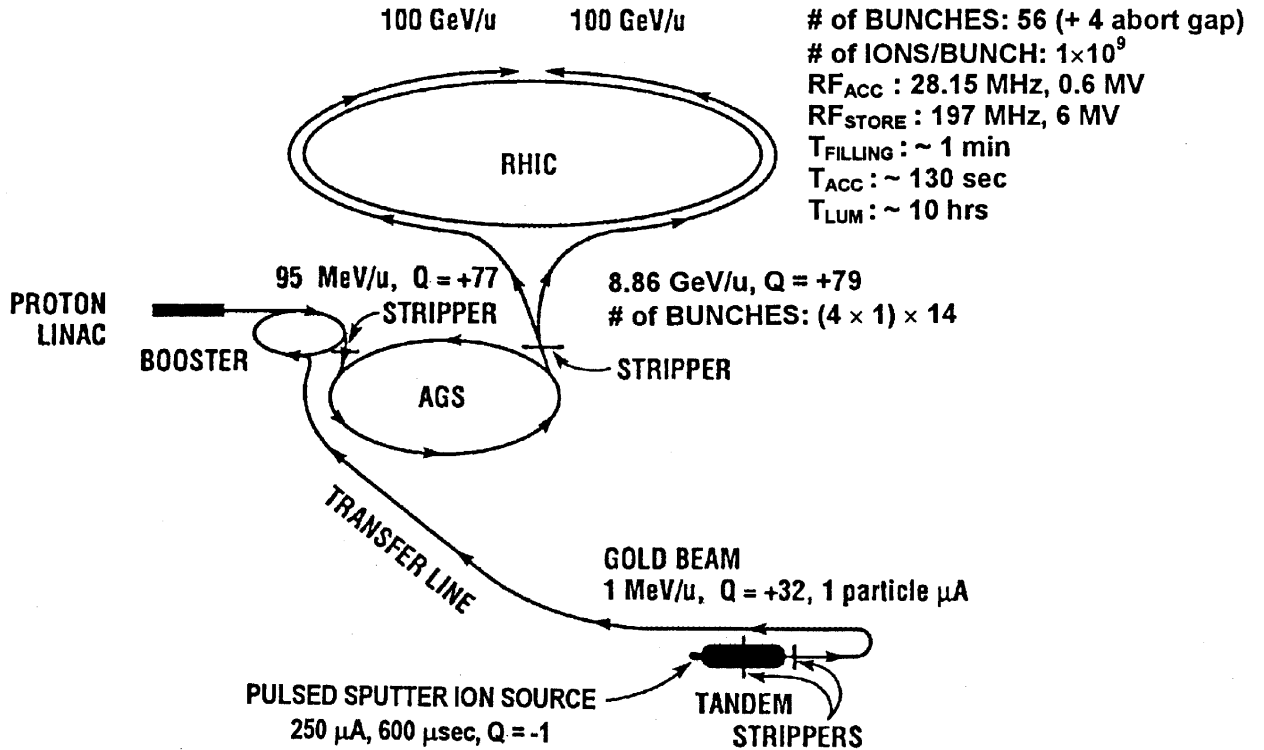


Figure 3.1: Schematic view of BNL-RHIC.

performance. For the PHENIX experiment, this detector is used for monitoring of the beam luminosity, event trigger, measurement of collision vertex, and centrality determination.

The start timing (T_0) and the vertex position (z_{vtx}) along the beam axis are obtained as:

$$T_0 = \frac{T_N + T_S}{2} - z_{N-S}/c, \quad (3.1)$$

$$z_{vtx} = \frac{|T_N - T_S|}{2} \cdot c, \quad (3.2)$$

where z_{N-S} stands for the distance between the detectors located at North and South, T_N and T_S are the average measured time of arriving particles at North and South, respectively. Figure 3.7 shows the z-vertex distribution measured by BBC and ZDC. A strong correlation between the vertex by BBC and that by ZDC is seen. The timing resolution of a single BBC element is 52 ± 4 psec (RMS) under the real experimental conditions.

3.2.2 PHENIX Central Arms

Each of the east and west central arm spectrometers covers the pseudo-rapidity range of $|\eta| < 0.35$ and 90 degrees in azimuthal angle. As shown in the upper panel of Fig. 3.2, each spectrometer consists of the layers of subsystems for tracking, particle identification and calorimetry. The west arm spectrometer consists of Drift Chamber (DC) at the radial distance of 2-2.4 m, Pad Chambers (PC1) at 2.45 m, Ring Imaging Cherenkov Detectors (RICH) at 2.6-4.0 m, Pad

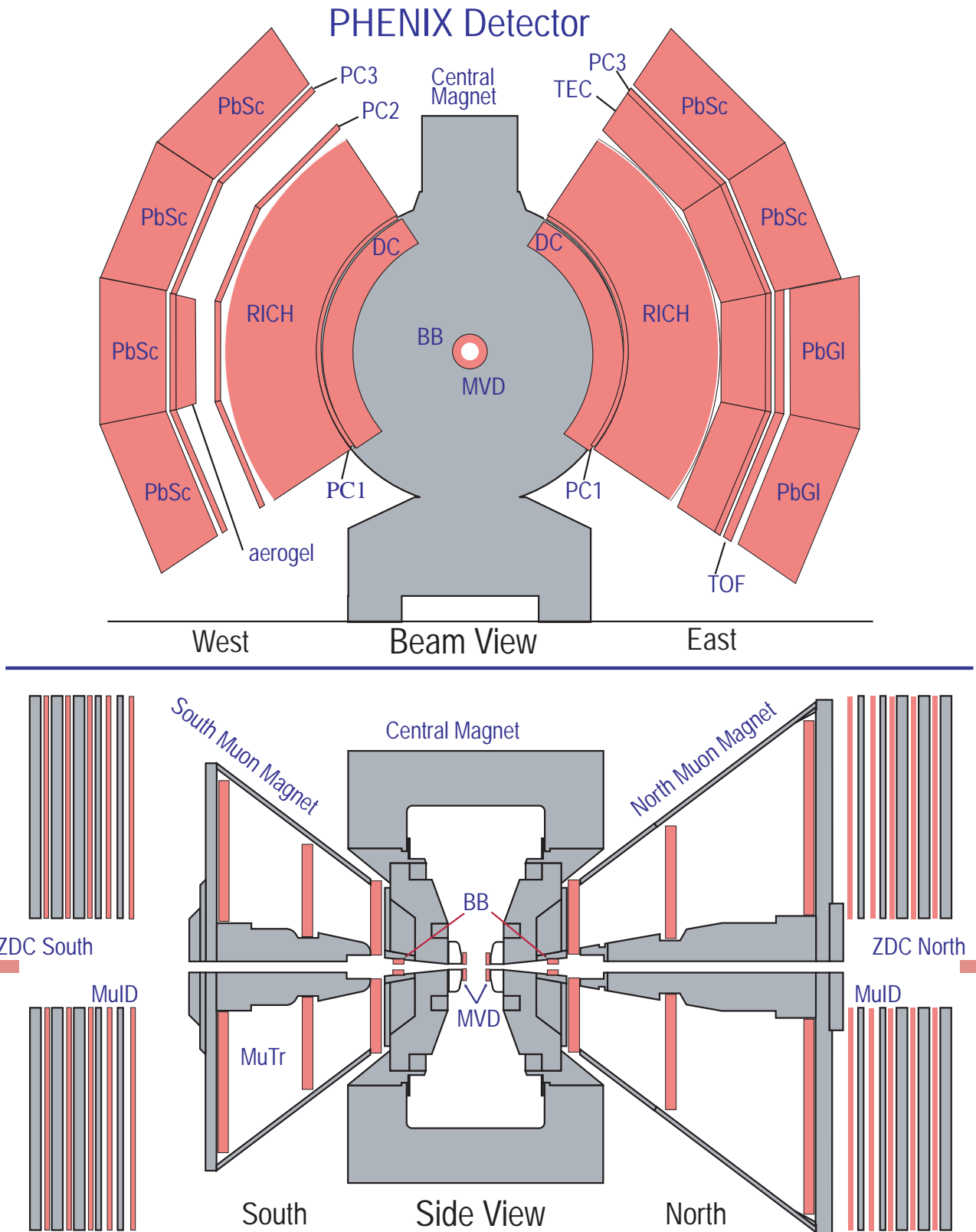


Figure 3.2: The PHENIX setup during the fourth RHIC beam period.

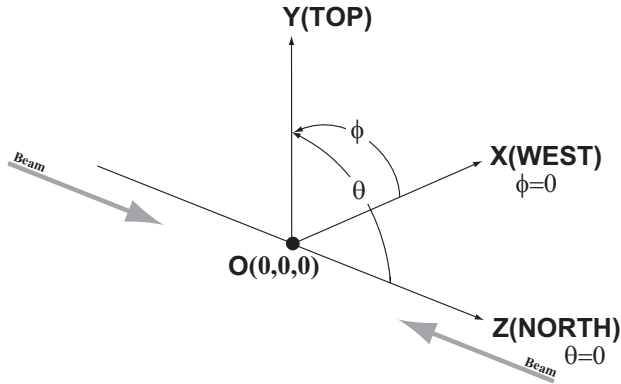


Figure 3.3: Definition of the PHENIX global coordinate.

Chamber (PC2) at 4.2 m, Aerogel Detector (AGEL) at 4.3-4.5 m, Pad Chamber (PC3) at 4.9 m, and Lead Scintillator electromagnetic calorimeters (PbSc-EMCal) at 5.07-6 m. The east arm spectrometer is composed of similar detectors as the west arm at the same radial locations. There are no PC2 and AGEL, but in addition 2 sectors of Time-Of-Flight (TOF) systems at 5.06 m, four layers of Time Expansion Chambers (TEC) at 4.1-4.8 m, two sectors of PbSc and 2 sectors of Lead Glass electromagnetic calorimeters (PbGl) at 5.07 m and 5.4 m, respectively.

A magnetic field is produced by the Central Magnet for momentum measurement of the charged particles [73]. Two concentric coils can provide an axial magnetic field of $\int B dl = 0.43\text{-}1.15 \text{ T}\cdot\text{m}$. In order to reduce the influence of the magnetic field on the several detector components, such as the photomultiplier tube, as much as possible, the exterior field at the radial field of $r > 2 \text{ m}$ from the vertex is required to be minimum. This requirement is satisfied by an appropriate arrangement of the flux return yoke, leading to a residual field integral of less than $\int_{l=2.4 \text{ m}}^{l=4 \text{ m}} B dl = 0.01 \text{ T}\cdot\text{m}$ at $\eta = 0$.

The characteristics of the each subsystems (tracking, particle identification and calorimetry) are discussed briefly in the following:

Tracking System

For the charged particle analysis, usually tracking starts at the Drift Chamber (DC) which is located at the edge of magnetic field. DC measures the deflection of charged particles in the magnetic field with a resolution of about $150 \mu\text{m}$ in the $r\text{-}\phi$ plane. It provides the momentum resolution of $\delta p/p = 0.7\% \oplus 1.0\% \times p (\text{GeV}/c)$ for π^\pm .

The tracking information obtained using the DC is utilized for pattern recognition through the various detectors of the central arms, such as Pad Chambers (PC) and Time Expansion Chambers (TEC). PCs are multi-wire proportional chambers located at different radii from the beam axis as described before [190].

The technical information of tracking subsystems are summarized in [15].

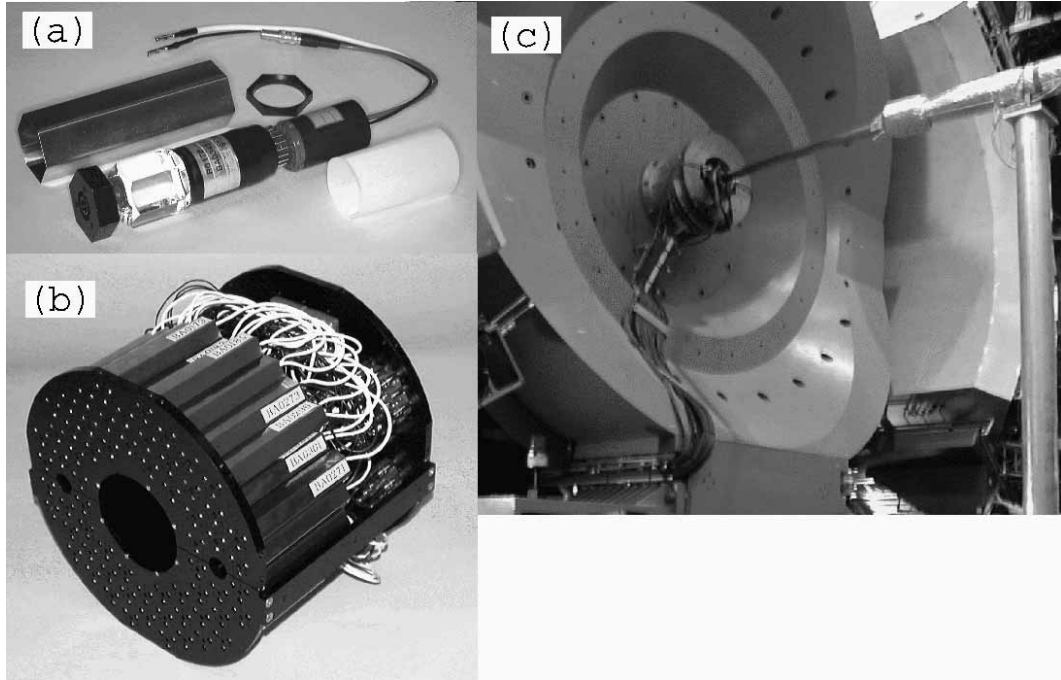


Figure 3.4: (a) Single Beam Beam counter consisting of one-inch mesh dynode photomultiplier tubes mounted on a 3 cm quartz radiator. (b) A BBC array comprising 64 BBC elements. (c) The BBC is shown mounted on the PHENIX detector. The beam pipe is seen in the middle of the picture. The BBC is installed on the mounting

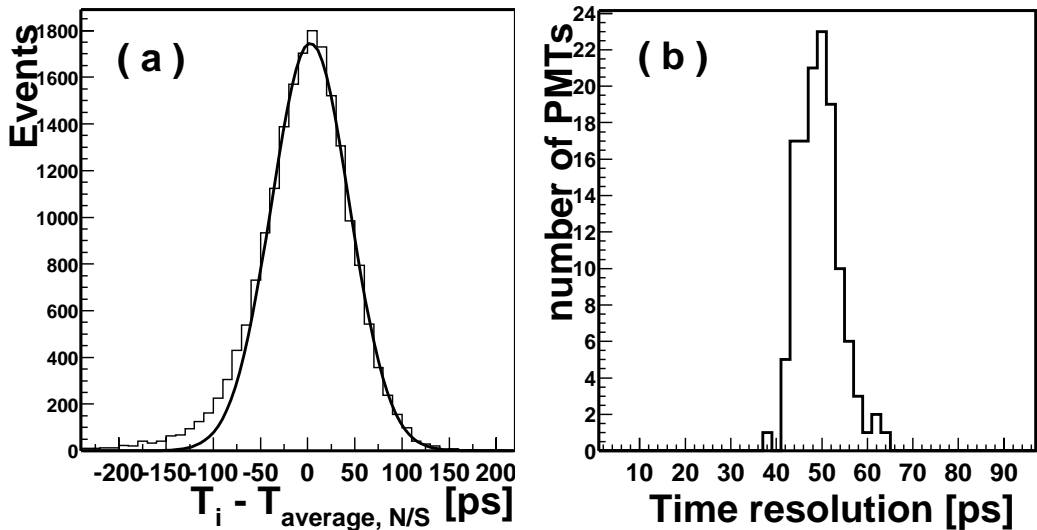


Figure 3.5: (a) Distribution of timing deviation for a typical BBC element from BBC averaged hit timing. (b) Profile of timing resolution for each BBC element.

Subsystem	rapidity coverage	$\delta\phi$	Purpose and Features
Beam Beam Counters (BBC)	$3.1 < \eta < 3.9$	2π	Minimum bias trigger vertex reaction plane determination start timing
Zero Degree Calorimeter (ZDC)	$\pm 2 \text{ mrad } (\eta \geq 6)$	2π	Minimum bias trigger
Central Magnet	$ \eta < 0.35$	2π	Up to $1.15 \text{ T}\cdot\text{m}$
South Muon Magnet	$-2.2 < \eta < -1.1$	2π	
North Muon Magnet	$1.1 < \eta < 2.4$	2π	
Drift Chamber (DC)	$ \eta < 0.35$	$\pi/2 \times 2$	momentum measurement $\frac{\delta m}{m} = 0.4\%$ at $m = 1 \text{ GeV}$
Pad Chamber (PC)	$ \eta < 0.35$	$\pi/2 \times 2$	track matching
Time Expansion Chamber (TEC)	$ \eta < 0.35$	$\pi/2$	track matching
Ring Imaging Cherenkov Detector (RICH)	$ \eta < 0.35$	$\pi/2 \times 2$	electron ID
Aerogel Detector (AGEL)	$0 < \eta < 0.35$	$\pi/4$	high-pT hadron ID
Time Of Flight (TOF)	$ \eta < 0.35$	$\pi/4$	hadron ID $\sigma < 100 \text{ psec}$
Electromagnetic Calorimeter			energy measurement
Lead-Scintillate	$ \eta < 0.35$	$\pi/2 + \pi/4$	fine granularity
Lead-Glass	$ \eta < 0.35$	$\pi/4$	
Muon Tracker (MuTr)	$-2.25 < \eta < -1.1$	2π	momentum measurement
	$1.15 < \eta < 2.44$	2π	
Muon Identifier (MuID)	$-2.25 < \eta < -1.15$	2π	muon ID
	$1.15 < \eta < 2.44$	2π	

Table 3.2: Summary of the PHENIX detectors.

Particle Identification

One of the main features of PHENIX detector is excellent capability of electron identification up to high- p_T . The Ring Imaging Cherenkov detector (RICH) plays a major role for the electron identification. It is composed of CO₂ gas volumes of 40 m^3 ($n-1 = 4.1 \times 10^{-4}$), and charged particles with velocities larger than the speed of light in the radiator medium emit Cherenkov radiation in a light cone that falls as ring on the RICH mirror system and is reflected onto photomultipliers. Because the thresholds for pions to emit Cherenkov radiation is higher than that for electrons, no pions are detected below $p = 4.65 \text{ GeV}/c$ [48].

The Time-Of-Flight Spectrometer (TOF) has timing resolution of about 100 psec, which allows to distinguish between kaons and protons up to $p = 4 \text{ GeV}/c$ and between pions and kaons up to $p = 2.4 \text{ GeV}/c$. Since the TOF detector is installed only in front of the lead-glass calorimeter, the identification of charged particle is also made with a time-of-flight measurement in the lead-scintillator calorimeter which has a nominal timing resolution of approximately 270 psec.

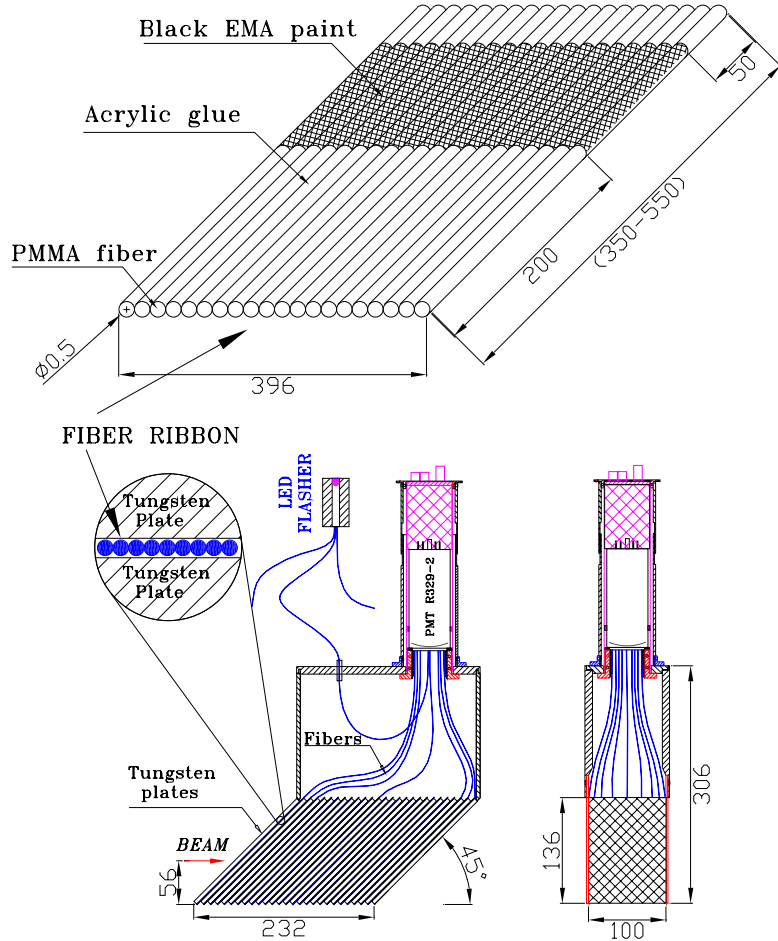


Figure 3.6: Mechanical design of the production tungsten modules in zero-degree calorimeter. Dimensions shown are in mm.

Calorimetry

The two types of electromagnetic calorimeter, lead-scintillator (PbSc) and lead-glass (PbGl), are located at the end of central tracking system. With their fine segmentation ($\Delta\eta \times \Delta\phi \approx 0.01 \times 0.01$), both calorimeters provide a good energy resolution and position resolution for the measurement of electromagnetic probes. Since the calorimeter is main subsystem for the study described in this report, the detail information of calorimeters are described in following section.

3.2.3 PHENIX Muon Arms

The primary function of the muon arm is the measurement of dimuons and single muons using the Muon Tracker (MuTr) and Muon Identifier (MuID) in the north and south muon arms [49]. These detectors cover the rapidity range of $1.2 < |\eta| < 2.4$.

The largest background of the muon measurement is mis-identified hadrons and secondary muons from hadron decays. These backgrounds are suppressed by the absorption of hadrons

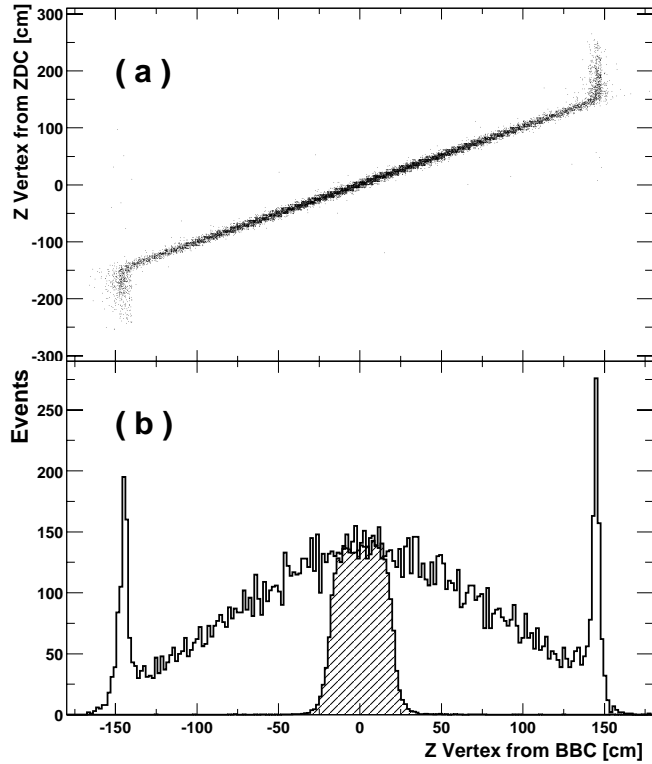


Figure 3.7: Vertex distribution measured by PHENIX inner detector. (a) Correlation of determined Z vertex between BBC and ZDC. (b) Z Vertex distribution from BBC. Hatched area corresponds to the events satisfying the PHENIX Local LVL1 trigger condition for vertex.

in the dense material of the Central Magnet and by the identification with MuID. The MuID consists of a sequence of steel absorber plates and streamer tube detectors. The thickness of the plate is optimized to let muons with an energy above 2.9 GeV penetrate completely, and the muons with $E > 1.9$ GeV can penetrate the material in front of the MuID. This condition leads to a pion/muon separation of $2 \cdot 10^{-4}$ to $3.9 \cdot 10^{-3}$ at the momentum region of $2 \text{ GeV}/c < p < 10 \text{ GeV}/c$. The muons which penetrate the MuID are tracked by MuTr, which consists of three layer of tracking chambers with cathode strip readout. The position resolution of the tracker is approximately $100 \mu\text{m}$ along the wire, which ensure the reconstruction of dimuons with a mass resolution of $6 \%/\sqrt{m_{\mu\mu}}$.

3.2.4 PHENIX Data Acquisition System

PHENIX is designed to make measurements for a variety of colliding systems from p+p to Au+Au. The occupancy in the detector varies from a few tracks in p+p interactions to approximately 15 % of all detector channels in central Au+Au interactions. The interaction rate at design luminosity varies from a few kHz for Au+Au collisions to approximately 500 kHz for p+p collisions. The PHENIX DAQ system [24, 25] is designed to be flexible enough to accommodate improvements in the luminosity. This is accomplished through the pipelined and dead-time-less features implemented to the detector front ends and the ability to accommodate

higher-level triggers.

The wide range of event sizes and luminosities present special challenges for triggering and data acquisition. In PHENIX it is necessary to measure low-mass lepton pairs and low p_T particles in a high-background environment. In order to preserve the high interaction rate capability, a flexible triggering system that permits tagging of events is constructed. The DAQ system has two levels of triggering denoted as level 1 (LVL1) and level 2 (LVL2). The LVL1 trigger is fully pipelined. The buffering in the pipeline is sufficient to handle fluctuations in the event rate so that dead-time is reduced to less than 5% for full RHIC luminosity. The LVL1 trigger and lower levels of the readout are clock-driven by bunch-crossing signals from the 9.4 MHz RHIC clock. The higher levels of readout and the LVL2 trigger are data-driven where the results of triggering and data processing propagate to the next higher level only after processing of a given event is completed.

The schematics of the PHENIX data acquisition system is shown in Fig. 3.8. Signals from the various PHENIX subsystems are processed by Front End Electronics (FEE) that convert detector signals into digital event fragments. This involves analog signal processing with amplification and shaping to extract the optimum time and/or amplitude information, development of trigger input data and buffering to allow time for data processing by the LVL1 trigger and digitization. This is carried out for all detector elements at every beam crossing synchronously with the RHIC beam clock. The timing signal is a harmonic of the RHIC beam clock and is distributed to the FEM's by the PHENIX Master Timing System (MTS). The LVL1 trigger provides a fast filter for discarding empty beam crossings and uninteresting events before the data is fully digitized. It operates in a synchronous pipelined mode, generates a decision every 106 nsec and has an adjustable latency of some 40 beam crossings.

Once an event is accepted the data fragments from the FEM's and primitives from the LVL1 trigger move in parallel to the Data Collection Modules (DCM). The PHENIX architecture was designed so that all detector-specific electronics end with the FEM's, so that there is a single set of DCM's that communicate with the rest of the DAQ system. The DCM's perform zero suppression, error checking and data reformatting. Many parallel data streams from the DCM's are sent to the Event Builder (EvB). The EvB performs the final stage of event assembly and provides an environment for the LVL2 trigger to operate. In order to study the rare events for which PHENIX was designed, it is necessary to reduce further the number of accepted events by at least a factor of six. This selection is carried out by the LVL2 triggers while the events are being assembled in the Assembly and Trigger Processors (ATP) in the EvB. The EvB then sends the accepted events to the PHENIX On-line Control System (ONCS) for logging and monitoring. The recorded raw data are sent to the RHIC Computing Facility (RCF) for sinking on the tape device in High Performance Storage System (HPSS). The raw data are converted into an intermediate data format for the analysis.

3.3 The Electromagnetic Calorimeter

The Electromagnetic Calorimeter (EMCal) [65] plays a main role in detecting photons coming from neutral decay modes. The EMCal is the major detector subsystem used for the analysis described in this report. The overview of the EMCal system, the detailed specification, and

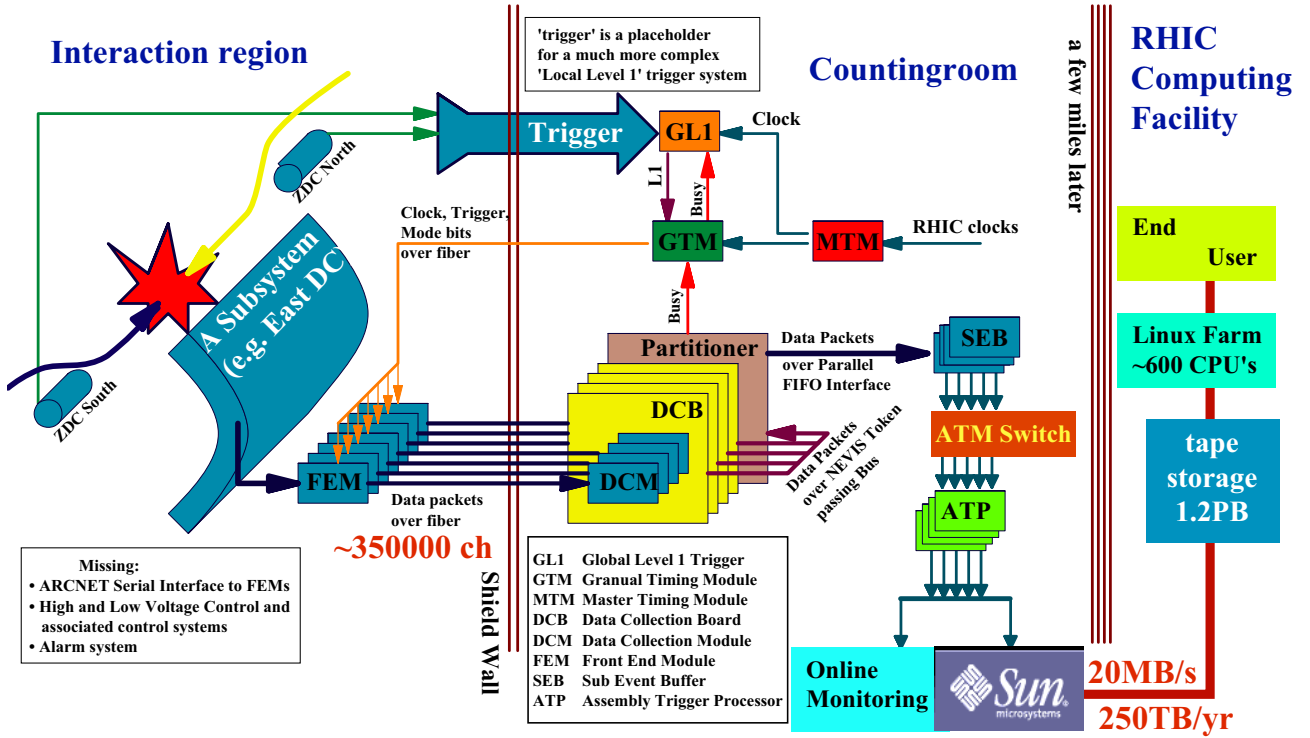


Figure 3.8: The block diagram of PHENIX Data Acquisition System.

the basic performance are described in this section.

In the PHENIX Central arm, two types of different EMCAL are installed. There are six sectors of shashlik type lead-scintillator sandwich calorimeter (PbSc) and two sectors of lead-glass Cherenkov calorimeter (PbGl). Table 3.3 summarize their basic parameters. A super-module consists of channels, and a sector consists of super-modules and total 8 sectors are installed in the PHENIX central arms.

The PbSc is a sampling calorimeter while the PbGl is a Cherenkov detector. For the two detectors the granularity, energy resolution, linearity, response to hadrons, timing properties and shower shape at normal and non-normal impact on the face of the tower differ significantly. For instance, the PbGl has the best granularity and energy resolution but the PbSc has the best linearity and timing and the response to hadrons is better understood. These detectors provide a good possibility of internal cross-checks with their different systematics. In order to cover topics in physics programs, for example it was proposed to measure photons and pi0s in p+p/Au+Au and to measure weak bosons in polarized proton collisions, the EMCAL is designed to satisfy the following requirements:

- coverage of a wide energy range extending from a few hundred MeV to 80 GeV
- a 2 % accuracy in the calorimeter energy scale to measure the cross sections of single photons and π^0 's with an accuracy of 10 %

	PbSc	PbGl
type	66 – Scintillator+Lead	Cherenkov
radiation length (X_0) [mm]	21	29
Moliere radius [mm]	30	37
cross section of a channel [mm^2]	52.5×52.5	40×40
depth [mm (X_0)]	375 (18)	400 (14)
$\Delta\eta$ of a channel	0.011	0.008
$\Delta\phi$ of a channel	0.011	0.008
number of channels in a super-module	144 (12 \times 12)	24 (4 \times 6)
number of super-modules in a sector	18 (3 \times 6)	192 (12 \times 16)
number of total sectors	6	2
number of total channels	15552	9216

Table 3.3: Summary of the EMCAL subsystem.

- fine granularity of $\Delta\eta \times \Delta\phi \approx 0.01 \times 0.01$ to achieve an occupancy of less than 20 % in the central Au+Au collisions

3.3.1 Lead-Scintillator Calorimeter

The PbSc electromagnetic calorimeter is a shashlik type sampling calorimeter made of alternating tiles of lead and scintillator [86, 209]. As shown in Fig. 3.9, the basic building block is a module consisting of four (optically isolated) towers which are read out individually. Each PbSc tower contains 66 sampling cells consisting of alternating tiles of lead (0.4 cm) and scintillator (0.4 cm). The scintillator is made of Polystyrene (1.5 % PT/0.01 % POPOP). The edges of the tiles are plated with Al. These cells are optically connected using the 36 longitudinally penetrating wavelength shifting fibers for light collection. Light is read out by 30 mm ϕ FEU115M phototubes at the back of the towers. Thirty six modules are attached to a backbone and held together by welded stainless steel skins on the outside to form a rigid structure called a supermodule. Details of the design and methods of construction of the PbSc modules are given in [115].

Calibration and Monitoring System

The calibration and monitoring system is based on a UV laser which supplies light to the calorimeter through a series of optical splitters and fibers. The block diagram of the monitoring system is schematically shown in Fig. 3.10 [114]. The YAG-laser light are split by 3 steps and delivered into 3888 modules in total. The laser amplitude is monitored by a phototube and photo diodes in all the light splitters. Since the operation condition has changed from the time of construction and the gain drift during the data taking should be corrected, this laser calibration system is established to normalize the initial energy calibration, which has been obtained by utilizing cosmic ray for all towers during construction. The gain of the amplifier for the photo diodes is monitored by test pulses.

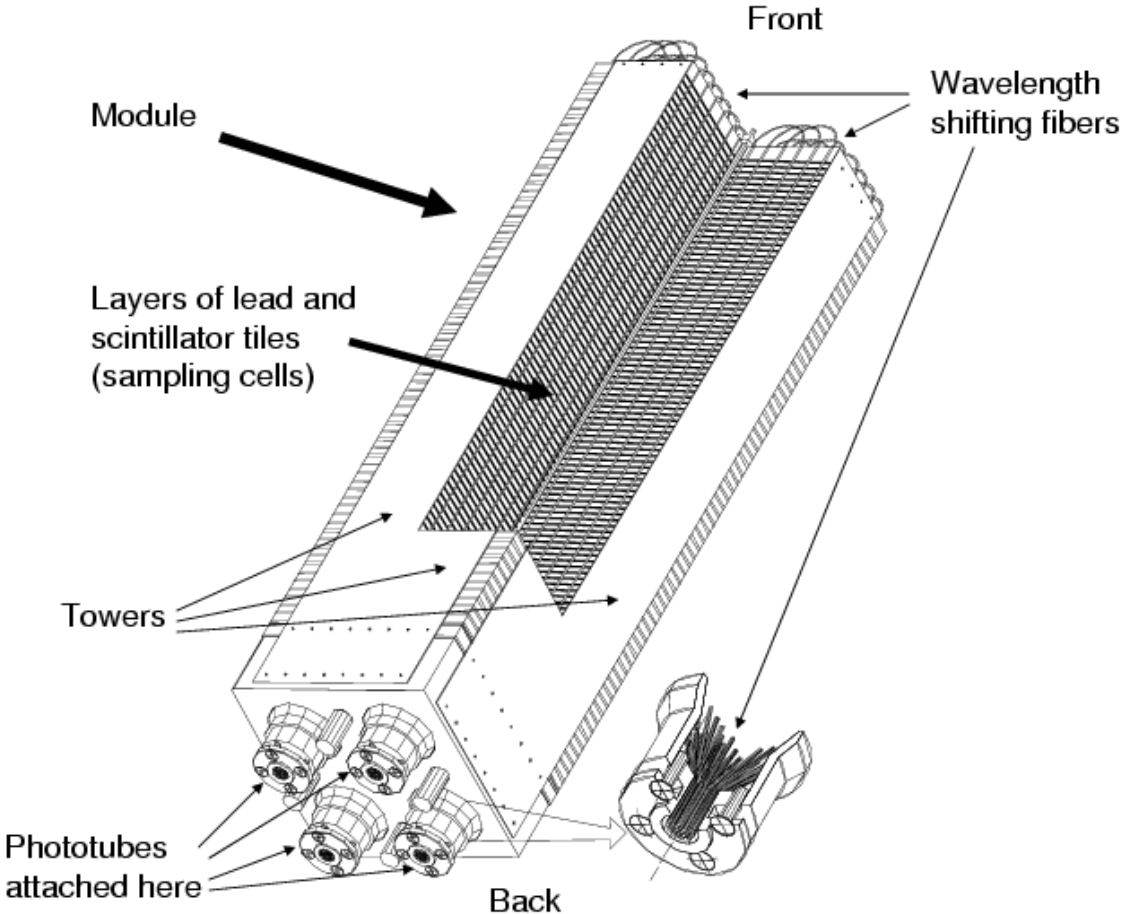


Figure 3.9: The cross-section of Lead-Scinti Calorimeter showing a stack of scintillator and lead plates, wavelength shifting fiber readout and leaky fiber inserted in the central hole.

3.3.2 Test Beam Performance of PbSc Calorimeter

Since PbSc Calorimeter is a major detector which is used for the π^0 and photon analysis, the fundamental characteristics is described in this section in detail. The basic performance, energy resolution, linearity, position resolution and hadron rejection has been measured at BNL in the energy range up to 7 GeV [115]. In order to extend these measurements to the energy range up to 80 GeV, a beam test has been performed at the CERN H6 beam line in 1998 [82].

Energy Linearity and Resolution

The measured energy divided by the energy of electron beam as a function of the incident beam energy in the calorimeter is presented in Fig. 3.11. Data are normalized at 1 GeV. The finite light attenuation length (100 cm) in the WS fibers is a major contributor to the response non-uniformities at the low end of the energy scale, although this effect is mitigated by the fact that each fiber is looped back as shown in Fig. 3.9, and the light collected always has a short and a long path to the phototube. Other contributors at low energies are coarse sampling and

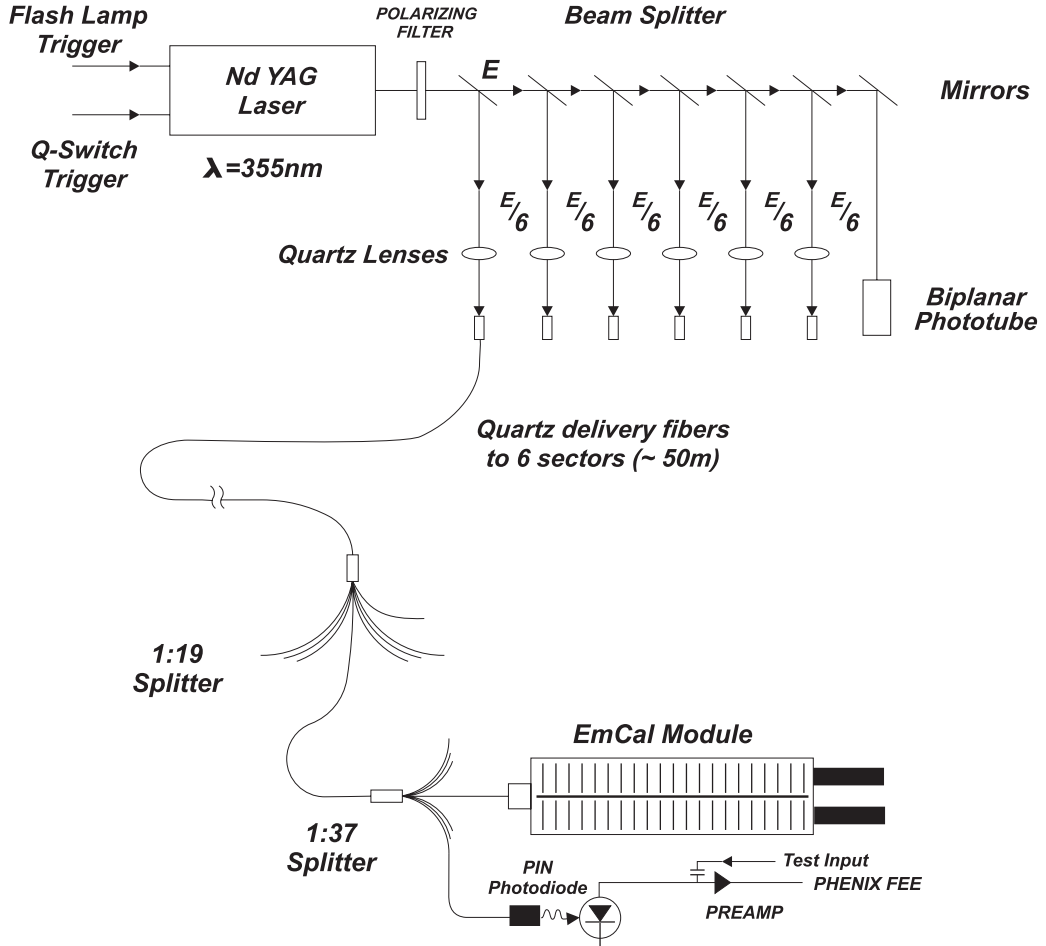


Figure 3.10: The PbSc setup for run-by-run calibration and monitoring.

energy leakage at the front face. At high momenta the positive effect of the light attenuation in the fibers is overcompensated by the negative effect of energy leakage from the back of the calorimeter. As the result, the effect of nonlinearity is about a factor of 2 lower than what one would expect from the effect of light attenuation alone. The nonlinearity due to the attenuation in the fibers are corrected with the form of $\exp(x_0 \ln(E)/\lambda) = E^{x_0/\lambda}$, where $\lambda = 120$ cm. The correction of both effects are applied in the data.

The energy resolution is obtained using electron and positron beams with the well-calibrated momentum. Figure 3.12 shows the energy resolution obtained by both beam tests at CERN and BNL. They can be fitted with a linear or quadratic expressions. Only statistical errors are taken into account in the fits. An additional 1 % systematic error is estimated based on the reproducibility of the measurements at each energy point. The results of the fits are

$$\frac{\sigma_E}{E} = 1.2 \% + \frac{6.2 \%}{\sqrt{E \text{ (GeV)}}} \quad (\text{a linear expression}), \text{ and} \quad (3.3)$$

$$= 2.1 \% \oplus \frac{8.1 \%}{\sqrt{E \text{ (GeV)}}} \quad (\text{a quadratic expression}), \quad (3.4)$$

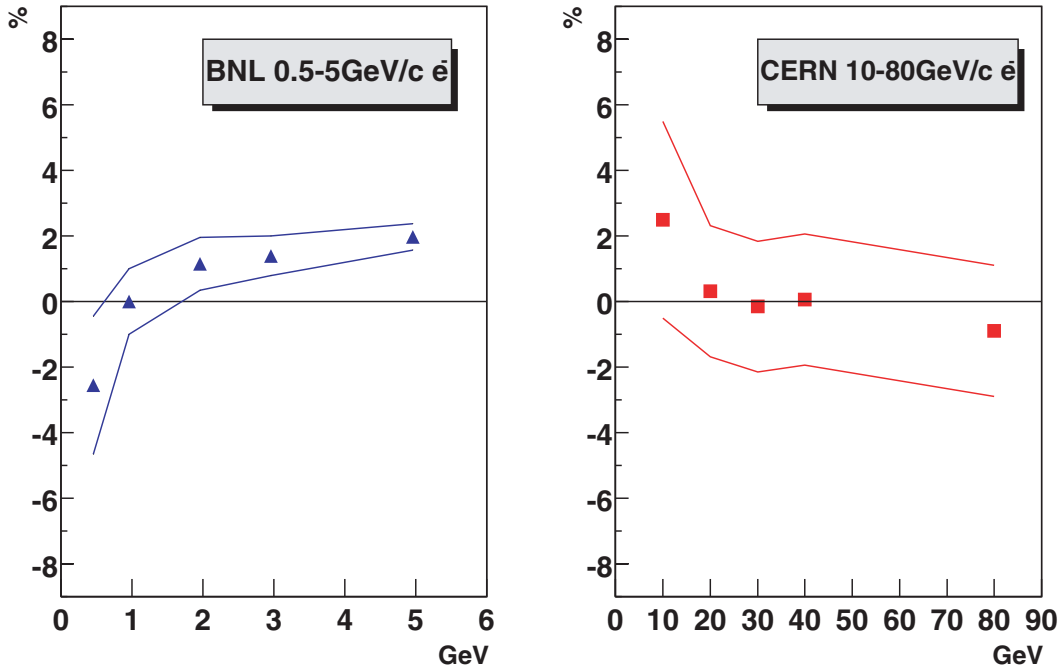


Figure 3.11: The energy linearity of PbSc calorimeter obtained from both beam tests at BNL (left) and CERN (right). The solid lines show total systematic uncertainties in the analysis.

where \oplus denotes a root of the quadratic sum, i.e. $\alpha \oplus \beta = \sqrt{\alpha^2 + \beta^2}$. The angular dependence of the resolution is negligible. They are valid in the energy region of 0.5 GeV to 80 GeV within 1 % systematic uncertainty.

Position Resolution

Using electron and positron at the well-known impact position on the surface of the EMCAL in the test beam, the position resolution is evaluated with the logarithmic method [81]. Figure 3.13 shows the position resolution obtained from both beam tests at CERN and BNL. The points can be fitted by a formula:

$$\sigma_x(0^\circ) [\text{mm}] = 1.4 [\text{mm}] + \frac{5.9 [\text{mm}]}{\sqrt{E (\text{GeV})}}. \quad (3.5)$$

The particles hit the calorimeter with an oblique angle, an additional term is estimated from the GEANT [107] simulation and the AGS test beam. It is added in quadrature to the resolution as:

$$\sigma_x(\theta) [\text{mm}] = (20.0 [\text{mm}] \cdot \sin(\theta)) \oplus \sigma_x(0^\circ), \quad (3.6)$$

where θ is the incident angle of the particle in the surface of the calorimeter.

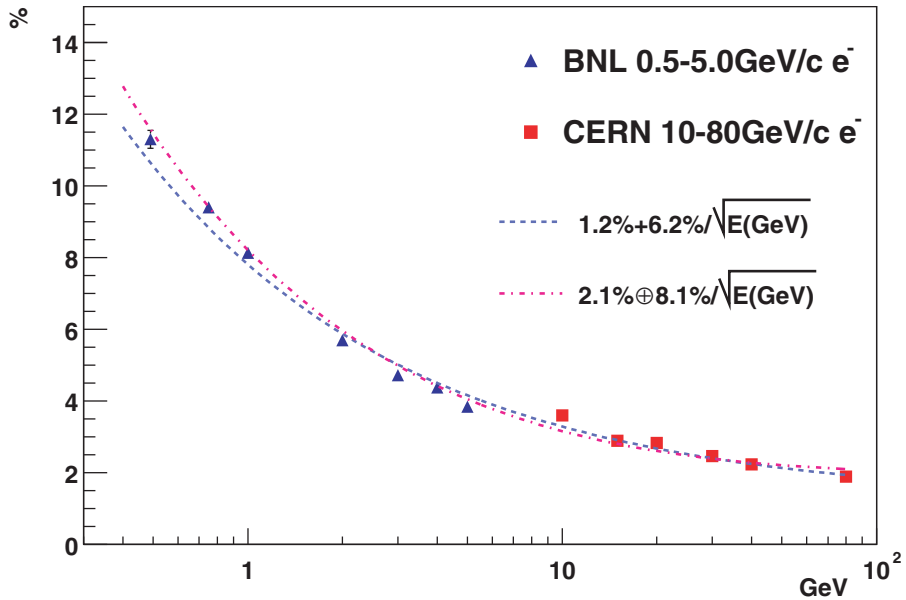


Figure 3.12: The energy resolution of PbSc calorimeter given by test beam results. A dashed line shows the result of fitting by a linear formula, $\sigma_E/E = 1.2\% + 6.2\%/\sqrt{E} \text{ (GeV)}$. A dashed dotted line shows the result of fitting by a quadratic formula, $\sigma_E/E = 2.1\% \oplus 8.1\%/\sqrt{E} \text{ (GeV)}$.

3.3.3 Lead-Glass Calorimeter

The PbGl calorimeter was previously used in the WA98 experiment at CERN, where direct photons were observed for the first time in heavy ion collisions [42]. After the disassembly of the WA98 experiment 9216 elements of the former LEDA1 calorimeter were transported to BNL and reassembled into two sectors of the PHENIX-EMCal.

The PbGl is a Cherenkov detector (55 % PbO and 45 % SiO₂, $n = 1.648$, critical energy (E_c) = 16 MeV). Though Cherenkov radiation is a negligible source of energy loss, it is very useful for particle detection and energy measurements because the number of produced Cherenkov photons per unit length is constant, and the total length of all positron and electron tracks of a shower is connected linearly to the energy of the primary particle [171].

Each lead-glass sector consists of supermodules, each forming a self-contained detector with its own reference system as shown in Fig. 3.14. One supermodule is formed by an array of 4 lead-glass modules, each with a size of $4 \times 4 \times 40 \text{ cm}^3$ and wrapped in reflecting mylar foil and shrink tube.

The response of the PbGl electromagnetic calorimeter was studied extensively in test beams at the AGS (BNL) and SPS (CERN) to investigate the performance of the device with respect to energy, position and timing measurements and their variation with energy, position and angle of incidence. As a result, the each characteristics are parameterized as followings:

- energy resolution

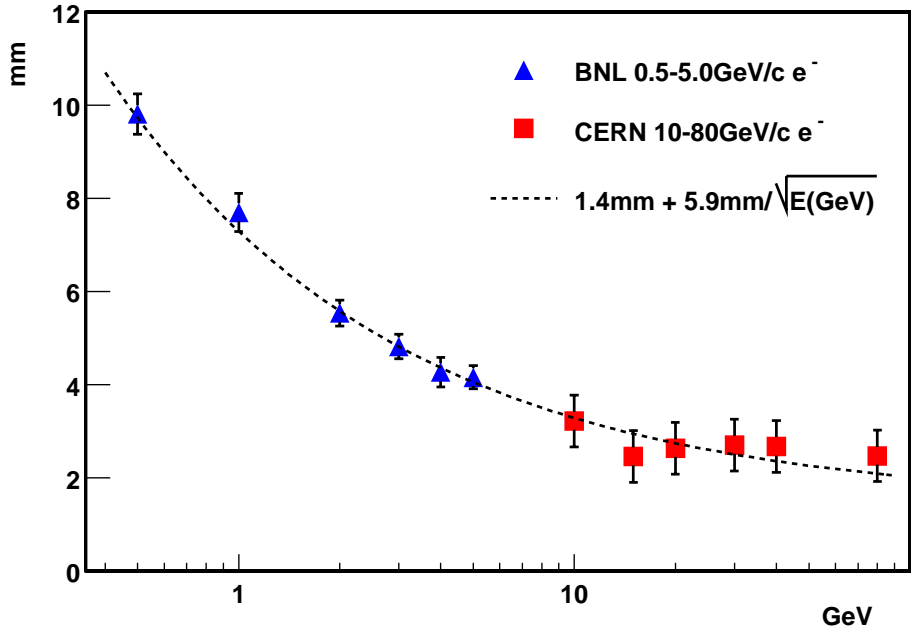


Figure 3.13: Position resolution obtained by beam tests. A dashed line shows the result of fitting, $1.4 \text{ mm} + 5.9 \text{ mm}/\sqrt{E \text{ (GeV)}}$.

$$\frac{\sigma(E)}{E} = \frac{5.9 \%}{\sqrt{E \text{ (GeV)}}} \oplus 0.8 \% \quad (3.7)$$

- position resolution

$$\sigma_x(E) = \frac{5.9 \text{ mm}}{\sqrt{E \text{ (GeV)}}} \oplus 0.2 \text{ mm.} \quad (3.8)$$

- timing resolution

$$\sigma_t(E_{Dep}) = \frac{3.75 \text{ nsec}}{\sqrt{500 \cdot E_{Dep} \text{ (GeV)}}} \oplus 0.075 \text{ nsec,} \quad (3.9)$$

where E_{Dep} is an energy deposit in a center tower.

3.3.4 Calorimeter Front-End Electronics

The readout electronics for the EMCal system conform to the general PHENIX Front-End Electronics (FEE) scheme [26] which includes periodic sampling synchronous with the RHIC RF clock and pipelined, deadtime-less conversion and readout.

On every event, for either physics or calibration data, each EMCal PMT emits a negative current pulse and each of these is processed as shown in Fig. 3.15. There is no preamp or

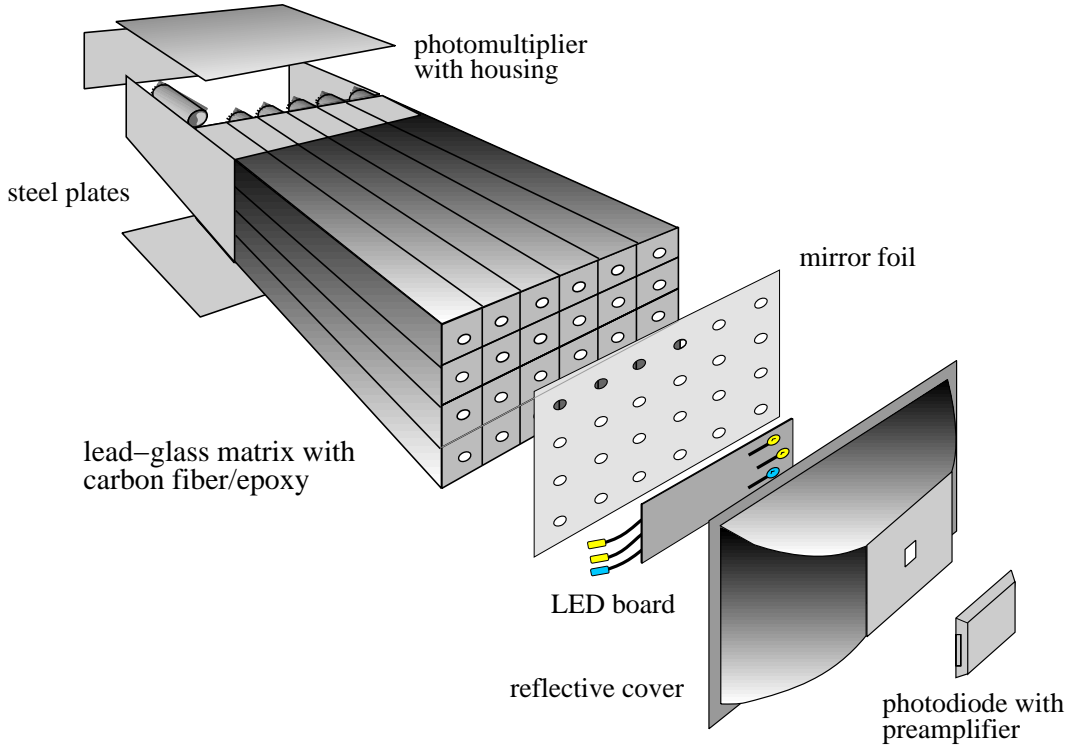


Figure 3.14: The schematic view of a Lead-Glass Supermodule including the reference system.

shaping stage other than passive integration. The 93Ω resistor terminates the signal line from the PMT so the voltage profile at point **A** shown in Fig. 3.15 simply follows the current profile from the PMT which is a pulse with a ≤ 5 nsec rise time. The charge is collected onto the 500 pF capacitor so the voltage profile at point **B** shown in Fig. 3.15 follows the integral of the current. The current pulse is a step function with a ~ 100 nsec rise time. A large register sets the quiescent voltage of $+4$ V to allow the accumulation of negative pulse. All of the following analog processing stages up to ADC and TDC conversion are carried out within an ASIC chip [126], as illustrated in Fig. 3.15. This chip was custom designed for the EMCAL system. Each of these ASIC chips services four PMT channels and also contains the circuitry for the fast trigger function.

In the arrival time measurement the voltage pulse is discriminated, either in a leading-edge mode or a constant-fraction mode. The discriminator firing starts a voltage ramp generator. The ramp is stopped on the next edge of the RHIC clock providing a common-stop mode TAC for each channel. The ramp voltage is sampled and converted by the AMU/ADC, then final reported ADC value then varies linearly with the pulse arrival time.

The charge signal is put through a Variable Gain Amplifier (VGA), and the gain can be optimized remotely in range of $\times 4 - \times 12$ with 5-bit resolution. The dynamic range of physics signals from the EMCAL is quite large and the detector is expected to resolve energy deposits from 20 MeV up to 15 – 30 GeV with a noise contribution from the electronics of no more than 0.1 % for large signals and 5 MeV for small signals. This range is impossible to cover with

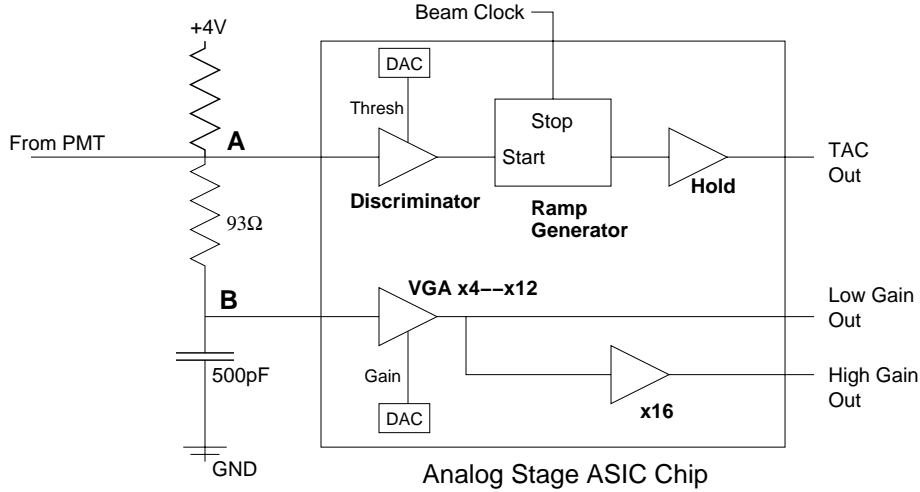


Figure 3.15: Block diagram of the energy and timing measurement circuits for EMCal. A signal from PMT used for timing information and charge information with a termination of $93\ \Omega$. All of the following analog processing stages up to ADC and TDC conversion are carried out within an ASIC [126] chip.

a single 12-bit ADC conversion. Thus the energy signal is converted twice with two different levels of amplification. The “low gain” signal is converted straight from the VGA and the “high gain” signal is converted separately after a second stage of $\times 16$ amplification.

The voltage waveforms from the high- and low-gain energy stages and the TAC for each channel are sampled once per RHIC clock tick and stored in a series of Analog Memory Units (AMU’s) as in several other PHENIX FEE systems [25]. Each waveform is sampled into a ring buffer of 64 AMU’s, effectively preserving it for 64 RHIC clock ticks or about $7\ \mu\text{sec}$. Upon receiving a LVL-1 Accept instruction, the FEM identifies the energy and TAC AMU cells corresponding to the event. These AMU cells are then taken out of the ring buffer and converted in the ADC. To compensate constant offset voltage among AMU cells, two AMU cells are readout, “pre” and “post” in Fig. 3.16, and “pre” corresponds to a time before the signal starts, and “post” corresponds to a time after the integrated signal reaches its maximum. Integrated charge stored in AMU memory cell is digitized by the subtraction of ADC values for “pre” and “post” cell. The formatted data for each event is then sent to a PHENIX Data Collection Module (DCM) via GLINK across a PHENIX standard optical fiber.

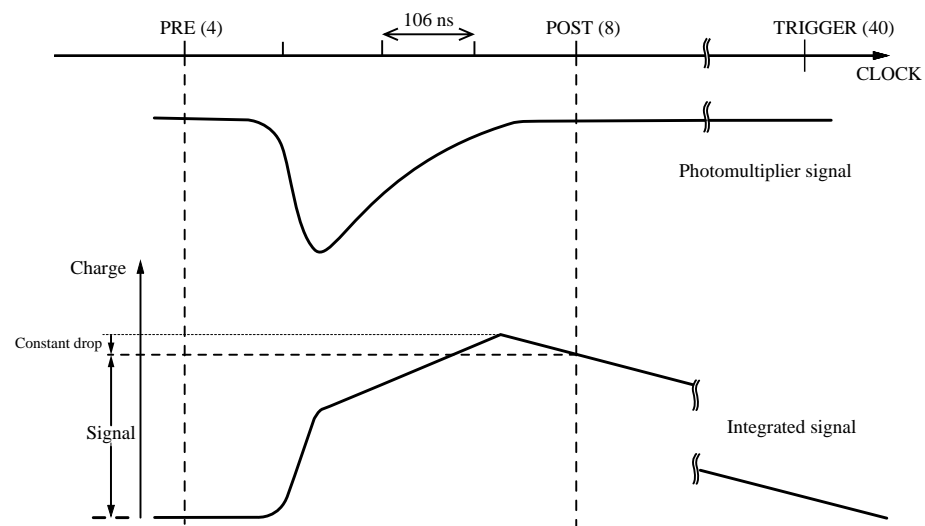


Figure 3.16: Schematics of the AMU sampling against with timing. Upper figure is input signal and bottom figure is integrated charge in AMU cell.

Chapter 4

Run Conditions

During the RHIC-Year4 run (Jan. 1st, 2004 – May 14, 2004), the Au+Au at $\sqrt{s_{\text{NN}}} = 200$ GeV collisions were collected with the PHENIX spectrometer. This analysis was based on these data. The beam and trigger conditions are described briefly in this chapter.

4.1 Beam Conditions

Table 4.1 summarizes the beam condition in the RHIC Year-4 Au+Au Run. PHENIX recorded the integrated luminosity of 0.24 nb^{-1} out of the delivered luminosity of 1.37 nb^{-1} in Au+Au collisions with $\sqrt{s_{\text{NN}}} = 200$ GeV. The delivered luminosity to PHENIX is measured with the ZDC. Figure 4.1 shows the integrated luminosity of Au+Au run delivered by RHIC as a function of elapsed day.

Quality	Value
\sqrt{s} per nucleon	100 GeV
Beam current	$\sim 10^9$ Au/bunch
Number of bunches	45
Initial ZDC rates	12 kHz
Initial luminosity	$10^{26} \text{ cm}^{-2}\text{s}^{-1}$
Luminosity lifetime	2.5 hrs

Table 4.1: Typical Beam Conditions for the 100GeV/u Au

4.2 Trigger Conditions

The data were taken with the “Minimum Bias” trigger. The logic of Minimum Bias (MB) trigger for Au+Au collisions is defined as:

$$\text{MinimumBias} \equiv \text{BBCNS} \geq 2 \cap \text{ZDCNS} \cap (|z_{\text{bbc}}| < 38 \text{ cm}), \quad (4.1)$$

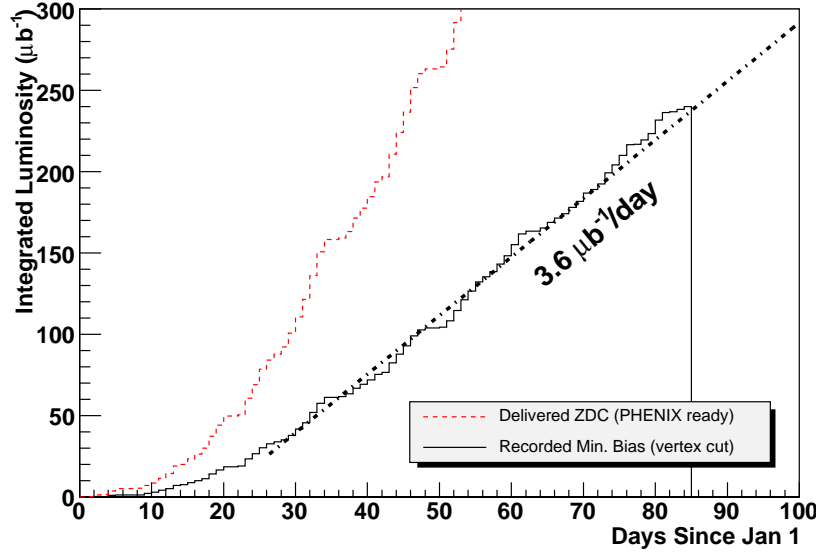


Figure 4.1: The integrated luminosity in Year-4 Au+Au run at $\sqrt{s_{\text{NN}}} = 200$ GeV comparing with delivered luminosity to PHENIX by RHIC, as a function of elapsed days. Straight lines in the figures show the fitted line, which indicates the data of $3.6 \mu\text{b}^{-1}$ is recorded by PHENIX every day on an average.

where BBCNS ≥ 2 means that at least 2 hits are required in both the north and south BBC. ZDCNS denotes that both the north and south ZDC have at least one neutron hit. z_{bbc} is z-vertex obtained by the BBC Level-1 (BBCLL1) trigger online. \cap is the symbol of logical AND. The triggered Au+Au event rate was about $1 \sim 2$ kHz, and the live rate of data acquisition was about $80 \sim 60$ %. Figure 4.2 shows z-vertex distribution of BBC, and its run dependence.

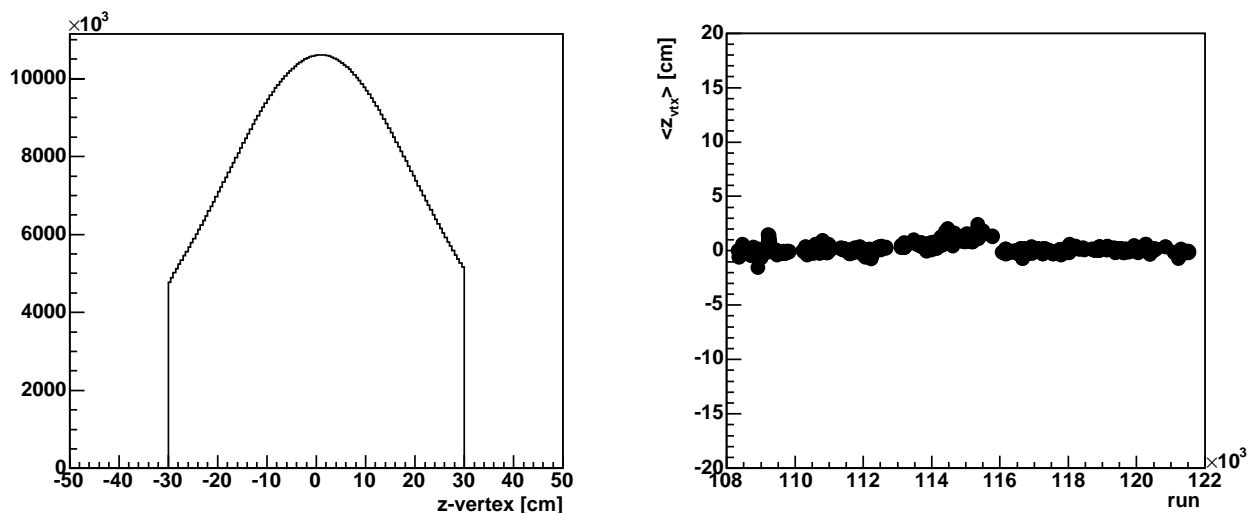


Figure 4.2: z -vertex distribution measured by BBC at Year-4. Left: z -vertex distribution. Right: mean of z -vertex distribution as a function of run number. The offline vertex cut ($|z_{bbc}| < 30$ cm) is applied.

Chapter 5

Data Analysis

5.1 Outline

In this chapter, the data analysis of π^0 and photon measurement are described. At first, the simulation procedures are mentioned briefly in Sec. 5.2. The trigger selection and centrality determination are explained in Sec. 5.3. The method of photon measurement with PbSc is explained in Sec. 5.4. The procedure of the calibration and its result are discussed in the section. The energy calibration of the PbSc calorimeter is most important to obtain the yield. The analysis of the measurement of π^0 and direct photon are described in Sec. 5.5 and following Sec. 5.6, respectively. Finally, the parameterization procedure to get π^0 and direct photon cross-section in p+p collisions at the same \sqrt{s} will be discussed in Sec. 5.7. The cross-section will be used for the calculation of nuclear modification factor R_{AA} .

The invariant yield is the yield per event and can be compared with invariant cross-section in p+p collisions and theoretical calculations. The invariant yield is expressed by the Lorentz invariant form:

$$E \frac{d^3n}{dp^3} = \frac{d^3n}{p_T dy dp_T d\phi} \simeq \frac{d^2n}{2\pi p_T dy dp_T}. \quad (5.1)$$

For getting the invariant yield, the raw π^0 and photon yield are obtained from the experimental data. To obtain π^0 and photon yield, corrections for geometrical acceptance, particle identification efficiency, and overlapping effect in high multiplicity environment were estimated. The details of the extraction of raw yield, and calculation of correction factor will be described in each section.

5.2 Simulation Procedure

In order to obtain the corrected physics values, one have to apply the correction factors on the measured raw values. The estimations of the corrections rely on simulations for some extent at least.

As shown in Fig. 5.1, simulation procedure is factorized into three steps: event generation, simulate detector response to the generated particle, and the evaluation of output. The event generators used in this study are followings:

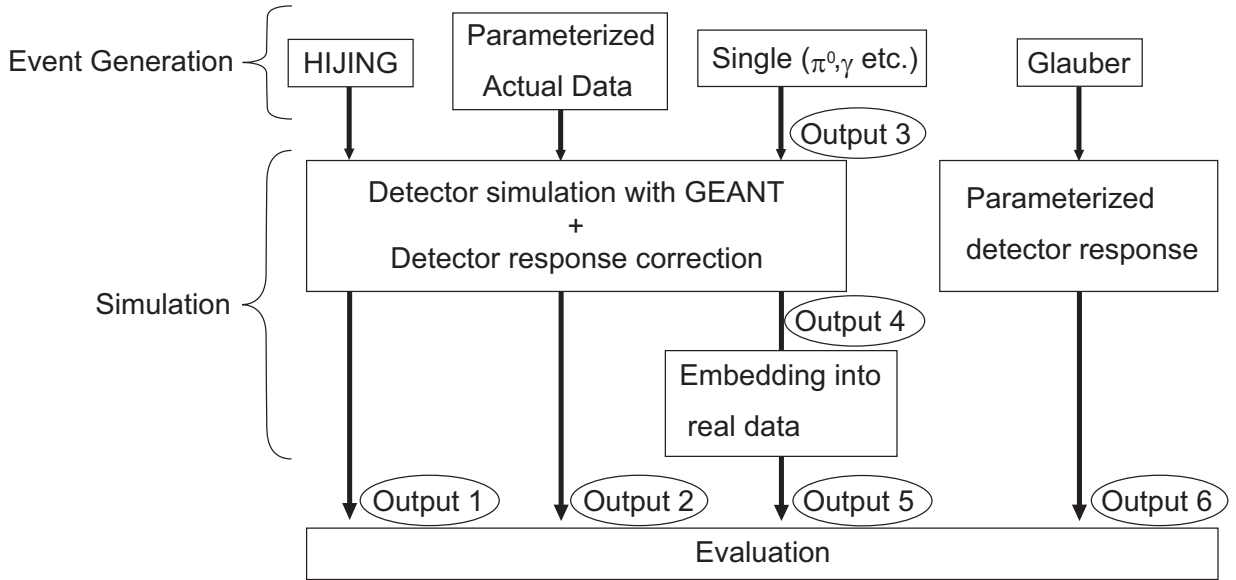


Figure 5.1: Simulation Procedure. Each outputs (Output 1 – 5) are used on demand.

- HIJING (Heavy Ion Jet INteraction Generator): relativistic heavy ion collisions event generator developed by M. Gyulassy and X.N. Wang [227]. The role of minijets in nucleon-nucleon, nucleon-nucleus and nucleus-nucleus reactions at collider energies is emphasized.
- Parameterized Actual Data: the measured p_T spectra of π^0 , π^\pm , K^\pm , p , and \bar{p} [29] are parameterized, and used for the event generator. The parameterizations of n and \bar{n} based upon p and \bar{p} data are also included. These are generated in flat rapidity range of $-2 < y < 2$.
- Single π^0 , γ , and neutral hadrons: single particles with a flat spectra in the p_T range of 0 – 25 GeV/c, with a flat rapidity distribution ($|y| < 0.5$), and with a uniform ($|z| < 30$ cm) vertex distribution are produced. Especially, 20 M π^0 s and γ s are generated. The rapidity distribution of particles produced in Au+Au collisions is flat in y , which is supported by the measurement of the rapidity distribution of charged particles by RHIC-PHOBOS [85].
- Particle generation is simulated with Glauber Model, and the response for the particles is simulated with parameterized detector response. This simulation is used for the centrality determination. Details will be described at next section.

To simulate the PHENIX detector response for the input particle, GEANT 3.21 is used mainly. The each subsystems of PHENIX spectrometer are located in the simulation virtually. The GEANT output is corrected with the obtained parameterization by beam test result.

The output data from simulated single π^0 and γ samples are, then, embedded into real Au+Au events. The simulated deposited energy in EMCAL tower is merged with real data, and clusters are reconstructed through clustering algorithm. Using this technique one can determine corrections that account for the detector response as well as for the effects due to overlapping clusters in a real event environment. The real event, which is merged with a

single π^0 (or γ) sample, is required to have a similar vertex position with the generated π^0 ($|z_{\text{real}} - z_{\text{simulated}}| < 5 \text{ cm}$).

During the each simulation steps, various outputs are produced (Output 1 – 5 in Fig. 5.1) and used for the analysis on demand.

5.3 Measurement of the Event Characteristics

In this section, the minimum bias trigger definition and centrality determination using global detector will be discussed.

5.3.1 Minimum Bias Trigger Definition and Efficiency

A sample of minimum bias events is selected according to the condition on the BBC and ZDC. As a event trigger, a coincidence defined in Eq. 4.1 is required. In addition, an offline collision vertex cut of $|z_{\text{vertex}}| < 30 \text{ cm}$ is required.

The efficiency of the minimum bias trigger is studied by a Monte Carlo simulation. In the simulation, response for all 128 PMT tubes and the BBCLL1 board logic are tuned to match the real data. HIJING simulated events (Output 1 in Fig. 5.1) are used to determine the trigger efficiency for our condition of event selection. The result of trigger efficiency for $\sqrt{s_{\text{NN}}} = 200 \text{ GeV}$ is

$$\epsilon^{\text{trigger}}(\text{Au} + \text{Au}, \sqrt{s_{\text{NN}}} = 200 \text{ GeV}) = 92.3 \% \pm 0.4 \% (\text{stat.}) \pm 1.6 \% (\text{sys.}) \quad (5.2)$$

The systematic errors are studied by varying the TDC (Time Digital Converter) threshold for each PMT (used by the BBCLL1 trigger) and the input dN/dy and collision vertex distribution from HIJING [152, 188].

5.3.2 Centrality Determination

The events, selected by the minimum bias trigger described above are classified according to the centrality. Both the total energy measured by the ZDC and the total charge measured by the BBC are sensitive to the impact parameter of the Au+Au collisions, and are used for the centrality determination. The ZDC measures spectator neutrons that are not bound in deuterons or heavier fragments. The BBC measures the number of charged particles at forward rapidity, ($3.0 < \eta < 3.9$). The collision centralities are determined from the measured correlation between the fractional charge deposited in the BBC and the fractional energy deposited in the ZDC

Figure 5.2 shows the measured correlation between the ZDC energy and the BBC charge, and each centrality is shown as a different color. The boundaries of centralities are set by the so-called “clock”-method [169]. The samples are divided into different centralities by an angle ϕ_{cent} in the BBC – ZDC plane determined as:

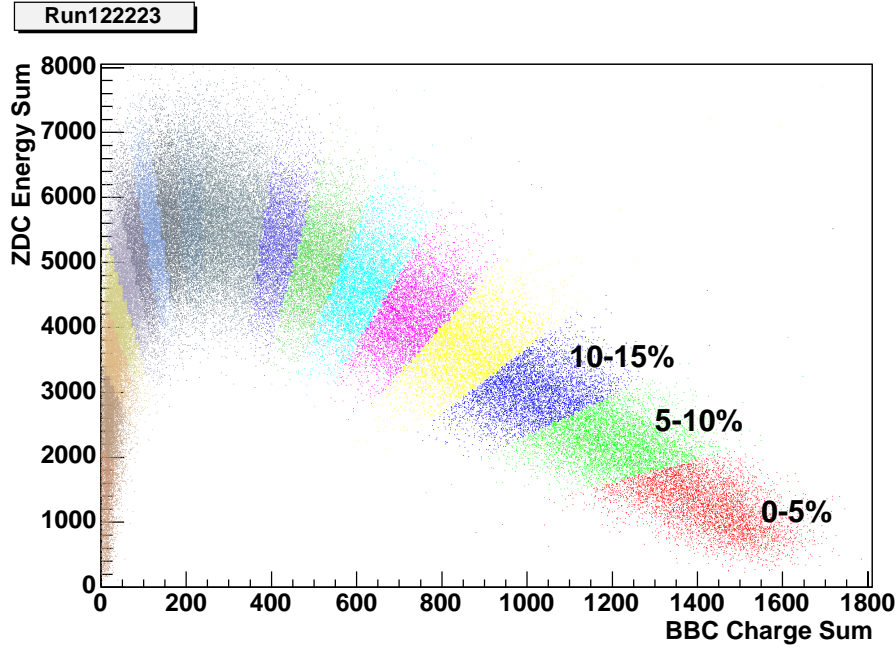


Figure 5.2: Centrality determination in PHENIX. The correlation of ZDC energy and BBC charge, together with centralities determined by the clock method.

$$\phi_{\text{cent}} = \arctan \left(\frac{(Q_{BBC} - Q_0)/Q_{\max}}{E_{zdc}/E_{\max}} \right), \quad (5.3)$$

where E_{\max} stands for the maximum energy in the ZDC and Q_{\max} is the maximum charge equivalent measured by BBC. The value of $Q_0 \sim 250$ is determined based on a simple simulation of the BBC and ZDC signal with the Glauber model of the Au+Au collisions. The detail of the Glauber simulation will be described in the next section. The boundaries of centralities for ϕ_{cent} is determined to make flat centrality distribution. The boundaries are listed in Appendix D.1.

5.3.3 The Glauber Model

In order to compare the yield in relativistic heavy ion collisions with that in p+p collisions quantitatively, it is necessary to estimate the geometrical parameters, such as an impact parameter of the two nuclei $\langle b \rangle$, the number of binary collisions $\langle N_{\text{coll}} \rangle$ and participating nucleons $\langle N_{\text{part}} \rangle$, as a function of centrality. These are estimated with a Monte Carlo simulation based on the Glauber model (Output 6 in Fig. 5.1), where the simulation includes the detector responses of the BBC and ZDC [169]. The idea of the Glauber model is introduced at Sec. 2.2.2.

In the simulation, 79 protons and 118 neutrons are distributed in each of the two Au nuclei according to the Woods-Saxon nuclear density distribution as introduced at Sec. 2.2.2. The radius and diffusivity of the Au nucleus are set to 6.37 fm and 0.54 fm, respectively, and a nucleon-nucleon inelastic cross section (σ_{nn}) is 42 mb. The radius is given by Eq. 2.12 and is close to measured value of 6.38 fm [116]. Using the parameters, the geometrical parameters (b ,

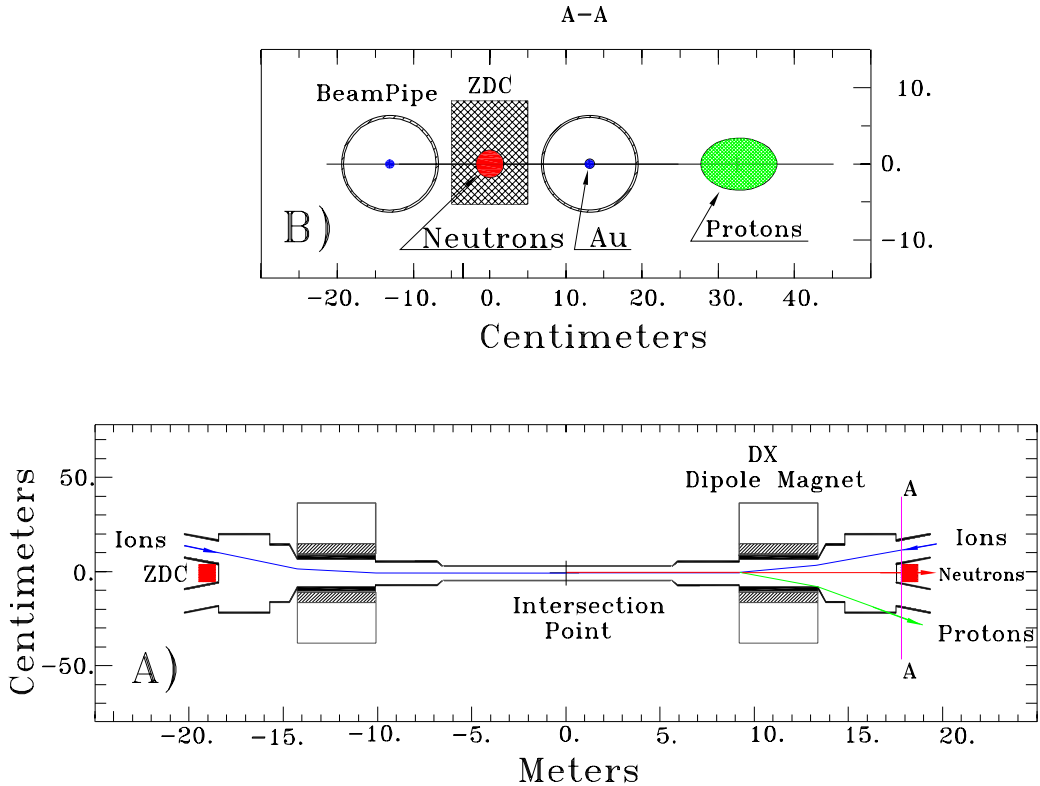


Figure 5.3: Side viewing of the collision region (a) and “beam’s eye” view of the ZDC location (b) indicating deflection of protons and charged fragments (with $Z/A \sim 1$ downstream of the “DX” Dipole magnet.)

N_{part} and N_{coll}) are determined event by event, and the detector responses of BBC and ZDC are simulated for each event. Events are generated in a certain impact parameter range, e.g. of $0 - 20$ fm.

The default assumption for the simulation of the BBC signal is that the charged particle multiplicity is proportional to the number of participants. The number of charged track is sampled according to a Poisson distribution with the mean value of ~ 0.5 per N_{part} . The mean value is chosen so that the minimum bias trigger efficiency is 92.3 %.

For a given collision, the neutrons that do not collide with other nucleons are counted as forward going neutrons towards the ZDC, while the protons which do not collide are not counted as shown in Fig. 5.3. In real collisions, these spectator neutrons may miss the ZDC acceptance due to the intrinsic p_T from their Fermi motion inside the Au nuclei or because they may be bound in deuterons or heavier fragments and thus swept away by the magnets. This “neutron loss probability” depends on centrality, and the probability is larger in peripheral collisions because a larger fraction of the spectator neutrons may reside in composite fragments. The “neutron loss probability” (p_{loss}) is parametrized as:

$$p_{loss} = 1 - (1 - p_{loss}^{frag.})(1 - p_{loss}^{acc.}), \quad (5.4)$$

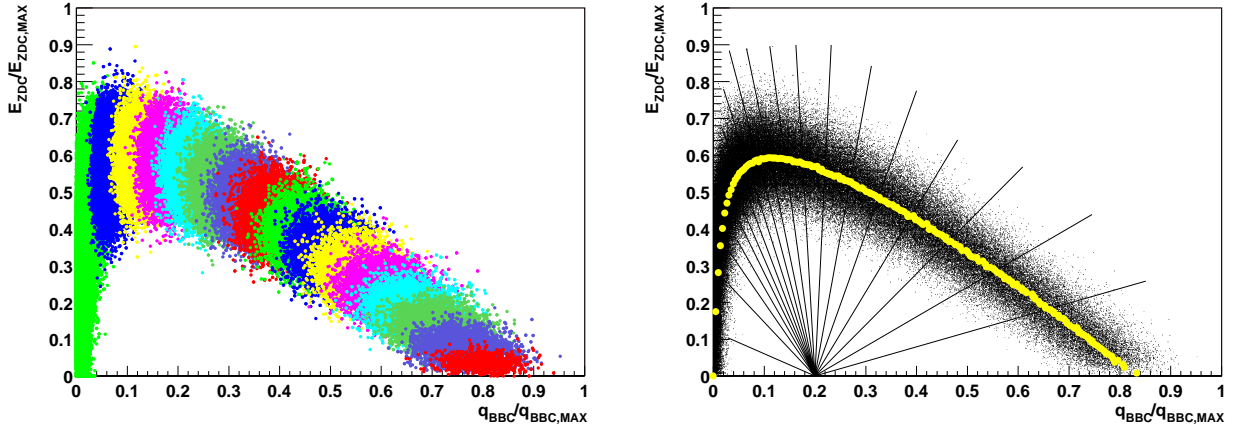


Figure 5.4: The simulated result of the BBC-charge and ZDC-energy correlation based on the Glauber simulation for each centrality. Left: BBC charge and ZDC energy correlation for each N_{part} . The i -th blob corresponds to a cut of $25(i - 1) \leq N_{part} \leq 25i$ (i.e. $N_{part} \in [0, 25], [25, 50] \dots, [375, 400]$ from left to right). Right: illustration of centrality definition with clock-method for simulation.

where

$$p_{loss}^{acc.} = 0.2857 \quad (5.5)$$

is the acceptance loss probability for free neutrons, and

$$p_{loss}^{frag.} = 0.3305 + 0.0127b + e^{(b-17)/2}, \quad (5.6)$$

is the probability of the neutron bound in charged composite fragments. The $p_{loss}^{frag.}$ used in the simulation are taken from the results from NA49 experiment which has separately measured the number of neutrons, protons, and fragments in the forward direction in Pb+Pb collisions at 158A GeV [66].

In addition, the energy of the neutrons are smeared according to the ZDC energy resolution:

$$\frac{\sigma_E}{E} = \frac{218\%}{\sqrt{E \text{ (GeV)}}}. \quad (5.7)$$

The left panel of Fig. 5.4 shows how the ZDC and BBC signals are correlated varying with the number of participants. The simulated BBC-ZDC correlation can be classified with clock-method as well as real data as shown in the right panel of Fig. 5.4. The average geometrical parameters, $\langle b \rangle$, $\langle N_{part} \rangle$, $\langle N_{coll} \rangle$ and $\langle T_{AA} \rangle$, are obtained for each centrality class. The result of the calculation can be found in Appendix D.2.

The systematic error of the geometrical parameters are estimated by varying the model assumption:

- nucleon-nucleon cross-section reduced to 35 mb (default is 42 mb)

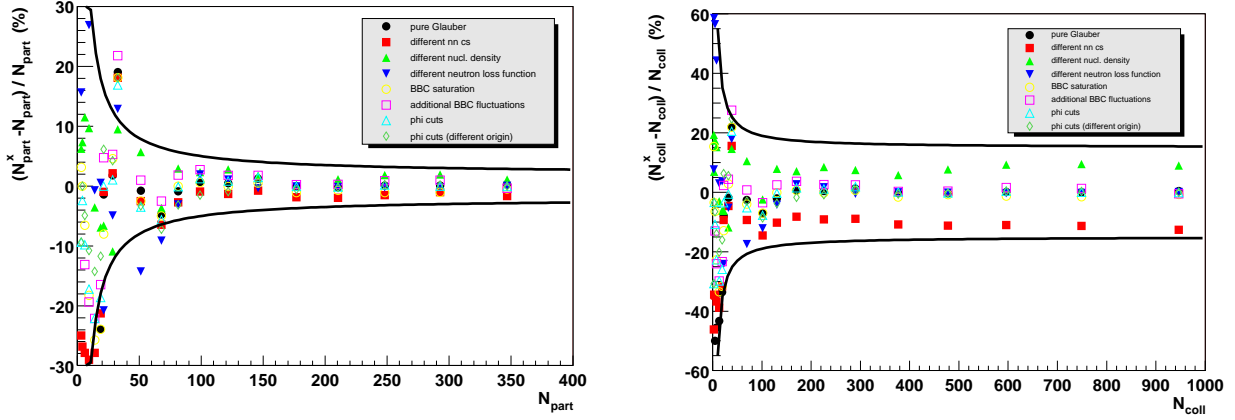


Figure 5.5: Systematic Uncertainty of the $\langle N_{part} \rangle$ (left figure) and $\langle N_{coll} \rangle$ (right figure) as a function of Centrality.

- different parameters for the Woods-Saxon distribution defined in Eq. 2.11: $R = 6.35$ fm, $a = 0.53$ fm
- different parameterization of the neutron loss probability function used in the ZDC simulation
- different smearing function for the BBC response

Figure 5.5 shows the systematic error for $\langle N_{part} \rangle$ and $\langle N_{coll} \rangle$. The systematic uncertainties are parameterized as followings:

$$\frac{\delta \langle N_{part} \rangle}{\langle N_{part} \rangle} = 0.02 + \frac{3}{\langle N_{part} \rangle}, \quad (5.8)$$

$$\frac{\delta \langle N_{coll} \rangle}{\langle N_{coll} \rangle} = 0.15 + \frac{4}{\langle N_{coll} \rangle}. \quad (5.9)$$

5.3.4 Measurement of Reaction Plane

Due to the strong graduation of the pressure along with the angle respect to reaction plane, a strong azimuthal anisotropy of the particle production is observed at RHIC as illustrated in Fig. 5.6. PHENIX has previously published measurements of elliptic flow using an event-by-event measured reaction plane [36, 22, 32]. The non-negligible azimuthal anisotropy should be taken into account not only for the azimuthal anisotropy analysis, but also for the invariant yield analysis. Especially, the large amount of combinatorial background is estimated with event mixing method for each reaction plane bins, because the PHENIX dose not have symmetric detector acceptance along $r \cdot \phi$ -axis and the distribution of the multi-particles should be similar for each mixed events in order to reconstruct the combinatorial background precisely.

The calibrated charge from each of the 2×64 quartz radiators in the BBC's is converted into an estimate for the number of charged particles within the acceptance of each detector,

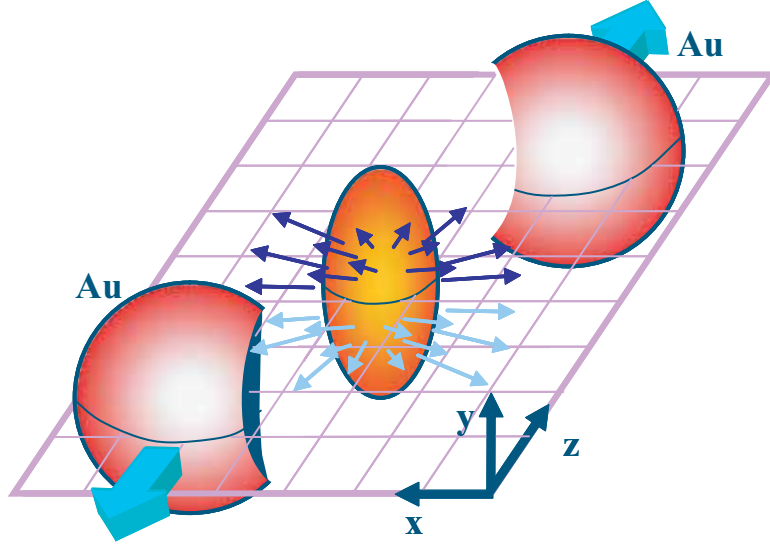


Figure 5.6: Schematic View of the strong elliptic flow at RHIC. Due to the strong graduation of the pressure along with the angle respect to reaction plane, a strong azimuthal anisotropy of the particle production is observed at RHIC.

N_i , using the measured single-particle peak centroid. For the reaction plane measurement the measured N_i values are adjusted so that each ring of counters in the BBC's is given the same total adjusted multiplicity, N_i^{adj} . This reduces the weight of the inner rings of detectors which have the fewest counters covering the full azimuthal angle range. Then, the angle of the reaction plane Ψ is obtained from the formula

$$\tan(2\Psi) = \frac{\sum_i N_i^{adj} \sin(2\phi_i) - \langle \sum_i N_i^{adj} \sin(2\phi_i) \rangle}{\sum_i N_i^{adj} \cos(2\phi_i) - \langle \sum_i N_i^{adj} \cos(2\phi_i) \rangle}, \quad (5.10)$$

where ϕ_i stands for the azimuthal angle of the center of a given radiator. The average is taken over many events, and corrected for the target run. The subtraction of the average centroid position in Eq. 5.10 removes the bias in the reaction plane measurement resulting from non-zero angle of the colliding beams, non-uniformities in detector acceptance, and other similar effects. A final correction is applied to remove non-uniformities at the 20 % level in the Ψ distribution.

5.3.5 Criteria of Good Run Selection

Detector configuration could change during the operation, and a bias on the measurement would be made easily. Bad runs would make the unexpected bias to data, and the bad run candidates are selected with the following criteria:

- The runs where the centrality distribution is not flat are excluded. While the ϕ angle for the centrality determination is fixed by the stable runs, the centrality distributions of some runs are not flat distribution and have some bump, on the contrast to the typical

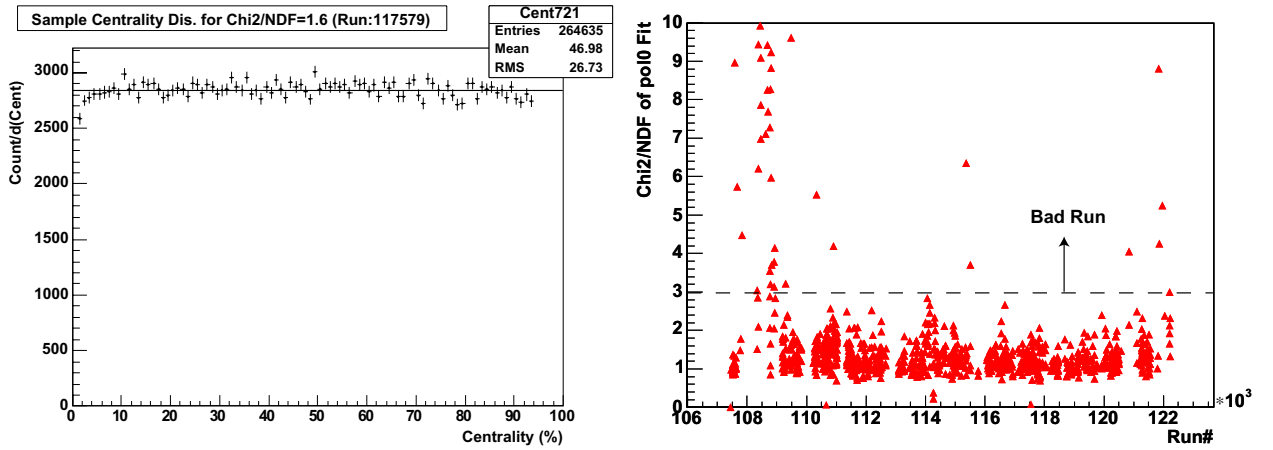


Figure 5.7: Centrality distribution measured by BBC and ZDC correlation. Left: Typical centrality distribution. Right: χ^2/NDF of fitted pol0 to centrality distribution as a function of run number. The runs where $\chi^2/\text{NDF} > 3$ are not used for the analysis.

centrality distribution as shown in the left panel of Fig. 5.7. Each centrality distributions are fitted with the first order polynomial, and each χ^2/NDF are evaluated as the flatness of centrality distribution as shown in right panel of Fig. 5.7. About 5 % of total number of events are excluded due to the bad flatness ($\chi^2/\text{NDF} > 3$).

- The runs where reaction plane distribution is not flat are excluded. As well as the evaluation for centrality, the flatness of the reaction plane distribution is evaluated by fitting.
- The runs where EMCal can not measure energy of electromagnetic clusters are excluded. The stability of energy linearity and resolution of EMCal is evaluated based on the π^0 peak position and MIP peak position. While some of the runs are excluded due to the bad EMCal condition, most of runs pass this criteria.

Appendix I.1 summarize run numbers which are used for this analysis.

5.4 Photon Measurement with PbSc-EMCal

In this section, measurement of photons in the PHENIX-EMCal detector is discussed. It includes the clustering algorithm for the electromagnetic clusters, energy calibration and photon identification.

While there are two types of the electromagnetic calorimeter, PbSc and PbGl, only PbSc calorimeter was used in this analysis. There are a few reasons why PbGl is not used:

- The measurement with PbGl has disadvantage for statistics due to the small acceptance. Especially it was not operational for about a half of the entire run.

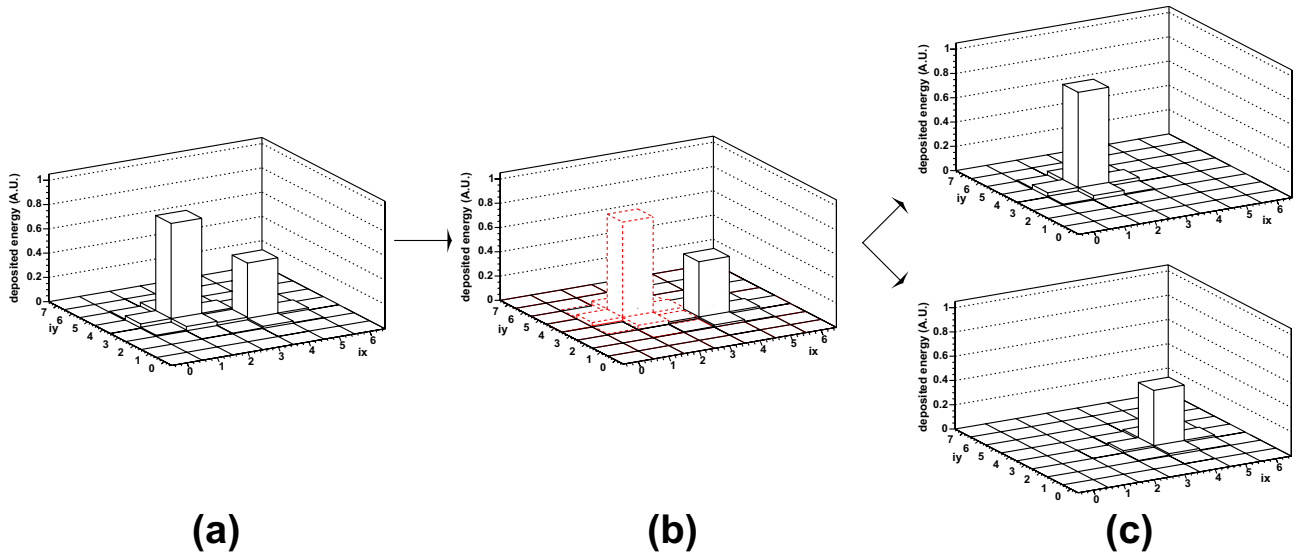


Figure 5.8: Procedure of the cluster splitting. (a) The towers which share at least same edge on each other are gathered into an isolated cluster. (b) isolated cluster is split into two “peak-area” clusters. (dotted red and solid black) (c) The split clusters are evaluated based on the shower profile, and recognized as split clusters if they pass the shower profile test.

- It was turned out there were large gain fluctuations tower by tower comparing with PbSc, which caused a large systematic error from the energy scale uncertainty. The PbGl calorimeter shows a stronger variation of the measured photon energy with the angle of incidence on the detector surface, at 20° the measured energy is reduced by 5 % compared to perpendicular incidence (0°), while in the PbSc the effect is about 2 %.

5.4.1 Clustering Algorithm

The deposited energy in each towers are clustered to reconstruct the deposited shower as following procedure. At first, a noise threshold of 10 MeV is applied for each tower. The towers which share at least same edge on each other are gathered into an isolated cluster. Since such isolated cluster might be composed of more than one particles, more sophisticated cluster is tried to be determined by assuming that they are all photons. An isolated cluster is split into two “peak-area” clusters in the way that the number of “peak-area” clusters is equal to the number of local maximum in the isolated cluster. A local maximum is a module above the peak threshold (80 MeV) with the maximum amplitude in the 3×3 towers region surrounding it. The energy of a tower within the 5×5 area from the two peaks is shared into the two “peak-area” clusters according to amplitude and positions of the maxima using parameterized shower profile. The split clusters are evaluated based on the shower profile (χ^2 method described later), and recognized as split clusters if they pass the shower profile test. Figure 5.8 shows the procedure of cluster splitting where the cluster is expected to be composed of two electro magnetic clusters.

Reconstruction of Hit Position

Owing to the lateral segmentation of the EMCal, the impact position of a particle based on the center of gravity with a correction by a hit angle. The center of gravity is given by:

$$x_{cent} = \frac{\sum_i^{all} E_i x_i}{\sum_i^{all} E_i}, \text{ and } y_{cent} = \frac{\sum_i^{all} E_i y_i}{\sum_i^{all} E_i}, \quad (5.11)$$

where (x_i, y_i) is the position within a sector of the i -th module of the cluster and E_i is its energy. For non-zero angular incidence the projection of the shower maximum on the detector surface does not correspond to the impact position x_{true} . The connection between the center of gravity of a shower and x_{true} is influenced by the finite size of the modules. During the clustering process the center of gravity is corrected for these dependencies based on test beam results and simulations to the actual impact point on the detector surface, assuming that the particle is a photon [185].

Reconstruction of Energy

The hit occupancy of the EMCal is extremely large due to the large number of multiplicity of charged particles and photons in the heavy ion collisions. Each panels in Fig. 5.9 show the event display of deposited energy in a EMCal tower unit. The hit occupancy is about 15 % for the PbSc in the most central Au+Au collisions at $\sqrt{s_{NN}} = 200$ GeV. In such as extreme condition, the deposited energy in a cluster is easily affected by other clusters unlike at the test beam. For instance, the observed ionization energy for the minimum ionizing particles increases by ~ 6 % in central Au+Au collisions. In order to make the bias caused by the high multiplicity condition small, it was proposed to sum only a few towers, instead of taking all towers, for energy measurement. A few towers are named as “core” towers. This idea comes from the fact that about 80 % of energy deposits on only one tower when a photon hit on the center of the tower. This technique of taking only the “core” towers enables EMCal to survive such an extreme condition in the heavy-ion collisions. The E_{core} energy of a cluster is defined as

$$E_{core} = \Sigma_i^{core} E_i^{meas}, \quad (5.12)$$

where E_i^{meas} is the measured energy in i -th tower and Σ_i^{core} is defined as summing of the “core” towers. The “core” towers are defined as the following condition:

$$\frac{E_i^{pred}}{E_{all}^{meas}} > 0.02, \text{ and} \quad (5.13)$$

$$E_{all}^{meas} = \Sigma_i^{all} E_i^{meas}, \quad (5.14)$$

where E_{all}^{meas} is the sum of measured energy in all towers belonging to the “peak-area” cluster, E_i^{pred} is the predicted energy using the shower profile in i -th tower [101]. The energy fraction of

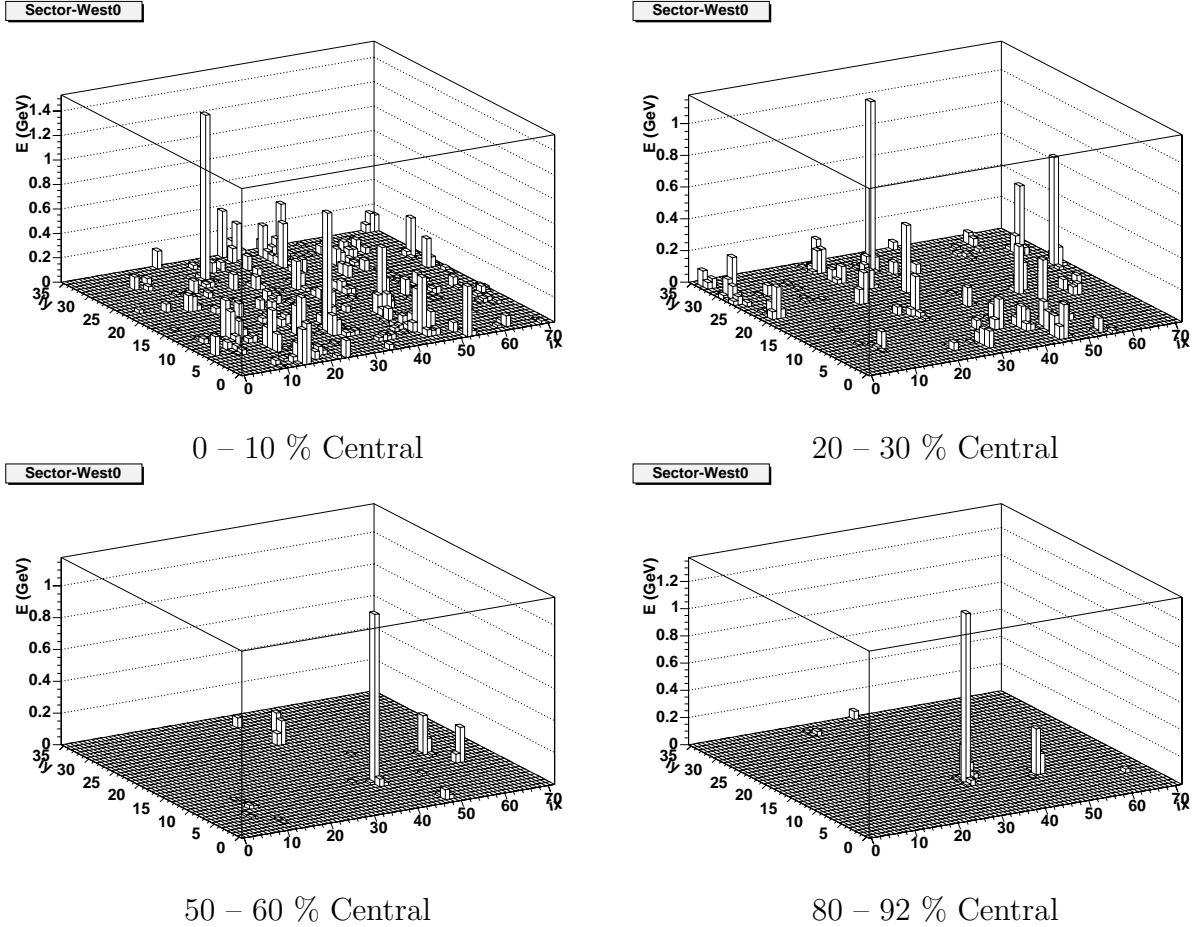


Figure 5.9: Event display of the deposited energy on EMCal sector (West0) for each centrality condition. “ix” and “iy” in the figures are tower id (“ix” corresponds to along the beam line).

the E_{core} to the total energy depend on the incident angle, position and energy. The dependence is parameterized with the obtained performance in beam test:

$$\frac{E_i^{pred}}{E_{all}^{meas}} = p_1(E_{all}^{meas}, \theta) \cdot \exp\left(-\frac{(r/r_0)^3}{p_2(E_{all}^{meas}, \theta)}\right) + p_3(E_{all}^{meas}, \theta) \cdot \exp\left(-\frac{(r/r_0)}{p_4(E_{all}^{meas}, \theta)}\right), \quad (5.15)$$

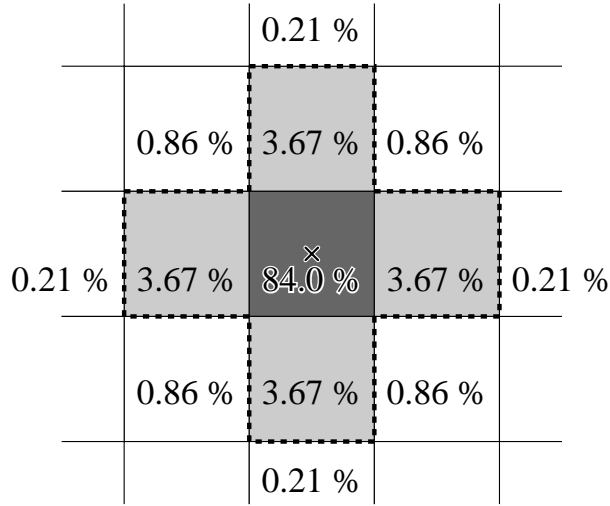
where r is the distance between the center of tower and the center of gravity, r_0 is the size of unit EMCal tower (5.54 cm), θ is the angle of incidence with respect to a perpendicular on the detector surface, and $p_i(E, \theta)$ are parameterized to be:

$$p_1(E, \theta) = 0.59 - (1.45 + 0.13 \ln E) \sin^2 \theta, \quad (5.16)$$

$$p_2(E, \theta) = 0.26 + (0.80 + 0.32 \ln E) \sin^2 \theta, \quad (5.17)$$

$$p_3(E, \theta) = 0.25 + (0.45 - 0.036 \ln E) \sin^2 \theta, \quad (5.18)$$

$$\text{and } p_4(E, \theta) = 0.42. \quad (5.19)$$



Perpendicular hit on the center of tower.

Figure 5.10: An example of expected shower energy fraction in towers in the case of perpendicular hit of photon on the center of a tower. Surrounded five towers by dotted line is used for E_{core} calculation.

For example, Fig. 5.10 shows a profile of expected shower energy fraction in towers in the case of perpendicular hit of photon on the center of a tower. The average number of towers belonging to the “core” towers is 4 towers. The E_{core} contains 91.8 % energy of the total energy on an average. Such an E_{core} energy represents an estimate of the true energy of a photon impinging on the PbSc unbiased by background contributions from other particles produced in the same event and depositing energy in the neighborhood of a given cluster.

The deviation of the deposited energy in each towers are parameterized as the variance σ_i^2 given with the corrections for angle of incidence, $f(E, \theta) = 4/0.03 \cdot \sqrt{E} \cdot \sin^4 \theta$, and on losses to the total energy due to the thresholds used in the clustering, $q(E) = 0.005^2 + 0.0014^2 \cdot E^2$ (GeV²), as in following equation:

$$\sigma_i^2 = q(E_{all}^{meas}) + C \cdot E_i^{pred} \cdot \left(1 - \frac{E_i^{pred}}{E_{all}^{meas}} + f(E_{all}^{meas}, \theta) \cdot \left(1 - \frac{E_i^{pred}}{E_{all}^{meas}} \right) \right), \quad (5.20)$$

where $C = 0.03$ (GeV²) is the scale for energy fluctuations in the shower given by test beam data. σ_i will be used for the evaluation of the shower profile, and details will be described later.

Correction on the Energy of Photons

The number of towers used for E_{core} depends on the the hit position and angle on the tower surface. The E_{core} calculation definitely neglects the contribution from the shower tail, and causes deficit of shower energy. In the case of Fig. 5.10, ~ 4 % of shower energy is missing. The total energy fraction relative to the expected total energy are estimated based on the Monte Carlo simulation which uses the parameterization given by test beam data. The correction on the E_{core} for algorithm itself and input angle is parameterized as:

$$\frac{E_{core}}{E_{core}^{corr}} = a_1 \cdot (1 - a_2 \sin^4 \theta \cdot (1 - a_3 \cdot \ln E_{core})), \quad (5.21)$$

where $a_1 = 0.918$, $a_2 = 1.35$, and $a_3 = 0.003$. Here, Eq. 5.21 gives the correction on E_{core} and the corrected E_{core} will be noted as E_{core} at the following discussions, though the corrected E_{core} is noted as E_{core}^{corr} in Eq. 5.21.

From the test beam data, it is known that, as the light generated by a shower travels from its source to the PMT via fibers, it is attenuated. Since the depth of the shower varies logarithmically with the energy, this attenuation gives rise to a non-linear energy response for particles as shown in Sec. 3.3.2. The nonlinearity due to the attenuation in the fibers are corrected in the following form:

$$\exp(x_0 \ln(E)/\lambda) = E^{x_0/\lambda}, \quad (5.22)$$

where $\lambda = 120$ cm is attenuation length, and x_0 is the effective path length of the scintillation light. The shower leakage are also estimated as 1 % at 10 GeV and 4 % at 100 GeV of photon. The correction of both effects are applied in the data.

The additional contribution on the energy resolution due to this algorithm and correction is estimated. The additional contribution was estimated based on the π^0 mass peak width and results in an additional constant term of 3 %, which is larger than the nominal energy resolution of 2.1 % in Eq. 3.3. The use of E_{core} instead of the total cluster energy for photon reconstruction, helped to reduce considerably the effects of cluster overlaps in central Au+Au collisions.

5.4.2 Calibration of Energy Scale

In this section, the procedure of the energy scale correction will be described. The calibration of the energy scale is one of the important tasks for the measurement of π^0 and photon, because a few % deviation of the energy scale corresponds to the large change in the invariant yield due to the steep falling of the energy spectra. Figure 5.11 shows how much uncertainty for π^0 and photon yield is caused by the uncertainty of absolute energy scale. It depends on the shape of the spectrum and it is estimated based on the fitted function for π^0 spectrum in $\sqrt{s_{NN}} = 200$ GeV Au+Au collisions. The uncertainty of the energy scale of 1 % corresponds to the uncertainty of the invariant yield of about 8 %.

There are several quantities which can be used for the calibration of EMCAL energy scale. In this analysis, electron, π^0 and minimum ionizing charged particles (MIP) are used. Particularly overall energy scale of PbSc was obtained and checked using MIP peak and π^0 peak. Energy Correction for PbSc was obtained with the following procedure:

1. Tower by tower relative energy correction was determined based on the peak position of π^0 and MIP using p+p data. The p+p data was taken just after the Au+Au run. The tower by tower relative energy correction was checked with Au+Au data based upon the peak position of π^0 and MIP. Figure 5.12 shows the improvement of π^0 peak and width in p+p and Au+Au collisions after the tower by tower calibration.

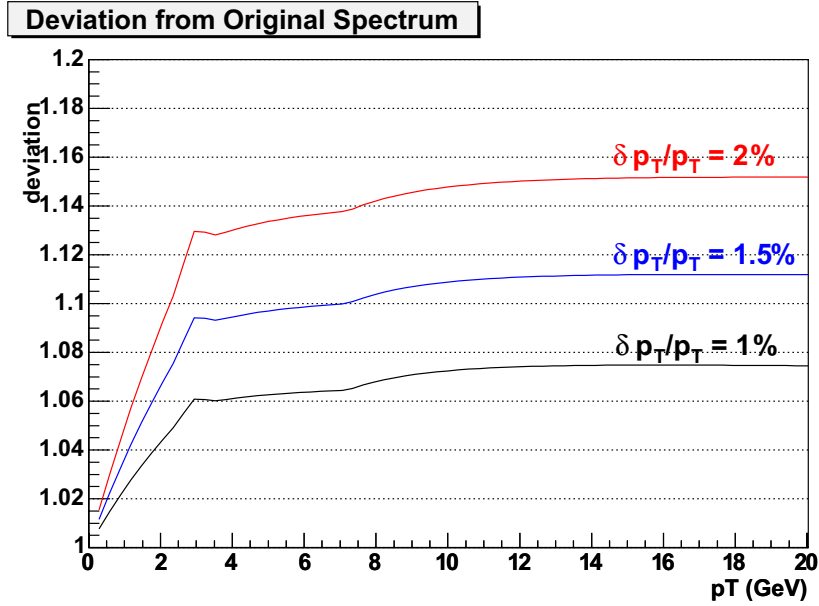


Figure 5.11: The uncertainty of π^0 and photon yield due to the uncertainty of the absolute energy scale. The uncertainty of the energy scale of 1 % corresponds to the uncertainty of the invariant yield of about 8 %.

2. Figure out Run groups while gains are stable, and calculate correction factor for each group based on the MIP peak position. Figure 5.13 shows the run dependence of the MIP peak position and π^0 peak position for sector East2.
3. Determine over all absolute energy scale correction based on the π^0 peak position compared with the expected π^0 peak position which is simulated with GEANT (Output 5 in Fig. 5.1). In order to minimize the overlapping effect for the calibration using π^0 , only peripheral events are used for the absolute energy correction.
4. The non-linearity energy scale correction is made based on the E/p of electron clusters,

$$E_{core}^{corr} * = 1 / (1 + 0.0688 e^{-2.92 \cdot E_{core}^{corr}}). \quad (5.23)$$

Table 5.1 summarize the correction factor for each sector and run periods, where “base” in the table means run period (106900-116134, 117924-120499, 121344-121531 and 121810-122225), where EMCAL energy scale is stable as far as checking the MIP peak.

The tower dependence of energy scale is further checked using electron tracks. Electron tracks are selected with RICH detector and the momentum of the electron tracks are measured with the PHENIX tracking system. A fiducial cut to reject the tracks which hit the edge of sector is applied. E/p as a function of tower-number along x-axis (along beam line) and y-axis (along the ϕ) is shown in Fig. 5.14. It is stable within 1 %.

In the following sections, the corrected E_{core} (E_{core}^{corr}) will be denoted as E_{core} .

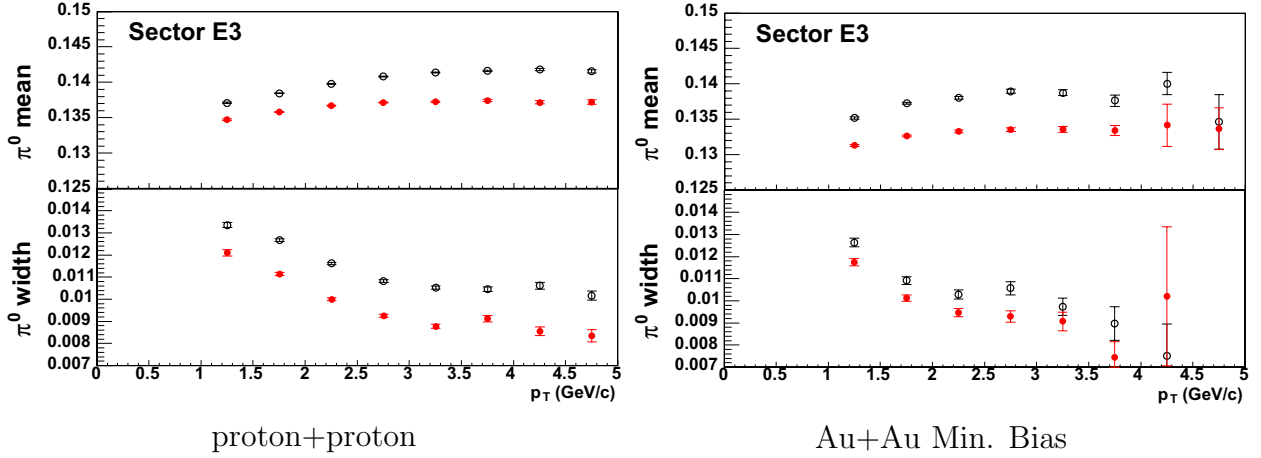


Figure 5.12: Result of Tower by Tower Energy Correction. Mean (upper) and sigma (bottom) of π^0 peak as a function of p_T . Black open circles are changed to red closed circles after the tower by tower correction.

Sector	Overall base correction	Run period correction			
		116135–116744	116745–117923	120500–121343	121532–121809
E0	1.	1.	1.	1.	1.
E1	1.	1.	1.	1.	1.
E2	1.0337	1.1753	1.1081	0.9899	1.2626
E3	1.0375	same as base	same as base	same as base	1.2700
W0	1.0375	same as base	same as base	same as base	1.3126
W1	1.0283	same as base	same as base	same as base	1.1771
W2	1.0291	same as base	same as base	0.9680	1.3143
W3	1.0253	same as base	same as base	same as base	1.3562

Table 5.1: Parameters of the final corrections applied to the cluster energy.

5.4.3 Method of Photon Identification

In this section, the method used for the identification of photon clusters are described. At the beginning, a moderate energy threshold cut of $E > 0.2$ GeV is applied to exclude dust-clusters. According to the single photon simulation (Output 4 in Fig 5.1), a lot of small fragment clusters which have the energy of ~ 100 MeV are made due to the clustering algorithm. Such clusters cause the large combinatorial background for π^0 measurement, especially for central events. Then the energy threshold is applied to reduce the background.

It is required that the central tower (tower with the largest energy in a cluster) is not at the edges of a sector. If any of the central tower's immediate neighbor-towers is a bad tower (3 towers by 3 towers square around), the cluster is also excluded. Bad module maps were shown in Fig. I.1 of Appendix I.2. The acceptance losses were taken care of with corrections.

Cuts based upon shower-shape are used to distinguish between showers produced by photons/electrons and hadrons, because the pattern of energy deposit is quite different. The analytical parametrization of the energy sharing (shown in Eq. 5.15) and its fluctuations (Eq. 5.20)

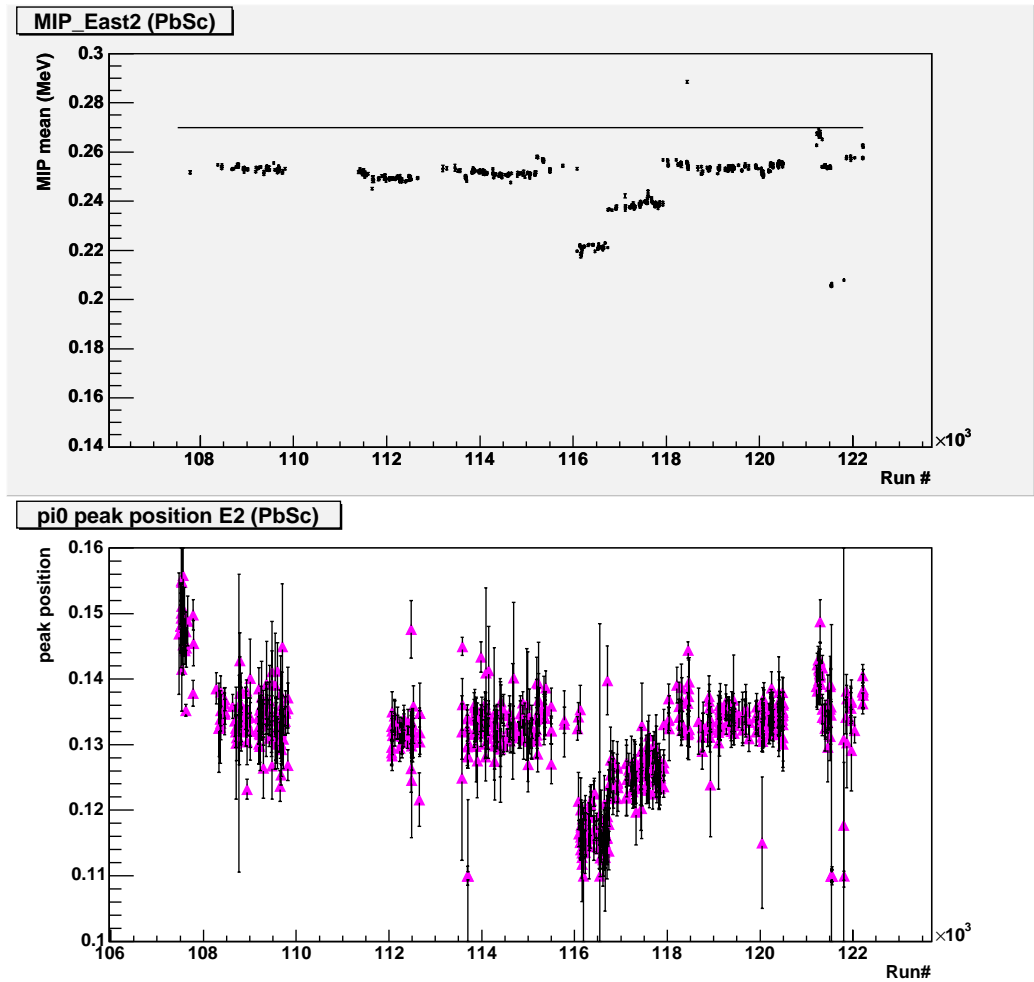


Figure 5.13: Peak position of MIP (upper) and π^0 (bottom) signal as a function of Run# (Au+Au Min. Bias). The black line shown in upper figure stands for the expected MIP peak position according to the material budget of PbSc-EMCal (~ 270 MeV).

is employed for the identification of electromagnetic clusters. The χ^2 is calculated with the parameterization,

$$\chi^2 = \sum_i \frac{(E_i^{pred} - E_i^{meas})^2}{\sigma_i^2}, \quad (5.24)$$

where E_i^{meas} is the energy measured in tower i and E_i^{pred} is the predicted energy for an electromagnetic particle of total energy $\sum_i E_i^{meas}$. This χ^2 value characterizes how electromagnetic a particular shower is and can be used to discriminate against hadrons. The important feature of this method is that the fluctuations are also parameterized. The χ^2 distribution was found to be close to the theoretical one and it is almost independent of the energy or the impact angle of the electron. The χ^2 distribution for 2 GeV/c electrons and pions are shown in Fig. 5.15. The arrow marks the χ^2 cut corresponding to 90 % electron efficiency, which corresponds to

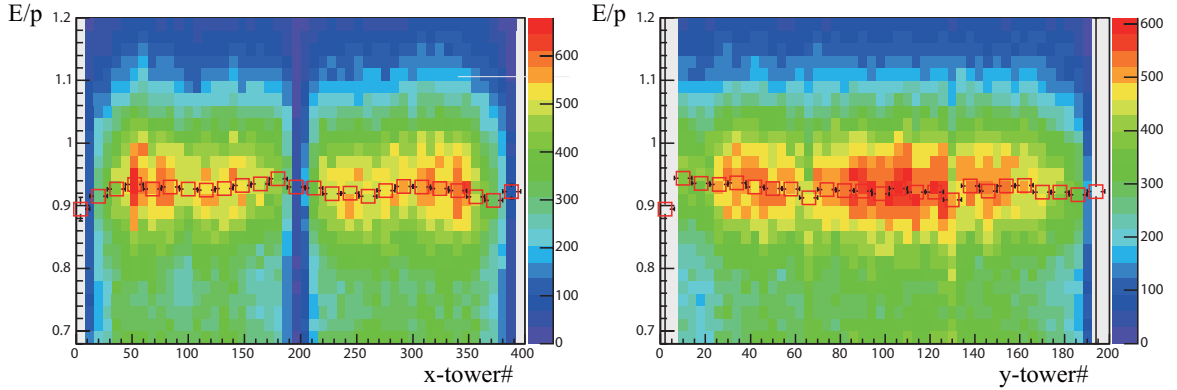


Figure 5.14: Tower dependence of the energy scale. Left and right figure show E/p as a function of tower-number along x-axis (along beam line) and y-axis (along the ϕ), respectively. All PbSc sectors are combined.

efficiency of $\sim 20\%$ for pions. The default cut to identify photons is set to $\chi^2 < 3$. This is determined based on the signal-to-noise ratio and detection efficiency.

In addition to this χ^2 cut, four different cuts for PbSc were developed, which are so-called “Stochastic cuts”. The basic idea behind the “Stochastic cuts” is that the shower-shape is characterized with more than one quantities, e.g. the χ^2 defined above, the ratio of energy deposit in the central tower and the total cluster energy, the ellipticity of the shower, and so on. Whereas these quantities are not independent to each other, they are not perfectly correlated with each other. A small χ^2 value is already an indication that the shower is a photon, but if most of its energy is in the center tower, this would be an additional indication. The functions in “Stochastic cuts” are similar to a likelihood-function. At first, based upon GEANT simulations (Output 1 in Fig. 5.1), the efficiency curve, $\epsilon_{cut\ var.}(threshold)$, for each individual shower shape variable (or combinations) is determined as a function of the cut value. The efficiency is defined as

$$\epsilon_{cut\ var.}(threshold) = \frac{N_{photons-pass-cut}}{N_{non-photons-pass-cut}}. \quad (5.25)$$

These cuts were made for maximizing the cleanliness of the photon purity rather than the photon efficiency. Then, the threshold is determined to be the value where $\epsilon_{cut\ var.}(threshold)$ is highest value (plateau). The product of each variable $\Pi_i f(cut\ var.)$ is calculated for each cluster and if it is above a threshold, the cluster is accepted as a photon.

Timing information from the calorimeter can be used both for particle identification and in the pattern recognition to find overlapping showers. For energy deposits in the tower ≤ 0.5 GeV, the calorimeter timing resolution is nearly constant at ~ 120 psec for electrons and photons and ~ 270 psec for pions where shower fluctuations are the major contributor to the resolution. However, it was turned out that timing correction is not enough to identify the high energy clusters. In this thesis, the timing information is not used for particle identification.

The cuts used in the analysis are summarized as followings:

NoCut: only $E > 0.2$ GeV and 3 by 3 bad tower exclusion are applied.

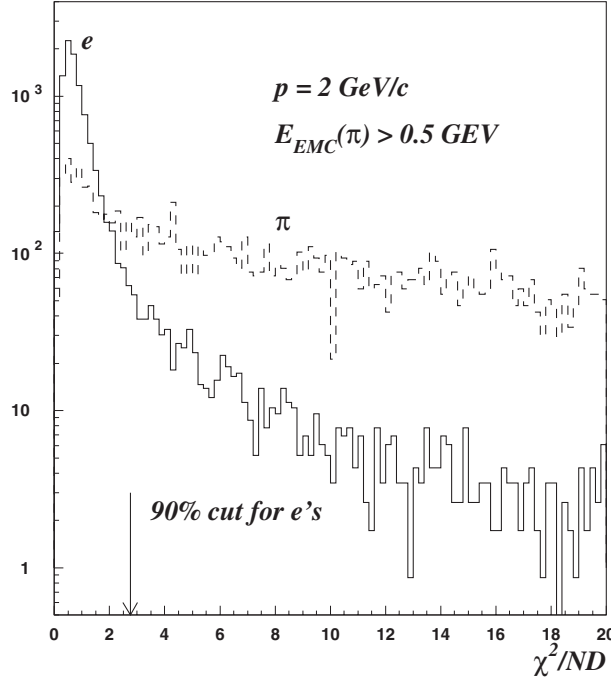


Figure 5.15: The χ^2 distribution for $2 \text{ GeV}/c$ electron and pion (with energy deposit above minimum ionization) samples. The arrow marks the χ^2 cut corresponding to 90 % electron efficiency.

Cut0: $\chi^2 < 3.0$

Cut1: $(0.3 + 4 \exp(-E_{all}/E_{cent})) \cdot (1.9 - 0.67 \chi^2) \cdot (1.0 - \exp(-8 \text{padisp}(1)/\text{padisp}(0))) > 1.4$ (Stochastic Cut 1)

Cut2: $(0.3 + 4 \exp(-E_{all}/E_{cent})) \cdot (1.9 - 0.67 \chi^2) > 1.4$ (Stochastic Cut 2)

Cut3: $(0.3 + 4 \exp(-E_{all}/E_{cent})) \cdot (1.9 - 0.67 \chi^2/\text{twrhit}) \cdot (1.0 - \exp(-8 \text{padisp}(1)/\text{padisp}(0))) > 1.4$ (Stochastic Cut 3)

Cut4: $(0.3 + 4 \exp(-E_{all}/E_{cent})) \cdot (1.9 - 0.67 \chi^2) > 2.0.$ (Stochastic Cut 4)

where E_{cent} is the energy in the central tower, $\text{padisp}(1)$ and $\text{padisp}(0)$ are the dispersions along the principal axis of the shower, twrhit is the number of towers in the cluster. Note that the functional form in Stochastic cut 2 and Stochastic cut 4 are the same, the only difference is the threshold (1.4 and 2.0).

For the $\chi^2 < 3.0$ cut and Stochastic cut 2, efficiencies to hadrons (e.g. π^+ , K^+ , p , \bar{p}) and electrons are obtained from the GEANT simulation (Output 2 in Fig. 5.1), and are shown in Fig. 5.16 as a function of energy. While Stochastic cut 2 achieves the stronger hadron rejection, the efficiency is quite low (~ 0.5) comparing with the standard $\chi^2 < 3$ cut. The criteria of the cut strongly depends on the analysis, and the strong cut is necessary in the case of photon identification from large background (e.g. low- p_T photon in Au+Au central collisions). On the other hand, loose cut but high efficiency, such as the $\chi^2 < 3$ cut, is suitable for the identification

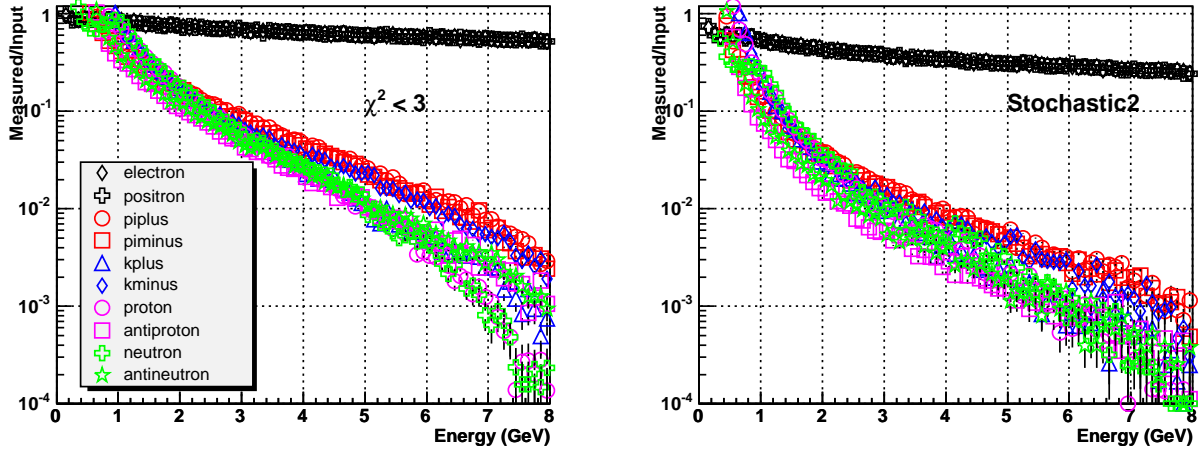


Figure 5.16: Measured energy with respect to input energy for each hadrons and electrons. Left figure shows the ratio for the clusters which pass the $\chi^2 < 3$ cut. Right figure shows the ratio for the clusters which pass the Stochastic cut 2. Note that the ratio is possible to be more than 1. Most of hadrons make a peak around 270 MeV (MIP).

of rare photons from small background, (e.g. identification of photons in peripheral collisions). In this analysis, the $\chi^2 < 3$ cut is mainly used, while other cuts are used to estimate systematic errors.

5.5 Analysis for Neutral Pion Measurement

The procedure of π^0 counting, calculation of efficiency and estimation of systematic study is described in this section. For the measurement of π^0 invariant yield, invariant mass method is used. The invariant yield of π^0 per event is given by

$$\frac{1}{N_{\text{event}}} \cdot \frac{1}{2\pi p_T} \cdot \frac{d^2 N_{\pi^0}}{dp_T dy} = \frac{1}{N_{\text{event}}} \cdot \frac{1}{2\pi p_T} \cdot \frac{1}{c_{\text{bin-shift}}} \cdot \frac{N_{\pi^0}^{\text{corr}}(\Delta p_T, \Delta y)}{\Delta p_T \Delta y}, \quad (5.26)$$

where $c_{\text{bin-shift}}$ is the correction for the bin shifting due to the finite binning, and $N_{\pi^0}^{\text{corr}}$ is given by:

$$N_{\pi^0}^{\text{corr}} = \frac{1}{\epsilon_{\text{acc}} \cdot \epsilon_{\text{reco}}} \cdot N_{\pi^0}^{\text{raw}}, \quad (5.27)$$

where $N_{\pi^0}^{\text{raw}}$ is the extracted π^0 raw yield with invariant mass method, and ϵ_{acc} is the correction for the geometrical acceptance, and ϵ_{reco} is reconstruction efficiency. The ϵ_{reco} is obtained with embedding simulation (Output 5 in Fig. 5.1) in order to take into account the overlapping effect of large amount of backgrounds.

5.5.1 Extraction of Neutral Pion Signal

Procedure

The criteria for event selection and photon selection are described before. In the selected events, the invariant mass ($M_{\gamma\gamma}$) and the momentum ($\mathbf{p}_{\gamma\gamma}$) are calculated from all pairs of clusters which pass the photon cut, using the following formula:

$$M_{\gamma\gamma}^2 = 2 \cdot E_{core}(1) \cdot E_{core}(2) \cdot (1 - \cos \theta), \quad (5.28)$$

$$\mathbf{p}_{\gamma\gamma} = E_{core}(1) \cdot \mathbf{n}_1 + E_{core}(2) \cdot \mathbf{n}_2, \quad (5.29)$$

where $E_{core}(1)$ ($E_{core}(2)$) is the corrected core energy (E_{core}) of cluster 1 (2), \mathbf{n}_1 (\mathbf{n}_2) is the unit vector of cluster 1 (2), and θ is the opening angle between the two photons (i.e. $\cos \theta = \mathbf{n}_1 \cdot \mathbf{n}_2$). \mathbf{n}_1 and \mathbf{n}_2 are calculated from the hit positions at the front face of the calorimeter and the vertex position obtained from the BBC (given by Eq. 3.2). For the improvement of signal-to-noise ratio of π^0 peak, followings are required to $\gamma\gamma$ pairs:

1. the opening angle of two clusters is limited by $\cos \theta < 1. - (0.0425^2)/(2 \cdot E_{core}(1)(\text{GeV}) \cdot E_{core}(2)(\text{GeV}))$, which cuts out the π^0 invariant mass region below 42.5 MeV.
2. the energy asymmetry between the clusters, $\alpha = |E_{core}(1) - E_{core}(2)|/(E_{core}(1) + E_{core}(2))$, is less than 0.8.
3. both clusters are in a same EMCAL sector.

Especially, item 2 is applied to reject high- p_T combinatorial $\gamma\gamma$ pairs. The angular distribution of the $\gamma\gamma$ pairs in the π^0 rest frame, $d\sigma/d\cos\theta^*$, is constant, which leads to a flat distribution in the measured energy asymmetry of the two photons from π^0 decay.

$$\alpha = \frac{|E_{core}(1) - E_{core}(2)|}{E_{core}(1) + E_{core}(2)} \cong \beta |\cos\theta^*|, \quad (5.30)$$

where $\beta = p/E \sim 1$ is the velocity of π^0 . On the other hand, high- p_T combinatorial pairs are strongly peaked near $\alpha = 1$. One of the reason for such structure is the steeply falling spectrum of photon candidates. For this reason, a cut on α is used to reduce the combinatorial background.

Samples of the $\gamma\gamma$ invariant mass are shown in Fig. 5.17. The $\gamma\gamma$ invariant mass distribution in 0 – 10 % and 80 – 92 % central collisions with above cuts are also shown for measured p_T range in Appendix H.

Background Subtraction

Figure 5.17 shows invariant mass distributions for π^0 candidates with $2.0 < p_T < 3.5 \text{ GeV}/c$ for central and peripheral Au+Au collision. The background under the clear π^0 mass peak in these

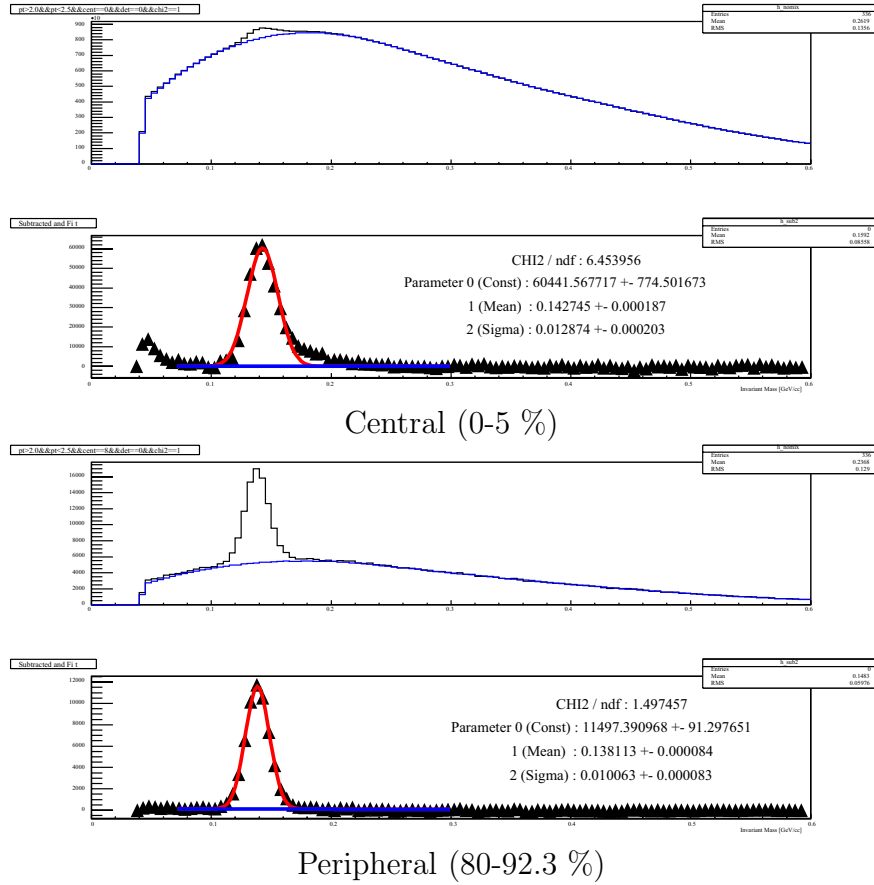


Figure 5.17: Sample output of π^0 extraction program. This plot shows π^0 -peak measured with the PbSc in the range $2.0 < p_T < 2.5$ GeV in the most central events (0-5 %) and in the most peripheral events (80-92.3 %). The top plot shows the invariant mass distribution in real events along with the scaled mixed events background. The middle plot shows the π^0 after background subtraction, and finally, the bottom plot shows the Gaussian fit to the π^0 peak.

figures is mostly due to combinatorial mixing of photons from different decaying π^0 's or from pairs containing non-photon clusters that nonetheless pass the cuts for photon identification.

The distribution of the backgrounds were determined using an “event mixing” technique. Photons are paired both within the same event (real histograms) and across events (mixed event histograms). Only events of the same centrality class, reaction plane class and vertex class are mixed. Up to 5 events per event class are buffered for mixing. Our centrality bins for mixing were 0-5 %, 5-10 %, 10-15 %, 15-20 %, 20-30 %, 30-40 %, 40-50 %, 50-60 %, 60-70 %, 70-80 %, and 80-93 % as shown in Fig. 5.18; the reaction plane bins were 10 degree wide from -90° to 90° ; the vertex bins were 5 cm wide from -30 cm to 30 cm. The mixed event histograms are normalized to the corresponding real photon pair invariant mass distributions below and above the π^0 peak. The mixed event background is then subtracted from the real distribution to reproduce the true π^0 invariant mass spectrum, which in turn is fitted with a Gaussian. The peak position, width, yield with their respective errors are all recorded on the count sheet (see Figs. 5.17). The yield is determined by counting the number of entries in the histogram in

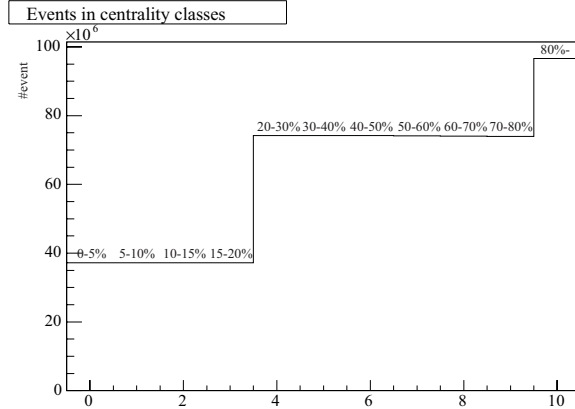


Figure 5.18: Number of events in the nominal centrality bins used for event mixing.

100 MeV to 180 MeV after the background subtraction. Results for the minimum bias events are obtained by adding up the subtracted yields from the narrower centrality bins.

5.5.2 Estimation of Neutral Pion Efficiency

Geometrical Acceptance of $\gamma\gamma$ Pairs from π^0

The geometrical acceptance is calculated with generated π^0 s (Output 3 in Fig. 5.1). A single π^0 is decayed into two γ s and the π^0 is considered as accepted π^0 if the two γ s are hit EMCAL towers. The bad towers and neighboring towers rejected in the analysis of real data are also rejected. The pure geometrical acceptance for $\pi^0 \rightarrow \gamma\gamma$ pairs in PbSc (ϵ_{acc} in Eq. 5.27) is shown in Fig. 5.20.

Estimation of Detection Efficiency with Embedding

The reconstruction efficiency for π^0 s (ϵ_{reco} in Eq. 5.27) is defined as:

$$\epsilon_{reco}(p_T) = \frac{f(p_{T\text{measured}})}{f(p_{T\text{input}})}, \quad (5.31)$$

where $f(p_{T\text{input}})$ denotes the input spectrum of π^0 s for which both decay photons lie on an active region of the detector, and $f(p_{T\text{measured}})$ is the actually measured spectrum.

The reconstruction efficiency is determined using single π^0 embedding simulation output (Output 5 in Fig 5.1). Before the generated π^0 from GEANT simulation are embedded into real data, an additional energy smearing of 2 % for each tower is applied. The additional smearing is applied to reproduce the measured width of π^0 mass peak. The possible reasons which would cause the additional smearing is the additional correction factor for E_{core} and the fluctuation of the calibration factor tower by tower. In the GEANT procedure, one also has control on the effects of photon conversions, as the GEANT simulation includes the material budget in front of the EMCAL and the information of photon conversion is kept for evaluation in the correction estimation.

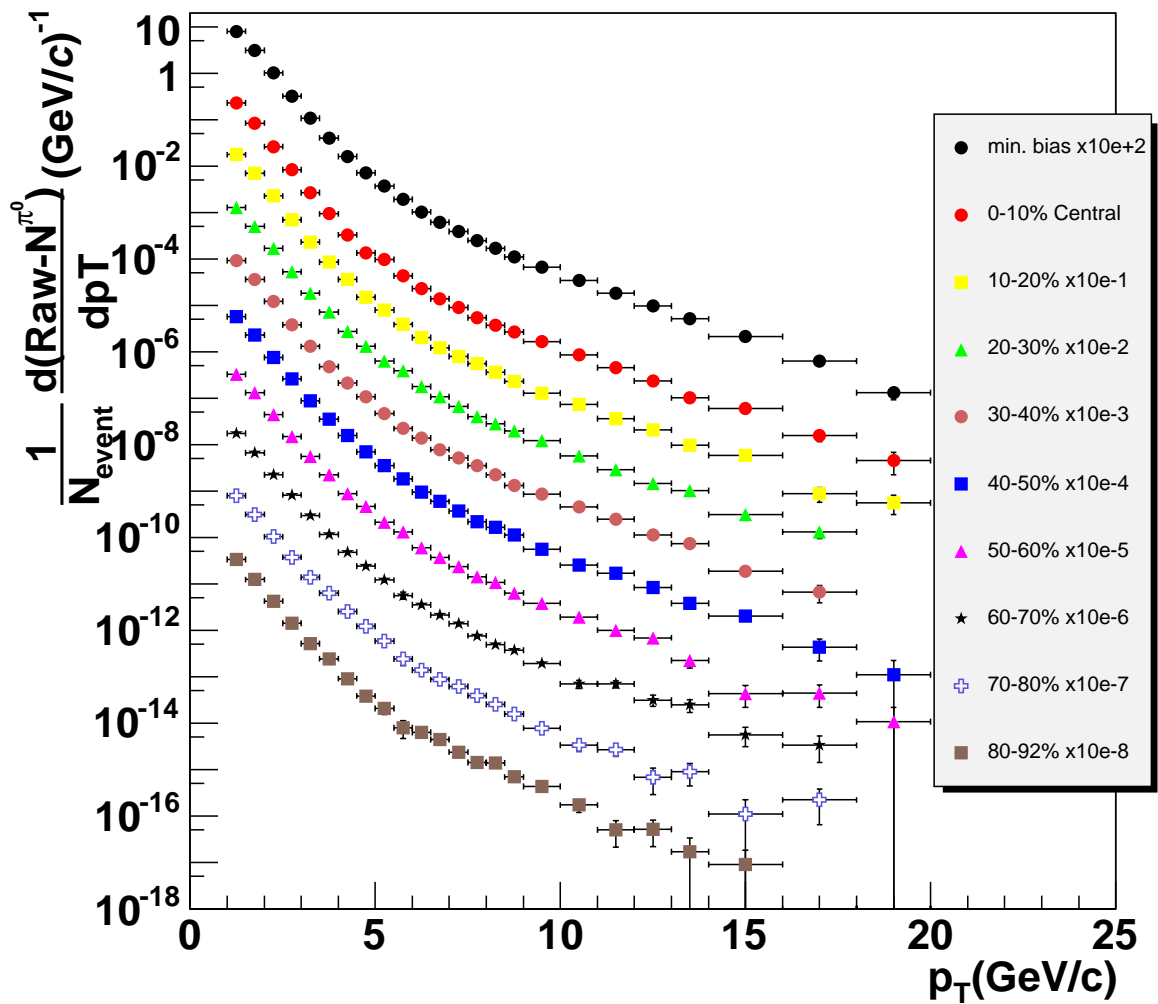


Figure 5.19: Number of counted raw π^0 s with the invariant mass method for each centrality bin.

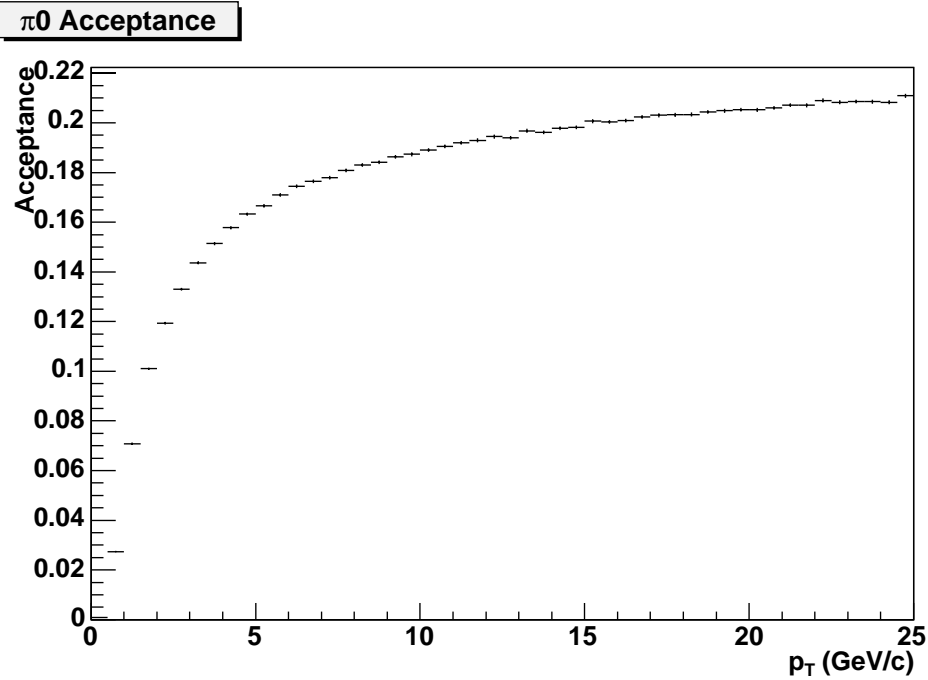


Figure 5.20: Geometrical Acceptance for $\pi^0 \rightarrow \gamma\gamma$ pairs in PbSc as a function of $\pi^0 p_T$.

The $\gamma\gamma$ pairs are reconstructed from GEANT output through the same procedure as for the real $\gamma\gamma$ reconstruction. The simulated yield is obtained as functions of invariant mass (M), measured $\pi^0 p_T$ (p_T), input $\pi^0 p_T$ (p_T^{in}), and cluster multiplicity (N_{mul}): $N_{\gamma\gamma}(M, p_T, p_T^{in}, N_{mul})$. The reconstruction efficiency given in Eq. 5.31 is calculated with the following relation:

$$\epsilon_{reco}(p_T) = \frac{1}{\int f_{\pi^0}(p_T) \cdot \int w_{cent}(N_{mul}) \cdot N_{\pi^0}^{in}(p_T, N_{mul}) dN_{mul}} \quad (5.32)$$

$$\times \int \int \int_{m_{low}}^{m_{up}} w_{cent}(N_{mul}) \cdot f_{\pi^0}(p_T^{in}) \cdot N_{\gamma\gamma}(M, p_T, p_T^{in}, N_{mul}) dM dp_T^{in} dN_{mul}, \quad (5.33)$$

where $f_{\pi^0}(p_T)$ is the $\pi^0 p_T$ spectrum, $N_{\gamma\gamma}(p_T, N_{mul})$ is the input yield and $w_{cent}(N_{mul})$ is the function to weight the yield with the cluster multiplicity:

$$w_{cent}(N_{mul}) = N_{mul} \cdot \frac{N_{event}(N_{mul})}{\int N_{event}(N'_{mul}) dN'_{mul}}, \quad (5.34)$$

where $N_{event}(N_{mul})$ is the distribution of cluster multiplicity for given centrality. The centrality dependence of efficiency is determined with the function. In Eq. 5.32, the integrated mass window ($m_{low} < m_{\gamma\gamma} < m_{up}$) is constant ($m_{low} = 100 \text{ MeV}/c^2$, $m_{up} = 180 \text{ MeV}/c^2$) as well as raw π^0 yield extraction.

In Eq. 5.32, the simulated yield is weighted by the cluster multiplicity and input π^0 spectrum. The π^0 yield is weighted by the cluster multiplicity to take into account the fluctuation of the multiplicity distribution, which could affect the efficiency. While the weighting with the number

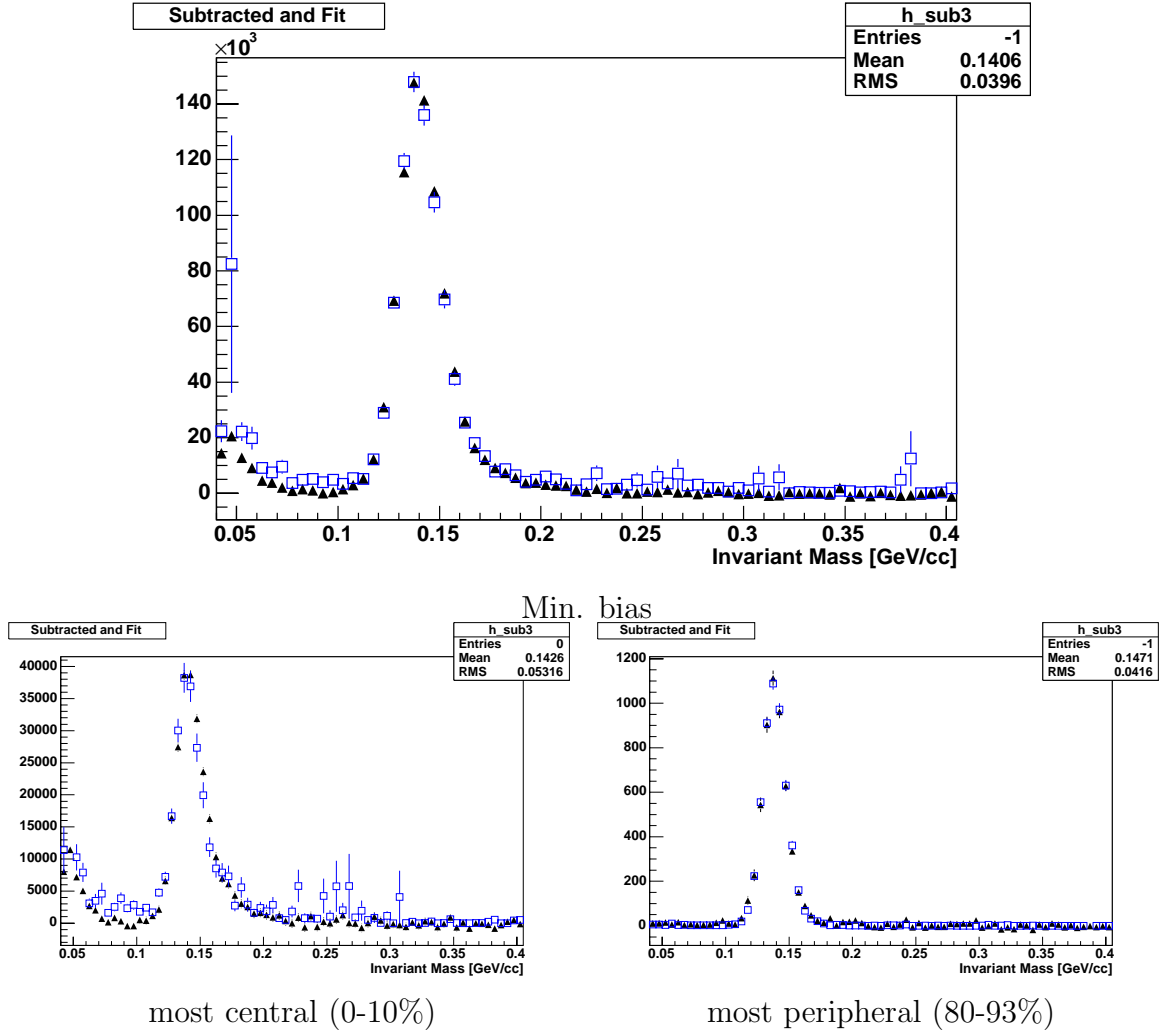


Figure 5.21: π^0 mass peaks in the p_T range of $2.0 - 3.0$ GeV/ c in PHENIX minimum bias, most central and most peripheral central bin. Black triangles are real data and blue open boxes are from π^0 embedding.

of π^0 s is more preferable than that with cluster multiplicity, cluster multiplicity is used instead. The weighting with number of π^0 was tried with some iteration, but there are not significant deviation by a factor of $< 1\%$ on the π^0 yield. The yield is also weighted by the input π^0 spectrum to get the correct energy folding of the π^0 spectrum with the resolution. This weighting is iterated, with the fit of the p_T dependence of the input weights adjusted as the estimate of the efficiency correction improves, until the procedure converges within the nearly p_T -independent statistical error of the embedded sample.

Figure 5.21 shows $\gamma\gamma$ invariant mass distributions of the real data and those using embedding simulation. The peak in central events shows tail at high-mass region (i.e. around $150 \sim 200$ MeV/ c^2). It is found that the tail is caused by the overlapping clusters and the original cluster gets a part of energy from the overlapping clusters. Figure 5.22 and Fig. 5.23 show the comparisons of π^0 mass peak and width between the real π^0 and simulated π^0 . The π^0 mass peak and width is well reproduced by the simulation. The fitting of π^0 invariant mass

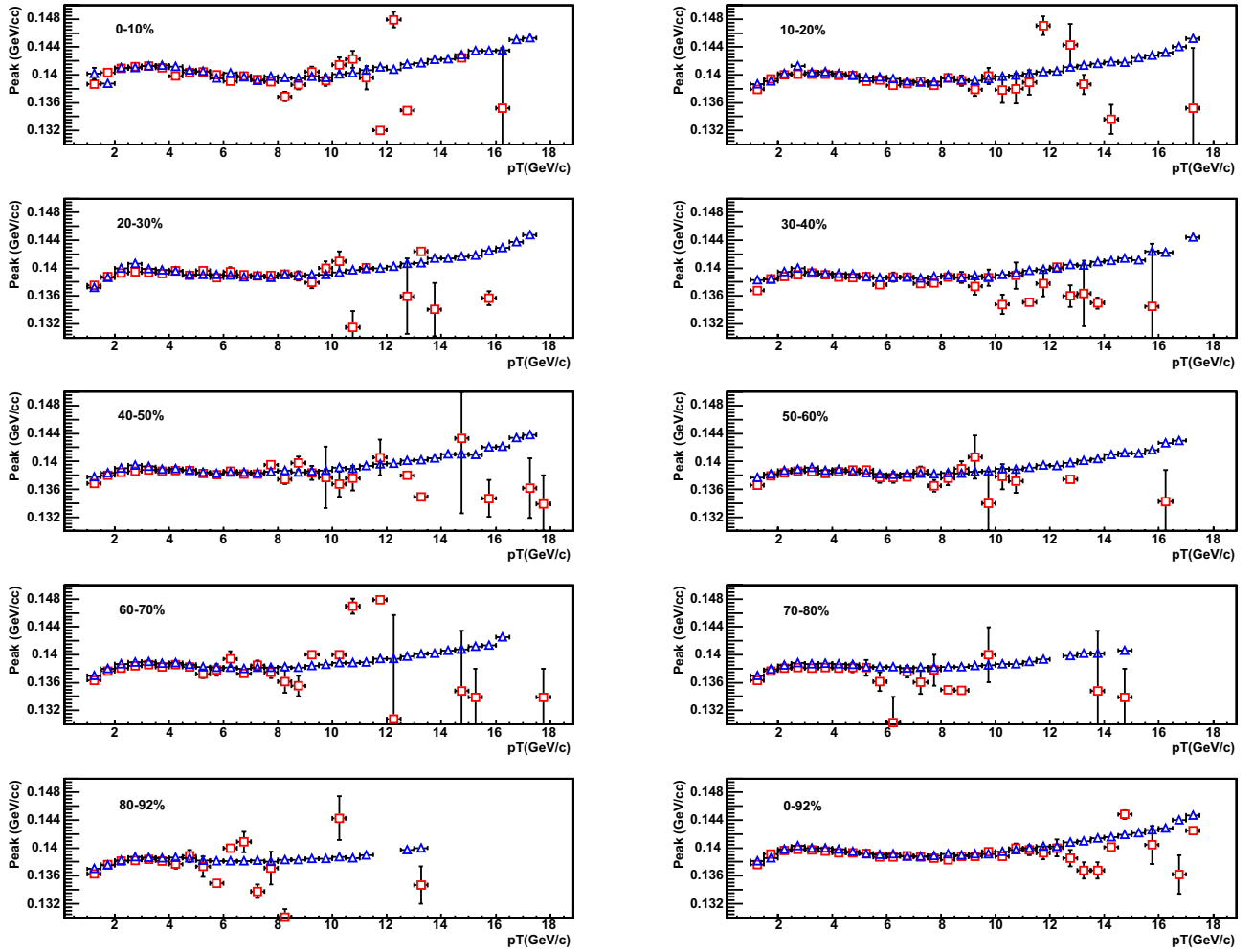


Figure 5.22: Comparison of the PbSc π^0 peak positions in real data and π^0 embedding events for each centrality selection. Red is real data and blue is embedding.

spectrum with Gaussian function is failed for high- p_T region due to the low statistics, then there are deviations between real and simulation at high- p_T .

Finally, the efficiency of single π^0 is obtained as $\epsilon_{acc} \times \epsilon_{reco}$ in Eq. 5.27. It is shown in Fig. 5.24. The efficiency falls above 12 GeV/*c*. This is because parts of $\gamma\gamma$ pairs from high- p_T π^0 s are recognized as a single cluster due to the finite tower size. This effect is called as “ π^0 merging effect” in this thesis. Systematic error due to this effect is expected to be the largest one among the errors on π^0 invariant yield. While the correction for this effect is included in the simulation, some detail studies are described at the next paragraph.

Simulation Study for π^0 Merging Effect

Two photons from one π^0 are sometimes reconstructed as one cluster due to the PHENIX clustering algorithm and finite size of EMCAL towers. The segment size of a PbSc tower is 5.5 cm \times 5.5 cm and the Moliere radius of PbSc is about 3 – 4 cm. Naively the π^0 clusters are merged when the distance between two clusters are less than ~ 11 cm, which is corresponding

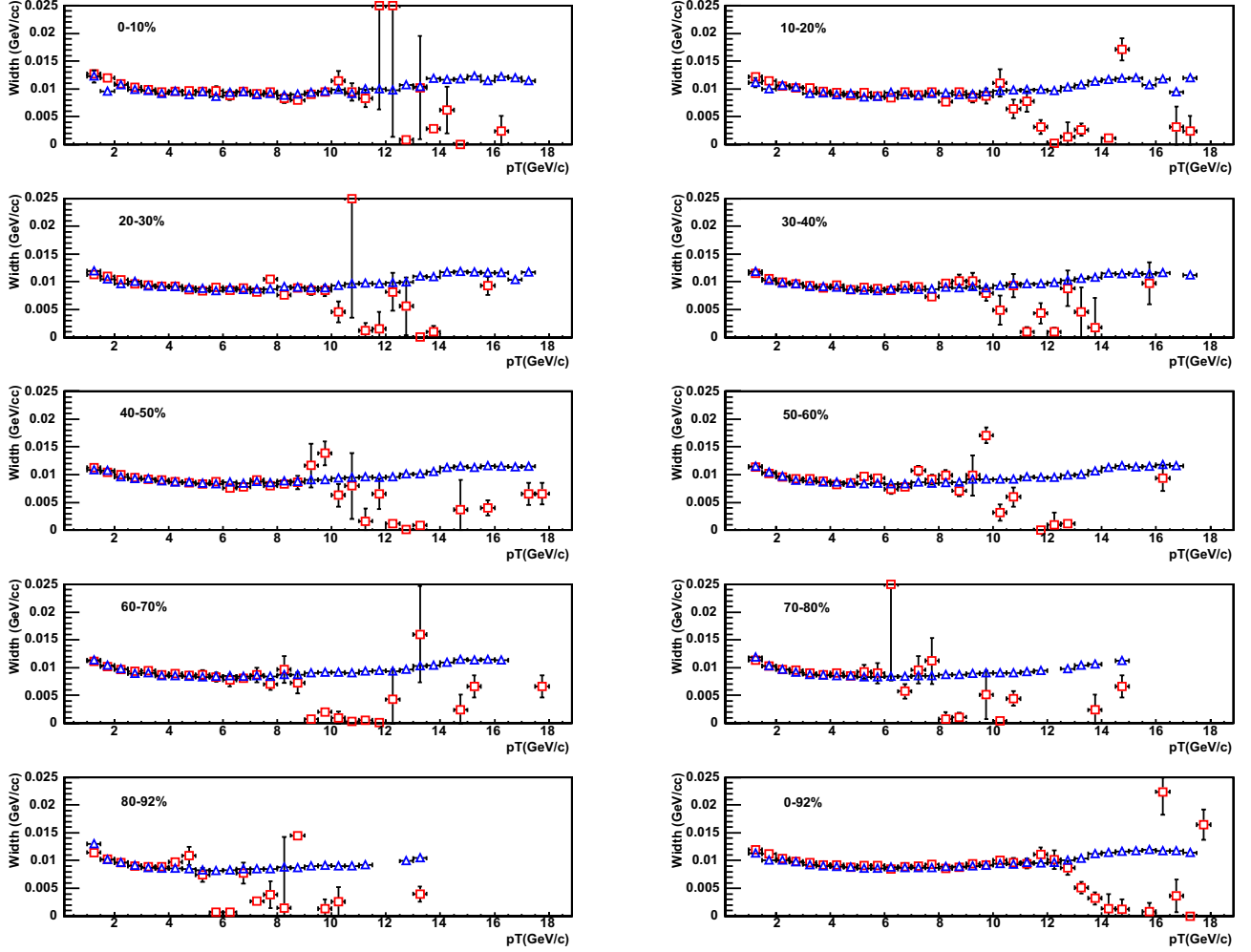


Figure 5.23: Comparison of the PbSc π^0 peak widths in real data and π^0 embedding events for each centrality selection. Red is real data and blue is embedding.

to $p_T(\pi^0) > 12 \text{ GeV}/c$.

In order to parameterize the π^0 merging effect, a simulation study was carried out with π^0 single simulation output (Output 4 in Fig 5.1). Figure 5.25 shows the correlation between “deltaR” and $\pi^0 p_T$. Here, “deltaR” is defined as the distance of projected points of 2 γ s from same π^0 on the EMCAL surface. It can be seen that 2-clusters whose deltaR are less than ~ 8 cm are not reconstructed, and this effect is significant at the $p_T(\pi^0)$ range of more than $12 \text{ GeV}/c$. As shown in left panel of Fig. 5.26, the merging probability ($\epsilon(p_T, \alpha)$) is obtained as functions of the p_T of π^0 and energy asymmetry of two photons, $\alpha = |E_{\text{core}}(1) - E_{\text{core}}(2)| / |E_{\text{core}}(1) + E_{\text{core}}(2)|$.

The π^0 merging probability as a function of p_T is compared with the expectation from beam test result. The shower shape of electromagnetic clusters in EMCAL towers is parameterized based on beam test result. Figure 5.27 shows the comparison of cluster merging probability obtained from GEANT simulation (Output 4 in Fig. 5.1) and that from beam test parameterization. There are about 5 % systematic discrepancy between the two results. The discrepancy is included into the systematic error of π^0 merging correction.

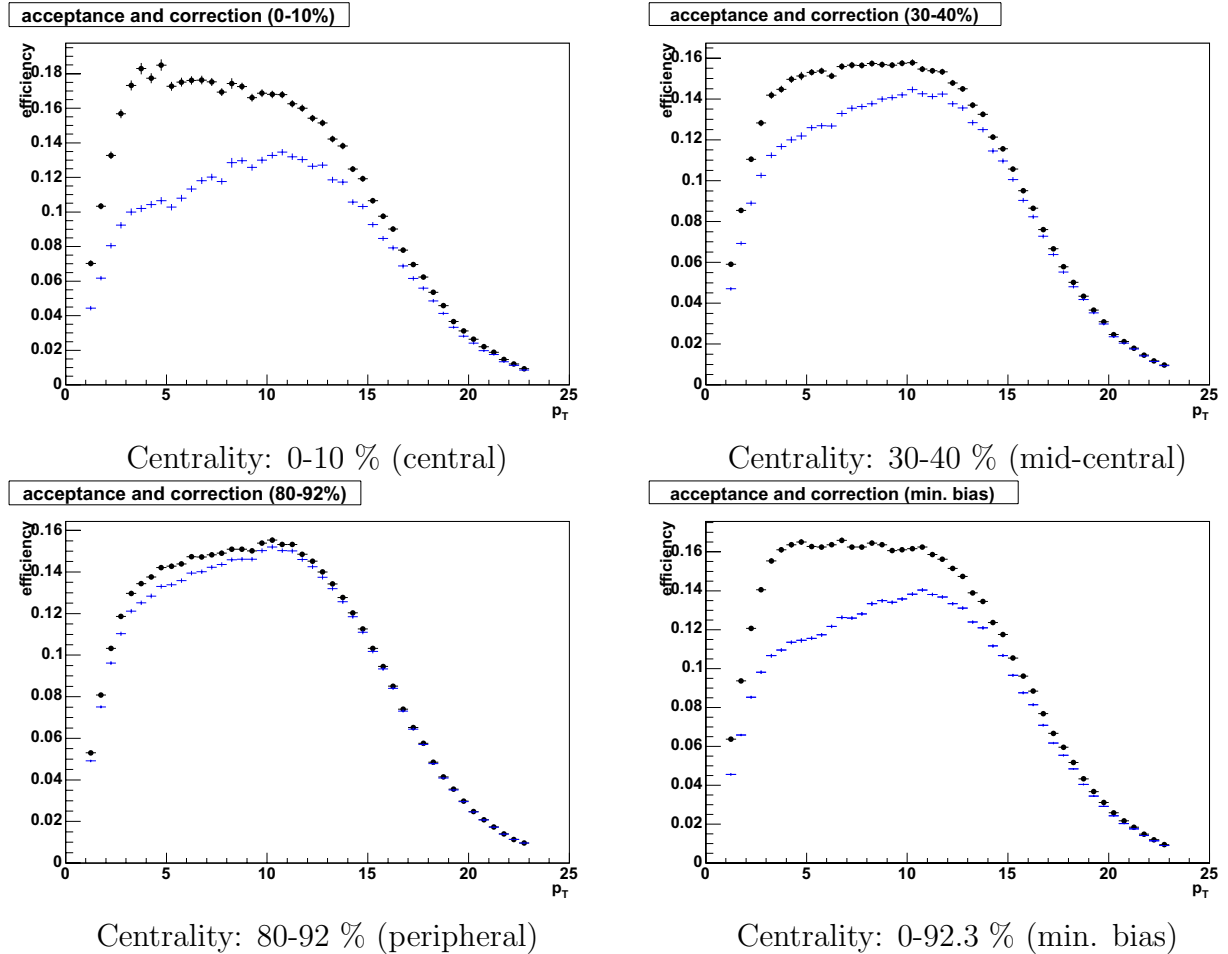


Figure 5.24: π^0 acceptance and efficiency correction for PbSc ($\epsilon_{acc} \times \epsilon_{reco}$) obtained from π^0 embedding. Black circles are for no particle identification and Blue crosses are for $\chi^2 < 3$ cut condition.

In order to estimate the over-lapping effect in high multiplicity condition on π^0 merging, the merging probability is estimated for actual high multiplicity environment using embedded π^0 simulation results (Output 5 in Fig. 5.1). Figure 5.28 shows the result of π^0 merging probability for each cases. As a result, effect of over-lapping on π^0 merging is quite small comparing with the systematic discrepancy between the simulation result and beam test result shown in Fig. 5.27.

Contribution from Off-Vertex π^0 s

π^0 s which are not from the collision vertex may also be reconstructed and contribute to the raw pion count. There are two major sources of such pions: real secondaries (from nuclear interaction with structural elements of the detector) and feed-down pions from decay of higher mass mesons (the primary source is K_S^0).

Simulations using HIJING (Output 1 in Fig 5.1) are used for the study of this contribution. Figure 5.29 shows the p_T dependence of ratio of secondary π^0 , where both decay photons are in the acceptance. Clearly at higher p_T almost all contribution comes from K_S^0 . The contribution

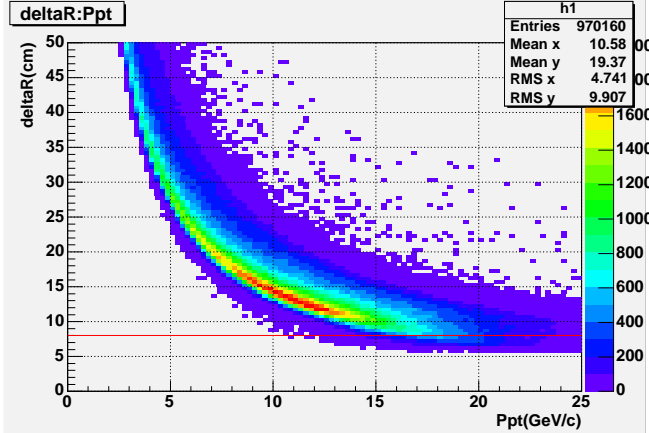


Figure 5.25: Correlation between δR , distance between two clusters on the EMCAL surface, and $\pi^0 p_T$.

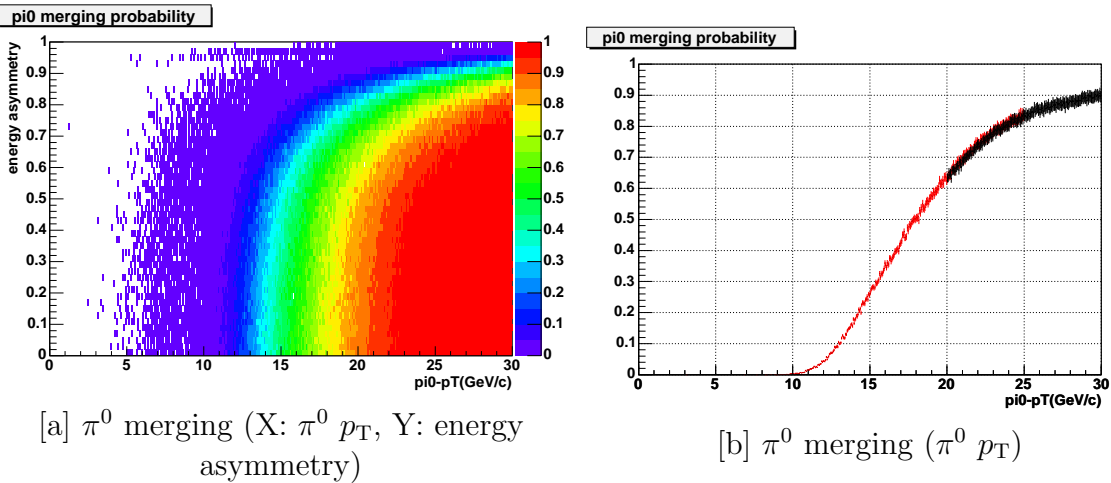


Figure 5.26: [a] π^0 merging probability as a function of $\pi^0 p_T$ and energy asymmetry.
[b] π^0 merging probability as a function of $\pi^0 p_T$.

from K_S^0 decay is also evaluated with single π^0 and K_S^0 simulation (Output 4 in Fig. 5.1). Figure 5.30 shows the estimated spectra of true- π^0 and secondary π^0 from K_S^0 decays, and the ratio of secondary π^0 is shown at right panel. The fraction of secondary π^0 s from K_S^0 decays is consistent with the estimation with HIJING simulation. Since the life time of K_S^0 is long ($c\tau = 2.68$ cm), the vertex position of secondary π^0 s are shifted as going to higher p_T . Then, it is expected that the fraction of secondary π^0 s from K_S^0 decays whose reconstructed mass is in the π^0 mass window will reduce as going to higher p_T . The systematic error of 3 % for correction for off-vertex π^0 s are assigned as a result.

Bin-Shift Correction

The bin-shift (binning) correction takes into account that the data points of the π^0 spectra are plotted at the center of a given interval. Due to the exponentially falling spectrum and finite p_T interval, the measured yield is larger than corrected one at the bin center. So a correction

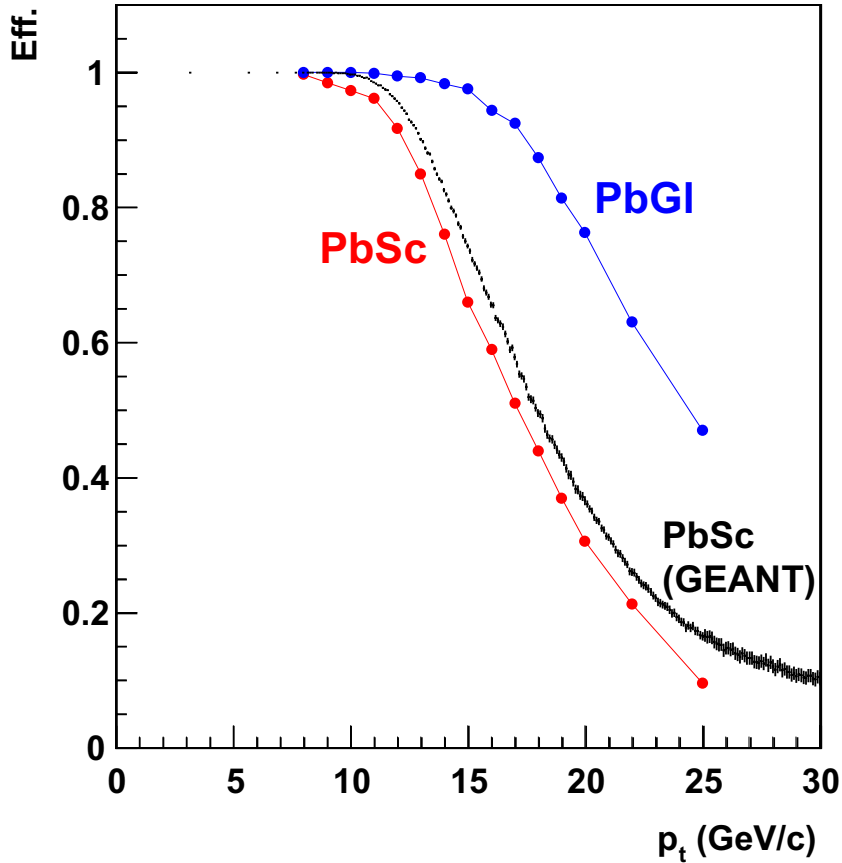


Figure 5.27: Comparison of π^0 survival probability from merging obtained from GEANT simulation and that from beam test parameterization.

($c_{bin-shift}$ in Eq. 5.26) has to be applied; either the data points are moved horizontally keeping their y-value or the points are moved vertically keeping their p_T -values. The second method is employed because the different spectra will keep their x-values and can thus be compared much better by taking point-to-point ratios. First a function $f(p_T)$ is used to parameterize the π^0 spectrum. The correction is given by the ratio of the average value of the function inside the p_T interval with a given width Δ and of the value of the function f at the bin center, p_T^c , as following:

$$c_{bin-shift} = \frac{1/\Delta \cdot \int_{p_T^c - \Delta/2}^{p_T^c + \Delta/2} f(p_T) dp_T}{f(p_T^c)} . \quad (5.35)$$

The function $f(p_T)$ used to parameterize the π^0 spectrum is expressed with Hagedorn function and power-law function, which are connected with the Wood-Saxon type transition function:

$$E \frac{d^3\sigma}{dp^3} = T(p_T) \cdot \frac{A_1}{(1 + p_T/p_0)^{n_1}} + (1 - T(p_T)) \cdot \frac{A_2}{p_T^{n_2}}, \quad (5.36)$$

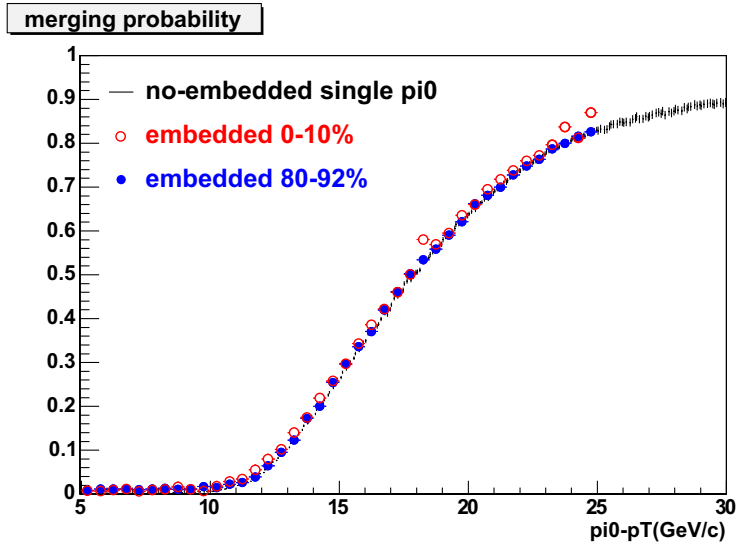


Figure 5.28: Merging probability of embedded π^0 as a function of π^0 p_T .

where

$$T(x) = \frac{1}{1 + \exp(s \cdot x + t)}. \quad (5.37)$$

Since the production processes change as looking at higher- p_T π^0 from soft to hard, two type functions connected with a transition function ($T(x)$) are used.

5.5.3 Systematic Errors on Neutral Pion Measurement

The various sources of systematic errors are described in this sections. All errors are taken as 1σ errors. The systematic errors are summarized in Table 5.2. The p_T dependence of the systematic error is shown at Appendix G.1. The systematic errors are categorized as followings:

Type A p_T -uncorrelated error; it might be p_T -correlated and the correlation is not known (e.g. points at low- p_T might move down while points at high- p_T move up).

Type B p_T -correlated error; all points move in the same direction.

Type C p_T -correlated error; all points move by the same factor (scale error).

The following sections describe in some detail how the errors were estimated.

Peak Extraction

This systematic error can be estimated from the consistency between different peak counting method in π^0 measurement. Figure 5.31 shows the ratio, $\#\pi^0(2\sigma \text{ window})/\#\pi^0(\text{fixed}(0.1-0.18 \text{ GeV}/c^2) \text{ window})$ for central events.

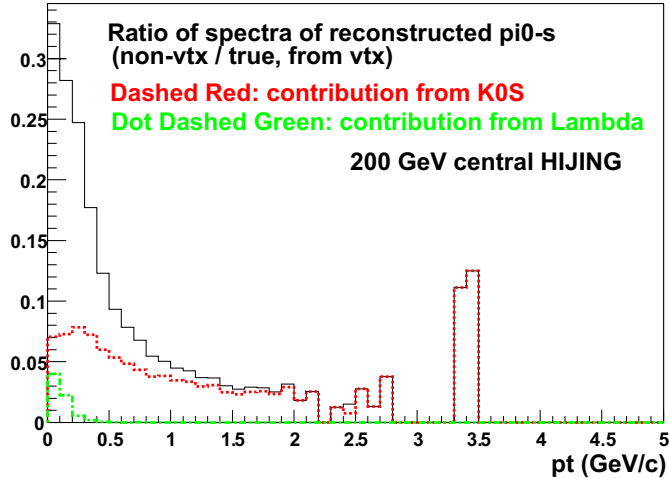


Figure 5.29: Ratio of reconstructed secondary π^0 s to all π^0 s in HIJING events. Above 1 GeV/c the ratio levels off at 4 % and is dominated by K^0_S decays [119].

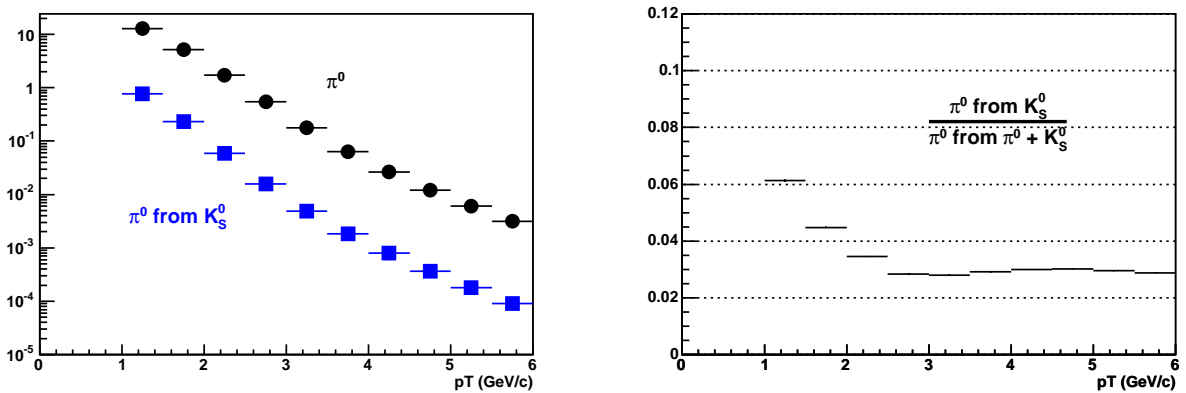


Figure 5.30: The estimation of off-vertex π^0 from K^0_S decay. Left figure shows π^0 spectra from K^0_S decay comparing with measured π^0 . Right figure shows the fraction of π^0 from K^0_S .

	p_T indep.	2 GeV/c	6 GeV/c	10 GeV/c	16 GeV/c	type
peak extraction	6 %					A
energy scale		6.5 %	9 %	9 %	9 %	B
particle-ID efficiency		10 %	10 %	10 %	10 %	B
merging corr.		0 %	0 %	17 %	30 %	B
Conv. corr.	3.0 %					C
off-vertex	3.0 %					C
Total		14 %	15 %	23 %	33 %	

Table 5.2: Systematic errors of the neutral pion invariant yields. The error sum for a given p_T column is the quadratic sum of the p_T -dependent errors given in that column and the p_T -independent errors. The errors are given for PbSc

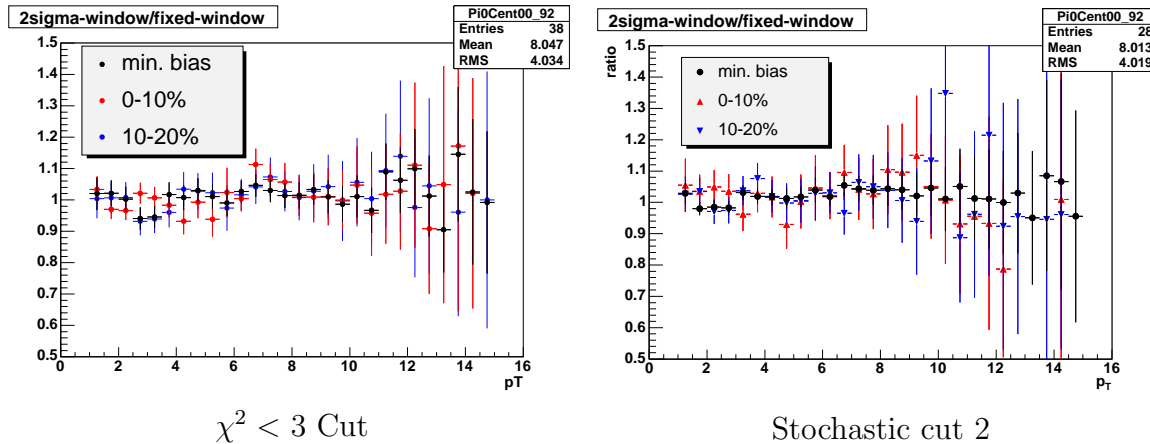


Figure 5.31: Ratio of corrected π^0 yield between different mass window cut. $\#\pi^0(2\sigma \text{ window})/\#\pi^0(\text{fixed}(0.1 - 0.18 GeV}/c^2) \text{ window})$. Left figure shows the ratio for $\chi^2 < 3$ cut, right figure shows the ratio for Stochastic cut 2.

The error in the peak extraction is also estimated from the ratio of raw $\# \pi^0$ (normal run)/raw $\# \pi^0$ (thick converter run). In the special run, the $\sqrt{s_{\text{NN}}} = 200$ GeV Au+Au data are taken with a thick photon converter (8.5 % X_0) installed on the beam pipe itself. Once a π^0 decay photon is converted, the magnetic field ensures that the e^+ and e^- ends up very far from each other in the calorimeter, i.e. they never reconstruct into a single cluster with the proper (original γ) energy. The corresponding π^0 is thus lost, and not counted in the raw yield. Then at any given centrality and any given p_T the ratio of raw yields with converter in and out should be constant (~ 85 %), and the variation of this ratio is a measure of the uncertainty of the peak extraction procedure itself.

As a result, the error on the π^0 peak extraction is estimated to be $\sim 6\%$.

Energy Scale

After energy calibration, the π^0 masses from the real data and the simulation agree well by a factor of $\sim 1\%$ as shown in Fig.5.17. Therefore, the systematic uncertainty on the absolute

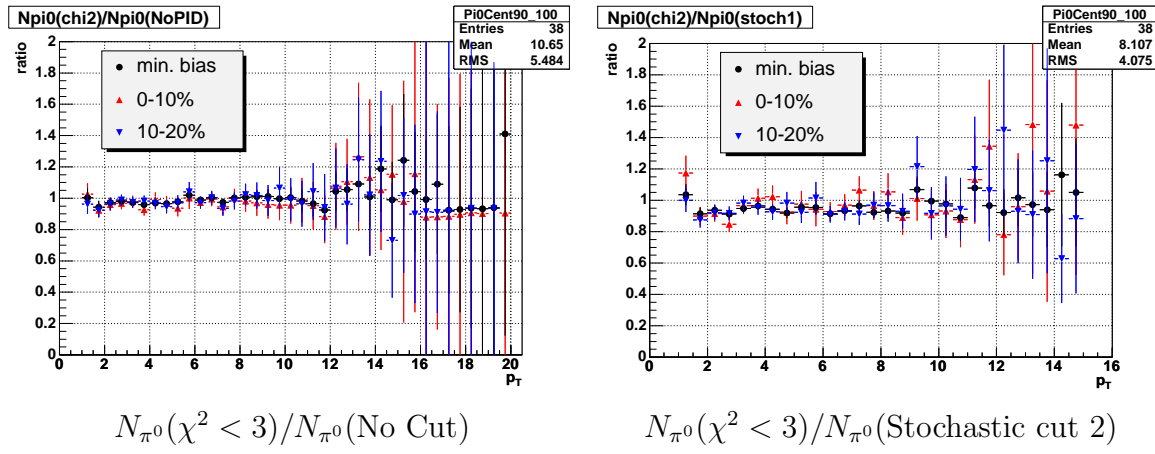


Figure 5.32: Ratio of corrected π^0 yield between different cut.

energy scale is estimated to be 1 %, which corresponds to the uncertainty on the yield of (6 – 9 %) as shown in Fig. 5.11.

Particle Identification Efficiency

The particle identification efficiency for reconstruction can be evaluated with the comparison of corrected spectra with different particle identification cuts. Figure 5.32 shows the ratios of corrected spectra with and without the $\chi^2 < 3$ cut for the different centralities. The agreement is within 10 % with the largest deviations in the central bins. The overlapping effect makes it difficult to estimate the efficiency, is main contribution which make the large uncertainty.

π^0 Merging Correction

As shown in Fig. 5.26, the detection efficiency of π^0 s is quite small at very high- p_T region. Therefore, the estimation of the merging effect is a large source of the systematic errors. In order to know how well it is estimated, some systematic studies are done as followings:

- There are systematic deviation between the π^0 merging probability obtained from test beam data, and from GEANT simulation. The systematic offset on π^0 yield due to the deviation is estimated as shown in the red line of Fig. 5.33.
- π^0 yields between different asymmetry bin are checked. π^0 merging probability is different with different asymmetry (i.e. different opening angle) as shown in Fig. 5.26. The blue boxes in Fig. 5.33 shows the ratio of corrected π^0 yield between different energy asymmetry cuts. For statistics advantage, π^0 without shower shape cut with minimum bias events are used for the evaluation.
- The error was estimated based upon the difference of direct photon excess ratio between different cut (black points in Fig. 5.33). The systematics of background photon between the different cuts are quite different. Details will be discussed at direct photon section (Sec. 5.6.3).

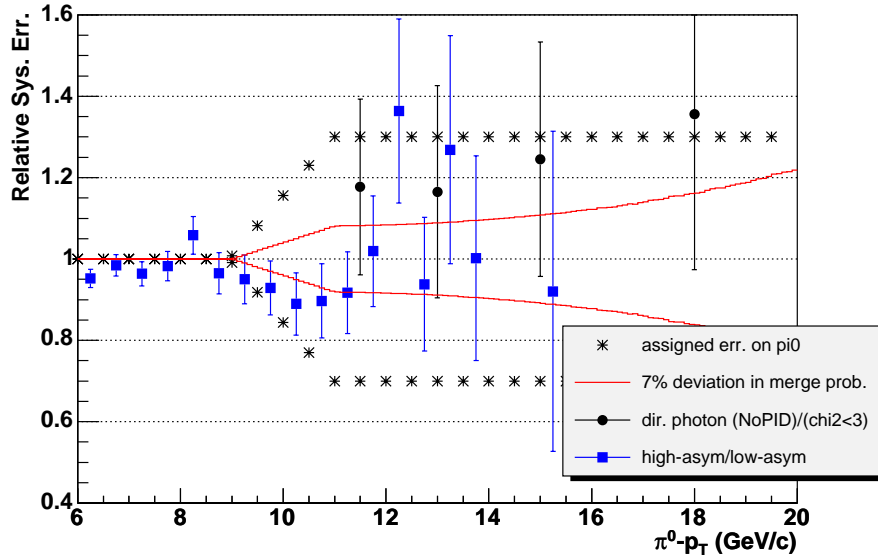


Figure 5.33: Systematic error for π^0 merging correction shown with plots which are used to estimate the error. Black stars show the assigned systematic error. Red lines are estimated deviation due to the difference of merging probability between test beam and GEANT simulation. Blue boxes are ratio of corrected π^0 yield between different energy asymmetry cut. Black circles are scaled ratio obtained from the direct photon excess ratio with different cut.

- In p+p collisions, another way is used to measure high- p_T π^0 s via identifying merged photons: they should not match single shower profile, or by other words, the value of “ χ^2 ” should be large. The probability to identify merged photons using shower profile measurements is close to 100 % for $p_T(\pi^0) < 20$ GeV/c. The invariant yield measured with this method shows the consistent result within the error.

Based upon the above studies, the systematic error is assigned as the black stars in Fig. 5.33.

Conversion Correction

The systematic error on the conversion correction is estimated from the study for the single gamma conversion probability, which will be discussed in later section. The error on π^0 yield can be obtained as approximately 2 times larger error on gamma yield.

5.6 Analysis for Direct Photon Measurement

For the extraction of the direct photon signal, subtraction method has been used. π^0 mesons are reconstructed via their two-photon decay mode and the corrected yield are obtained as described in the previous sections. The p_T spectra of direct photons are obtained by subtracting the spectra of decay photons estimated based on the measured π^0/η from the p_T spectra of inclusive photons.

In this section, the procedure of inclusive raw photon measurement and calculation of efficiency is described at first. Then, the estimation of the background from hadrons, subtraction of the background and estimation of systematic error on photon yield will be explained.

5.6.1 Measurement of Inclusive Photon Spectra

The invariant yield of inclusive photon per event is given by

$$\frac{1}{N_{\text{event}}} \cdot \frac{1}{2\pi p_T} \cdot \frac{d^2 N_{\text{inclusive}\gamma}}{dp_T dy} = \frac{1}{N_{\text{event}}} \cdot \frac{1}{2\pi p_T} \cdot \frac{1}{c_{\text{bin-shift}}} \cdot \frac{N_{\text{inclusive}\gamma}^{\text{corr}}(\Delta p_T, \Delta y)}{\Delta p_T \Delta y}, \quad (5.38)$$

where $c_{\text{bin-shift}}$ is the bin-shift correction, and $N_{\text{inclusive}\gamma}^{\text{corr}}$ is given by:

$$N_{\text{inclusive}\gamma}(p_T) = \frac{1 - X_{\text{hadron}}}{\varepsilon_\gamma \cdot a_\gamma \cdot (1 - p_c)} \cdot N_{\text{cluster}}(p'_T) \cdot c_{\text{folding}}. \quad (5.39)$$

Here $N_{\text{cluster}}(p'_T)$ denotes the EMCal cluster p'_T -distribution (typically after particle identification cuts), X_{hadron} is the ratio of the remaining hadron hits to all hits that satisfy the particle identification cuts, ε_γ is the (p_T and centrality dependent) photon reconstruction efficiency, a_γ is the geometrical acceptance and p_c denotes the probability of photon conversion. The reason why p'_T , not p_T , is used is that measured p_T is smeared due to the EMCal energy resolution, and the steeply falling slope become flatter. Then, additional correction, c_{folding} , is applied to obtain original p_T spectrum.

Scanning of Real Data to Get Raw Inclusive Photon Spectra

Procedures for extraction of the raw photon yield ($N_{\text{cluster}}(p'_T)$) is similar to those for π^0 . The criteria for event selection and cluster selection are exactly the same as used for π^0 . Figure 5.34 shows raw inclusive photon spectra (energy spectra) measured with PbSc up to $p_T = 20$ GeV/c.

Geometrical Acceptance Correction

The geometrical acceptance (a_γ in Eq. 5.39) is calculated using single photon simulation (Output 3 in Fig. 5.1). The bad towers and neighboring towers are rejected in the simulation as well as in the analysis of real data. The acceptance of photon in PbSc is shown in Fig. 5.35, and is ~ 0.23 .

Background from Hadrons

The ratio of the remaining hadrons to the selected clusters that satisfy the particle identification cuts are estimated using the simulation, where input particles are parameterized based upon actual data (Output 2 in Fig. 5.1). Figure 5.36 shows an example of input spectra (0-10 % central). The each cuts made for photon identification are applied to the clusters from hadrons, and the survived clusters are obtained as a function of p'_T ($f_{\text{hadron}}(p'_T)$). The hadron

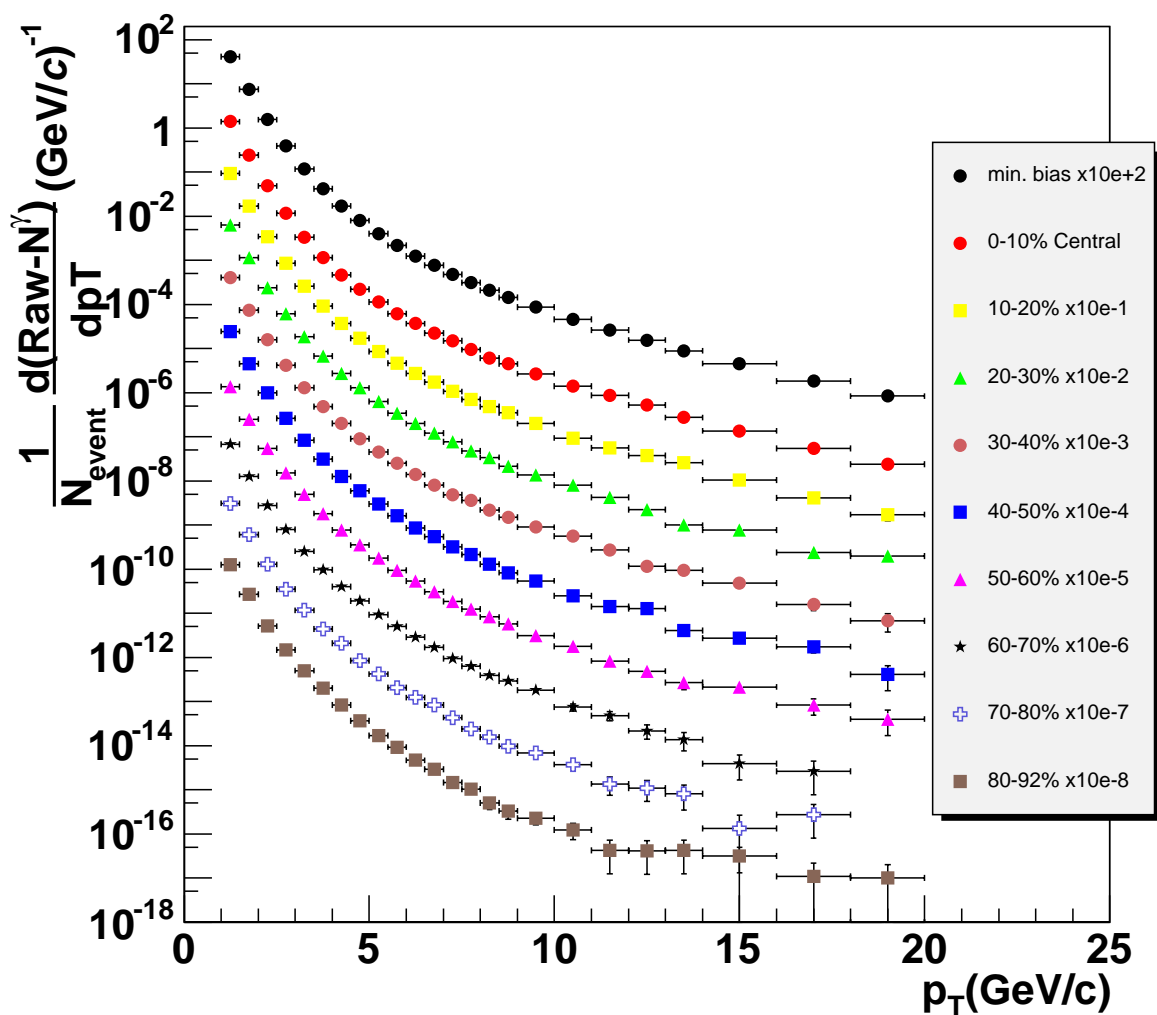


Figure 5.34: Raw energy spectra measured with PbSc.

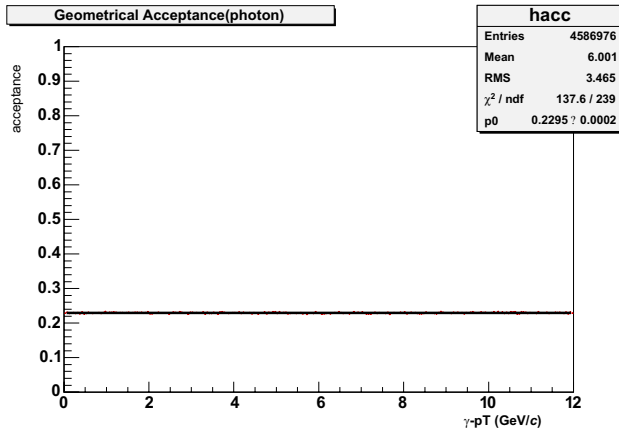


Figure 5.35: Acceptance for single photons in PbSc.

contamination (X_{hadron} in Eq. 5.39) is then defined at any given p'_T as the ratio of $f_{\text{hadron}}(p'_T)$ to the cluster yield $f_{\text{cluster}}(p'_T)$ at the same p_T . The spectra $f_{\text{hadron}}(p'_T)$ and $f_{\text{cluster}}(p'_T)$ are folded with the detector response. Figure 5.37 shows the fraction of the non hadronic clusters as a function p_T ($1 - f_{\text{hadron}}/f_{\text{cluster}}$, which is $1 - X_{hadron}$).

The results depend on how well hadrons are described by the simulation, both their overall energy deposit and the shape of hadron showers where the particle identification cuts depend (including the effects for overlaps if multiplicities are high). While the hadron contribution is small above $p'_T = 4 - 5 \text{ GeV}/c$, the uncertainty of the hadron contribution is a major source of error at low- p'_T .

As shown in Fig. 5.37, Stochastic cuts can reject the hadron contamination effectively. Without particle identification cut, it is expected to be a large amount of hadron contamination in low to mid- p'_T region, and the systematic error of this estimation is large comparing with the Stochastic cut result.

Embedding Study for Photon Measurement

In order to determine the single photon detection efficiency and energy smearing function which is used for making the unfolding correction, an embedding outputs (Output 5 in Fig. 5.1) are used. As well as the embedding of the simulated π^0 s, an additional energy smearing of 2 % for each tower is applied before the simulated single γ s are embedded into real data. The embedded γ s are accumulated for each cluster multiplicity and weighted by the multiplicity of clusters which hit EMCAL.

The photon identification efficiency (ϵ_γ in Eq. 5.39) is given as $\text{ACC}(p_T)/\text{ORG}(p_T)$, where p_T is true p_T of embedded real photons, $\text{ORG}(p_T)$ is the energy spectrum before cut is applied, and $\text{ACC}(p_T)$ is that after a cut is applied. Single photon efficiencies are estimated as functions of γ - p_T and centrality as shown in Fig. 5.38. In this calculation, the clustering efficiency is assumed to be 100 %. There is always at least one cluster found for photons above $1 - 2 \text{ GeV}/c$, so the assumption is reasonable for the energy range in interest for this analysis.

The smearing functions (ratio of reconstructed to original photon energy $E_{\text{core}}/E_{\text{org}}$ as functions of E_{org} and centrality) are obtained from same simulation output. Figure 5.39 shows

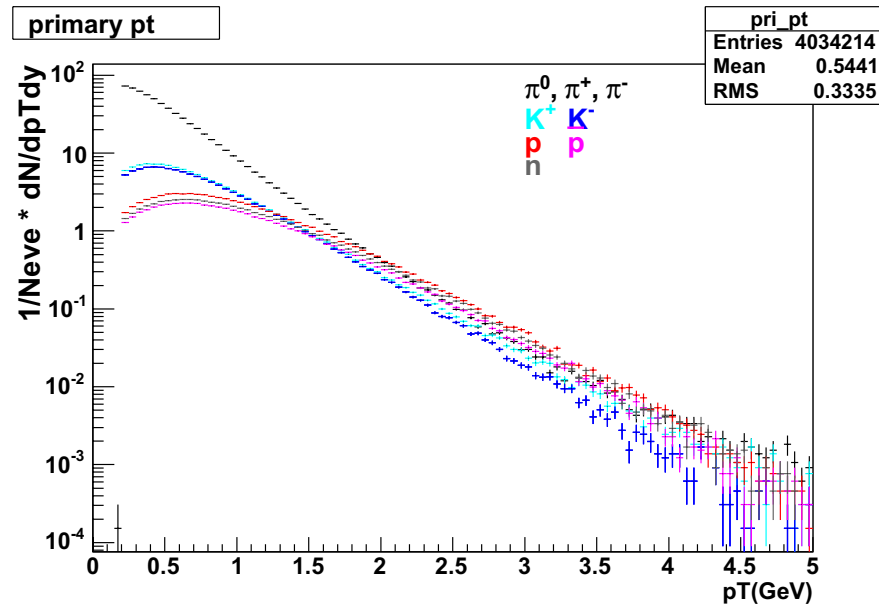


Figure 5.36: Example of input hadron spectra for the estimation of hadron contamination.

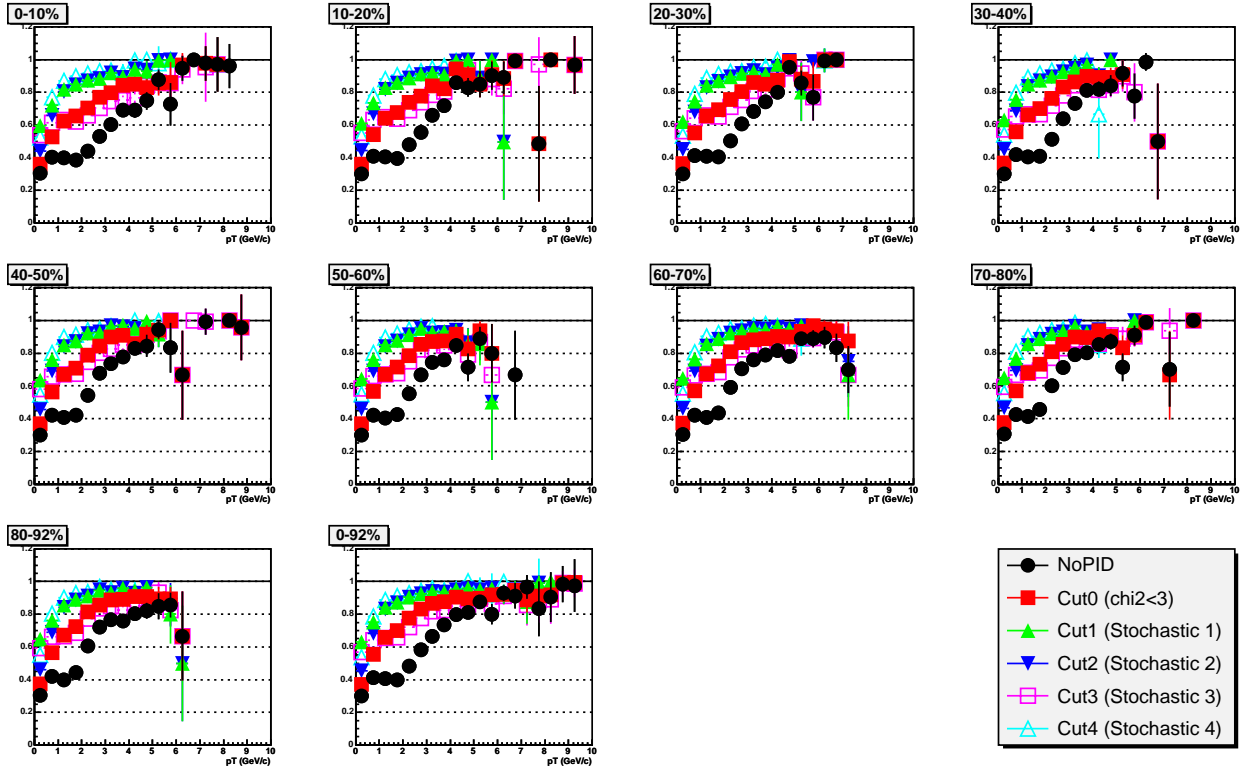


Figure 5.37: Estimation of the Hadron contamination as a function of measured p_T : the ratio of the photon hits to all hits as a function of measured p_T for each centrality.

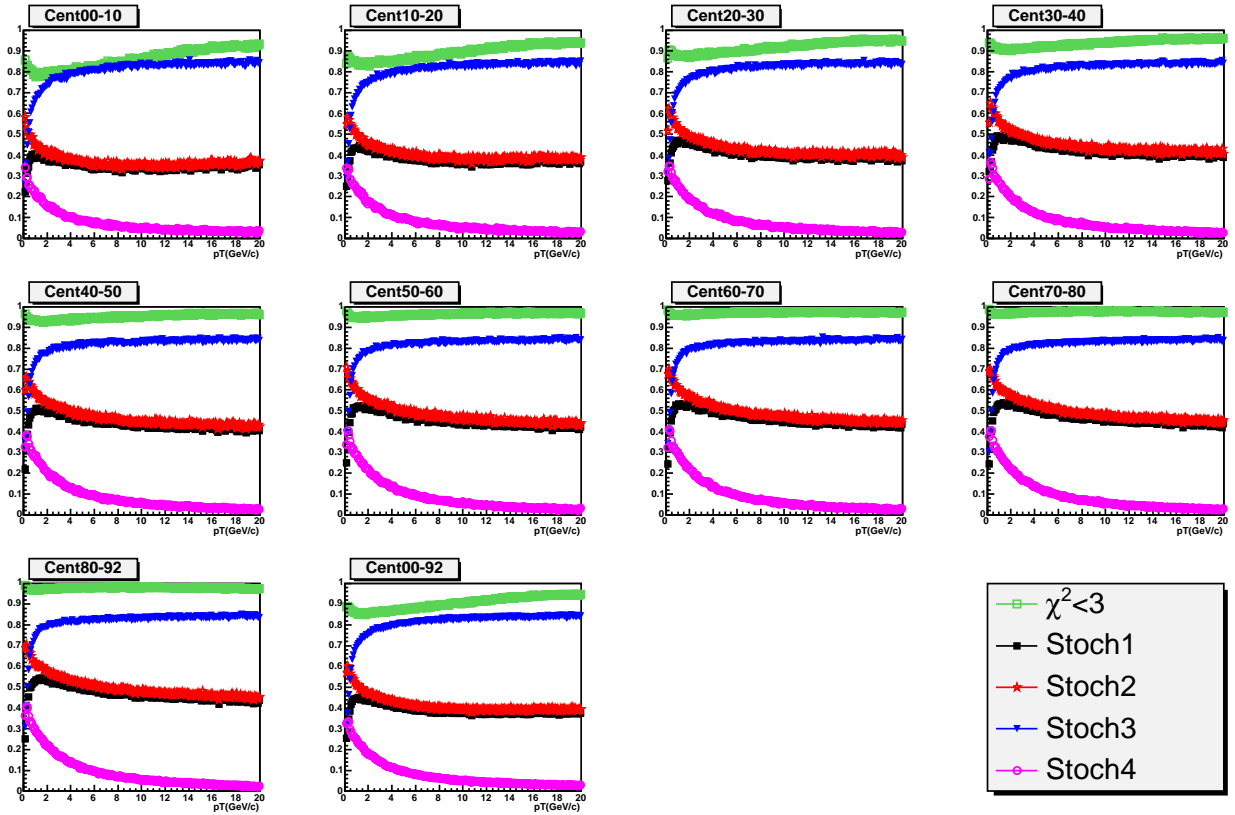


Figure 5.38: particle identification efficiency under some cuts for single photons in PbSc for each centrality.

smearing functions for 500 – 600 MeV and 1 – 1.1 GeV photons where no particle identification is applied and where a Stochastic cut is applied. The effect of overlaps is clearly visible as the long tail in central events. In the case of Stochastic cut, there are less overlap effect owing to strong hadron rejection. Smearing is a consequence of energy resolution of calorimeter itself and additional effects mainly from shower overlapping. The smearing function are made for different cuts and centrality.

Unfolding of the Effect of Energy Smearing

In order to correct the flattening effect on the spectrum due to the finite energy resolution and steeply falling slope, the effect of the smearing is unfolded using the smearing function. Using the smearing function obtained from embedding study, the correction for the unfolding is made as following:

- Single photon generated events (Output 3 in Fig. 5.1) are used for the calculation.
- For each single photon, smeared- p_T (p'_T in Eq. 5.39), which fluctuate as in smearing function with mean value of p_T , is given. 2-dimensional maps which show the correlation between input p_T and output p'_T are made for each cut and centrality.

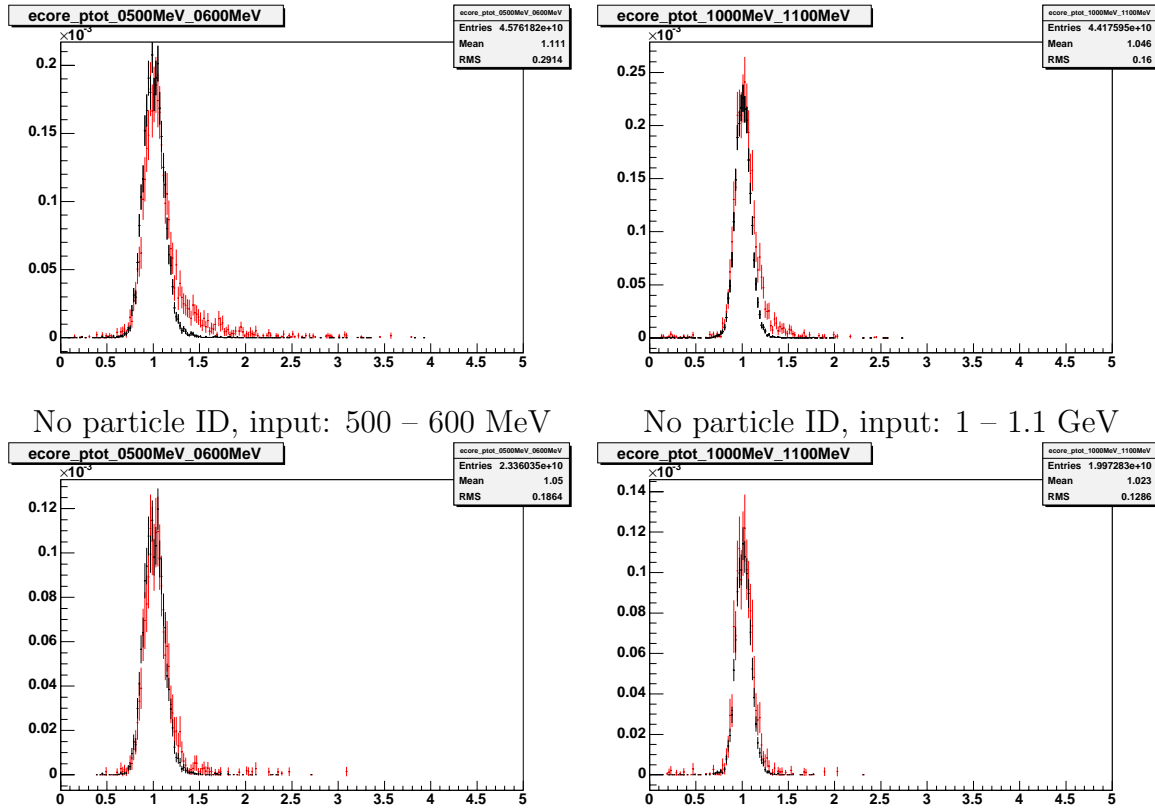


Figure 5.39: Smearing functions ($E_{\text{core}}/E_{\text{org}}$ ratios) for each simulated photons embedded in real data for peripheral (black) and central (red) events. The effect of overlaps is clearly visible as the long tail in central events. In the case of Stochastic cut, there are small overlap effect due to strong hadron rejection.

- Weight the p_T -axis of the map using the fitted function (Fig. 5.40-[a,b]) of raw energy spectrum.
- Project the 2-dimensional map to p'_T -axis ($N^\gamma(p'_T)$) and to p_T -axis ($N^\gamma(p_T)$) (i.e. two histograms are made). $N^\gamma(p_T)$ should be same as the function for weighting. Then, the correction is obtained as $N^\gamma(p'_T)/N^\gamma(p_T)$. (Fig. 5.40-[c])
- Apply the correction to raw spectra and get a new fitting function and iterate same procedure until the correction parameter converges. (Figure 5.40-[d-f]) As shown in Fig. 5.40-[f], the first iteration is enough to get the correction for unfolding.

In order to estimate systematics of this unfolding procedure, unfolded spectra with above procedure is smeared again and divided by original spectra. Figure 5.41 shows the ratio. There is large systematics (9 %) especially for low- p_T region (below 3 GeV/c), and this is expected due to the systematics of fitting for raw spectra. The systematics is taken into account as the systematic error on photon measurement.

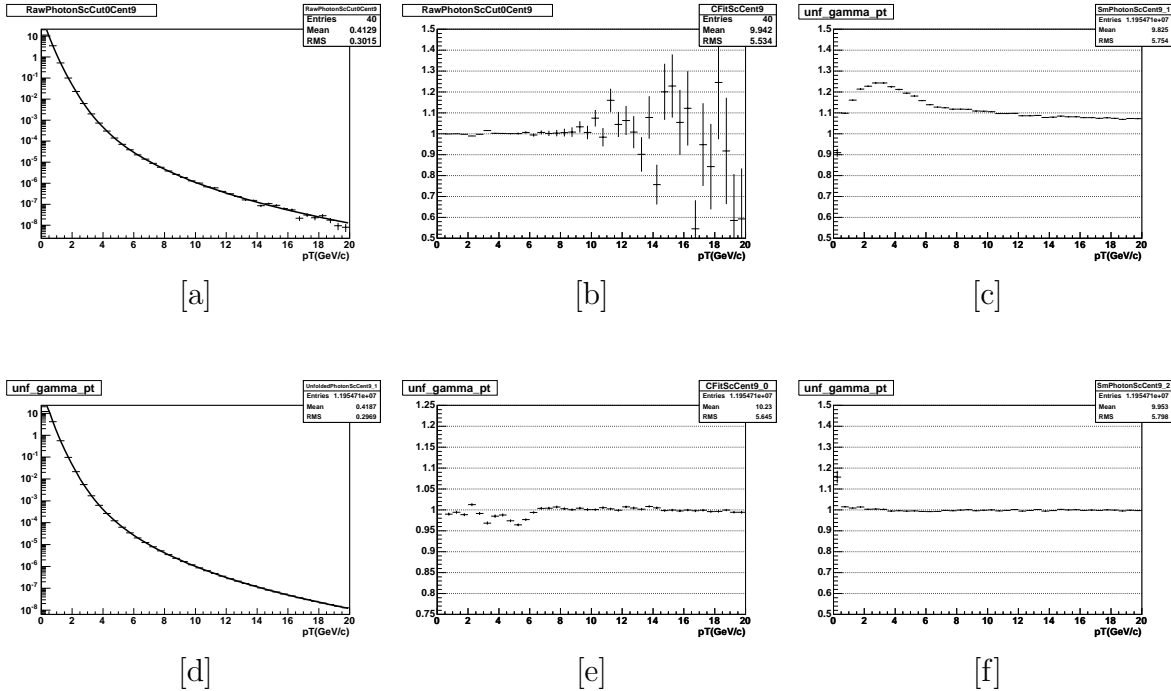


Figure 5.40: Figures for checking of unfolding procedure. [a] raw energy spectra fitted with the combine of Hagedorn and Power-law function. [b] (data point)/(fit) for checking how will fitting is done. [c] Correction factor obtained from Unfolding ($\text{gamma}(pT')/\text{gamma}(pT)$). [d] re-fitting for unfolded spectra. [e] (data point)/(fit) of “[d]”. [f] Correction factor obtained after iteration.

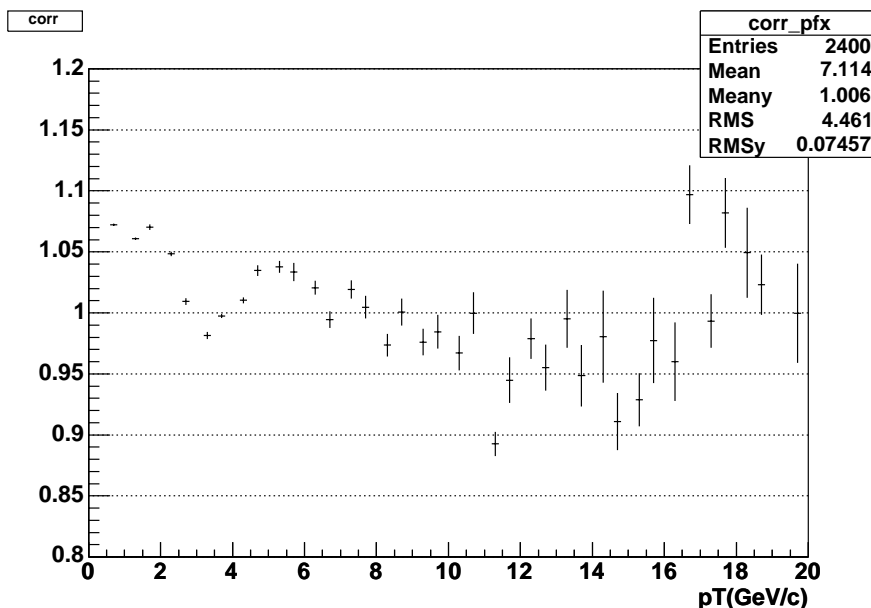


Figure 5.41: re-smeared photon spectrum over original raw spectrum.

Correction for γ Conversion

The correction for the conversion losses of photons is obtained from the full simulation of the single photon samples (Output 4 in Fig. 5.1). The conversion probability due to the materials in front of EMCAL is summarized in Table 5.3.

	Beam Pipe	DC	PC1	RICH	PC2	AGEL	TEC	PC3	TOF	total
PbSc (W0,2,3)					2.1 %	-	-	-	-	10.1 %
PbSc (W1)	0.3 %	0.9 %	1.2 %	3.2 %		6.2%	-	2.3 %	-	14.8 %
PbSc (E2,3)					-	-	5.6 %		-	12.7 %
PbGl (E0,1)					-	-			1.2 %	13.7 %

Table 5.3: Conversion probability due to the material in front of EMCAL.

Two associated corrections are taken into account for this correction. At first, the electron-positron pairs or one of the pairs from γ conversion would be reconstructed as their primary photon. Especially, e^+e^- pair coming from a conversion at the out of magnetic field ends up in a same cluster, since the opening angle of the e^+e^- pair is vary small and there is no magnetic field to bend them away from each other. As described in Sec. 3.2.2, the magnetic field is small at the radial range of $r > 2$ m from vertex, where most of the detector is mounted and most of the conversion e^+e^- pairs end up in a same cluster. The e^+e^- pair conserves the energy of primary photon and satisfies the identification cuts for photons. According to the single photon simulation for the sector W0 (10.1 % conversion probability), the 8.7 % of all photons are converted but e^+e^- (or e) end up in a cluster and deposit the energy of primary photon. The 1.4 % of all photons are converted and lost.

In addition to this effect, the difference of the detector response between photon and electron should be taken into account. Figure 5.42 shows the energy smearing function for photon ($1 < p_T < 1.5$ GeV/c) comparing with that for electron. The mean of the smearing function for electron clusters is small than that for photon clusters by a factor of ~ 3 %. Because of the steep falling of energy spectra and this difference, the part of electron-positron pairs from conversion is lost. Based upon the difference of unfolding correction between “conversion” and “non-conversion”, the effective loss due to this effect is estimated to be 5 %.

Off-Vertex Photon

The main source of off-vertex photon are decay photons which are secondary of long lived particles, and photons from secondary interactions. Off-vertex photons are estimated with HIJING simulation (Output 1 in Fig. 5.1). Figure 5.43 shows the spectrum of inclusive gammas and off-vertex gammas. As a result, the contribution of off-vertex gamma is estimated to be about 1 % above 1.5 GeV/c, and is included in the systematic error.

Bin-Shift Correction

Bin-shift correction ($c_{bin-shift}$ in Eq. 5.38) is applied as well as π^0 analysis.

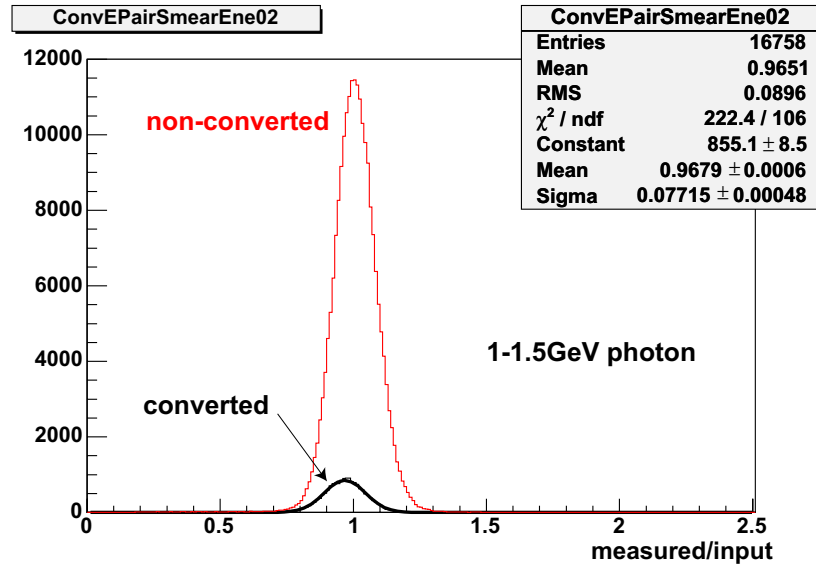


Figure 5.42: Smearing function of converted photons (red) and non-converted photons (black). The photon samples of $1 < p_T < 1.5$ GeV/c are picked up. The mean position of the smearing function for conversion clusters is small than that for non-converted photon clusters by a factor of $\sim 3\%$.

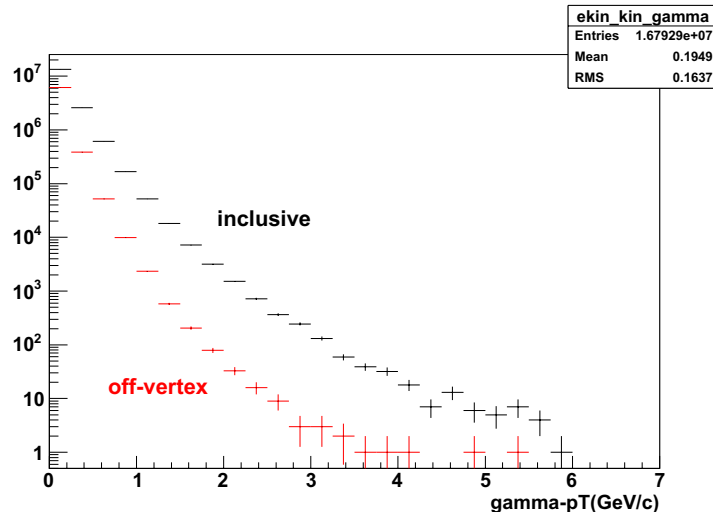


Figure 5.43: Spectrum of inclusive gamma and off-vertex gamma in minimum bias Au+Au collisions. Only gammas which hit EMCAL is filled.

5.6.2 Direct Photon Yields

In this section, the procedure to obtain direct photon excess ratio and spectra from inclusive photon spectra and π^0 spectra is described. While there are many components of the systematic error on inclusive photon and π^0 yield, many systematic errors cancel in the ratio of inclusive photon yield over neutral pion yield ($N_{\text{meas}}^\gamma(p_T)/N_{\text{meas}}^{\pi^0}(p_T)$). The cancellation affects:

- The error on the energy scale, which completely cancels if it is an overall scale factor
- The uncertainty in the efficiency calculation, which partially cancels as the single photon efficiency has a direct impact on the two-photon efficiency needed for the invariant mass analysis of the π^0
- The systematic error due to the conversion correction, which partially cancels for the same reason

Therefore, the expected yield of background photons originating from decays of hadrons ($N_{\text{bkgd}}^\gamma(p_T)$) divided by the fit function of π^0 s ($N_{\text{fit}}^{\pi^0}(p_T)$), which is used for the decay photon calculation, is compared to the measured ratio:

$$\frac{N_{\text{meas}}^\gamma(p_T)/N_{\text{meas}}^{\pi^0}(p_T)}{N_{\text{bkgd}}^\gamma(p_T)/N_{\text{fit}}^{\pi^0}(p_T)} = \frac{N_{\text{meas}}^\gamma(p_T)}{N_{\text{bkgd}}^\gamma(p_T)}. \quad (5.40)$$

This is equivalent to the direct comparison of measured photons to decay photons, since the measured π^0 spectrum and the input π^0 fit function for the decay photon calculation are identical, and cancel each other (i.e. $N_{\text{meas}}^{\pi^0}(p_T)/N_{\text{fit}}^{\pi^0}(p_T) \sim 1$). This assumed cancellation of the π^0 yield introduces a small systematic error of approximately 3 %, as it is only sensitive to variations of the shape of the spectrum, not to the overall normalization. The double ratio as defined in Eq. 5.40 is unity in the absence of direct photons, and the direct photon signal is seen as an excess above one.

In the case that an excess is observed, the invariant yield of direct photons is obtained after the subtraction of the background from decays of hadrons. This is also done using the double ratio defined in Eq. 5.40:

$$\frac{1}{2\pi p_T N_{\text{event}}} \frac{d^2 N_{\text{direct}}^\gamma}{dp_T dy} = \left(1 - \frac{N_{\text{bkgd}}^\gamma(p_T)/N_{\text{fit}}^{\pi^0}(p_T)}{N_{\text{meas}}^\gamma(p_T)/N_{\text{meas}}^{\pi^0}(p_T)} \right) \cdot \frac{1}{2\pi p_T N_{\text{event}}} \frac{d^2 N_{\text{meas}}^\gamma}{dp_T dy}. \quad (5.41)$$

For the calculation of direct photon invariant yield, the systematic errors, which are canceled out in the direct photon double ratio, does not cancel, and are taken into account.

Background from Decays of Hadrons

The estimation of background photons from hadrons is determined with the single hadron simulation as followings.

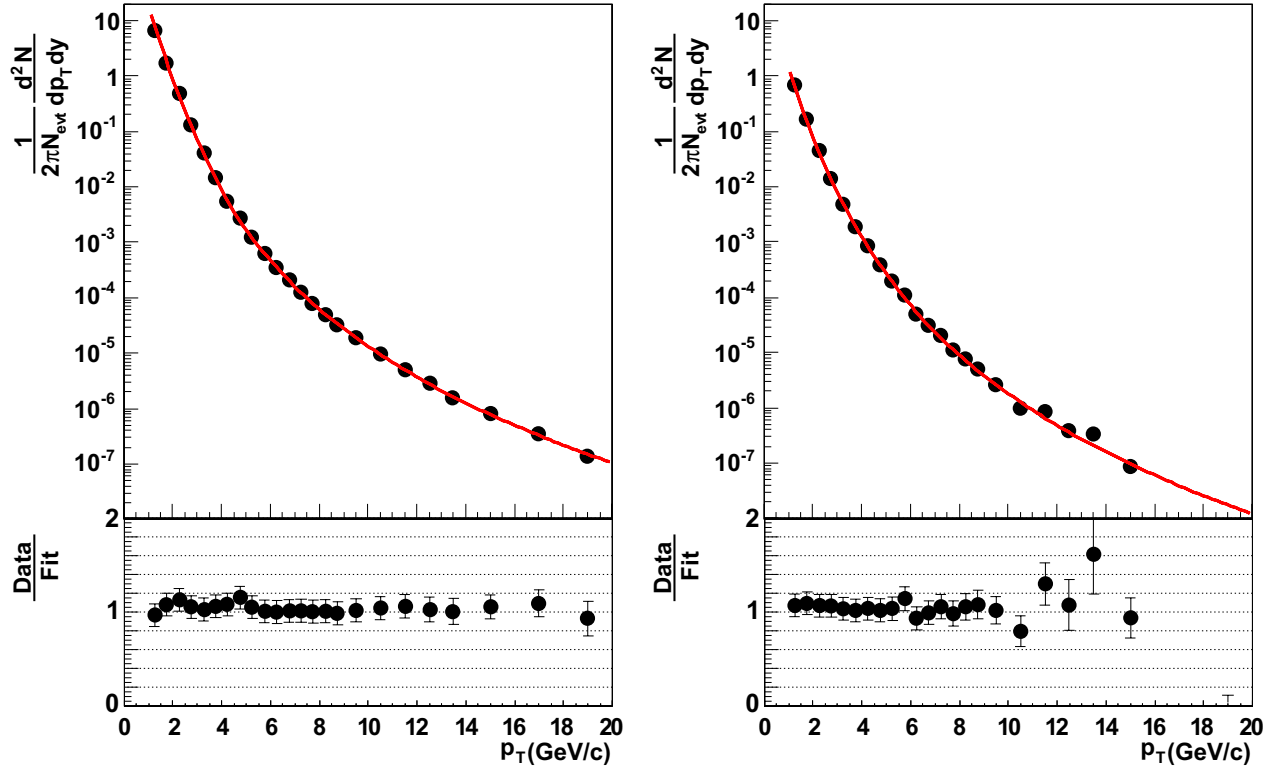


Figure 5.44: Parameterization of the π^0 measurement for two different centralities (Left: min. bias, Right: 60-70 %) and comparison with the data to the default fit Eq. 5.36.

- Hadron samples which makes photon backgrounds through its decay are generated (Output 3 in Fig. 5.1).
- The 2-dimensional map which shows the correlation between the p_T of decay photon from the hadron and the p_T of input hadron is made.
- Weight the input hadron p_T -axis of the map using the function of the input hadron spectrum.
- Project the 2-dimensional map to decay photon p_T -axis. The projected histogram is the invariant yield of decay photon.

The input spectrum to this simulation is the parameterization of the π^0 yield as measured within the same data sample used for the direct photon analysis. The parameterization of the yield is given by Eq. 5.36 and is fit to the result of the π^0 yield. The parameterization and the default fit are shown for two centralities in Fig. 5.44. They describe the data well.

The hadrons which are taken into account in the background estimation are summarized in Table 5.4. The decay of the π^0 is the largest contribution to the background for the direct photon measurement. It accounts for approximately 86 % of the total expected background as shown in Fig. 5.45, which shows the photon background yield divided by input π^0 yield estimated with Monte Carlo calculation of decays of hadrons in minimum bias events. The π^0 measurement includes not only directly produced π^0 s, but also those from decays of hadrons

with π^0 s in their final state. Thus it is not necessary to take into account photons produced in secondary π^0 decays, e.g. from $\eta \rightarrow 3\pi^0$ with a branching ratio of 32.51 %.

State	Mass (MeV)	R_{h/π^0}	Decay mode	Branching ratio
π^0	134.98	-	$\gamma\gamma$	98.798 %
			$e^+e^-\gamma$	1.198 %
η	547.8	0.45	$\gamma\gamma$	39.43 %
			$\pi^+\pi^-\gamma$	4.68 %
			$e^+e^-\gamma$	$6.0 \cdot 10^{-3}$
			$\pi^0\gamma\gamma$	$7.2 \cdot 10^{-4}$
			$\mu^+\mu^-\gamma$	$3.1 \cdot 10^{-4}$
ρ^0	769.0	1.0	$\pi^+\pi^-\gamma$	$9.9 \cdot 10^{-3}$
			$\pi^0\gamma$	$6.0 \cdot 10^{-4}$
			$\eta\gamma$	$3.0 \cdot 10^{-4}$
ω	782.6	1.0	$\pi^0\gamma$	8.92 %
			$\eta\gamma$	$4.9 \cdot 10^{-4}$
η'	957.8	1.0	$\rho^0\gamma$	29.5 %
			$\omega\gamma$	3.0 %
			$\gamma\gamma$	2.12 %
			$\mu^+\mu^-\gamma$	$1.0 \cdot 10^{-4}$
K_S^0	497.65	1.0	$\pi^0\pi^0$	31.05 %

Table 5.4: Dominant sources of background photons from decays of hadrons and the employed m_T scaling factors relative to the π^0 measurement R_{h/π^0} . The listed masses, decay branches, and branching ratios are taken from [237].

On the contrast to the π^0 measurement, the other heavier hadrons are not measured. Then, the m_T scaled function ($p_T \rightarrow \sqrt{p_T^2 - m_{\pi^0}^2 + m_{hadron}^2}$) to π^0 spectrum is employed to produce a spectrum of hadrons and to estimate the back ground photons from other sources. For the scaling, the normalization factor R_{h/π^0} in Tab. 5.4 is applied to the spectra.

The second most important contribution to the decay background after the π^0 is formed by the two photon decay of the η meson ($\eta \rightarrow \gamma\gamma$). The η production has been measured in the PHENIX experiment for various colliding systems. The η yield was found to obey the m_T scaling well with a relative scaling factor of ~ 0.45 [34], which is consistent with the world average of the η yield to π^0 yield ratio.

The K_S^0 has no significant decay with photons in the final state. However, due to its relatively long lifetime of $\tau = 0.9 \cdot 10^{-10}$ s and the relativistic time delay, it may decay far from the collision vertex, and the π^0 s originating from $K_S^0 \rightarrow \pi^0\pi^0$ may not be reconstructed in the invariant mass analysis. To estimate the maximum contribution due to this effect, the secondary decay photons are included in the background calculation. As for all other hadrons m_T scaling is assumed for the K_S^0 . The scaling factor can be inferred from the ratio of identified charged pions to kaons as measured by the PHENIX experiment [29]. It is only known up to p_T

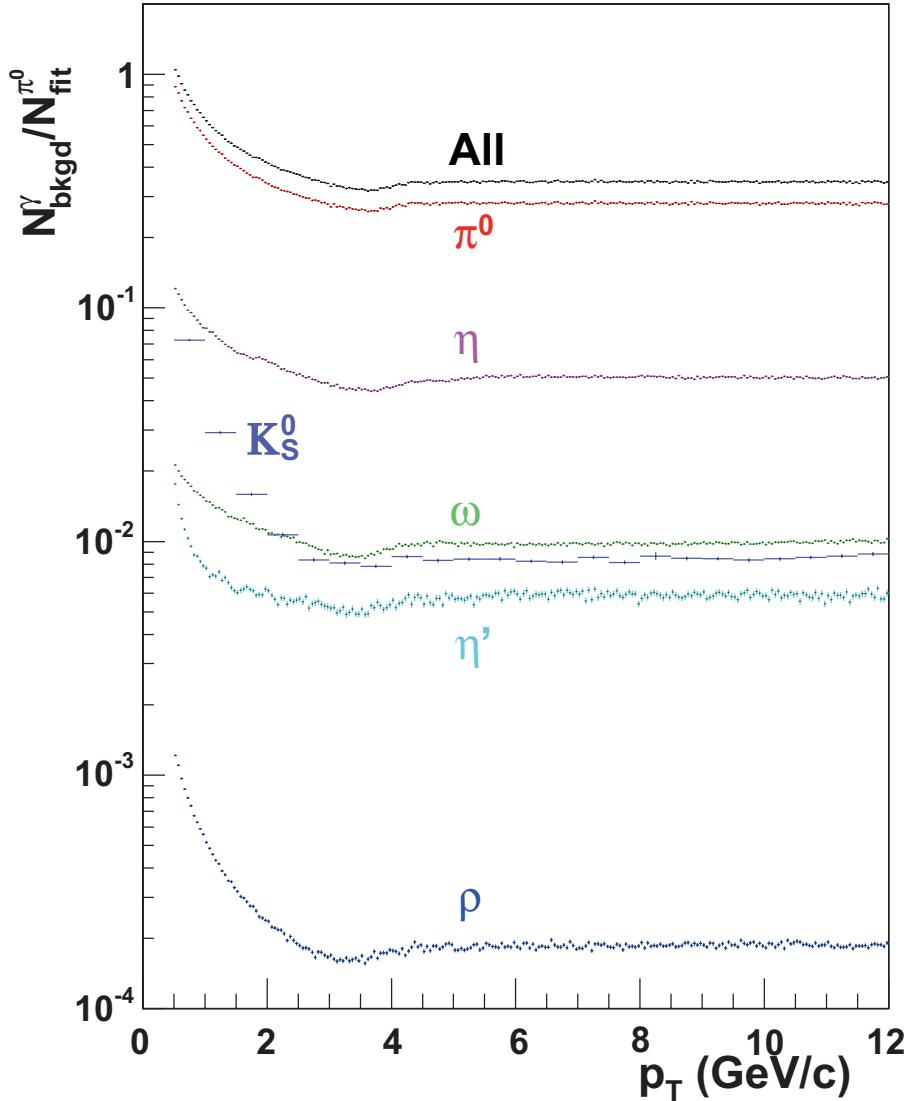


Figure 5.45: Photon background yield from decays of hadrons divided by input π^0 yield in minimum bias events. The secondary decay photons from $K_S^0 \rightarrow \pi^0\pi^0$ are fully included.

$= 2$ GeV/ c and depends strongly on centrality with a value of 0.7 (central) ~ 0.45 (peripheral). A scaling factor of one as an upper limit is taken for the limitation of the photons from K_S^0 . The left panel of Fig. 5.46 shows the raw spectra of secondary decay photons from K_S^0 comparing with that of photons from all π^0 decay. The ratio of each spectrum is shown on right panel of Fig. 5.46, and which shows the plateau at $p_T > 2.5$ GeV/ c . The contribution from K_S^0 is shown on Fig. 5.45, and the contribution is quite negligible rather than that from other sources (π^0 and η).

The relative scaling factor for the contribution from the hadrons $,\rho^0$, ω , η' , and K_S^0 , are set to be one. At RHIC, the ρ^0 is measured by STAR experiment [10], and the ω and K_S^0 is measured by PHENIX experiment [162, 184] via the hadron decay channel. The *hadron/* π^0 ratio is consistent with one or smaller. As a result of the estimation of the background photons from the such hadrons, the contribution is expected to be negligible ($\sim 1\%$) compared with

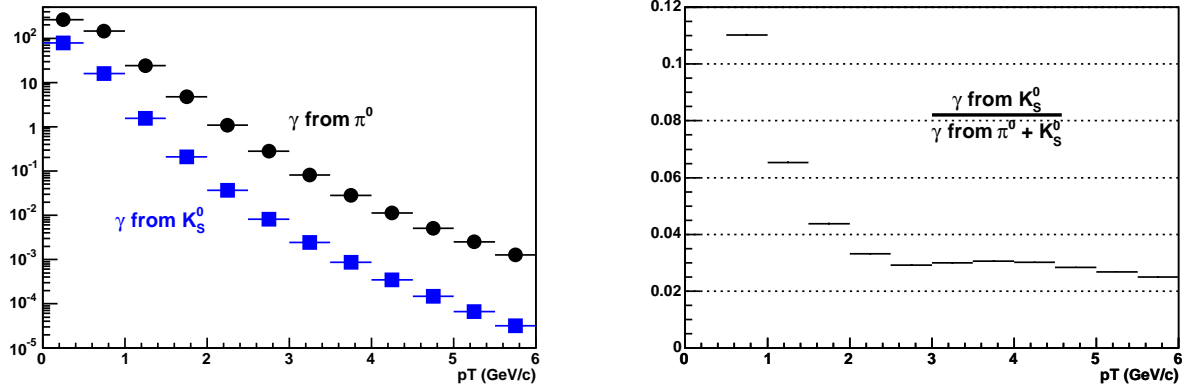


Figure 5.46: The estimation of background photon from K_S^0 decay. Left figure shows photon spectra from K_S^0 decay comparing with that from π^0 . Right figure shows the fraction of photon from K_S^0 comparing with that from π^0 .

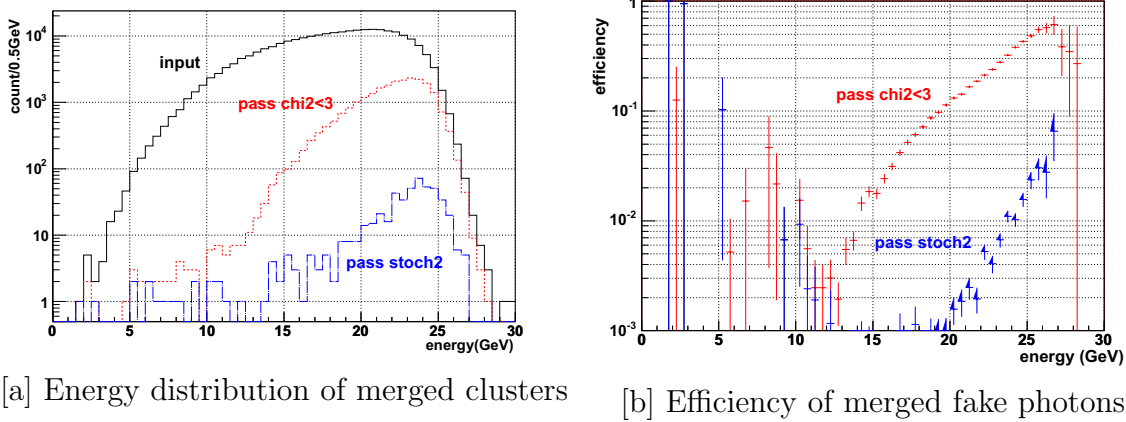
the background from π^0 and η . Then the upper limit of the contribution is included in the systematic error.

π^0 Merging Effect on Background Photons

One of the most crucial investigation needed to get direct photon yield up to 20 GeV/c is that for the π^0 merging effect. As described at Sec. 5.5.2, parts of $\gamma\gamma$ pairs from high- p_T π^0 s are clusterized as one cluster due to the finite tower size.

For getting direct photon spectra, background photon coming from decay background of hadrons is estimated using Monte Carlo calculation. At the high- p_T region of above 15 GeV/c, part of 2-clusters coming from π^0 s are detected as 1-clusters and this effect should be taken into account. Actually, it is hard to separate merged cluster with any algorithm and such algorithm will make additional effect, such as bias of energy scale. Then, the effect is taken into account during the background calculation, while corrected inclusive photon spectra can not be obtained directly.

For the calculation of $N_{\text{bkgd}}^{\gamma}(p_T)/N_{\text{fit}}^{\pi^0}(p_T)$, the same merging probability which is obtained from single π^0 simulation, described at Sec. 5.5.2, is used for every centrality condition, and the centrality dependence of merging correction is added to systematic uncertainty. In addition to the cluster merging effect due to the small opening angle of high- p_T π^0 , it should be taken into account that merged cluster could be thrown away by the cut for photon identification. Because the shower shape of a merged cluster is quite different from that of electromagnetic cluster, the merged cluster is likely to fail the shower shape cuts, such as $\chi^2 < 3$ cut and Stochastic cuts. Using simulated high- p_T single π^0 s which are used for the parameterization of π^0 merging probability, rejection power of shower shape cut for merging cluster are estimated. Figure 5.47 shows the simulation result of the efficiency of merged cluster. The [a] of Fig. 5.47 shows the energy distribution of merged clusters comparing with the energy distribution of merged clusters which pass the each shower shape cut. While the p_T distribution of input π^0



[a] Energy distribution of merged clusters

[b] Efficiency of merged fake photons

Figure 5.47: Survival ratio of the cluster where two photons from a π^0 end up in a same cluster, Figure [a]: black line shows the input distribution of merged cluster as a function of energy of measured cluster. And “ $\chi^2 < 3$ ” cut(red) or “Stochastic cut 2”(blue) cut are applied for the merged clusters. The strong rejection of merged clusters are shown. Figure[b]: efficiency of merged cluster as a function of measured energy (red:” $\chi^2 < 3$ ”, blue:”Stochastic cut 2”).

is flat from $p_T = 0$ GeV/c to $p_T = 25$ GeV/c, there are small samples at low-energy region since two photons from a π^0 do not end up in a same cluster. The [b] of Fig. 5.47 shows the efficiency of merged clusters. Most of the merged clusters are rejected if the cut of “ $\chi^2 < 3$ ” is applied. Even 15 GeV/c merged cluster is rejected with a rejection power of about 50. If Stochastic cut 2 is applied, merged clusters are almost rejected up to 20 GeV/c.

The probability of merged cluster which pass “ $\chi^2 < 3$ ” cut , (π^0 where 2 secondary γ s are merged as one cluster and the cluster pass cut)/(all π^0), is evaluated as a function of $\pi^0 p_T$ as shown in Fig. 5.48.

$N_{\text{bkgd}}^\gamma(p_T)/N_{\text{fit}}^{\pi^0}(p_T)$ is estimated with the Monte Carlo calculation which is for the decays of hadrons described before. The merging effect is also taken into account in the Monte Carlo calculation. The π^0 merging probability and rejection power of the merging cluster using shower shape cut is obtained as a function $\pi^0 p_T$ and energy asymmetry from the previous study (shown in Fig. 5.26). In the Monte Carlo calculation, the events are divided into the following cases:

Case 1: Two clusters are observed separately. (Both two clusters are counted in background yield.)

Case 2: Two clusters merge and the cut ($\chi^2 < 3$) accept them as single photons. (Merge cluster ($p_T = p_T(1) + p_T(2)$) is counted in background yield.)

Case 3: Two clusters merge but the shower shape cut ($\chi^2 < 3$ or Stochastic cut) doesn't accept them as single photons. (No cluster is accepted.)

Figure 5.49 shows $N_{\text{bkgd}}^\gamma(p_T)/N_{\text{fit}}^{\pi^0}(p_T)$ obtained with the Monte Carlo calculation. Shower shape cut can throw out the most of merged clusters. $N_{\text{bkgd}}^\gamma(p_T)/N_{\text{fit}}^{\pi^0}(p_T)$ decreases as p_T goes

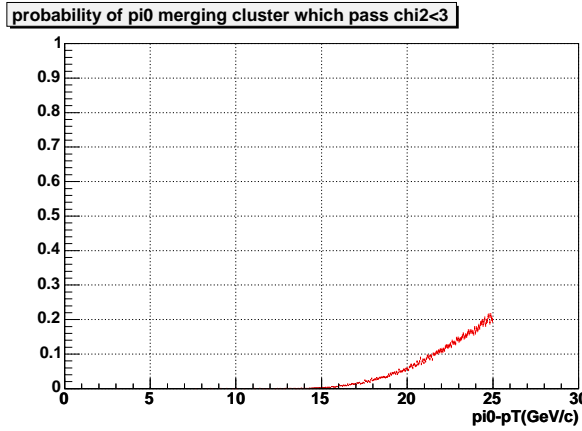


Figure 5.48: the probability of merged cluster which pass $\chi^2 < 3$ cut is evaluated as a function of $\pi^0 p_T$.

to higher- p_T when shower shape cut is applied. If the two cluster can be separated completely, $N_{\text{bkgd}}^\gamma(p_T)/N_{\text{fit}}^{\pi^0}(p_T)$ is flat at $p_T > 5 \text{ GeV}/c$.

While the direct photon spectra are obtained using Eq. 5.41, additional correction is needed in order to obtain direct photon excess ratio which does not depend on detector environment. To simplify the explanation, the photon yield coming from each sources are categorized as in Tab. 5.5. The difference between $N_{\text{meas}}^\gamma(p_T)$ and $N_{\text{incl}}^\gamma(p_T)$ is whether the correction for the merging effect is applied or not. Then, $N_{\text{meas}}^\gamma(p_T)$ and $N_{\text{incl}}^\gamma(p_T)$ are identical at medium- p_T region. There is same difference between $N_{\text{bkgd}}^\gamma(p_T)$ and $N_{\text{corr-bkgd}}^\gamma(p_T)$.

$N_{\text{direct}}^\gamma(p_T)$	Direct photon yield.
$N_{\text{meas}}^\gamma(p_T)$	Measured inclusive photon yield given by Eq. 5.39, where correction for π^0 merging effect is not applied.
$N_{\text{bkgd}}^\gamma(p_T)$	Background photon yield estimated with the Monte Carlo calculation which takes merging effect into account (Red or Blue curve in Fig. 5.49).
$N_{\text{incl}}^\gamma(p_T)$	Correct inclusive photon yield.
$N_{\text{corr-bkgd}}^\gamma(p_T)$	Correct background photon yield (Black curve in Fig. 5.49).

Table 5.5: The photon yield coming from each sources.

The relations between the $N^\gamma(p_T)$ s in Tab. 5.5 are:

$$N_{\text{meas}}^\gamma(p_T) = N_{\text{direct}}^\gamma(p_T) + N_{\text{bkgd}}^\gamma(p_T), \quad (5.42)$$

$$N_{\text{incl}}^\gamma(p_T) = N_{\text{direct}}^\gamma(p_T) + N_{\text{corr-bkgd}}^\gamma(p_T). \quad (5.43)$$

Then, the correct direct photon excess ratio is obtained as:

$$\frac{N_{\text{incl}}^\gamma(p_T)}{N_{\text{corr-bkgd}}^\gamma(p_T)} = \frac{N_{\text{direct}}^\gamma(p_T)}{N_{\text{corr-bkgd}}^\gamma(p_T)} + 1 \quad (5.44)$$

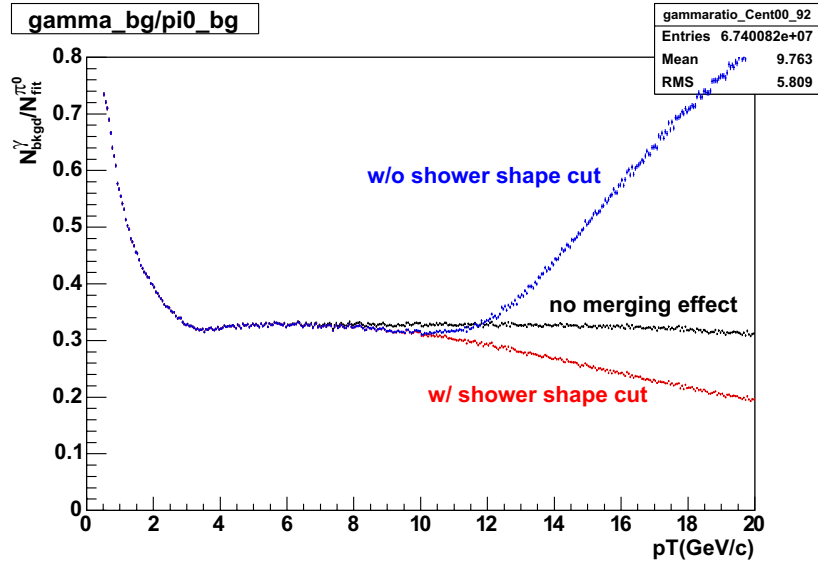


Figure 5.49: $N_{\text{bkgd}}^\gamma(p_T)/N_{\text{fit}}^{\pi^0}(p_T)$ obtained with Monte Carlo which takes merging effect into account for each assumption. Black: assume EMCAL granularity is perfect and any 2 gamma can be detected separately. Red: using actual EMCAL and merged clusters are rejected with shower shape cut. Blue: using actual EMCAL and shower shape cut is not applied, merged clusters are taken into the spectra.

$$= \frac{N_{\text{meas}}^\gamma(p_T) - N_{\text{bkgd}}^\gamma(p_T)}{N_{\text{corr-bkgd}}^\gamma(p_T)} + 1 \quad (5.45)$$

$$= \frac{N_{\text{bkgd}}^\gamma(p_T)}{N_{\text{corr-bkgd}}^\gamma(p_T)} \left(\frac{N_{\text{meas}}^\gamma(p_T)}{N_{\text{bkgd}}^\gamma(p_T)} - 1 \right) + 1. \quad (5.46)$$

The correction factor of $N_{\text{bkgd}}^\gamma(p_T)/N_{\text{corr-bkgd}}^\gamma(p_T)$ is estimated with the result of Monte Carlo simulation shown in Fig. 5.49.

$N_{\text{meas}}^\gamma(p_T)/N_{\text{meas}}^{\pi^0}(p_T)$ and Direct photon Excess Ratio

Figure 5.50 and 5.51 show the $N_{\text{meas}}^\gamma(p_T)/N_{\text{meas}}^{\pi^0}(p_T)$ comparing with $N_{\text{bkgd}}^\gamma(p_T)/N_{\text{fit}}^{\pi^0}(p_T)$ using $\chi^2 < 3$ cut and Stochastic cut 2, respectively. Due to the π^0 merging effect, systematic reduction of γ background is seen. The $N_{\text{meas}}^\gamma(p_T)/N_{\text{meas}}^{\pi^0}(p_T)$ is larger for central events, while $N_{\text{bkgd}}^\gamma(p_T)/N_{\text{fit}}^{\pi^0}(p_T)$ is similar for all centrality.

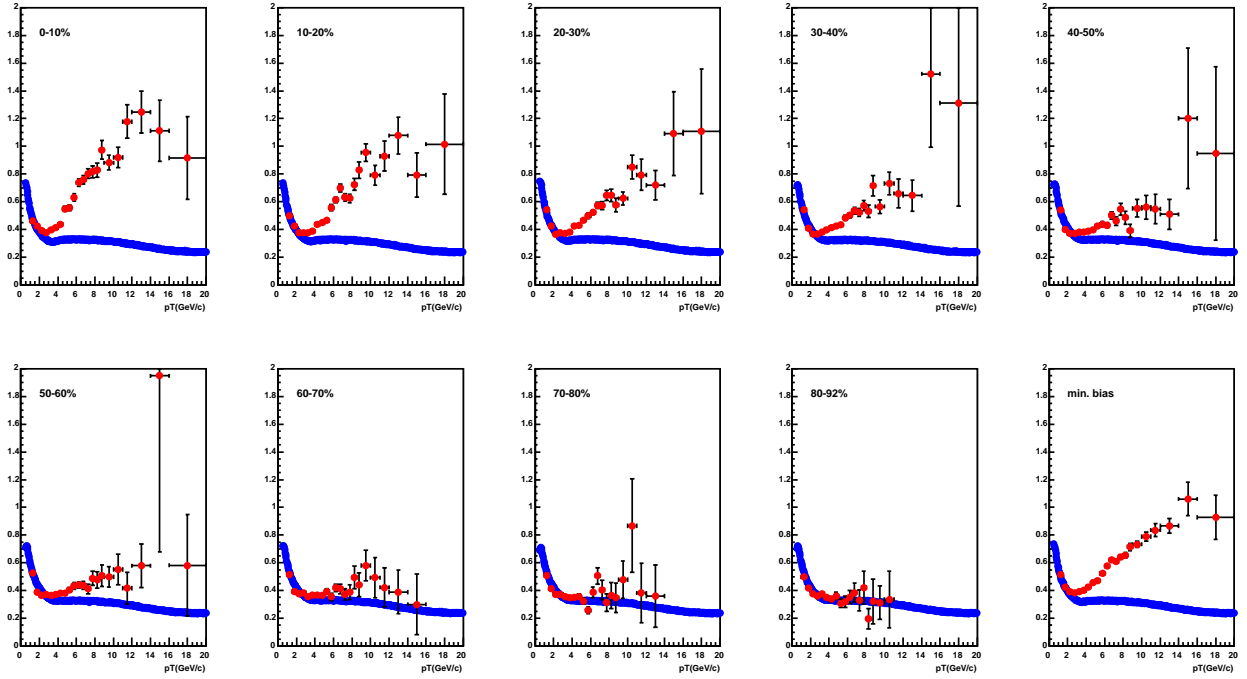


Figure 5.50: $N_{\text{meas}}^{\gamma}(p_T)/N_{\text{meas}}^{\pi^0}(p_T)$ (red) comparing with $N_{\text{bkgd}}^{\gamma}(p_T)/N_{\text{fit}}^{\pi^0}(p_T)$ (blue) in the case of $\chi^2 < 3$ cut.

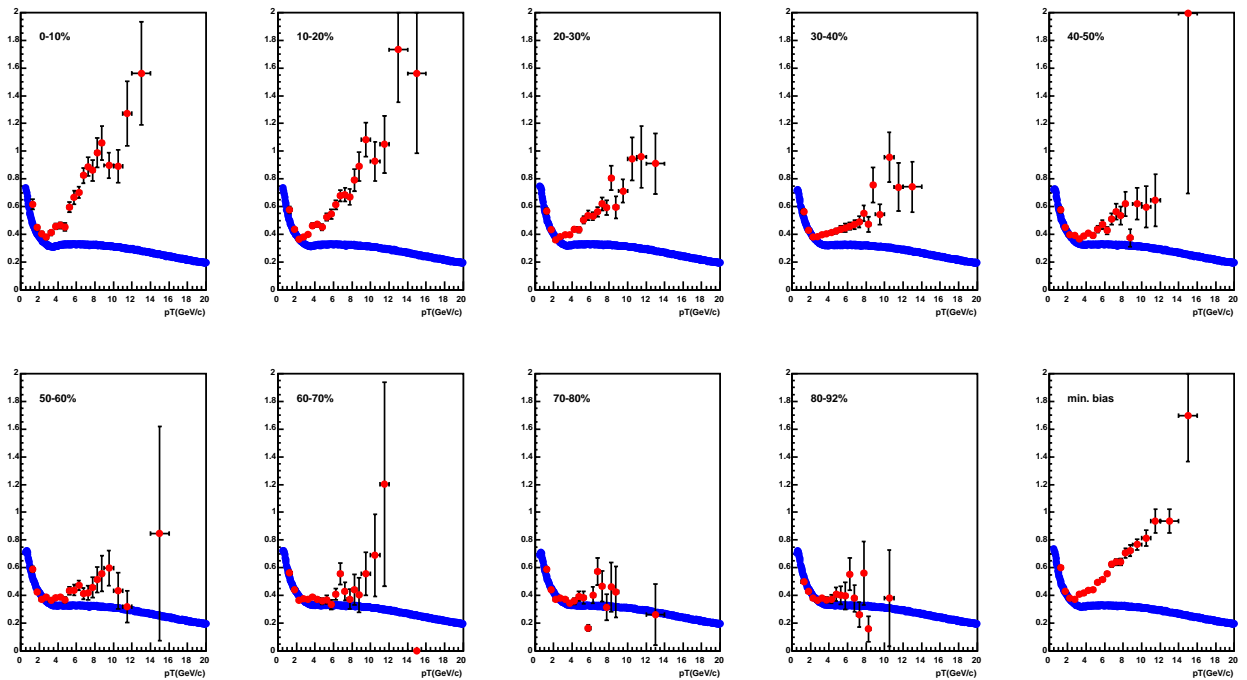


Figure 5.51: $N_{\text{meas}}^{\gamma}(p_T)/N_{\text{meas}}^{\pi^0}(p_T)$ (red) comparing with $N_{\text{bkgd}}^{\gamma}(p_T)/N_{\text{fit}}^{\pi^0}(p_T)$ (blue) in the case of Stochastic cut 2.

5.6.3 Systematic Errors on Direct Photon Measurement

The various sources of systematic errors are described in this sections. All errors are taken as 1σ errors. The systematic errors on inclusive photon yield, direct photon excess ratio, and direct photon invariant yield are, respectively, summarized in Tab. 5.6, Tab. 5.7, and in Tab. 5.8, which are characterized as well as the error on π^0 measurement which is described in section 5.5.3. And the p_T dependence of each errors are shown in Appendix G.2, and Appendix G.3.

	p_T indep.	2 GeV/c	6 GeV/c	10 GeV/c	type
energy scale	1.5 %	6.5 %	9 %	9 %	B
hadron contamination		7 %	6 %	3 %	B
off-vertex		2 %	2 %	2 %	B
Conv. corr.					C
γ unfolding		8.7 %	6.1 %	6 %	B
Total		13 %	13 %	11 %	

Table 5.6: Systematic errors on the inclusive photon invariant yields. The error sum for a given p_T column is the quadratic sum of the p_T -dependent errors given in that column and the p_T -independent errors.

	p_T indep.	2 GeV/c	6 GeV/c	12 GeV/c	18 GeV/c	type
peak extraction	6 %					A
energy scale		3 %	3 %	3 %	3 %	B
off-vertex		2 %	2 %	2 %	2 %	B
hadron contamination		7 %	6 %	3 %	3 %	B
γ unfolding		9 %	6.2 %	5 %	5 %	B
N^η/N^{π^0}	2 %					C
merging corr.		0 %	0 %	20 %	22 %	B
$N_{\text{bkgd}}^\gamma/N_{\text{meas}}^{\pi^0}$ fit		4 %				A
Conv. corr.	1.5 %					C
Total		14%	12%	22%	24 %	

Table 5.7: Systematic errors on the direct photon excess double ratio. The error sum for a given p_T column is the quadratic sum of the p_T -dependent errors given in that column and the p_T -independent errors.

As described before, the part of the systematic error on the direct photon excess ratio is canceled out. The energy scale uncertainty is estimated based on the π^0 peak position and to be 3 % on the excess ratio. The following sections describe in some detail how the errors were estimated.

	Central Events		Peripheral Events		type
	6 GeV/c	12 GeV/c	6 GeV/c	12 GeV/c	
peak extraction	4.6 %	1.7 %	30.0 %	10.0 %	A
energy scale	16.1 %	11.5 %	54.0 %	24.0 %	B
off-vertex	3.8 %	2.6 %	10.0 %	3.3 %	B
hadron contamination	10.4 %	3.9 %	35.4 %	8.0 %	B
γ unfolding	11.0 %	6.4 %	37.1 %	13.3 %	B
N^η/N^{π^0}	1.5 %	0.6 %	10.0 %	3.3 %	C
merging corr.	0.7 %	5.6 %	4.5 %	33.3 %	B
$N_{\text{bkgd}}^\gamma/N_{\text{meas}}^{\pi^0}$ fit	3.0 %	1.1 %	20.0 %	2.9 %	A
Conv. corr.	2.9 %	2.0 %	9.0 %	4.0 %	C
Total	23.3 %	15.3 %	84.5 %	45.5 %	

Table 5.8: Systematic errors on the direct photon yield. The error sum for a given p_T column is the quadratic sum of the p_T -dependent errors given in that column and the p_T -independent errors.

Correction for Hadron Contamination

The hadron contamination is estimated with GEANT simulation and the detector response code. The results depend on how well hadrons are described by the simulation: both their overall energy deposit and the shape of hadron shower. For low- p_T region, the hadron contamination is quite large as shown in Fig. 5.37. The related error is estimated by comparing fully corrected inclusive photon spectra, calculated with different particle identification criteria. Figure 5.52 shows the ratio of fully corrected inclusive photon spectra, measured with different criteria. The error is relatively small at high- p_T because the hadron contribution is dominant at low- p_T region (around MIP). And there is large deviation between No particle identification and other particle identifications at $p_T = 0 - 3 \text{ GeV}/c$, which means that the hadron contamination is not fully reproduced with GEANT simulation. The systematic error of 8 – 3 % is assigned.

Correction for π^0 Merging Effect

The systematic error is propagated from the error on π^0 invariant yield.

As one of the methods for the estimation of systematic error, a systematic check of high- p_T direct photons using different particle identification cuts is done. The idea is coming from the large discrepancy between the $N_{\text{bkgd}}^\gamma(p_T)/N_{\text{fit}}^{\pi^0}(p_T)$ with shower shape cut and that without shower shape cut (No particle ID). As we described before, the shower shape cut throw away the π^0 merging clusters because of the non-standard shower shape of merged clusters. Then, the background gamma yield measured with shower shape cut is smaller than the yield that we expect. As shown in Fig. 5.49, the $N_{\text{bkgd}}^\gamma(p_T)/N_{\text{fit}}^{\pi^0}(p_T)$ is quite different systematics in the case of no particle identification. This property can be used for the systematic check of direct photon analysis for the high- p_T region where merging effect is crucial.

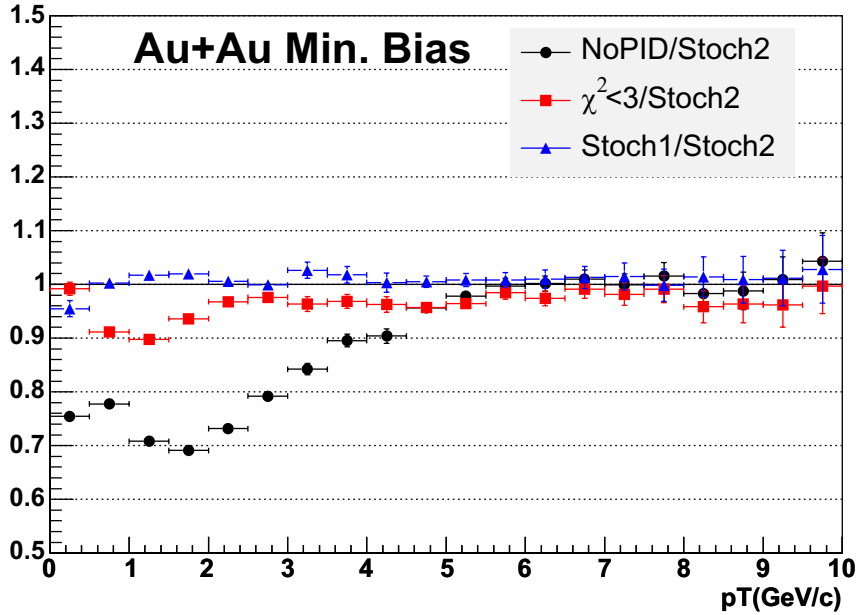
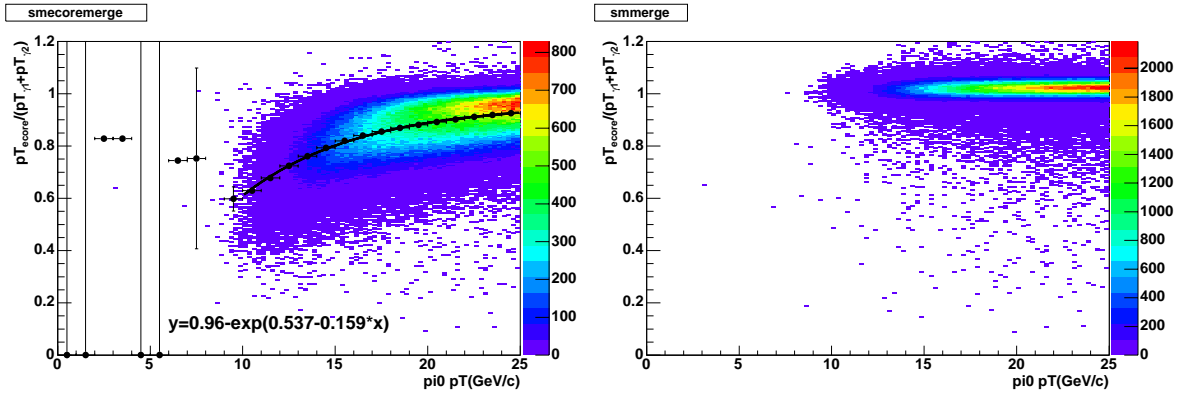


Figure 5.52: Ratio of fully corrected inclusive photon spectra, measured with different criteria to Stochastic cut 2 in min. bias events

One of the main problems to measure high- p_T direct photon without particle identification cut is energy smearing of merged clusters due to the “ E_{core} ” algorithm. For the calculation of E_{core} , the detected cluster is assumed to be a single electromagnetic cluster. During the calculation of E_{core} , the energy deposited in surrounding towers are get rid of and a correction on the energy is applied. The correction makes the energy smaller than input energy in the case of merged cluster. The predicted energy in Eq. 5.13 is estimated based upon the energy which is deposited in center tower. In the case of merged cluster, the center position is not reconstructed properly and it will exclude the towers where non-negligible energy is deposited. The energy correction does not take the exclusion into account, and tends to be smaller. The left panel in Fig. 5.53 shows the correlation between the smeared energy and $\pi^0 p_T$. As going to the higher- p_T , the shape of merged clusters is getting close to the single electromagnetic clusters, and the smearing function is getting close to one.

In order to measure the inclusive photon spectra without shower shape cut, original energy is used for the analysis in spite of E_{core} . Original energy is not corrected and not smeared due to the algorithm although signal-to-noise ratio is worse than E_{core} . The hadron contamination and energy smearing are calculated for original energy with same procedure as described in previous sections. Figure 5.54 shows $N_{\text{meas}}^\gamma(p_T)/N_{\text{meas}}^{\pi^0}(p_T)$ comparing with $N_{\text{bkgd}}^\gamma(p_T)/N_{\text{fit}}^{\pi^0}(p_T)$ ratio for each cut condition ($\chi^2 < 3$ and No particle ID). The increasing of both $N_{\text{meas}}^\gamma(p_T)/N_{\text{meas}}^{\pi^0}(p_T)$ and $N_{\text{bkgd}}^\gamma(p_T)/N_{\text{fit}}^{\pi^0}(p_T)$ can be seen when shower shape cut is not applied. Figure 5.55 shows direct photon excess double ratio for each particle identification (No particle identification, $\chi^2 < 3$ and Stochastic cut 2). The results are used for the estimation of systematic error ($\sim 22\%$ at high- p_T).



[a] $p_T(E_{core})$ against with merged $p_T(\pi^0)$ [b] $p_T(E)$ against with merged $p_T(\pi^0)$.

Figure 5.53: correlation of energy smearing of merged π^0 clusters and input $p_T(\pi^0)$.

[a] in the case of measurement with E_{core} . [b] in the case of measurement with original energy.

Conversion Correction

The mean material budget in front of PbSc EMCAL is 11.6 % X_0 [118]. The gamma conversion probability is obtained from [128]

$$P_{\text{conv}} = 1 - \exp\left(-\frac{7}{9}X_0(\%)\right) = 8.6(\%), \quad (5.47)$$

which is smaller than the probability estimated based on GEANT full simulation (tabulated in Tab. 5.3) by a factor of 1.5 %. It corresponds to the deviation on π^0 yield by a factor of 3 %, which is obtained from $1 - (1 - \Delta P_{\text{conv}})^2$.

Also, the uncertainty of the effective conversion correction is estimated to be $\sim 1\%$ with varying the following parameters:

- energy smearing (2 – 5 %)
- function for weighting the spectrum

$N^\eta(p_T)/N^{\pi^0}(p_T)$ Ratio

The $N_{\text{bkgd}}^\gamma(p_T)/N_{\text{fit}}^{\pi^0}(p_T)$ is calculated based upon the measured π^0 invariant yield and other hadron sources, such as η , ω and K_S^0 , which are reproduced with m_T scaling. The uncertainty from the reproduction with m_T scaling is estimated based on the $N^\eta(p_T)/N^{\pi^0}(p_T)$ ratio. Figure. 5.56 shows the shows $N^\eta(p_T)/N^{\pi^0}(p_T)$ ratio in p+p, d+Au, and Au+Au minimum bias and three centrality classes (0 – 20 %, 20 – 60 %, 60 – 92 %). Both the empirical m_T scaling and the PYTHIA calculation can reproduce the data within the error.

Based on the uncertainty on the asymptotic R_{h/π^0} ratio, the uncertainty on the $N_{\text{bkgd}}^\gamma(p_T)/N_{\text{fit}}^{\pi^0}(p_T)$ is estimated to be 2 %.

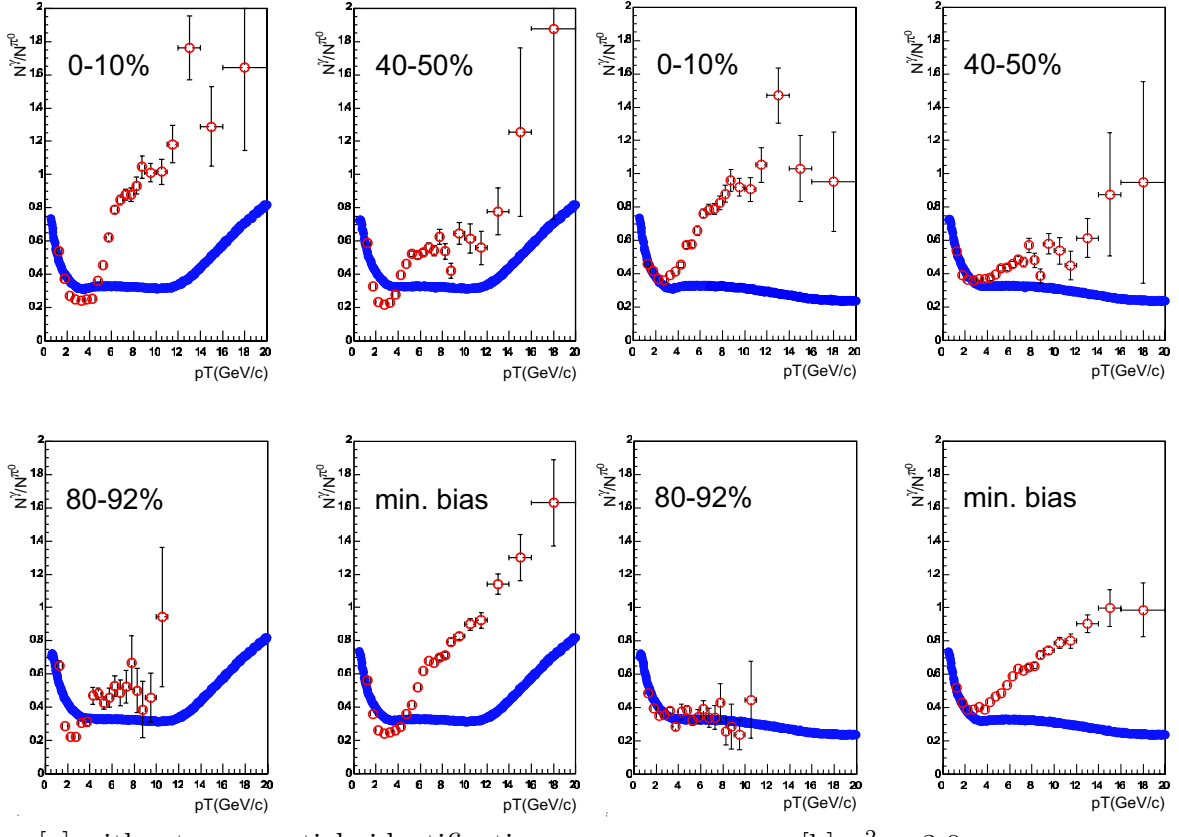


Figure 5.54: $N_{\text{meas}}^{\gamma}(p_T)/N_{\text{meas}}^{\pi^0}(p_T)$ (red open circle) comparing with $N_{\text{bkgd}}^{\gamma}(p_T)/N_{\text{fit}}^{\pi^0}(p_T)$ (blue closed circle) without shower shape cut [a] and with shower shape cut [b]

Error Propagation to Direct Photon Spectrum

Direct photon yield can be obtained as described in Eq. 5.41. The error on direct photon yield should be propagated from each components properly.

To simplify the calculation, $R(p_T)$ is defined as the direct photon excess ratio in Eq. 5.40: “ $(N_{\text{meas}}^\gamma(p_T)/N_{\text{meas}}^{\pi^0}(p_T))/(N_{\text{bkgd}}^\gamma(p_T)/N_{\text{fit}}^{\pi^0}(p_T)) = N_{\text{meas}}^\gamma(p_T)/N_{\text{bkgd}}^\gamma(p_T)$ ”. Then, direct photon yield, $N_{\text{direct}}^\gamma(p_T)$, can be obtained as:

$$N_{\text{direct}}^{\gamma}(p_{\text{T}}) = N_{\text{meas}}^{\gamma}(p_{\text{T}}) \cdot \left(1 - \frac{1}{R(p_{\text{T}})}\right) \quad (5.48)$$

When the error components are factorized as “ $N_{\text{meas}}^\gamma(p_T)$ ” and “ $N_{\text{bkgd}}^\gamma(p_T)$ ”, the error on direct photon invariant yield can be propagated as following:

$$(\delta N_{\text{direct}}^\gamma(p_T))^2 = (\delta N_{\text{meas}}^\gamma(p_T))^2 \left(\frac{\partial N_{\text{direct}}^\gamma(p_T)}{\partial N_{\text{meas}}^\gamma(p_T)} \right)^2 + (\delta N_{\text{bkgd}}^\gamma(p_T))^2 \left(\frac{\partial N_{\text{direct}}^\gamma(p_T)}{\partial N_{\text{bkgd}}^\gamma(p_T)} \right)^2 \quad (5.49)$$

$$= (\delta N_{\text{meas}}^\gamma(p_T))^2 + (\delta N_{\text{bkgd}}^\gamma(p_T))^2. \quad (5.50)$$

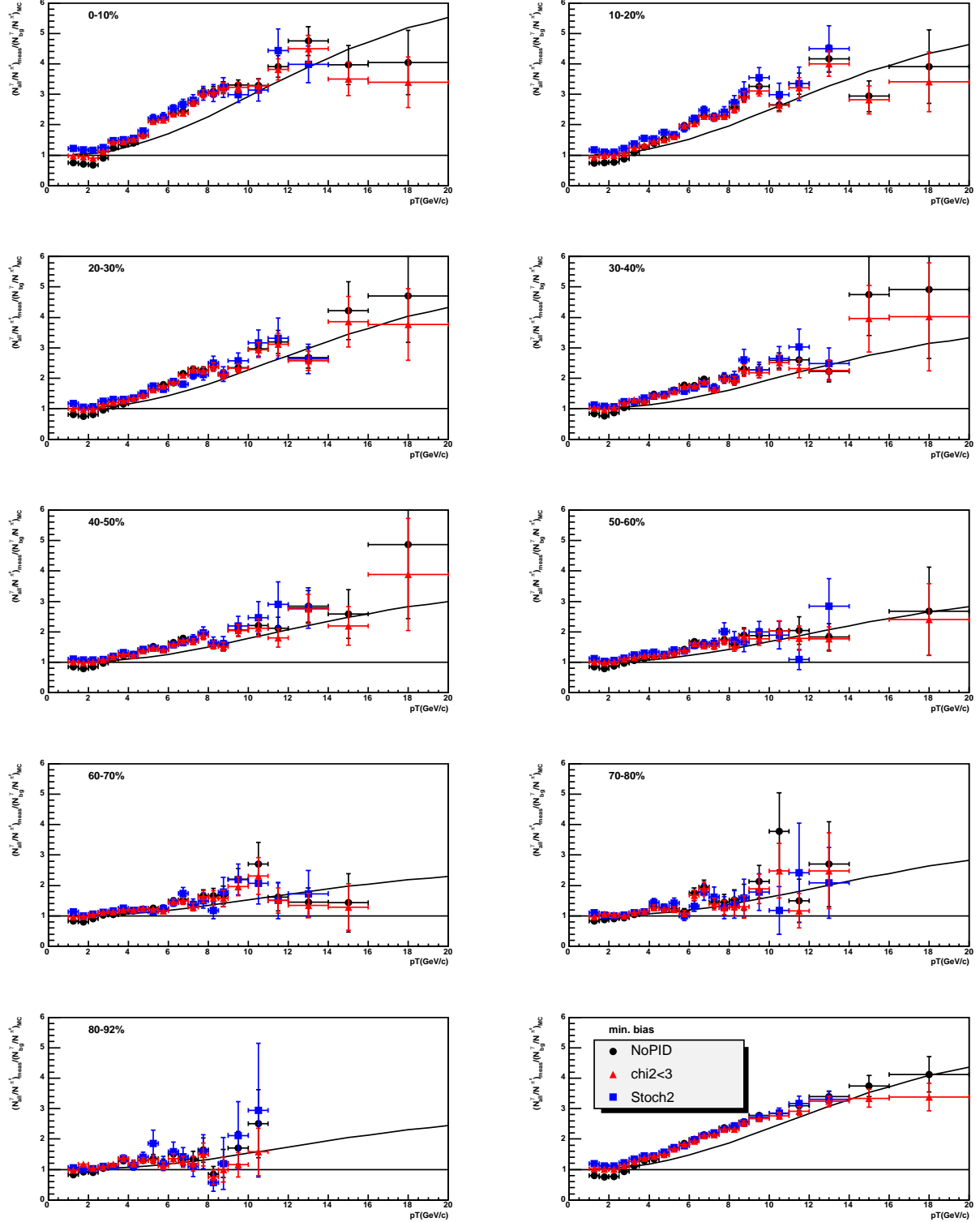


Figure 5.55: Direct photon excess ratio for each particle identification and centrality. Only statistic errors are shown. The ratio obtained without any particle identification is consistent with others within the statistic error. The expected curves which takes only pQCD contribution into account are shown.

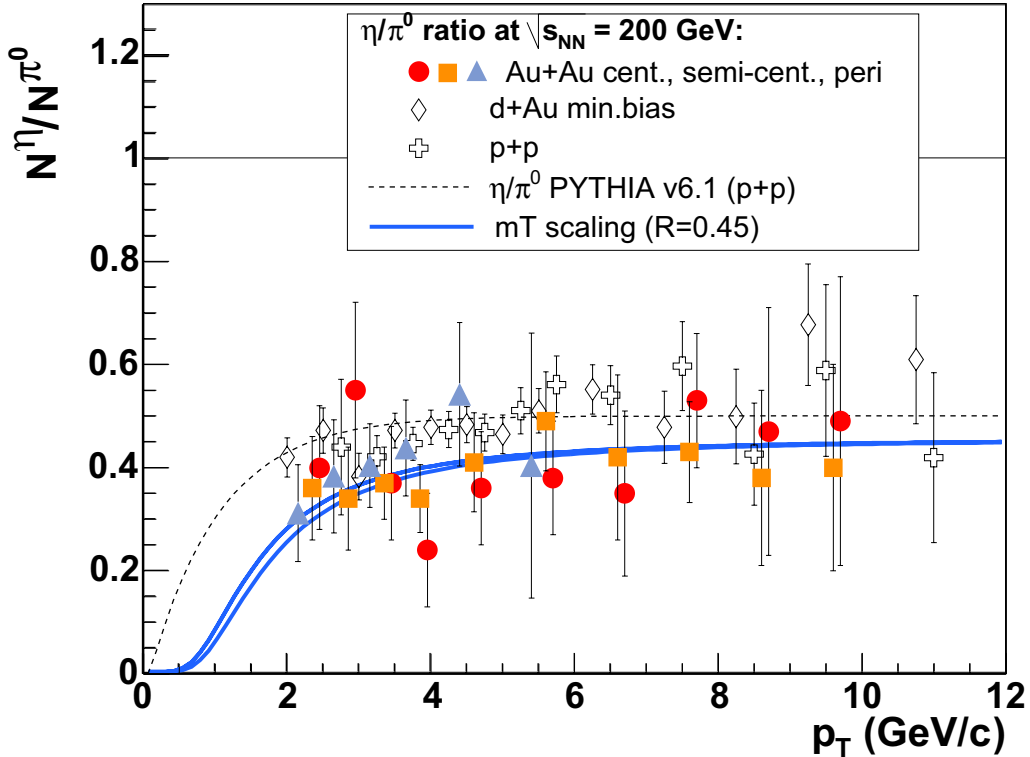


Figure 5.56: $N^\eta(p_T)/N^{\pi^0}(p_T)$ ratio in p+p, d+Au, and Au+Au minimum bias and three centrality classes (0 – 20 %, 20 – 60 %, 60 – 92 %). The error bars include all point-to-point errors. The dashed line is the prediction of PYTHIA [201] for p+p at this \sqrt{s} energy. The area between two blue solid lines indicates the empirical m_T -scaling prescription with power-law exponent $n = 10. - 14.$ ($\sigma \propto p_T^{-n}$), and an asymptotic $R_{h/\pi^0} = 0.45$ ratio. A few $N^\eta(p_T)/N^{\pi^0}(p_T)$ ratios have been slightly displaced to the left or right (± 50 MeV/c) along the p_T axis to improve the clarity of the plot.

Then,

$$\left(\frac{\delta N_{\text{direct}}^\gamma(p_T)}{N_{\text{direct}}^\gamma(p_T)} \right)^2 = \left(\frac{R(p_T)}{R(p_T) - 1} \right)^2 \left(\frac{\delta N_{\text{meas}}^\gamma(p_T)}{N_{\text{meas}}^\gamma(p_T)} \right)^2 + \left(\frac{1}{R(p_T) - 1} \right)^2 \left(\frac{\delta N_{\text{bkgd}}^\gamma(p_T)}{N_{\text{bkgd}}^\gamma(p_T)} \right)^2 \quad (5.51)$$

Systematic errors for the hadron contamination, gamma unfolding and so on (errors listed in Tab. 5.6) are included in $\delta N_{\text{meas}}^\gamma(p_T)$. $\delta N_{\text{bkgd}}^\gamma(p_T)$ includes systematic errors listed in Tab. 5.7 except for the error for hadron contamination and γ unfolding. As seen in the equation, as going to the higher p_T region, the signal-to-noise ratio of direct photon signal is improved and systematic errors on background gamma spectra become smaller. It means systematic error on direct photon spectra from π^0 merging is 10 %, even if systematic error of 20 % is assigned on double ratio for the central events.

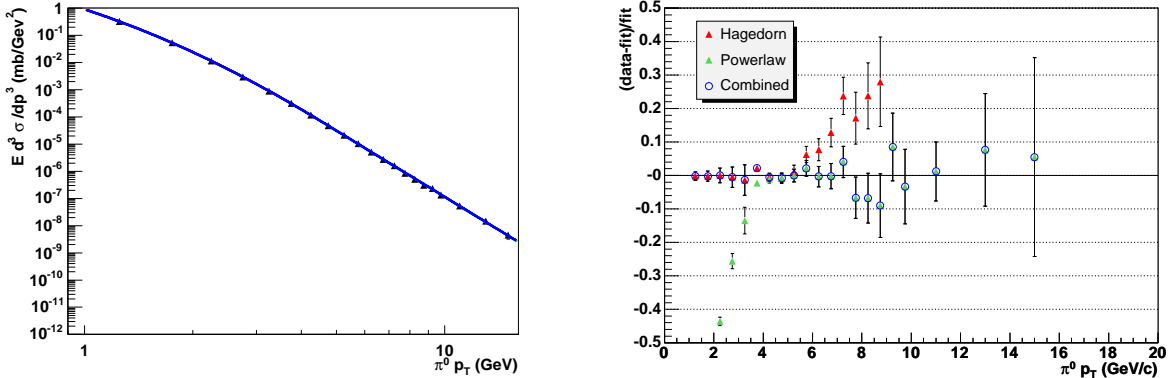


Figure 5.57: Parameterization of the neutral pion cross-section in $\sqrt{s} = 200$ GeV p+p collisions. Left: Parameterization of the final p+p π^0 cross-section in [19] obtained by the fitting together with the data points on a log-log scale. Right: Relative deviations of the data points from the fit [97].

5.7 Parameterization of Cross-Section in p+p Collisions

Here, the procedure of a parameterization of the π^0 and direct photon cross section in p+p. The RHIC-Year3 final π^0 data and RHIC-Year5 preliminary direct photon data are parameterized. This parameterization takes out point-by-point fluctuations of the p+p reference spectrum for the calculation of the nuclear modification factor for Au+Au collisions, R_{AA} . An emphasis was put on obtaining the correct representation of the data at the highest values of p_T .

5.7.1 Parameterization of Neutral Pion Cross-Section in $\sqrt{s} = 200$ GeV p+p Collisions

The p_T range of neutral pion spectrum shown on Fig. 2.7 is extended [19]. The neutral pion spectrum is parameterized using the Eq. 5.36. As described at Sec. 5.5.2, Eq. 5.36 consists of the Hagedorn function and power-low function. The two functions are connected using Wood-Saxon transition function. The left panel of Fig. 5.57 shows the comparison of π^0 cross-section in p+p collisions and parameterization. When the data are fitted, only statistic errors are taken into account, and the systematic errors are applied to the obtained parameterization as the same relative errors that are applied to the data points. As a fitting result, the π^0 cross-sections in $\sqrt{s} = 200$ GeV p+p collisions are parameterized as:

$$E \frac{d^3 \sigma}{dp^3} = T(p_T) \cdot \frac{229.6}{(1 + p_T/1.466)^{10.65}} + (1 - T(p_T)) \cdot \frac{14.43}{p_T^{8.103}} [\text{mbarn GeV}^{-2} c^3], \quad (5.52)$$

where

$$T(x) = \frac{1}{1 + \exp(\frac{x-4.5}{0.114})}. \quad (5.53)$$

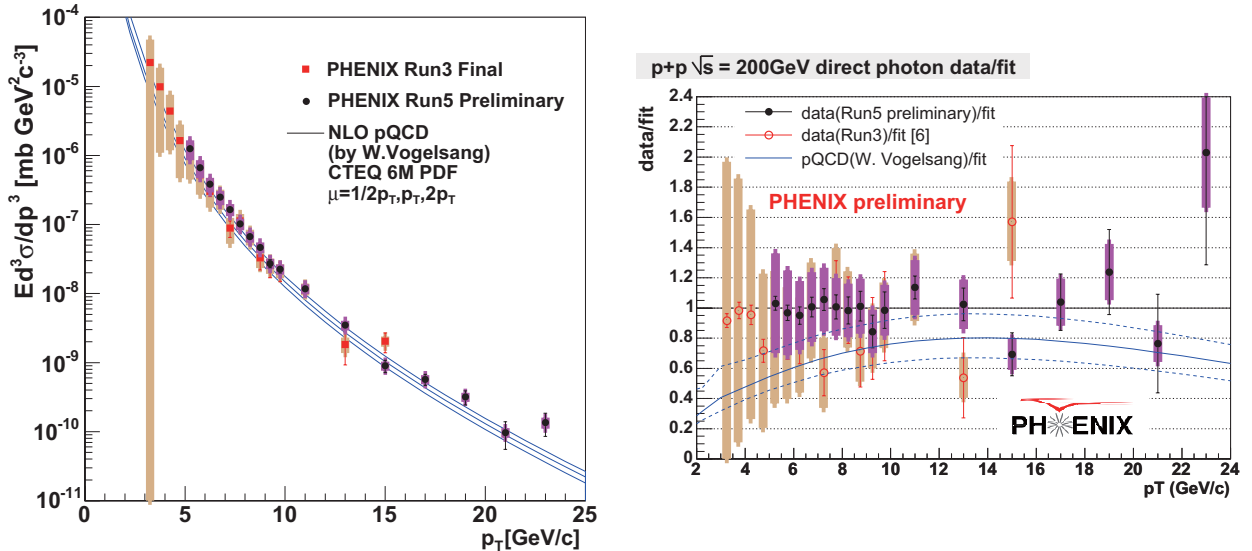


Figure 5.58: Left: Direct photon spectra compared with NLO pQCD calculations for three theory scales, μ . Brackets around data points show systematic errors. The bottom figure shows the comparison to the NLO pQCD calculation for $\mu = p_T$, with upper and lower curves for $\mu = p_T/2$ and $2p_T$. Right: ratio of data and parameterized curve. Bands around data points show systematic errors. For comparison, the NLO pQCD calculations, which are same as the lines shown in left figure, are shown as well.

The right panel of Fig. 5.57 shows the relative deviations of the data points from the fit. Two functions are connected smoothly, while each function itself only can not reproduce the cross-section for all p_T range.

5.7.2 Parameterization of Direct Photon Cross-Section in $\sqrt{s} = 200$ GeV $p+p$ Collisions

The direct photon spectra in $\sqrt{s} = 200$ GeV $p+p$ collisions based upon RHIC-Year3 data have been published in [39]. The new large amount of data recorded by PHENIX in RHIC-Year5 ($\int L = 3.8 \text{ pbarn}^{-1}$) makes it possible to extend the p_T range of the direct photon cross-section. The left panel of Fig. 5.58 shows the preliminary result for direct photon cross-section in $\sqrt{s} = 200$ GeV $p+p$ collisions. A NLO pQCD predictions [138], using CTEQ 6M parton distribution functions and the BFG II parton to photon fragmentation function, with three theory scales (μ) are shown as well. The data are consistent with the NLO pQCD calculation within the uncertainties.

For the measurement of the R_{AA} in Au+Au, the direct photon cross-section in $p+p$ collisions is parameterized using following function:

$$E \frac{d^3\sigma}{dp^3} = a \cdot p_T^{-(b+c \ln x_T)} \cdot (1 - x_T^2)^d, \quad (5.54)$$

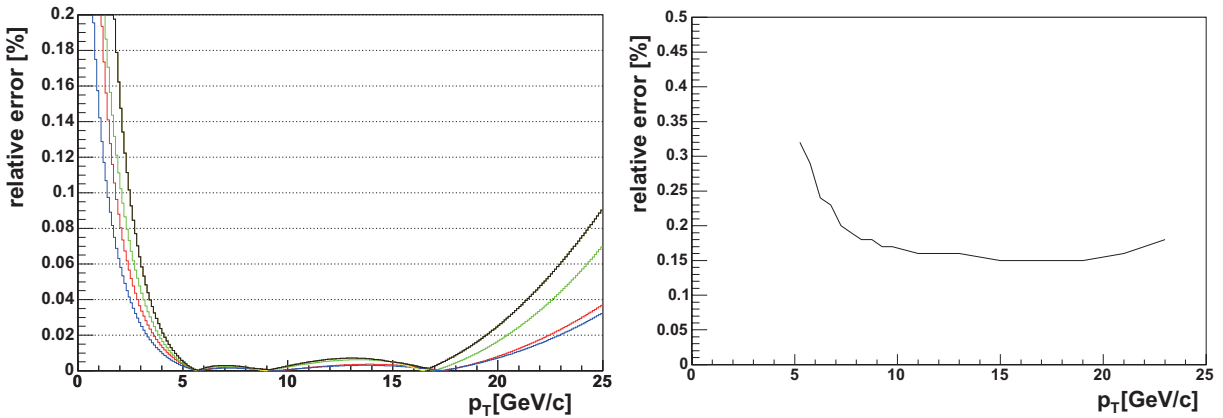


Figure 5.59: Left panel: results of various fits where one parameter is fixed (it's original value +/- its error) and the others are varied freely. Right panel: estimated total error of the fit from the statistical fluctuations of the data points. Upper curve: systematic errors of the fit to the Run-3 final data. Lower curve: systematic error of our fit to the Run-5 preliminary data.

where $x_T = 2p_T/\sqrt{s}$. The idea is to have a power law in p_T , and an additional fall-off with some power of $(1 - x_T)$. The power of p_T itself will not be constant over the whole spectrum, hence the $\ln x_T$ term in the exponent. As a fitting result, the direct photon cross-section in $\sqrt{s} = 200 \text{ GeV}$ p+p collisions is parameterized as:

$$E \frac{d^3\sigma}{dp^3} = 0.028 \cdot p_T^{-(6.478 + 0.145 \ln x_T)} \cdot (1 - x_T^2)^{3.99} [\text{pbarn GeV}^{-2} c^3]. \quad (5.55)$$

The right panel of Fig. 5.58 shows how well the parameterization describes the direct photon cross-section. The NLO pQCD calculations are also shown. Although the theoretical calculation can reproduce the experimental data within the uncertainties, the mean points of the data are systematically larger than the calculation.

5.7.3 Propagation of the Error on p+p Cross-Section

The systematic uncertainties of the data points, which have not been considered for the fit, are applied to the obtained parameterization as the same relative errors that are applied to the data points. For the statistical errors the propagation is more complicated. It is clear that by the parameterization the spectrum becomes smoother. When estimating the errors of the fit to the p+p spectra, the statistic errors are handled as follows. First we fit the data with all parameters varying freely; each parameter has a value and an error. Next for each of the parameters we fix its value at +/- its error, and repeat the fit leaving the other parameters varying freely. Finally we take the ratio of all parameterizations to the default (very first) one and the envelope of these ratios is considered to be the error propagated from p_T -independent sources (statistical error). The procedure is illustrated on the left panel of Fig. 5.59 where

different colors indicate the fit results after fixing a parameter and varying the other three freely. The right panel shows the deduced systematic error for the Year5 p+p data.

Chapter 6

Results

6.1 Results on Neutral Pion Production in $\sqrt{s_{\text{NN}}} = 200 \text{ GeV}$ Au+Au Collisions

Figure 6.1 shows the measured invariant yields of π^0 produced in Au+Au collisions at $\sqrt{s_{\text{NN}}} = 200 \text{ GeV}$ plotted as a function of p_{T} for each centrality selection. They are given as invariant yield per unit rapidity at $y = 0$, per unit azimuth, and per event. The data points are tabulated in Tab. E.1 to E.10.

From fully corrected $\pi^0 p_{\text{T}}$ spectra, the nuclear modification factor (R_{AA}) which is defined at Sec. 2.3.3, is obtained as a function of p_{T} for each centrality as shown in Fig. 6.2. The parameterized cross section (Eq. 5.52) is used for the π^0 cross section in p+p collisions. The statistical and p_{T} -uncorrelated errors on p+p reference are included in the lines, and p_{T} -correlated systematic errors on p+p reference are included in the boxes. The scaling factors (T_{AA}) are tabulated in Tab. D.2. The $\pi^0 R_{\text{AA}}$ for nine centrality selections (0 – 10 % to 80 – 92 %) and minimum bias Au+Au collisions at $\sqrt{s_{\text{NN}}} = 200 \text{ GeV}$ are shown in Fig. 6.2. The data points of $\pi^0 R_{\text{AA}}$ are tabulated in Tab. E.11 to E.20.

The π^0 invariant yield in $\sqrt{s_{\text{NN}}} = 200 \text{ GeV}$ Au+Au collision is suppressed strongly compared with the binary scaled π^0 yield in p+p collision, and R_{AA} is almost constant at ~ 0.2 from $p_{\text{T}} \sim 4 \text{ GeV}/c$ up to $\sim 20 \text{ GeV}/c$ in the most central collisions. This suppression was not observed at the SPS, and this result is consistent with the previous RHIC data. The evaluation of theoretical calculations based upon the R_{AA} , are described at the next chapter.

6.2 Results on Direct Photon Production in $\sqrt{s_{\text{NN}}} = 200 \text{ GeV}$ Au+Au Collisions

Figure 6.3 shows the direct photon excess double ratio which is defined in Eq. 5.40 as a function of p_{T} for each nine centrality selections and minimum bias Au+Au collisions at $\sqrt{s_{\text{NN}}} = 200 \text{ GeV}$. The data points are tabulated in Tab. F.1 to F.10. While it is challenging to extract the direct photon signal due to the large background, an excess is observed at high- p_{T} and the magnitude increases with increasing centrality of the collision. The backgrounds are mainly

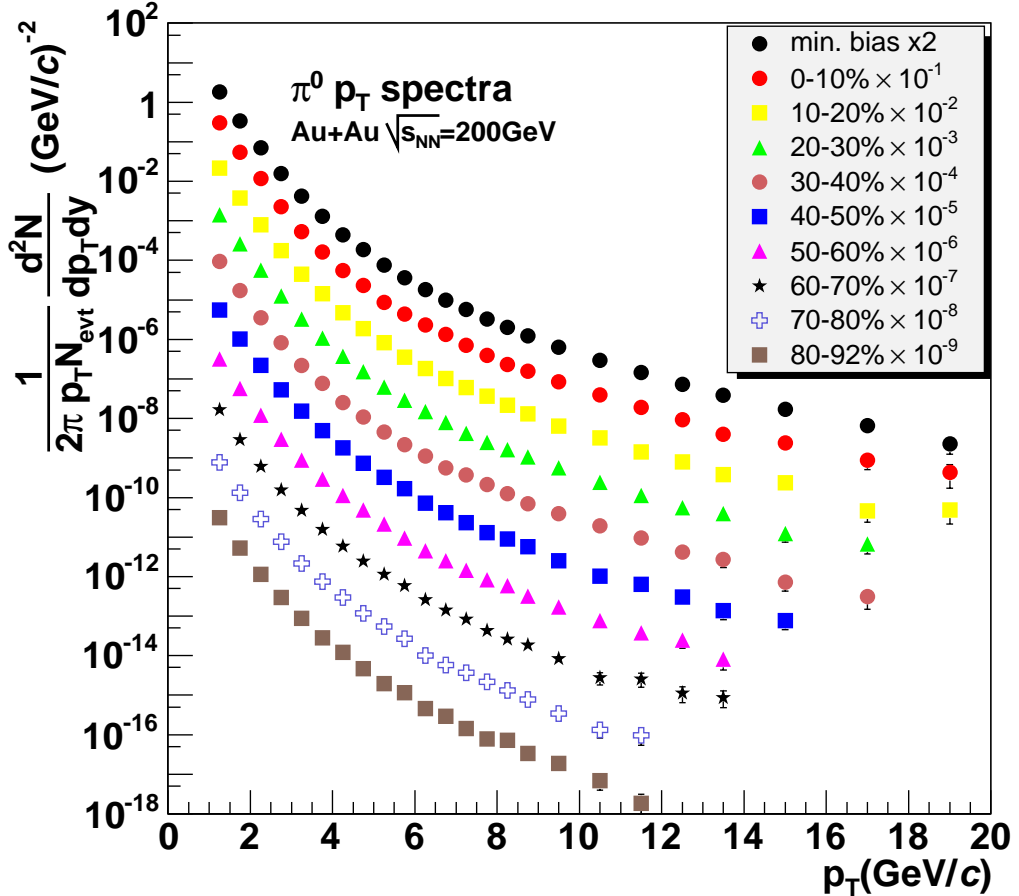


Figure 6.1: Neutral pion invariant yields as a function of p_T for nine centrality selections (0 – 10 % to 80 – 92 %) and minimum bias (top) Au+Au collisions at $\sqrt{s_{NN}} = 200$ GeV.

determined by the yield of high- p_T π^0 s. The strong suppression of neutral hadrons as seen in Fig. 6.2 allows to extract direct photons at the high momentum region. If the π^0 production is not suppressed, it will be hard to extract the direct photon signal even at high- p_T .

Figure 6.4 shows the invariant yields of direct photon produced in Au+Au collisions at $\sqrt{s_{NN}} = 200$ GeV, plotted as a function of p_T for each centrality selection. They are given as invariant yield per unit rapidity at $y = 0$, per unit azimuth, and per event. In the figure, binary scaled p+p direct photon cross sections parameterized as Eq. 5.55 are shown as the solid curves. The data points are tabulated in Tab. F.11 to F.20.

As shown in Fig. 6.5, the nuclear modification factor (R_{AA}) of direct photon as a function of p_T for nine centrality selections (0 – 10 % to 80 – 92 %) and minimum bias Au+Au collisions at $\sqrt{s_{NN}} = 200$ GeV are obtained from the p_T spectra. The parameterized cross section (Eq. 5.55) is used for the direct photon cross section in p+p collisions. In Fig. 6.5, the statistical and p_T -uncorrelated errors on p+p reference are included in the lines, and p_T -correlated systematic errors on p+p reference are included in the boxes. The data points of direct photon R_{AA} are

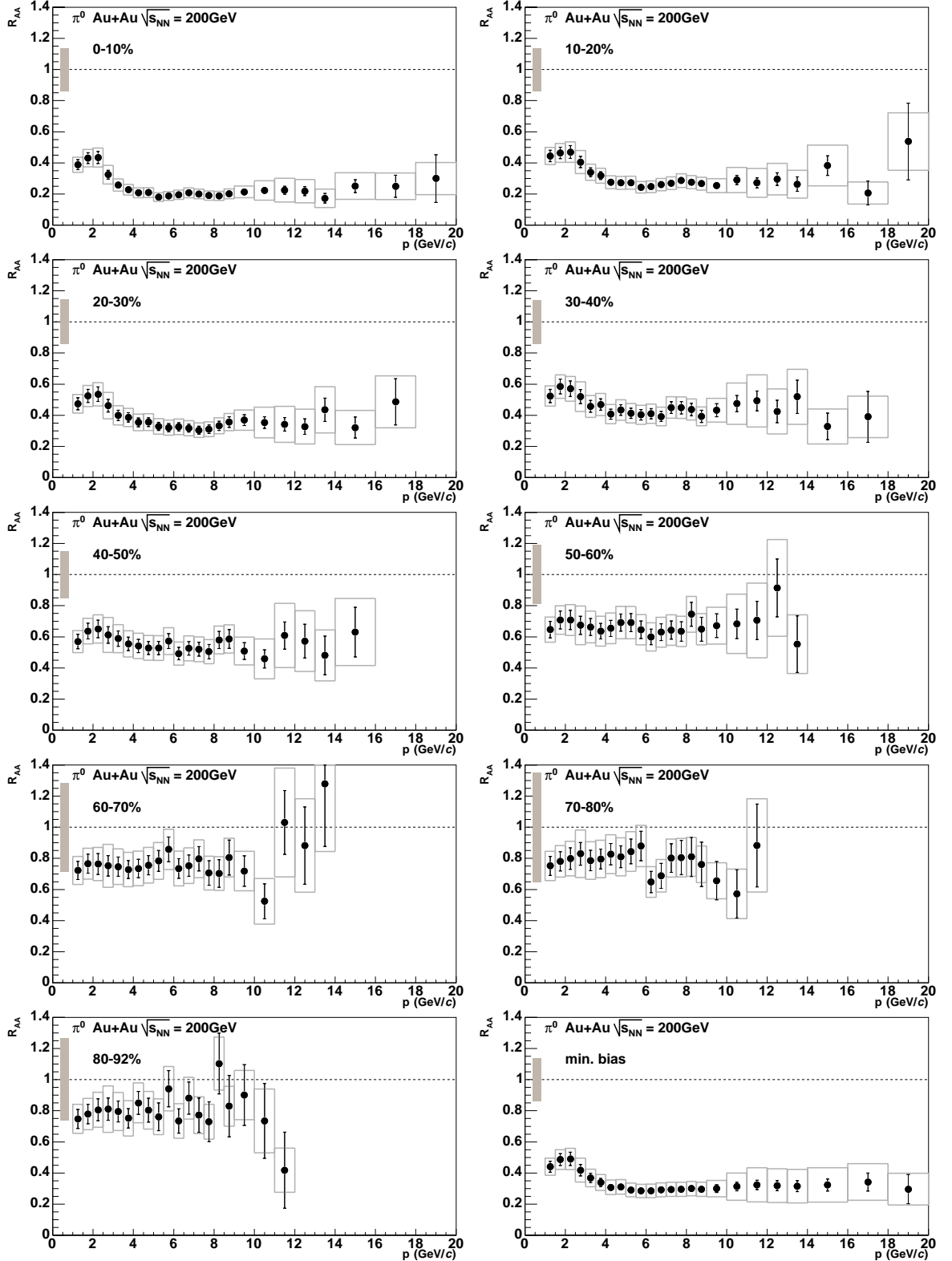


Figure 6.2: Neutral pion nuclear modification factor as a function of p_T for each centrality in Au+Au collisions at $\sqrt{s_{NN}} = 200$ GeV. In addition to the statistical and p_T -uncorrelated errors, point-to-point varying systematic errors are shown on the data points as boxes. An overall systematic error of R_{AA} normalization is shown at unity.

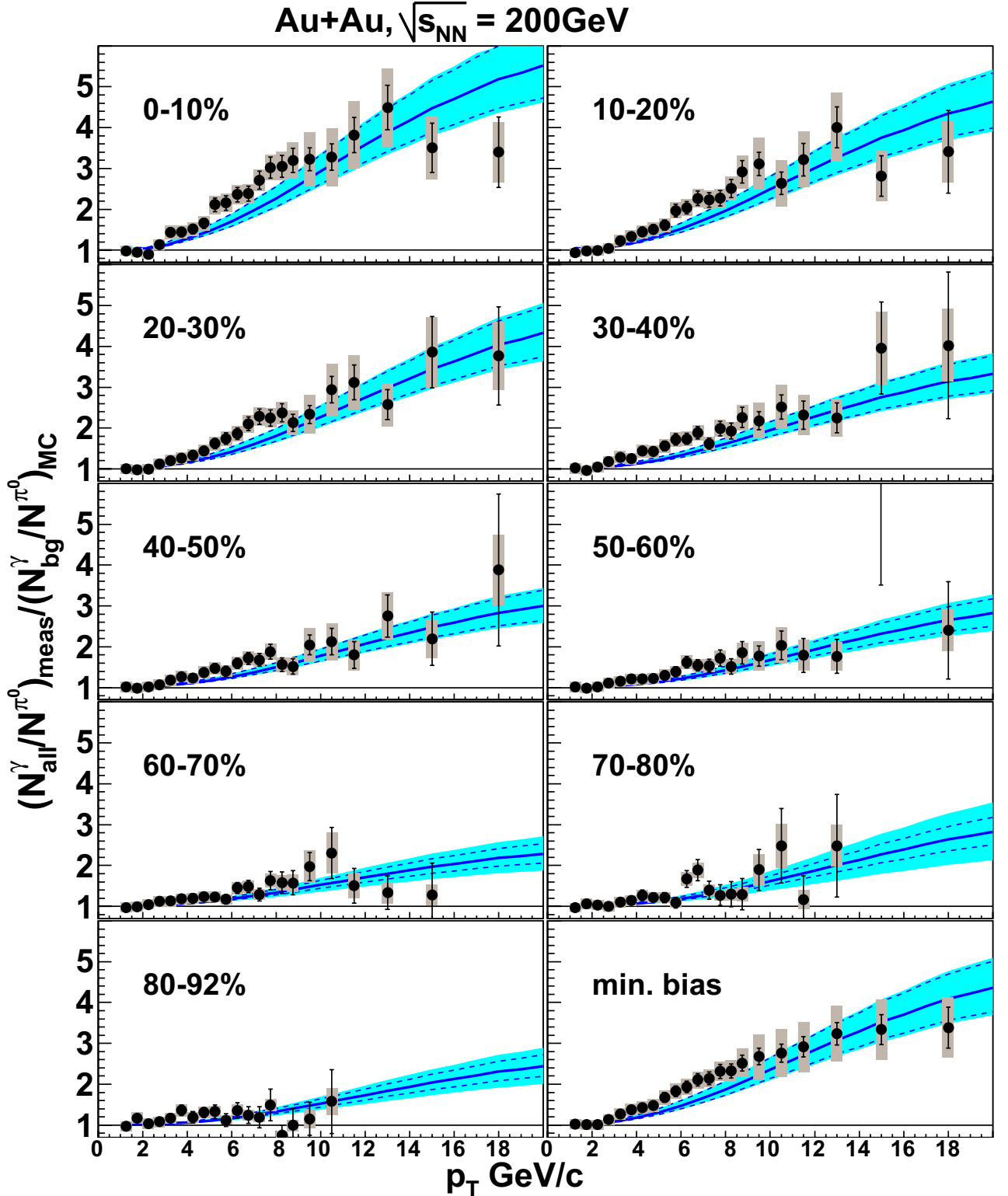


Figure 6.3: Direct photon excess double ratio as a function of p_T for nine centrality selections and minimum bias Au+Au collisions at $\sqrt{s_{NN}} = 200$ GeV. In addition to the statistical and p_T -uncorrelated errors, p_T -correlated errors are shown on the data points as bands. The solid curves are binary scaled pQCD calculations (dotted lines are theoretical uncertainty, and filled areas are quadratic sum of the theoretical uncertainty and the uncertainty on the binary scaling).

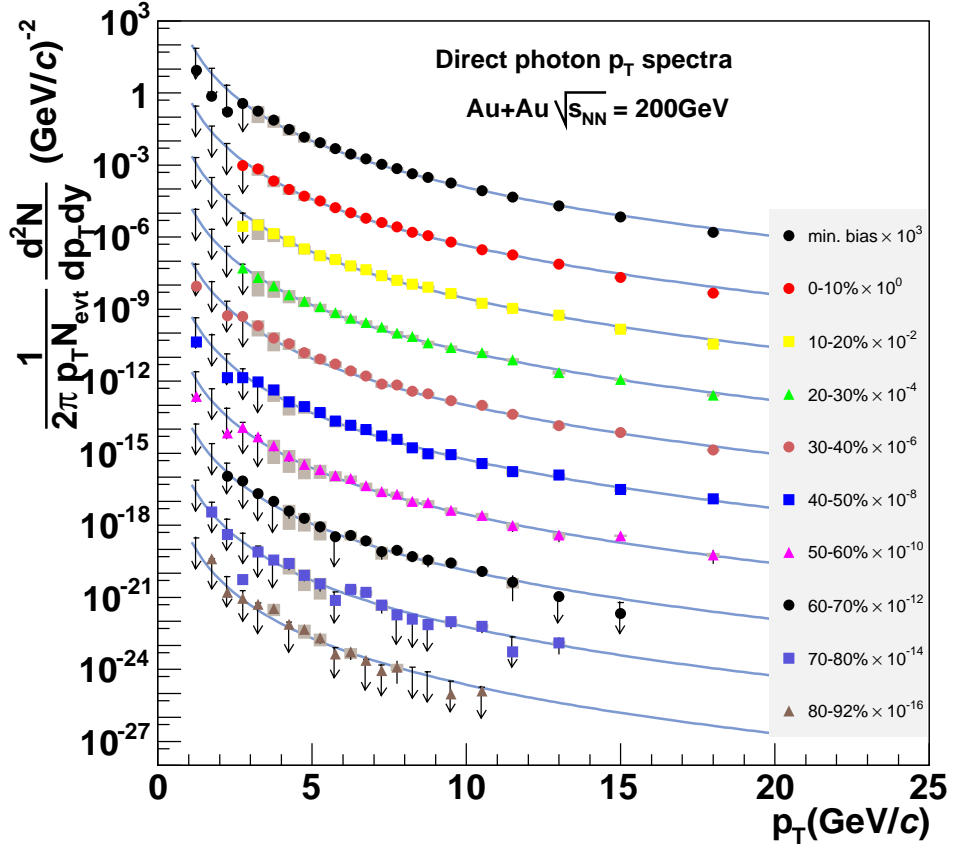


Figure 6.4: Direct photon invariant yields as a function of p_T for nine centrality selections and minimum bias Au+Au collisions at $\sqrt{s_{NN}} = 200$ GeV. In addition to the statistical and p_T -uncorrelated errors, p_T -correlated errors are shown on the data points as bands. Arrows indicate measurements consistent with zero yield with the tail of the arrow indicating the 90 % confidence level upper limit. The solid curves are binary scaled p+p direct photon parameterizations.

tabulated in Tab. F.21 to F.30. Since the errors on direct photon yield are quite large due to the small signal-to-noise ratio at $p_T < 5$ GeV/ c , only the R_{AAS} above 5 GeV/ c are shown. The R_{AA} of direct photons shown in Fig. 6.5 are consistent with unity within the error for all p_T range and centrality. And the R_{AA} of direct photons seems to show the hint of suppression at very high- p_T ($p_T > 14$ GeV/ c) region in the central collisions.

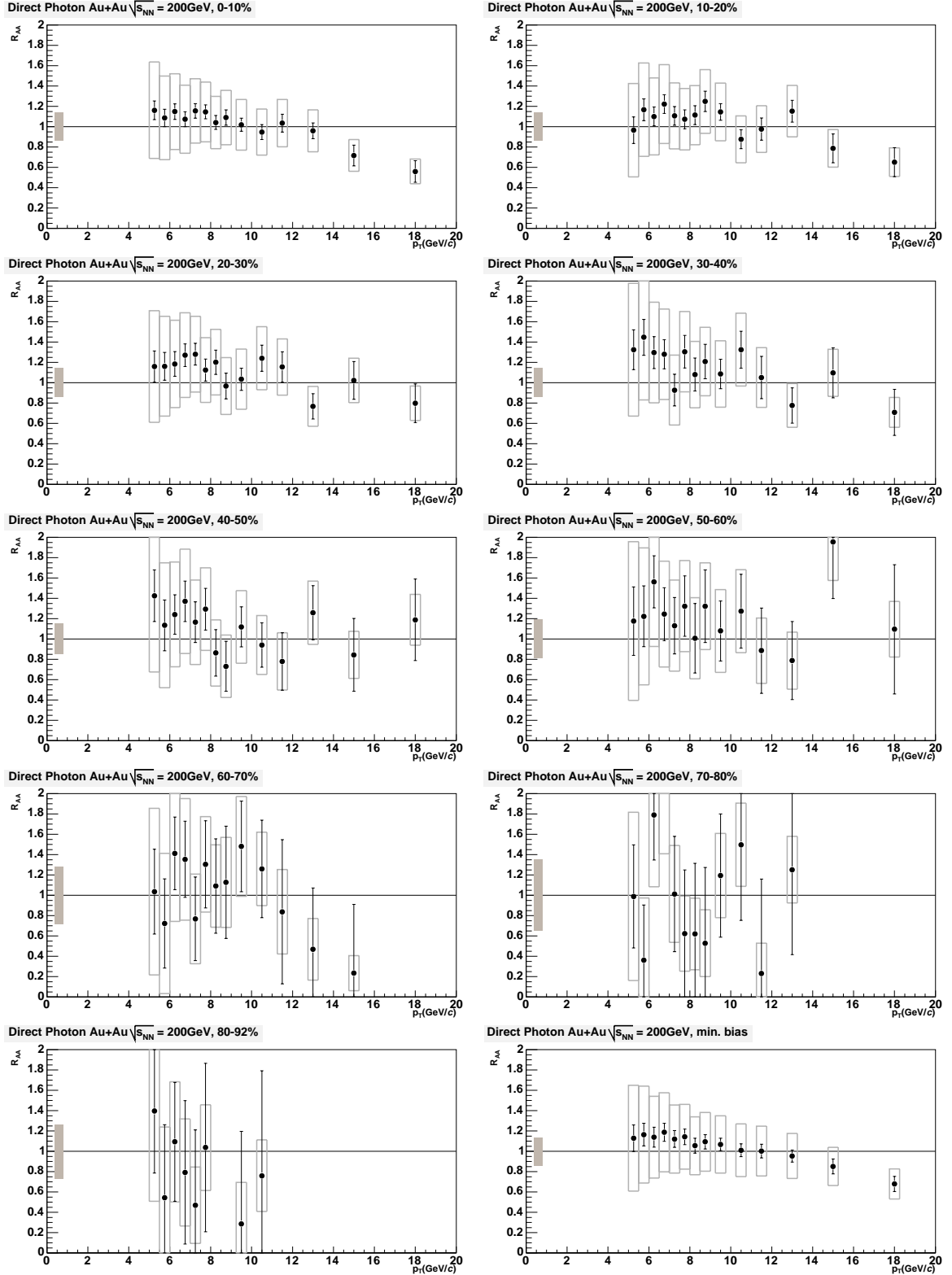


Figure 6.5: Direct photon nuclear modification factor as a function of p_T for each centrality in Au+Au collisions at $\sqrt{s_{NN}} = 200$ GeV. In addition to the statistical and p_T -uncorrelated errors, p_T -correlated errors are shown on the data points as boxes, and an overall systematic error of T_{AA} normalization is shown at unity.

Chapter 7

Discussions

7.1 Discussions on Neutral Pion Production in $\sqrt{s_{\text{NN}}} = 200 \text{ GeV Au+Au Collisions}$

As shown in Fig. 6.2, the π^0 yield in $\sqrt{s_{\text{NN}}} = 200 \text{ GeV Au+Au collision}$ is suppressed very strongly up to $\sim 20 \text{ GeV}/c$ compared with the binary scaled π^0 yield in p+p collision. Based upon the following experimental confirmation, the strong suppression is understood as not due to the initial state effect, but due to the final state effect in produced bulk matter in Au+Au collisions.

- If the high- p_T hadron suppression is due to the initial state effect, such as Cronin effect and nuclear shadowing, similar suppression should be shown in d+Au collisions as well as in Au+Au collisions. As shown in Fig. 2.16, the high- p_T hadron suppression was not observed in d+Au collisions. This indicates that any initial state modification of nuclear parton distributions has little effect on the production of hadrons, and the suppression in Au+Au collisions is due to the extended dense matter in the final state, that is absent in d+Au collisions.
- As shown in Fig. 2.17, the suppression pattern of high- p_T η is similar with that of high- p_T π^0 . It supports the mechanism of quenching does not depend on the species of the hadrons which are composed of light quarks, and the suppression occurs at the parton level prior to its fragmentation into hadrons.

In addition to the above confirmation, one should confirm that point-like scaling, and binary scaling of high- p_T hadron production relative to p+p collisions is well represented by the Monte Carlo calculation to conclude that the π^0 suppression due to the final state effect. Since photons produced directly in initial parton scatterings are essentially unaffected by the surrounding matter and not be quenched by the any final state effect, measurement of high- p_T direct photon invariant yield allows to confirm the binary scaling of high- p_T production in Au+Au collisions.

Figure 6.4 shows direct photon and $\pi^0 R_{\text{AA}}$ as a function of number of participants, and indicates that the direct photon yields are in agreement with a p+p measurement scaled by the number of binary nucleon collisions within experimental errors. As shown in Fig. 6.5, the R_{AA}

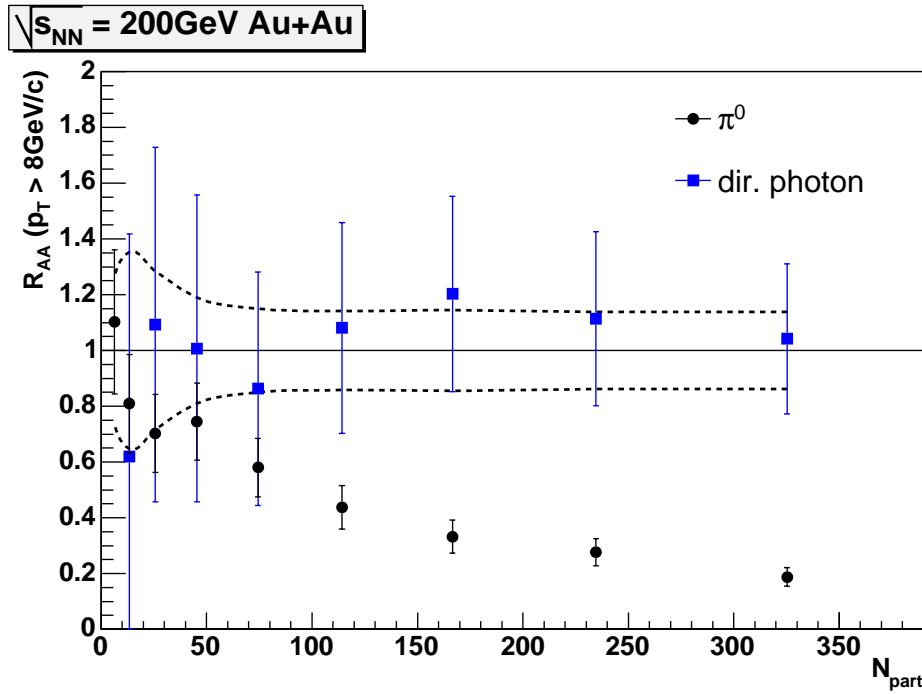


Figure 7.1: Direct photon (blue box) and π^0 R_{AA} (black circle) as a function of number of participants. For the measurement of R_{AA} , the yields are integrated above $p_T = 8 \text{ GeV}/c$. The error bars indicate the total error excluding the error on $\langle N_{coll} \rangle$ and dashed lines are root sum square of the error on $\langle N_{coll} \rangle$ and the normalization error for p+p reference.

of direct photons are consistent with unity within the error for all p_T range and centrality. The centrality dependence of the R_{AA} of high- p_T direct photon and π^0 represented as a function of the number of participating nucleons, $\langle N_{part} \rangle$, are shown in Fig. 7.1. Here, the invariant yield is integrated above $p_T = 8 \text{ GeV}/c$. The high- p_T direct photon production is observed to scale as the binary scaled p+p yield for all centralities. This is in contrast to the centrality dependence of the $\pi^0 R_{AA}$ ($p_T > 6 \text{ GeV}/c$) shown as the black circles in Fig. 7.1. It demonstrates pure point-like ($\langle N_{coll} \rangle$) scaling as a function of centrality relative to p+p collisions, and supports that binary scaling is well represented by Monte Carlo calculation which employs the Glauber model. The result provides confirmation that the observed large suppression of high- p_T hadron production in central Au+Au collisions is dominantly a final state effect in the produced medium.

While the R_{AA} s of direct photon are consistent with unity within the error for all p_T range and centrality, the R_{AA} of direct photon seems to become below unity at very high- p_T region ($p_T > 14 \text{ GeV}/c$) in the central collisions. The suppression can be interpreted as the consequence of nuclear effect. Figure 7.2 shows the direct photon R_{AA} in the most central collisions and minimum bias collisions (same as that in Fig 6.5). One of the possible effect on the direct photon production in Au+Au collision is so-called “isospin effect”. The PDF of constituent quarks of a proton (uud) is different from these of neutrons (udd), then the direct photon production in Au+Au collisions can not be represented completely only with the binary scaled p+p collisions. The magnitude due to this effect is obtained from the superposition of cross-section in p+p, p+n and n+n collisions:

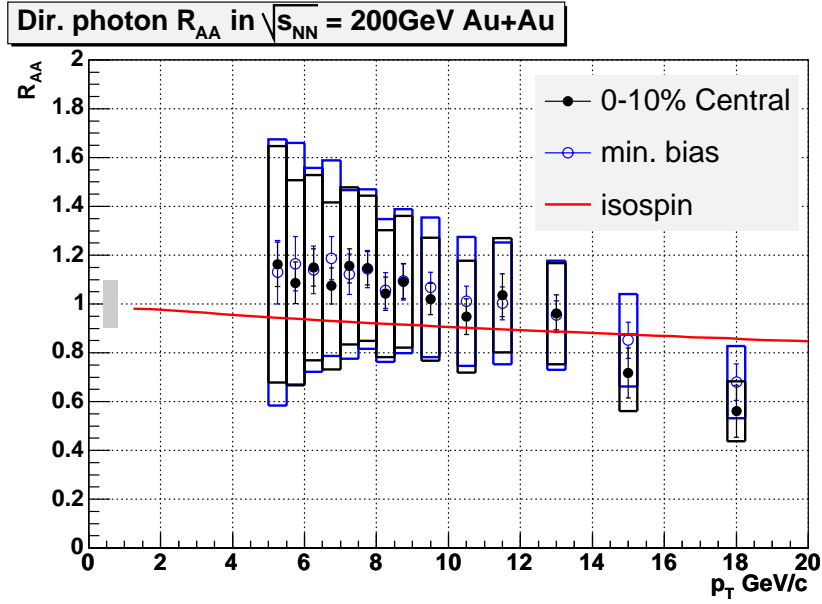


Figure 7.2: Comparison of Direct photon R_{AA} with the calculation which takes isospin effect into account empirically.

$$\sigma_{A+A} = \frac{1}{A^2} \cdot (Z^2 \cdot \sigma_{p+p} + 2Z(A-Z) \cdot \sigma_{p+n} + (A-Z)^2 \cdot \sigma_{n+n}), \quad (7.1)$$

where σ_{p+p} , σ_{p+n} and σ_{n+n} are respectively the cross-section of direct photon production in p+p, p+n and n+n collisions, and Z and A are respectively the number of protons and the atomic mass number of nucleus ($Z = 79$, $A = 197$ for Au). The each cross section is obtained using the proton parton distribution by the isospin conjugation assumptions: $u^p = d^n$, $d^p = u^n$, $\bar{u}^p = \bar{d}^n$, $\bar{d}^p = \bar{u}^n$. The isospin effects would be significant for photon production at large Bjorken x , at which the partonic process involves essentially the scattering of valence quarks. The solid red line shown in Fig. 7.2 represents the expected R_{AA} ($\sigma_{A+A}/\sigma_{p+p}$) where isospin effect is taken into account, and there would be $\sim 20\%$ direct photon suppression at $p_T = 20$ GeV/c. The σ_{p+p} , σ_{p+n} and σ_{n+n} are obtained from NLO pQCD calculation (private communication with W. Vogelsang). Such an effect is magnified in electromagnetic processes such as prompt photon production because of the valence quark electric charges. Then, it is negligible around $x \sim 0.01$, where the nucleon PDF is dominated by the gluons. And such suppression is not so large in case of π^0 production. The hint of direct photon suppression at high- p_T ($p_T > 14$ GeV/c) can be interpreted with the isospin effect, and it supports that binary scaling is well described.

7.2 Comparisons with Theoretical Models

The suppression of high- p_T π^0 production in central events can be interpreted as the energy loss of hard-scattered partons, predominantly via gluon bremsstrahlung emission, prior to their

fragmentation. This effect is known as jet quenching effect. In order to explain observed suppression and to extract physical parameters, the results for π^0 production are compared with some theoretical models which involve various effects such as parton energy loss, and initial state effects as described in Sec. 2.3. Some groups made the numerical calculations to extract the properties of formed high dense matter by RHIC. The elemental assumptions for the modification of high- p_T hadrons (i.e. parton energy loss and initial state effect) are almost same among the theoretical models. The differences between the theories are the evolution of the medium and the procedures used to relate the quenching calculation to the fireball geometry and its evolution. Followings list the four major schemes of approaches to the energy loss of hard scattered partons:

- Higher Twist Approach [221, 141, 226, 218, 219, 223, 239]
- GLV, Recursive Operator in Opacity [142, 143, 144, 145, 215]
- PQM, Path Integral in Opacity [235, 234, 197, 127, 68]
- AMY, Finite Temperature Field Approach [70, 72, 71, 165, 211]

The π^0 data will be compared with two major schemes, Higher Twist and GLV, to extract the physics information.

To take the time-space expansion of bulk matter into account, each schemes employ the dynamical models. One of the major dynamical models is longitudinal Bjorken expansion, which is introduced at Sec. 2.2.1. In the model, gluon density is estimated as:

$$\rho(\tau) = \frac{\tau_0}{\tau} \rho(\tau_0), \quad (7.2)$$

where

$$\tau_0 \rho_0 = \frac{1}{\pi R^2} \frac{dN^g}{dy}, \quad (7.3)$$

dN^g/dy is the initial gluon rapidity density at $\tau = \tau_0$.

7.2.1 Comparison with *Higher Twist* approach

The formalism proposed by X.N. Wang et al. is called *Higher Twist* approach. They express the suppression by the modification of fragmentation function ($D^{AA}(z) = D + D(\text{medium})$) as [220, 230]:

$$\widetilde{D}_{a \rightarrow h}(z) \approx \frac{1}{1 - \Delta z} D_{a \rightarrow h}\left(\frac{z}{1 - \Delta z}\right), \quad (7.4)$$

where Δz is connected to the fractional parton energy loss ($\Delta E/E$), which is calculated by the *Higher Twist* formalism. The origin of the Higher Twist approach is in the calculations of

medium enhanced higher twist corrections to the total cross section in DIS of large nuclei [193, 194]. The inclusion of power corrections to the leading twist cross sections is technique to calculate the modified fragmentation function. If the finite and expanding medium expressed is assumed, the total parton energy loss ΔE is approximated as a path integral:

$$\Delta E \approx \left\langle \frac{dE}{dL} \right\rangle L_{\text{eff}}, \quad (7.5)$$

where $\langle dE/dL \rangle$ is the averaged parton energy loss per unit length which is obtained from the numerical calculation and parameterized as:

$$\left\langle \frac{dE}{dL} \right\rangle = \epsilon_0 \frac{(E/\mu_0 - 1.6)^{1.2}}{7.5 + E/\mu_0}, \quad (7.6)$$

where E is the energy of hard scattered parton and μ_0 is factorization scale and chosen as $\mu_0 = 1.5$ GeV [218]. And the L_{eff} in Eq. 7.5 is the effective path length of hard scattered partons.

The left panel of Fig. 7.3 shows the $\pi^0 R_{AA}$ in central events compared to different theoretical calculations by X.N. Wang [219, 224]. The calculation which includes only the known initial state modifications, Cronin enhancement and nuclear shadowing, leads to a nuclear modification factor that is larger than unity. The prediction shown with a blue curve in the left panel of Fig. 7.3 corresponds to a parton energy loss of -7.3 GeV/fm in a static medium, which is 15 times large than the energy loss derived for normal nuclear matter [219]. However, the calculation can not reproduce the experimentally obtained flat p_T dependence of the suppression. Empirically it is known that a linear energy dependence of energy loss is needed in order to describe the p_T dependence [164, 186]. X.N. Wang et al. argued this linear energy dependence can be a manifest of the LPM effect [149, 224], which is the absorption of thermally produced gluons and the stimulated emission of gluons in the dense matter [217]. As the result of his new calculation where the LPM effect is taken into account, an increased energy loss for large transverse momenta is shown, and the data are described well, as the red curve in the left panel of Fig. 7.3.

7.2.2 Comparison with GLV formalism

One of the major theoretical approaches is proposed by M. Gyulassy, P. Levai and I. Vitev, where a systematic expansion of dense matter is used to treat the nonlinear (non-abelian) behavior of induced gluon radiation. The pQCD cross section for inclusive hadron production is given by:

$$\begin{aligned} \sigma^{AA} &= \sum_{abcd} \int dx_a dx_b dz_c \cdot f_{a/A}(x_a, Q^2) \cdot f_{b/B}(x_b, Q^2) \cdot \\ &\quad \sigma(ab \rightarrow cd) \cdot \int_0^1 d\epsilon P(\epsilon, E) \frac{z_{cd}^* D_{h/cd}^0(z_{cd}^*, Q^2)}{\pi z_c}, \end{aligned} \quad (7.7)$$

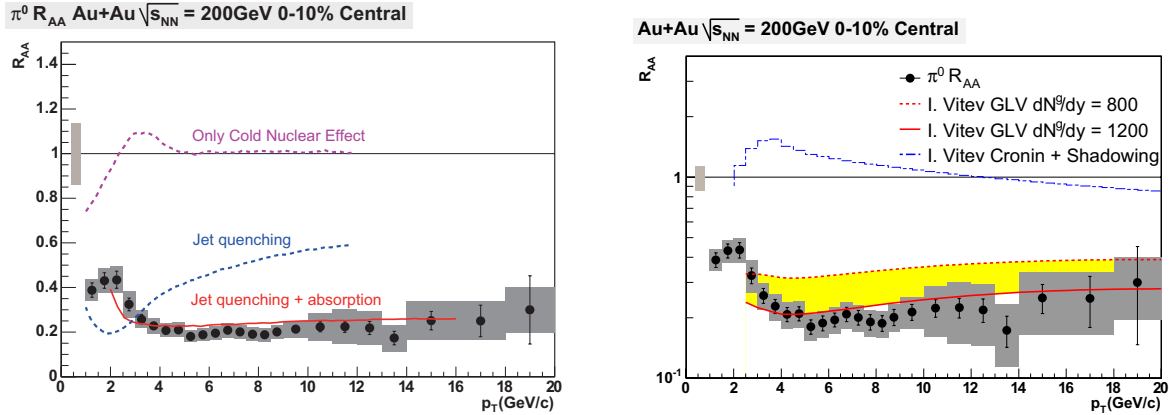


Figure 7.3: Comparison of π^0 R_{AA} with theoretical calculation. Right: compared to a model without jet quenching, only the known initial state effects are considered (purple dotted), the parton energy loss calculation in [219] without gluon absorption (blue dotted), and from [224] including gluon absorption (red solid). The expectations are given by X.N. Wang. Left: compared to a model without jet quenching, only the known initial state effects are taken into account (blue dotted), a model where the parton energy loss is taken into account under each initial gluon density in addition to the initial state effect [215] (red solid line). The expectations are given by I. Vitev.

where $P(\epsilon, E)$ is the distribution of the fractional energy loss ($0 \leq \epsilon \leq 1$) of a fast parton with energy E due to multiple gluon emission, the details are given in [143, 145]. Here, the simplified form of fractional radiative energy loss of a high energy parton is given by GLV formalism as:

$$\frac{\Delta E}{E} \approx C_2 \kappa(E) \int_0^L d\tau \tau \rho(\tau, r(\tau)), \quad (7.8)$$

where C_2 is the color Casimir of the jet parton and $\kappa(E)$ is a slowly varying function of the jet energy [147, 146]. Then, gluon jets are expected to lose about $9/4^*$ more energy than quark jets. On the assumption of the longitudinal Bjorken expansion Eq. 7.2 and constant $\kappa(E_0)$, the relation between the energy loss and initial gluon density is given as:

$$\epsilon = \frac{\Delta E}{E} \propto C_2 \int d\tau \tau \rho(\tau, r(\tau)) \propto C_2 \frac{R}{\pi R^2} \frac{dN^g}{dy} \propto C_2 N_{\text{part}}^{2/3}, \quad (7.9)$$

where initial gluon density (dN^g/dy) is assumed to be proportional to the number of participant (N_{part}). The magnitude of energy loss is proportional to the initial gluon density (dN^g/dy).

The right panel of Fig. 7.3 shows the nuclear modification factor for π^0 s in central events compared to theoretical calculations with GLV formalism [215, 143]. The inclusive numerical calculation for central Au+Au including all three nuclear effects (Cronin+Shadowing+Jet Quenching) are reported by I. Vitev as red curves. He concluded that the approximately constant suppression pattern of π^0 at $4 < p_T < 20$ GeV/ c is due to the compensation of the rate

*For SU(N) the second order Casimir, $C_{2i} = (N^2 - 1)/2N \equiv C_F$ for quarks in the fundamental ($d_i = N$) representation, while $C_{2i} = N \equiv C_A$ for gluons in the adjoint ($d_i = N^2 - 1 \equiv d_A$) representation.

of variation with p_T of the Cronin enhancement and jet quenching. At higher p_T ($14 \leq p_T \leq 20$ GeV/c), the softening of the initial jet spectra due to the EMC modification of the PDFs compensates for the reduced energy loss.

The relation between the energy loss and initial gluon density in Eq. 7.9 can be confirmed as following. As mentioned at Sec. 5.5.2, the high- p_T π^0 spectrum is expected to be approximately represented with power-law function. If the p_T independent suppression at high- p_T can be interpreted as the average fractional shift in the momentum of hard scattered partons, the non-quenched π^0 yield ($1/2\pi p_T \cdot dN^2/dydp_T$) and the quenched π^0 yield per nucleus-nucleus collision ($1/2\pi p_T \cdot dN_{quenched}^2/dydp_T$) can be represented as:

$$\frac{1}{2\pi p_T} \frac{d^2 N}{dydp_T} = \frac{A}{p_T^n}, \quad (7.10)$$

$$\frac{1}{2\pi p_T} \frac{d^2 N_{quenched}}{dydp_T} \rightarrow \frac{1}{2\pi p'_T} \frac{d^2 N_{quenched}}{dydp'_T}, \quad (7.11)$$

$$= \frac{1}{2\pi(1-\epsilon)p_T} \frac{d^2 N_{quenched}}{dydp_T} \frac{dp_T}{dp'_T}, \quad (7.12)$$

$$= \frac{1}{(1-\epsilon)^2} \frac{A}{p_T^n}, \quad (7.13)$$

$$= (1-\epsilon)^{(n-2)} \frac{A}{p'^n_T}, \quad (7.14)$$

where the π^0 whose quenched p_T is $p'_T = (1-\epsilon)p_T$. Then, the nuclear modification factor would be

$$R_{AA} = \left(\frac{1}{2\pi p_T} \frac{d^2 N_{quenched}}{dydp_T} \right) / \left(\frac{1}{2\pi p_T} \frac{d^2 N}{dydp_T} \right) = (1-\epsilon)^{(n-2)}. \quad (7.15)$$

Since the π^0 R_{AA} is more than 0.2 and $n \gg 1$ empirically, the parameter ϵ is small enough to represent the R_{AA} as:

$$R_{AA} \approx e^{-(n-2)\epsilon}. \quad (7.16)$$

If the relation between the fractional energy loss and N_{part} in Eq. 7.9 is employed:

$$R_{AA} \approx e^{-(n-2)\epsilon} = e^{-kN_{part}^{2/3}}, \quad (7.17)$$

where k is the proportionally coefficient (i.e. $\epsilon = N_{part}^{2/3}k/(n-2)$). Figure 7.4 shows the integrated R_{AA} of high- p_T π^0 ($p_T > 8$ GeV/c), comparing with the scaling of Eq. 7.17. The R_{AA} decreases as going to the central collision, and it can be represented with a fitting line which employs the scaling of Eq. 7.17, which is given by simplified GLV formalism Eq. 7.8 on the assumption of Bjorken expansion. As a result of fitting, the constant value of this scaling is $-3.46 \cdot 10^{-2}$, and the effective fractional energy loss can be extracted as:

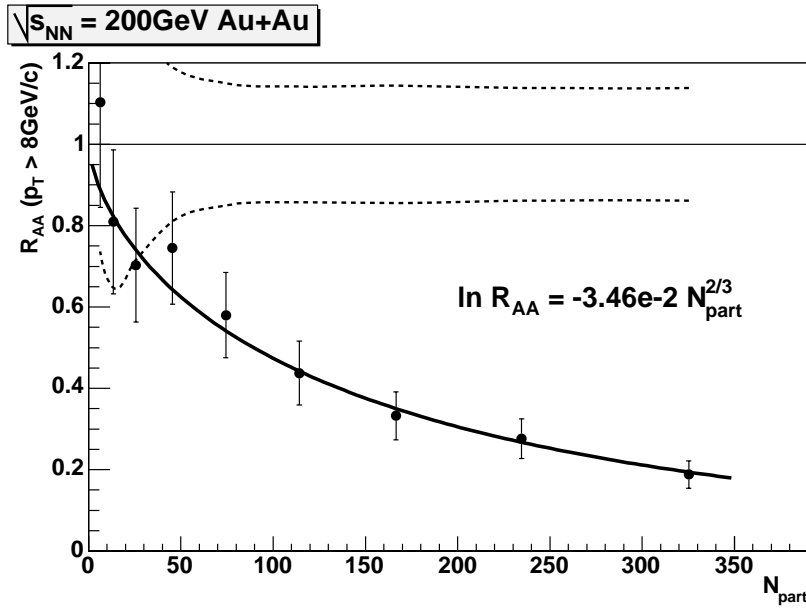


Figure 7.4: high- p_T π^0 R_{AA} as a function of N_{part} . The error bars indicate the total error excluding the error on $\langle N_{\text{coll}} \rangle$ and dashed lines are root sum square of the error on $\langle N_{\text{coll}} \rangle$ and the normalization error for p+p reference. Black solid line is the the fitting result of $N_{\text{part}}^{2/3}$ scaling as in Eq. 7.17.

$$\frac{\Delta E}{E} = \epsilon \approx 5.67 \cdot 10^{-3} N_{\text{part}}^{2/3}. \quad (7.18)$$

For example, a hard scattered parton is expected to lose its energy by a factor of 27 % on an average in the most central collisions ($\langle N_{\text{part}} \rangle = 325.2$).

7.2.3 Comparison of Direct Photon R_{AA} with Theoretical Models

The direct photon yields are in agreement with a p+p measurement scaled by the number of binary nucleon collisions within experimental errors. For low- p_T region ($p_T < 5 \text{ GeV}/c$), the direct photon yield in Au+Au collisions is consistent with the binary scaled p+p data, and the large enhancement due to the thermal photon contribution could not be observed.

While this agreement suggests that the initial hard scattering probability is not reduced, the direct photon yield measured in Au+Au collisions would be suppressed compared to binary scaled p+p measurement, because direct photons in the p+p collisions consist of prompt photons produced directly in hard scattering and jet fragmentation photons from hard scattered partons; the latter could be suppressed similarly as the π^0 case. As shown in the Fig. 2.10, it is estimated that $\sim 30\%$ out of direct photons are from the fragmentation process in NLO pQCD calculation. On the other hand, the Compton-like scattering of the jet partons with the medium (Sec. 2.4.3) might increase the photon rates.

Following lists the possible effect on the direct photon production:

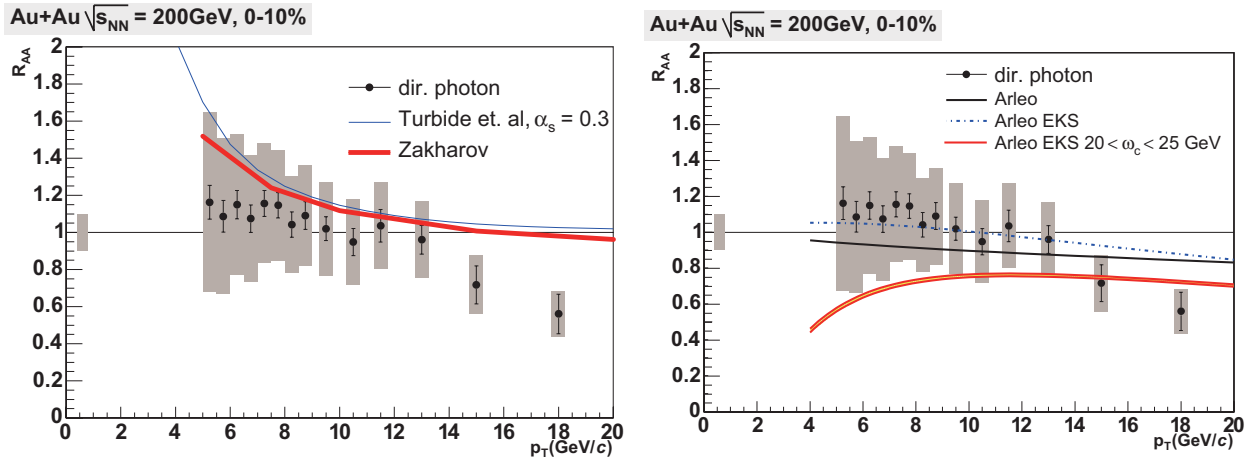


Figure 7.5: Comparison of direct photon R_{AA} with theoretical calculations (Left: S. Turbide *et al.* [211], and B.G. Zakharov [238], Right: F. Arleo [67]). In addition to the statistical and p_T -uncorrelated errors, p_T -correlated errors are shown on the data points as boxes, and an overall systematic error of T_{AA} normalization is shown at 1. The theoretical prediction shown on Right hand side by Arleo are done at leading-order on the assumption of (a) isospin (black solid), (b) isospin and shadowing (blue dotted), and (c) isospin, shadowing and parton energy loss (orange band) effects.

- initial state effect (nuclear shadowing and Cronin effect): small enhancement
- isospin effect: $\sim 20\%$ suppression at $20\text{ GeV}/c$
- thermal photon from QGP: negligible at high- p_T
- jet-quenching effect on fragmentation photon: suppression
- jet-photon conversion from QGP: enhancement

The each panel of Fig. 7.5 shows R_{AA} of direct photons in the most central (0-10 %) Au+Au collisions at $\sqrt{s_{NN}} = 200\text{ GeV}$, in comparison to several theoretical expectations which take the part of above effects into account [211, 238, 67]. In S. Turbide et al.'s calculation [211], the jet quenching, the thermal photon from QGP and the jet-photon conversion effects are taken into account, but isospin effect is not. Their calculation indicates the enhancement of direct photon production at $p_T \leq 13\text{ GeV}/c$, while it fails to reproduce the tendency at $p_T > 14\text{ GeV}/c$. In F. Arleo's calculation [67], jet-photon conversion is not taken into account, while jet-quenching effect, initial state effect (shadowing) and isospin effect are taken into account. His calculation indicates that direct photon might be suppressed by a factor of $20\% \sim 30\%$ at $p_T > 8\text{ GeV}/c$, and high- p_T data supports his estimation. In his calculation, the contribution from jet-photon conversion is not taken into account, and the difference at $p_T < 10\text{ GeV}/c$ might be due to this contribution.

The direct photon R_{AA} is also compared with the estimation taking the each dominant effects (jet-quenching effect, isospin effect and jet-photon conversion). The contribution from isospin

effect and jet-photon conversion are given by theoretical calculation, and the jet-quenching effect is estimated based upon the π^0 data empirically. On the assumption of no modification during the primary parton fragmentation, one can estimate how much fragmentation photons would be suppressed by the jet-quenching effect. For this estimation, Eq. 7.18 is used for the energy loss of fragmentation photon, whose fraction is obtained from NLO pQCD calculation as shown in Fig. 2.10. The data are compared with the expected R_{AA} which takes both isospin effect and jet-quenching effect into account shown as the curves in Fig. 7.6. As a result, though the data are still consistent with the expectation, the data tend to be larger than the expectation below 14 GeV/c.

One of the possible contribution which explains the deviation at the p_T region is sort of emission due to the existence of QGP (i.e. thermal emission and/or jet-photon conversion). Figure 7.7 shows the direct photon R_{AA} compared with expectation, where isospin effect, jet-quenching effect, thermal emission and jet-photon conversion are taken into account. The contribution of jet-photon conversion is given by S. Turbide ($T = 370$ MeV and $\tau_0 = 0.26$ fm/c) [211]. The expectation shows the good agreement with the data within the error. It supports that the agreement with NLO pQCD calculations might be a compensation of jet-photon conversion and energy loss of jet partons themselves.

7.2.4 Extraction of Bulk Matter Property based on $\pi^0 R_{AA}$.

The physical quantities of created matter, such as gluon density dN^g/dy , can be estimated based upon single π^0 spectra. It is important to understand how sensitive the extracted physical quantities from a hard probe is to a detailed understanding (and sufficiently realistic modeling) of bulk matter properties.

The probable parameter for given formalism is extracted using the likelihood function. The right panel of Fig. 7.8 shows the likelihood function ratio as a function of energy loss parameters which are varied in the Higher Twist formalism. The expected R_{AA} s by the Higher Twist formalism for each energy loss parameter (ϵ_0 in Eq. 7.6) are given by H. Zhang et al., and are compared with data as shown in the left panel of Fig. 7.8. The likelihood function ratio is the ratio of each likelihood in minimum likelihood (L_{min}), and the detail is explained in Appendix C. According to the comparison with the theoretical calculation using Higher Twist formalism [240], the initial energy loss parameter in the most central collision is estimated to be about 1.7 ± 0.3 GeV/fm. On the assumption of the longitudinal Bjorken expansion and a Wood-Saxon nuclear density, the effective path length in the most central collision is estimated to be about 3.5 fm. Using Eq. 7.5, the 10 GeV parton would lose 2.6 GeV on an average, which is consistent with the empirical estimation from Eq. 7.18. Taking $1/\tau$ evolution of the energy density, the averaged energy loss can be approximately expressed as:

$$\left\langle \frac{dE}{dL} \right\rangle \approx \frac{dE_0}{dL} \frac{2\tau_0}{R}, \quad (7.19)$$

where dE_0/dL is the initial energy loss. In the most central collisions, the $\langle dE/dL \rangle$ of 10 GeV/c parton is 0.75 (GeV/fm) and the initial energy loss is 4.3 GeV/fm on the assumption of formation time $\tau_0 = 0.6$ fm. The initial energy loss is about 10 times larger than the energy loss of

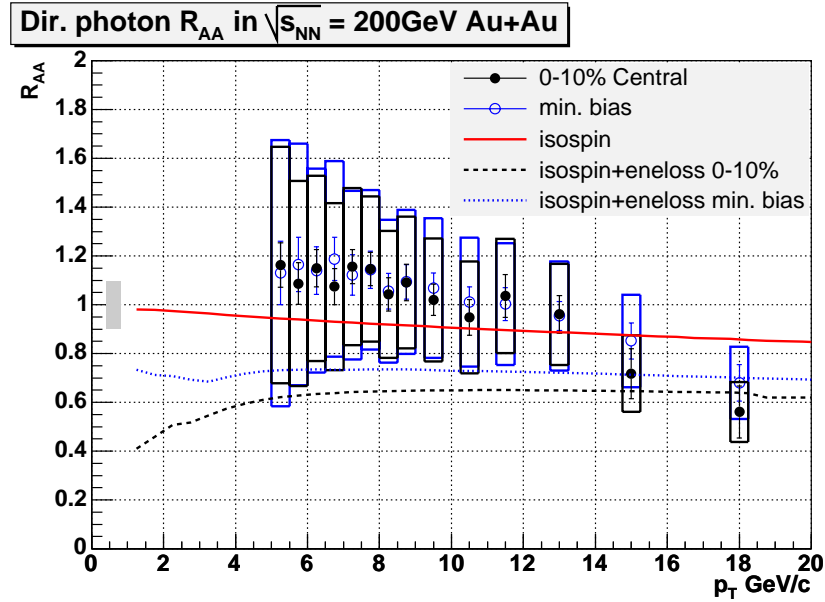


Figure 7.6: Comparison of Direct photon R_{AA} with the calculation which takes jet-quenching effect and isospin effect into account for minimum bias and 0-10 % central events. The fragmentation photon is assumed to be suppressed as well as π^0 , where the quenching factor is estimated empirically based upon Eq. 7.18.

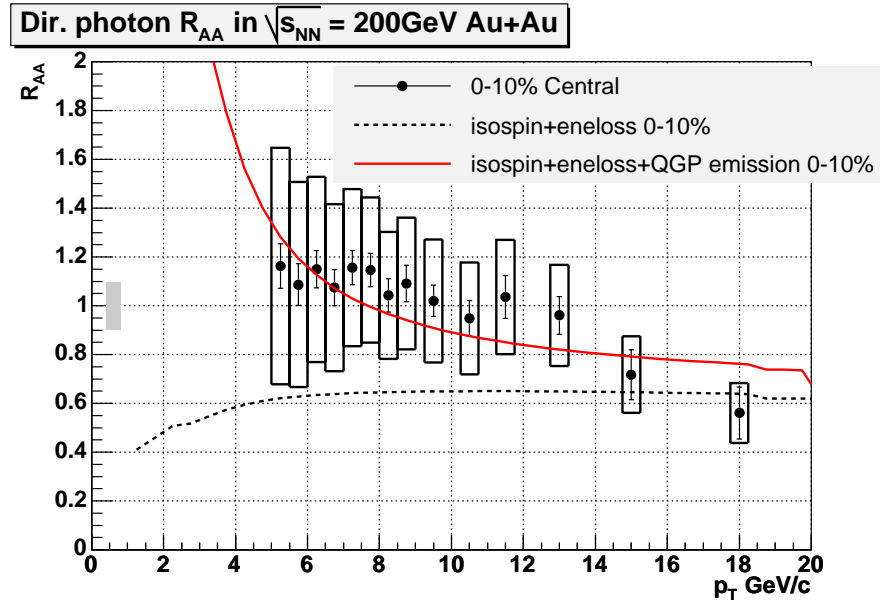


Figure 7.7: Comparison of Direct photon R_{AA} with the calculation which takes isospin effect, jet energy loss, and the emission from QGP into account. The isospin effect and jet energy loss is estimated empirically, and the numerical result in [211] is used for the emission from QGP, such as thermal emission and jet-photon conversion.

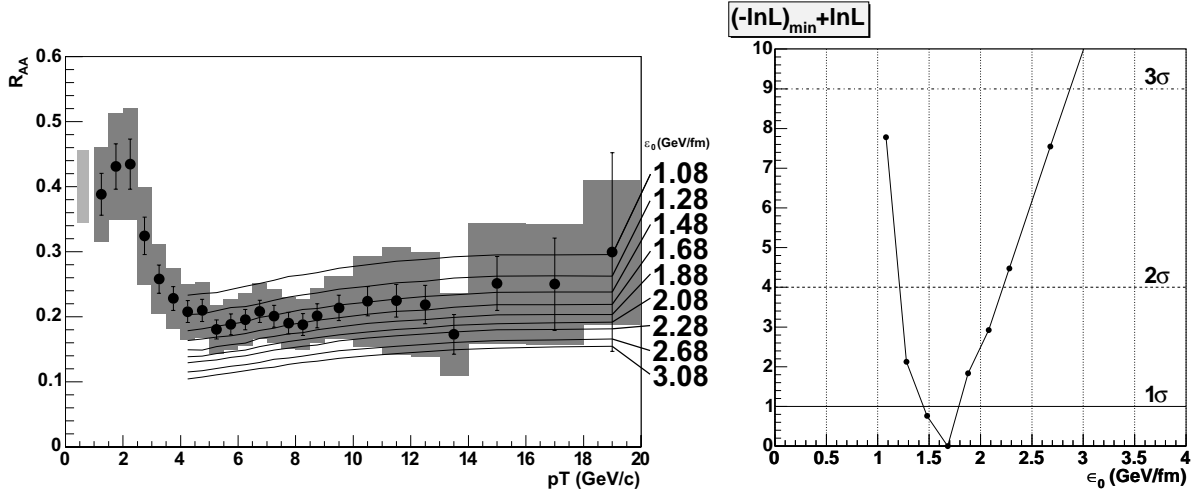


Figure 7.8: Likelihood function ratio as a function of energy loss parameter in Higher Twist formalism. Left: comparison of the data with the theoretical expectations which employ the Higher Twist formalism by H. Zhang et al. [240]. Right: Likelihood function ratio as a function of energy loss parameter in Higher Twist formalism.

partons in normal nuclear matter $dE_0/dL = 0.5 \text{ GeV}/\text{fm}$ which was extracted from HERMES data on DIS [225]. Since the parton energy loss in the thin plasma limit is proportional to the gluon number density, one can conclude that the initial gluon density reached in the central Au+Au collisions at 200 GeV should be about 10 times higher than the gluon density in a normal Au nucleus.

The theoretical calculations, where effective initial gluon density (dN_{eff}^g/dy) is free parameter, are also provided by I. Vitev who uses GLV formalism. According to the comparison with the theoretical calculation as shown in Fig. 7.9, the effective initial gluon density is estimated to be:

$$\frac{dN_{eff}^g}{dy} = \frac{dN^g}{dy} + \frac{C_F}{C_A} \frac{dN^{q+\bar{q}}}{dy} = 1300^{+300}_{-100}, \quad (7.20)$$

where $C_F/C_A = 5/9$ is the ratio of color Casimir.

On the other hand, the total parton density $dN^{parton}/y = dN^g/y + dN^{q+\bar{q}}/y$ is estimated to be ~ 1490 based upon the hydrodynamical model which is developed to reproduce kinetic and chemical equilibrium state of quarks and gluons, and its dynamical evolution [159]. The model succeeds to reproduce the soft hadron production [157]. From the combination of two estimation, the quark and gluon density can be estimated to be $dN^{q+\bar{q}}/y = 340$ and $dN^g/y = 1150$, respectively. In the case of chemical equilibrium, the gluon density is estimated to be ~ 550 (in the case of $N_{flavor} = 3$) based upon the result from hydrodynamical calculation, which is smaller than given gluon density, 1150. It can be interpreted as that chemical equilibrium is not formed yet at the time when hard-scattered partons pass through the bulk matter, and the matter is still gluon dominated. Just after the initial collision, the overlap region is expected

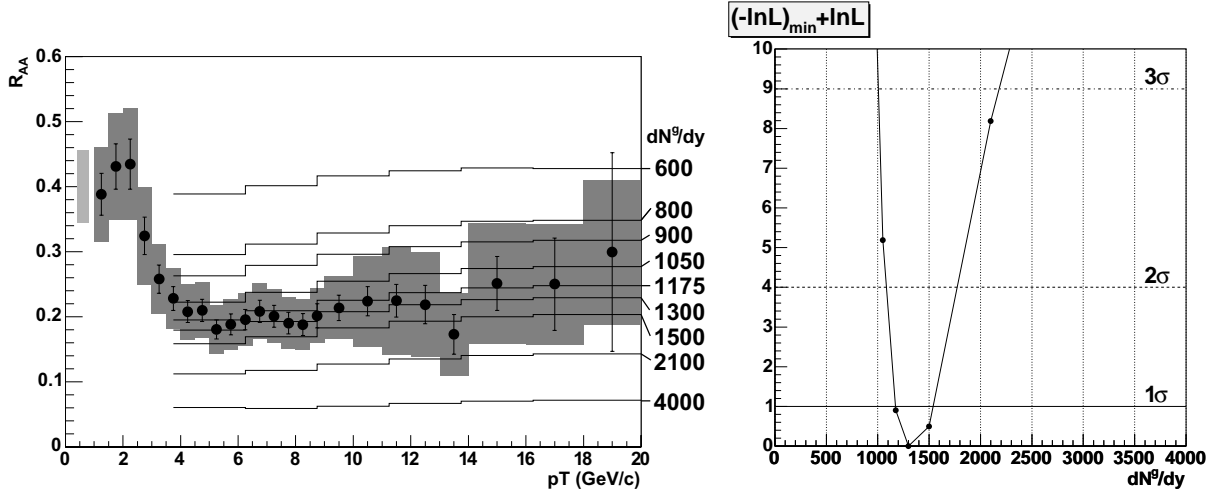


Figure 7.9: Likelihood function ratio as a function of energy loss parameter in GLV formalism [214]. Left: comparison of the data with the theoretical expectations which employ the GLV formalism by I. Vitev. Right: Likelihood function ratio as a function of energy loss parameter in GLV formalism.

to be dominated by gluons which have small Bjorken x , then the quark density increase by the reaction of gluon fusion ($gg \rightarrow q\bar{q}$) mainly. This picture of the dynamical evolution can be supported by the large gluon density estimated from the π^0 suppression.

If gluon dominated plasma is formed with the formation time of 0.6 fm^\dagger , the initial gluon density is estimated as:

$$\rho(\tau_0) = \frac{1}{S\tau_0} \frac{dN^g}{dy} = 17 \text{ [fm}^{-3}\text{].} \quad (7.21)$$

where S is the effective area of nuclei ($S \sim 120 \text{ fm}^2$ for Au). In the free gas case, the gluon density can be represented as:

$$\rho(T) = d_{gluon} \int_0^\infty \frac{1}{e^{p/T} - 1} \frac{4\pi p^2 dp}{(2\pi^3)}, \quad (7.22)$$

$$= \frac{d_{gluon}}{\pi^2} \zeta[3] \cdot T^3, \quad (7.23)$$

where d_{gluon} is the degree of freedom of gluons and $\zeta[3]$ is the integration of Bose-Einstein distribution. The $d_{gluon} = 2(\text{polarization}) \times 8(\text{color})$, and $\zeta[3] = 1.2$, the initial temperature (T_0) is about 400 MeV. In addition, the energy density of gluons is:

$$\epsilon(T = T_0) = d_{gluon} \frac{\pi^2}{30} T^4 \quad (7.24)$$

[†]In order to reproduce the experimentally observed strong elliptic flow at RHIC, the formation time of the QGP is required to be $0.6 - 1.0 \text{ fm}$ in hydrodynamics[160, 158]

$$= \frac{\pi^4}{30\zeta[3]} \cdot \rho(\tau_0) \cdot T \quad (7.25)$$

$$\approx 18 \text{ [GeV/fm}^3\text{]} \quad (7.26)$$

which support that the energy density of high dense matter produced by RHIC is 100 times larger than the energy density of normal nuclear matter (0.14 GeV/fm^3).

This measurement of the initial energy density is in agreement with other independent measurements:

- The estimation of energy density from the measured rapidity density of charged hadrons via the Bjorken formula [33, 83] supports $\epsilon_{Bj}\tau \sim 6 \text{ (GeV/fm}^2/c\text{)}$ in the most central Au+Au collisions at $\sqrt{s_{NN}} = 200 \text{ GeV}$. If the formation time of QGP is assumed to be 0.6 fm, the initial energy density is $\sim 10 \text{ GeV/fm}^3$.
- The initial energy density of the QGP required in hydrodynamical model to reproduce the observed strong elliptic flow at RHIC is $11 - 23 \text{ (GeV/fm}^3\text{)}$ [210, 160, 174, 158].

7.3 Comparison of $\pi^0 R_{AA}$ with single electron R_{AA} from heavy quark semi-leptonic decay

Strong suppression observed for high- p_T π^0 indicates that high- p_T scattered partons suffer a significant energy loss by gluon radiations in an extremely dense matter. At the parton level, most of the high- p_T π^0 s are expected to be the leading particle of light quarks (up and down quarks). Heavy quarks (charm and bottom quarks) are also interesting probes for the matter formed in heavy ion collisions. They are produced in the initial hard collisions via gluon fusion, and it is expected that NLO pQCD calculation can describe the production cross section of them because of their large quark masses. At the Tevatron, charm and beauty productions are studied and well described by NLO pQCD within the uncertainties [8, 109]. They propagate through the created medium, and may interact differently with the medium due to their heavy mass. There are theoretical predictions that the energy loss of heavy quarks is smaller than that of light partons. In vacuum, the gluon radiation is suppressed at $\theta < m_q/E_q$, where θ is the angle of gluon radiation with respect to quark direction, which is called “dead cone” effect [123].

For the study of behavior of heavy quarks, an indirect measurement was performed in the RHIC experiments, which is to measure single electrons ($0.3 < p_T < 9 \text{ GeV}/c$) from semi-leptonic weak decays of heavy quarks ($c/b \rightarrow D \rightarrow e+X$) in p+p and Au+Au collisions at $\sqrt{s_{NN}} = 200 \text{ GeV}$ [5, 11, 13, 30, 37]. Figure 7.10 shows single electron R_{AA} measured by PHENIX experiment up to $10 \text{ GeV}/c$ compared with $\pi^0 R_{AA}$. Very strong suppression is clearly seen at high- p_T , which is comparable to the suppression observed for π^0 . For low- p_T region ($p_T < 2 \text{ GeV}/c$), R_{AA} is consistent with unity. It indicates binary scaling of the total heavy-flavor yield works.

In the Fig. 7.10, the expected R_{AA} of light quarks (up and bottom), charm, bottom, gluon and single electrons from heavy flavor semi-leptonic decay are shown in the case of

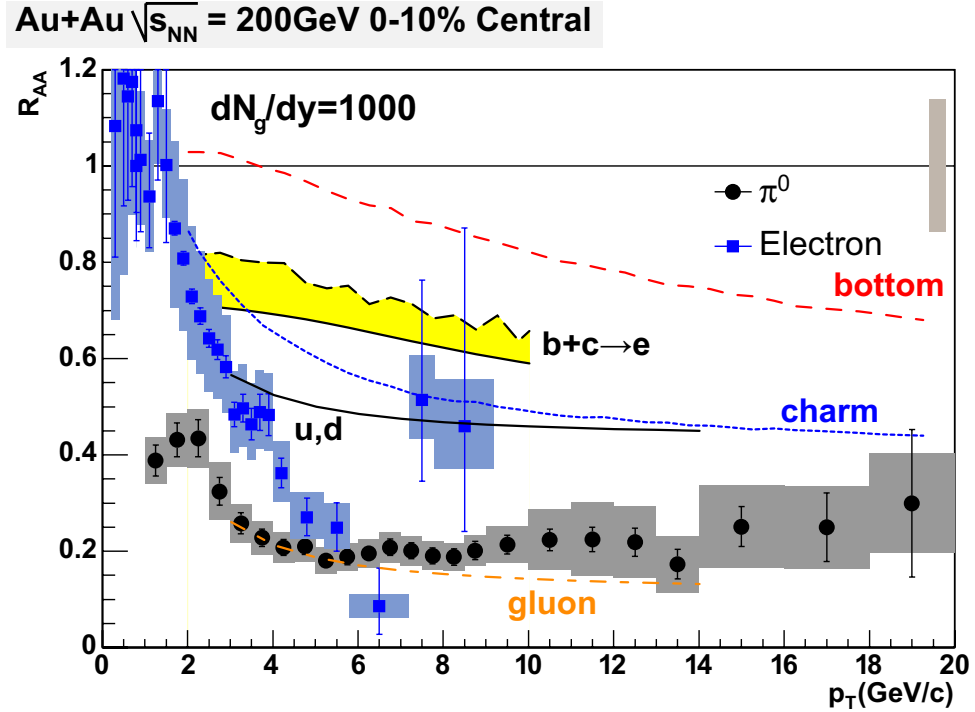


Figure 7.10: Comparison of the π^0 R_{AA} with single electron R_{AA} in central collisions (0-10 %) [11]. The error boxes on electron data depict point-by-point uncertainties of combined statistical and systematic errors, derived from Au+Au and p+p data. The box around $R_{AA} = 1$ in the right side shows the uncertainty of T_{AA} . In addition, the expected R_{AA} of light quarks (up and bottom), charm, bottom, gluon and single electrons from heavy flavor semi-leptonic decay are shown in the case of $dN^g/dy = 1000$ (from [122]).

$dN^g/dy = 1000$, which are estimated based upon the π^0 R_{AA} as described in previous section [122]. The theoretical calculation which takes the parton energy loss due to the gluon radiation into account can not reproduce the R_{AA} of the experimental single electron data. While there is an ambiguity on charm to bottom ratio which would affect the R_{AA} pattern, there should be other effect to explain the large suppression of single electrons. Based only on the single electron R_{AA} , the initial gluon density is estimated to be ~ 3500 , which is extremely larger than the estimation based on other experimental data and that from theoretical calculation.

One of the possible effects is collisional energy loss. The parton energy loss due to the elastic scattering of partons in dense matter was predicted as mentioned in Sec. 2.3.4. Recently, it is claimed that collisional and radiative energy losses are comparable in the case of heavy quarks, and it should strongly affect the heavy quarks R_{AA} [187, 121, 125]. However, the collisional energy loss affects the light quark production (i.e. π^0 R_{AA}) as well as heavy quark, while light quark is expected to emit the gluons easily and collisional energy loss is not dominant rather than heavy quark. It would affect the estimation of initial gluon density (dN^g/dy) based upon the π^0 R_{AA} , and the energy density of 18 GeV/fm³ might be over estimation. There are theoretical efforts to establish the model which can explain the strong suppression of both π^0

and single electron quantitatively [17, 156], which will tell the jet quenching mechanism and the detail information of extreme state of matter. Especially, an effort was made to include the collisional energy loss into GLV formalism to reproduce both π^0 and single electron R_{AA} [233]. It is important to measure heavy quark mesons directly, or to distinguish the charm and bottom contribution to the single electron production.

Chapter 8

Conclusion

Neutral pions and direct photons are measured up to 20 GeV/c at mid-rapidity with RHIC-PHENIX spectrometer in Au+Au collisions at $\sqrt{s_{NN}} = 200$ GeV. From the comparison with binary scaled p+p data, the nuclear modifications on the neutral pion and direct photon production in Au+Au collisions are studied as functions of p_T and centrality.

In the most central collisions, the suppression of neutral pion production at high- p_T has been observed, compared to the yield in p+p collision at same \sqrt{s} scaled by the number of underlying nucleon-nucleon collisions in Au+Au. The suppression is very strong by a factor of ~ 5 , and is almost constant from $p_T \sim 1$ GeV/c up to $p_T \sim 20$ GeV/c. In contrast, the direct photon yields in Au+Au collisions are in good agreement with the scaled p+p data.

Since most of high- p_T direct photons originate from initial hard-scattering processes and do not interact with the matter strongly, the agreement between measurement and the scaled p+p data of the direct photon yield suggests the initial hard-scattering probability is not reduced in the Au+Au collisions. It supports that point-like scaling, and binary scaling of high- p_T hadron production relative to p+p collisions is well represented by the Monte Carlo calculation which employs Glauber model. Therefore, the strong suppression of neutral pion production can be understood as due to the interaction of hard scattered partons in the created dense matter. While the direct photon yields in the most central Au+Au collisions seem to be below the binary scaled yield in p+p collisions at very high- p_T , this deviation can be interpreted as the consequence of the multiple effect on direct photon production: isospin effect, jet-quenching on fragmentation photon, and jet-photon conversion.

The strong neutral pion suppression is interpreted as the consequence of parton energy loss through gluon bremsstrahlung in the created dense matter (jet quenching). Theoretical schemes to reproduce the suppression have been developed, and major schemes can reproduce the p_T and centrality dependence of neutral pion suppression. Based on the comparison of neutral pion suppression pattern with a theoretical calculation by I. Vitev who employs GLV formalism, the effective gluon density (dN_{eff}^g/dy) of the dense matter produced in $\sqrt{s_{NN}} = 200$ GeV Au+Au collisions are estimated quantitatively to be about 1300^{+300}_{-100} . On the assumption of the formation of gluon dominated plasma with the formation time of 0.6 fm, the energy density is estimated to be 18 GeV/fm 3 from the gluon density, $dN^g/dy = 1300$. It is much larger than the expected critical energy density for QGP phase transition (1 GeV/fm 3).

Acknowledgment

It is a great pleasure to express my science gratitude to Prof. Hideki Hamagaki who has led me to this exciting and interesting field of science. I appreciate him for his continuous encouragement and appropriate teaching. He is also the PHENIX-J group leader and I thank the continuous financial support for the work at BNL. I would like to thank Dr. Gabor David and Dr. Takao Sakaguchi for their grate contribution to the entire parts of the study. Without their kind help, my work could have been reduced to being beside the mark. I would also like to pay my respect to Dr. Kyoichiro Ozawa for his persevering guidance, discussion, and support.

The financial support from PHENIX-J and RIKEN was essential to continue the work. The PHENIX experiment is supported by the U. S. Department of Energy under contracts to U. S.-Japan High Energy Physics Collaboration Treaty. I'd like to express many thanks to the all member of the PHENIX-J group for their support and help. I would like to thank the chief scientist of the radiation laboratory at RIKEN, Dr. Hideto En'yo for the support.

I would also like to thank all PHENIX collaborators for their excellent discussions, ideas and help. I am deeply grateful to the former PHENIX spokesperson, Prof. William A Zajc, current spokesperson Prof. Barbara Jacak, and deputy spokesperson, Dr. Yasuyuki Akiba, for their heartful administration of entire collaboration. I would like to thank Dr. Brant Johnson, Dr. Edward O'Brian, Prog. Jamie L. Nagle, and Dr. John Haggerty for their help and insight. I appreciate the kind instruction of the PHENIX analysis framework by Dr. Chris Pinkenburg, who debugged my messy programs. I'd like to thank the π^0 /photon analysis group, especially Mr. Baldo Sahlmueller, Dr. Christian Klein-Boesing, Prof. Saskia Mioduszewski, Mr. Robert Vertesi, Mr. Jozsef Imrek, Dr. Carla Vale, Dr. David L. Winter, Ms. Misaki Ouchida, and Dr. Martin L. Purschke. I also thank the p+p analysis group, especially Dr. Hisayuki Torii, Dr. Kensuke Okada and Dr. Sasha Bazilevsky. Discussions with them are important for me to understand the characteristics of electromagnetic calorimeter, and to learn the basics of physics analysis. I got the some idea for the analysis during the talk with them. I would also like to thank the members of the PHENIX Hard Scattering working group for their good ideas in the development of this analysis especially Dr. Michael J. Tannenbaum, and the conveners Dr. Jianguyong Jia, Dr. Justin Frantz, Dr. Stefan Bathe and Dr. Henner Buesching.

I would also like to thank all my other CNS, University of Tokyo and PHENIX collaborators for their excellent discussions, ideas and help. In particular, I would also like to thank my fellow CNS graduate students, past and present, Dr. Koichi Kino, Dr. Takuma Horaguchi, Mr. Takashi Matsumoto, Mr. Soichiro Kametani, Dr. Fukutaro Kajihara, Dr. Taku Gunji, Mr. Narumi Kurihara, Mr. Susumu X. Oda, Mr. Yuhei Morino, Mr. Syota Saito, Mr. Yorito L. Yamaguchi, Mr. Yoki Aramaki, Mr. Satoshi Sano and Mr. Akihisa Takahara. The member of the

CNS group are very helpful not only for my work but also my spending good time at BNL. I'd like to express many thanks to them.

I hope to express my thanks to all the staff of the RHIC project, Collider-Accelerator and Physics Department at BNL. Most of this analysis was done using RHIC computing facility (RCF) and RIKEN PHENIX Computing Center in Japan (CCJ). I appreciate all the staff of RCF and CCJ. I thank particularly Dr. Yasushi Watanabe and Dr. Satoshi Yokkaichi for their kind help and useful suggestions, which is crucial to process the large amount computing jobs effectively.

I appreciate all heartful support by the CNS and RIKEN secretaries, Ms. Midori Hirano, Ms. Kazuko Takeuchi, Ms. Ikuko Yamamoto, Ms. Takako Endo, Ms. Yukino Kishi, Ms. Naho Suzuki, Ms. Miwa Yamaguchi, Ms. Yuko Fujiwara, Mr. Ryosuke Maruyama, Ms. Tae-ko Ito and Ms. Noriko Kiyama for their support of the research. I express my appreciation to the BNL secretaries, Ms. Donna Earley, Ms. Jo-Ann Nastaja, Ms. Rachel Cacace and Ms. Lorraine Barry.

I am grateful to Prof. Hiroshi Sakamoto, Prof. Hiroyoshi Sakurai, Prof. Tomohiro Uesaka and Dr. Tetsufumi Hirano for their valuable advice. I would like to express my appreciation to Prof. Katsuo Tokushuku for his truly relevant advice and proof-readings.

Finally, I'd like to give thanks to my parents, Tsutomu and Takako, sisters, Yasuko and Yumiko, and wife for their encouragement. My wife, Aya Isobe, was keeping up with me even at BNL, and gave me moral support in a lot of ways.

Appendix A

Kinematic Variables

Lorentz Transformation

The four vector notation is :

$$x = \begin{pmatrix} t \\ x_1 \\ x_2 \\ x_3 \end{pmatrix} = \begin{pmatrix} x_0 \\ x_1 \\ x_2 \\ x_3 \end{pmatrix}, \quad x^2 = t^2 - \vec{x}^2 = x_0^2 - (x_1^2 + x_2^2 + x_3^2) \quad (\text{A.1})$$

Transverse Momentum

In this section the z-axis is chosen as the beam direction. The transverse momentum is defined in terms of two momentum components of a particle:

$$p_T^2 = p_x^2 + p_y^2 \quad (\text{A.2})$$

Rapidity and Pseudorapidity variable

$$\gamma = \frac{E}{m}, \quad \vec{\beta} = \frac{\vec{p}}{E}, \quad \vec{\beta}\gamma = \frac{\vec{p}}{m} \quad (\text{A.3})$$

The rapidity variable y of the particle is defined as:

$$y = \frac{1}{2} \ln \frac{(1 + \beta)}{(1 - \beta)} = \frac{1}{2} \ln \frac{(E + p_z)}{(E - p_z)} \quad (\text{A.4})$$

where, E is the energy of the particle, p_z is momentum fraction in z-axis. In the nonrelativistic limit, the rapidity of a particle travelling in the longitudinal direction is equal to the velocity of the particle in the units of the speed of light. The rapidity variable is transformed under a boost in z-axis with the velocity β as:

$$y \rightarrow y + \tanh^{-1} \beta \quad (\text{A.5})$$

Another variable which characterize the detected particle is pseudorapidity variable η .

$$\eta = -\ln[\tan(\frac{\theta}{2})] \quad (\text{A.6})$$

where θ is the angle between the particle momentum \mathbf{p} and z-axis. Since pseudorapidity requires only one measurement of θ , it is useful. Pseudorapidity η can be written in terms of rapidity y as:

$$\eta = \frac{1}{2} \ln \left[\frac{\sqrt{m_T^2 \cosh^2 y - m^2} + m_T \sinh y}{\sqrt{m_T^2 \cosh^2 y - m^2} - m_T \sinh y} \right] \quad (\text{A.7})$$

where m_T is the transverse mass of a particle:

$$m_T^2 = E^2 + \mathbf{p}_T^2 \quad (\text{A.8})$$

Center of Mass Energy

The center of mass energy of two colliding nuclei with p_i^u and rest mass m_i is calculated from the Lorenz invariant s variable:

$$s = (p_1 + p_2)^u \cdot (p_1 + p_2)_u \quad (\text{A.9})$$

Then the center of mass enrgy is defined as the square-root of s:

$$\sqrt{s} = \sqrt{m_1^2 + 2E_1E_2 - 2\mathbf{p}_1\mathbf{p}_2 + m_2^2} \quad (\text{A.10})$$

Where m_1 and m_2 represent the rest mass of the particle, respectively. The center of mass energy achieved by RHIC Year-2001 run is $\sqrt{s} = 200 \text{ GeV}$

The invariant mass M of the parent particle in two-body decay is defined as:

$$M = \sqrt{(E_1 + E_2) - (\mathbf{p}_1 + \mathbf{p}_2)} \quad (\text{A.11})$$

where E_i and \mathbf{p}_i are energy and momentum of daugter particles.

Appendix B

Functions to fit p_T spectrum

- Power-law

$$E \frac{d^3\sigma}{dp^3} = \frac{A}{p_T^n} \quad (\text{B.1})$$

According to QCD, it should be $n \simeq 8.1$ at high- p_T .

- Hagedorn

$$E \frac{d^3\sigma}{dp^3} = \frac{A}{(1 + p_T/p_0)^n}, \quad (\text{B.2})$$

which is Used by Hagedorn [153], UA1 and so on.

- Modified Hagedorn

$$E \frac{d^3\sigma}{dp^3} = \frac{A}{(\exp(-a \cdot T) + p_T/p_0)^n} \quad (\text{B.3})$$

- Combination of Power-law and Hagedorn

$$E \frac{d^3\sigma}{dp^3} = T(p_T) \cdot \frac{A_1}{(1 + p_T/p_0)^{n_1}} + (1 - T(p_T)) \cdot \frac{A_2}{p_T^{n_2}}, \quad (\text{B.4})$$

where $T(x)$ is the Wood-Saxon type transition function:

$$T(x) = \frac{1}{1 + \exp(s \cdot x + t)} \quad (\text{B.5})$$

Appendix C

Fits to data with Correlated Systematic Errors

Comparison of the theoretical predictions with experimental data including the correlated systematic errors is complicated when the systematic errors are taken as r.m.s. and assumed to be Gaussian distributed. Following is the proposed method in PHENIX collaboration to constrain the physics parameter from obtained data [208]. In the case of only point-to-point uncorrelated errors (statistical and/or systematic), the best parameter fit can be calculated via a log likelihood (or in the Gaussian limit χ^2) method [237], on the assumption of Gaussian distributed and characterization of the error by a root-mean square (RMS).

Prior to the probability of the given data, the likelihood function \mathcal{L} is defined as the following. y_1, y_2, \dots, y_n are n samples from a population with normalized probability density function $f(y, \vec{p})$ where \vec{p} represents a vector of k parameters. For instance y_i could represent a measurement of a cross section at the position x_i , where the probability density of the measurement is Gaussian distributed:

$$f(y, \vec{p}) = \frac{1}{\sqrt{2\pi\sigma^2}} \exp \frac{-(y - \mu)^2}{2\sigma^2}, \quad (\text{C.1})$$

where $\mu \equiv \langle y \rangle$, and σ stands for 1 standard deviation. If the samples are independent, then the likelihood function is defined as:

$$\mathcal{L} = \prod_i f(y_i, \vec{p}) = \frac{1}{\sigma_1 \sigma_2 \dots \sigma_n \sqrt{2\pi^n}} \exp - \left[\sum_{i=1}^n \frac{(y_i - \mu_i)^2}{2\sigma_i^2} \right]. \quad (\text{C.2})$$

If the samples are correlated for example via correlated systematic errors, then the full variance matrix must be used.

$$V_{ij} = \langle (y_i - \mu_i)(y_j - \mu_j) \rangle. \quad (\text{C.3})$$

The likelihood function becomes the more general form:

$$\mathcal{L} = \frac{1}{\sqrt{|V|}} \frac{1}{\sqrt{2\pi^n}} \exp - \left[\sum_{i=1}^n \sum_{j=1}^n \frac{(y_i - \mu_i)V_{ij}^{-1}(y_j - \mu_j)}{2} \right], \quad (\text{C.4})$$

where $|V|$ is the determinant of the variance matrix V . Note that Eq. C.4 reduces to Eq. C.2 if the correlations vanish so that the covariances are zero and V_{ij} is diagonal:

$$V_{ij} = \langle (y_i - \mu_i)(y_j - \mu_j) \rangle = \delta_{ij} \langle (y_i - \mu_i)^2 \rangle = \delta_{ij}\sigma_i^2. \quad (\text{C.5})$$

Gaussian probability distributions are common and there is a theorem of likelihood ratios for composite hypotheses, it is convenient to use the logarithm of the likelihood.

$$-2 \ln \mathcal{L} = \ln |V| + n \log 2\pi + \sum_{i=1}^n \sum_{j=1}^n (y_i - \mu_i) V_{ij}^{-1} (y_j - \mu_j). \quad (\text{C.6})$$

As described at Sec. 5.5.3, there are three kinds of errors: A) point-to-point random systematic errors and statistic error, B) correlated systematic errors, and C) overall systematic errors by which all the points move by the same fraction. The type B and type C systematic variations are represented as:

$$\Delta'y^b(sys)_i \equiv b_i \Delta z_b = b_i \epsilon_b \sigma_b = \epsilon_b \sigma_{b_i} \quad (\text{C.7})$$

$$\Delta'y^c(sys)_i / y_i \equiv \Delta z_c = \epsilon_c \sigma_c, \quad (\text{C.8})$$

where σ_{b_i} is known for all points and may be of either sign, as it is possible that one point could move up while its neighbor moves down; and by definition σ_c is the same for all points. Then the likelihood function which includes the variation ϵ_b and ϵ_c is:

$$\mathcal{L} = \prod_i f(y_i, \vec{p}) = \frac{1}{\sigma_1 \sigma_2 \dots \sigma_n \sigma_b \sigma_c} \frac{1}{\sqrt{2\pi}^{(n+2)}} \exp - \left[\sum_{i=1}^n \frac{(y_i + \epsilon_b \sigma_{b_i} + \epsilon_c y_i \sigma_c - \mu_i(\vec{p}))^2}{2\sigma_i^2} + \frac{\epsilon_b^2}{2} + \frac{\epsilon_c^2}{2} \right] \quad (\text{C.9})$$

where the last two terms represent $\Delta^2 z_b / (2\sigma_b^2) = \epsilon_b^2 \sigma_b^2 / (2\sigma_b^2)$ and $\Delta^2 z_c / (2\sigma_c^2) = \epsilon_c^2 \sigma_c^2 / (2\sigma_c^2)$, since the probability of the systematic displacements $f(\Delta z_{b,c})$ as Gaussian is assumed.

Then the likelihood ratio test is used to establish the confidence interval of the theoretical predictions $\mu_i(\vec{p})$. One can use

$$-2 \ln \mathcal{L} = \left[\sum_{i=1}^n \frac{(y_i + \epsilon_b \sigma_{b_i} + \epsilon_c y_i \sigma_c - \mu_i(\vec{p}))^2}{\sigma_i^2} + \epsilon_b^2 + \epsilon_c^2 \right], \quad (\text{C.10})$$

because the ratio of the likelihood of a given set of parameters \vec{p} to the maximum likelihood will be taken eventually when all the parameters ϵ_b , ϵ_c and \vec{p} are varied (the minimum value of Eq. C.10, which is called χ^2) so that the terms preceding the exponential in Eq. C.9 cancel because they are not varied. Equation C.10 follows the χ^2 -distribution with $n + 2$ degrees of freedom because it is the sum of $n + 2$ independent Gaussian distributed random variables.

Let $\hat{\epsilon}_b$, $\hat{\epsilon}_c$, \vec{p} represent the values of the parameters which give the maximum likelihood and let \vec{p}_0 represent any other set of parameters whose significance is evaluated of which k are constrained to be specific values and the rest are allowed to take on any value by re-minimizing $-2 \ln \mathcal{L}$. For large values of n , the “likelihood ratio”, $-2 \ln[\mathcal{L}(\vec{p}_0)/\mathcal{L}(\vec{p})]$, is χ^2 -distributed with k degrees of freedom.

First fit the theory to the data by minimizing Eq. C.10 by varying all the parameters to find $\hat{\epsilon}_b$, $\hat{\epsilon}_c$, \vec{p} . If the χ^2_{\min} for this fit for the $n + 2 - (m + 2) = n - m$ degrees of freedom, where m are the number of parameters in \vec{p} , is acceptable, then the theory is not rejected at this level. Then a confidence interval for testing any other set of k parameters constrained to specific values, \vec{p}_0 , can be found by again finding the minimum of Eq. C.10 for the k fixed values of \vec{p}_0 , by letting all the other parameters including ϵ_b and ϵ_c vary. The “likelihood ratio” $-2 \ln[\mathcal{L}(\vec{p}_0)/\mathcal{L}(\vec{p})] = -2[\ln \mathcal{L}(\vec{p}_0) - \ln \mathcal{L}(\vec{p})]$, colloquially $\chi^2(\vec{p}_0) - \chi^2_{\min}$ is χ^2 -distributed with k degrees of freedom, from which the confidence interval on the parameters can be evaluated.

Appendix D

Centrality Information

D.1 Boundary of Centrality

The the boundaries of centralities for ϕ_{cent} defined as Eq. 5.3 is determined Using the run segment (Run 116830 – 118898).

boundary	0-1 %	1-2 %	2-3 %	3-4 %	4-5 %	5-6 %	6-7 %	7-8 %	8-9 %	9-10 %
0	1.41902	1.37130	1.32578	1.28002	1.23386	1.18750	1.14094	1.09434	1.04794	1.00170
10	0.95578	0.91054	0.86594	0.82230	0.77982	0.73846	0.69822	0.65918	0.62162	0.58530
20	0.55038	0.51686	0.48474	0.45406	0.42458	0.39626	0.36922	0.34338	0.31870	0.29510
30	0.27258	0.25106	0.23046	0.21078	0.19194	0.17398	0.15674	0.14030	0.12454	0.10946
40	0.09494	0.08106	0.06778	0.05502	0.04278	0.03090	0.01954	0.00858	-0.00202	-0.01222
50	-0.02210	-0.03162	-0.04090	-0.04990	-0.05870	-0.06722	-0.07554	-0.08370	-0.09170	-0.09954
60	-0.10730	-0.11494	-0.12254	-0.13006	-0.13754	-0.14506	-0.15258	-0.16014	-0.16774	-0.17546
70	-0.18330	-0.19134	-0.19954	-0.20802	-0.21682	-0.22598	-0.23566	-0.24582	-0.25670	-0.26830
80	-0.28090	-0.29466	-0.30982	-0.32678	-0.34598	-0.36806	-0.39434	-0.42650	-0.46758	-0.52382
90	-0.60930	-0.77366	-1.54286							

Table D.1: Boundary of Centrality in $\sqrt{s_{\text{NN}}} = 200$ GeV Au+Au collisions.

D.2 Glauber Table

The results of the Glauber calculations are listed below. The centrality classes in the simulation were selected with the simulated BBC and ZDC signal for $\sqrt{s_{NN}} = 200$ GeV calculation [196].

Centrality	$\langle N_{part} \rangle$	sys. error	$\langle N_{coll} \rangle$	sys. error	T_{AA} (mb $^{-1}$)	sys. error	$\langle b \rangle$ (fm)	sys. error
0-10 %	325.2	3.3	955.4	93.6	22.75	1.56	3.2	0.2
10-20 %	234.6	4.7	602.6	59.3	14.35	1.00	5.7	0.3
20-30 %	166.6	5.4	373.8	39.6	8.90	0.72	7.4	0.3
30-40 %	114.2	4.4	219.8	22.6	5.23	0.44	8.7	0.4
40-50 %	74.4	3.8	120.3	13.7	2.86	0.28	9.9	0.4
50-60 %	45.5	3.3	61.0	9.9	1.45	0.23	11.0	0.4
60-70 %	25.7	3.8	28.5	7.6	0.68	0.18	11.9	0.5
70-80 %	13.4	3.0	12.4	4.2	0.30	0.10	12.8	0.5
80-92.3 %	6.3	1.2	4.9	1.2	0.12	0.03	14.1	0.6
min. bias	109.1	4.1	257.8	25.4	6.14	0.45	9.5	0.4

Table D.2: Results of $\sqrt{s_{NN}} = 200$ GeV Au+Au Glauber Calculations.

Appendix E

Neutral Pion Data Tables

E.1 Neutral Pion Invariant Yield in $\sqrt{s_{\text{NN}}} = 200$ GeV Au+Au Collisions

p_T	$1/2\pi p_T N_{\text{eve}} \cdot d^2N/dp_T dy$	statistic error	p_T uncorrelated error	p_T correlated error
1.25	3.0018e+00	6.4574e-02 (2.15 %)	2.1146e-01 (7.04 %)	3.3232e-01 (11.1 %)
1.75	5.4902e-01	1.0245e-02 (1.87 %)	3.8227e-02 (6.96 %)	6.3331e-02 (11.5 %)
2.25	1.1630e-01	2.1708e-03 (1.87 %)	8.0981e-03 (6.96 %)	1.4365e-02 (12.4 %)
2.75	2.2590e-02	4.2514e-04 (1.88 %)	1.5739e-03 (6.97 %)	2.9285e-03 (13 %)
3.25	5.3896e-03	1.1269e-04 (2.09 %)	3.7870e-04 (7.03 %)	7.2510e-04 (13.5 %)
3.75	1.6282e-03	3.6934e-05 (2.27 %)	1.1530e-04 (7.08 %)	2.1905e-04 (13.5 %)
4.25	5.5705e-04	1.4129e-05 (2.54 %)	3.9950e-05 (7.17 %)	7.4944e-05 (13.5 %)
4.75	2.2959e-04	6.3255e-06 (2.76 %)	1.6650e-05 (7.25 %)	3.0889e-05 (13.5 %)
5.25	8.7425e-05	2.7791e-06 (3.18 %)	6.4898e-06 (7.42 %)	1.1762e-05 (13.5 %)
5.75	4.3578e-05	1.7006e-06 (3.9 %)	3.3820e-06 (7.76 %)	5.8628e-06 (13.5 %)
6.25	2.2990e-05	5.8426e-07 (2.54 %)	1.6492e-06 (7.17 %)	3.0930e-06 (13.5 %)
6.75	1.3129e-05	3.7554e-07 (2.86 %)	9.5742e-07 (7.29 %)	1.7663e-06 (13.5 %)
7.25	7.0816e-06	2.2445e-07 (3.17 %)	5.2541e-07 (7.42 %)	9.5274e-07 (13.5 %)
7.75	3.9123e-06	1.4994e-07 (3.83 %)	3.0226e-07 (7.73 %)	5.2634e-07 (13.5 %)
8.25	2.3242e-06	1.0104e-07 (4.35 %)	1.8579e-07 (7.99 %)	3.1268e-07 (13.5 %)
8.75	1.5461e-06	7.3360e-08 (4.74 %)	1.2703e-07 (8.22 %)	2.0800e-07 (13.5 %)
9.5	8.4203e-07	3.3986e-08 (4.04 %)	6.5921e-08 (7.83 %)	1.3270e-07 (15.8 %)
10.5	3.9169e-07	2.1832e-08 (5.57 %)	3.4162e-08 (8.72 %)	1.0443e-07 (26.7 %)
11.5	1.8816e-07	1.3798e-08 (7.33 %)	1.8701e-08 (9.94 %)	6.1866e-08 (32.9 %)
12.5	9.3115e-08	9.5399e-09 (10.2 %)	1.1403e-08 (12.2 %)	3.0615e-08 (32.9 %)
13.5	3.9503e-08	6.0193e-09 (15.2 %)	6.5767e-09 (16.6 %)	1.2988e-08 (32.9 %)
15	2.4368e-08	3.3471e-09 (13.7 %)	3.7249e-09 (15.3 %)	8.0120e-09 (32.9 %)
17	8.7950e-09	2.3519e-09 (26.7 %)	2.4248e-09 (27.6 %)	2.8917e-09 (32.9 %)
19	4.2788e-09	2.1403e-09 (50 %)	2.1595e-09 (50.5 %)	1.4068e-09 (32.9 %)

Table E.1: Neutral Pion Invariant Yield as a function of p_T in $\sqrt{s_{\text{NN}}} = 200$ GeV Au+Au Collisions (0-10 % Central).

p_T	$1/2\pi p_T N_{\text{eve}} \cdot d^2N/dp_T dy$	statistic error	p_T uncorrelated error	p_T correlated error
1.25	2.1682e+00	3.9709e-02 (1.83 %)	1.5077e-01 (6.95 %)	2.4004e-01 (11.1 %)
1.75	3.7304e-01	5.8233e-03 (1.56 %)	2.5693e-02 (6.89 %)	4.3031e-02 (11.5 %)
2.25	7.9305e-02	1.2171e-03 (1.53 %)	5.4574e-03 (6.88 %)	9.7954e-03 (12.4 %)
2.75	1.7814e-02	2.7652e-04 (1.55 %)	1.2266e-03 (6.89 %)	2.3094e-03 (13 %)
3.25	4.4782e-03	7.5980e-05 (1.7 %)	3.0986e-04 (6.92 %)	6.0247e-04 (13.5 %)
3.75	1.4318e-03	2.5845e-05 (1.81 %)	9.9466e-05 (6.95 %)	1.9263e-04 (13.5 %)
4.25	4.6640e-04	9.2416e-06 (1.98 %)	3.2624e-05 (6.99 %)	6.2748e-05 (13.5 %)
4.75	1.8767e-04	4.4865e-06 (2.39 %)	1.3365e-05 (7.12 %)	2.5249e-05 (13.5 %)
5.25	8.3404e-05	2.3276e-06 (2.79 %)	6.0598e-06 (7.27 %)	1.1221e-05 (13.5 %)
5.75	3.5501e-05	1.2240e-06 (3.45 %)	2.6776e-06 (7.54 %)	4.7762e-06 (13.5 %)
6.25	1.8326e-05	4.2352e-07 (2.31 %)	1.3003e-06 (7.1 %)	2.4655e-06 (13.5 %)
6.75	1.0373e-05	2.7746e-07 (2.67 %)	7.4911e-07 (7.22 %)	1.3955e-06 (13.5 %)
7.25	6.0028e-06	1.8265e-07 (3.04 %)	4.4217e-07 (7.37 %)	8.0759e-07 (13.5 %)
7.75	3.7088e-06	1.2647e-07 (3.41 %)	2.7910e-07 (7.53 %)	4.9897e-07 (13.5 %)
8.25	2.1546e-06	8.7211e-08 (4.05 %)	1.6881e-07 (7.83 %)	2.8987e-07 (13.5 %)
8.75	1.2909e-06	6.2454e-08 (4.84 %)	1.0677e-07 (8.27 %)	1.7368e-07 (13.5 %)
9.5	6.3242e-07	2.8467e-08 (4.5 %)	5.1090e-08 (8.08 %)	9.9669e-08 (15.8 %)
10.5	3.2084e-07	1.8762e-08 (5.85 %)	2.8552e-08 (8.9 %)	8.5542e-08 (26.7 %)
11.5	1.4365e-07	1.1732e-08 (8.17 %)	1.5182e-08 (10.6 %)	4.7231e-08 (32.9 %)
12.5	7.9583e-08	8.5170e-09 (10.7 %)	1.0052e-08 (12.6 %)	2.6166e-08 (32.9 %)
13.5	3.7907e-08	5.8048e-09 (15.3 %)	6.3374e-09 (16.7 %)	1.2463e-08 (32.9 %)
15	2.3421e-08	3.2202e-09 (13.7 %)	3.5830e-09 (15.3 %)	7.7006e-09 (32.9 %)
17	4.5855e-09	1.6217e-09 (35.4 %)	1.6506e-09 (36 %)	1.5076e-09 (32.9 %)
19	4.8410e-09	2.1660e-09 (44.7 %)	2.1902e-09 (45.2 %)	1.5917e-09 (32.9 %)

Table E.2: Neutral Pion Invariant Yield as a function of p_T in $\sqrt{s_{\text{NN}}} = 200$ GeV Au+Au Collisions (10-20 % Central).

p_T	$1/2\pi p_T N_{\text{eve}} \cdot d^2N/dp_T dy$	statistic error	p_T uncorrelated error	p_T correlated error
1.25	1.4336e+00	2.4662e-02 (1.72 %)	9.9279e-02 (6.93 %)	1.5871e-01 (11.1 %)
1.75	2.6121e-01	3.8132e-03 (1.46 %)	1.7933e-02 (6.87 %)	3.0132e-02 (11.5 %)
2.25	5.6073e-02	7.8469e-04 (1.4 %)	3.8424e-03 (6.85 %)	6.9259e-03 (12.4 %)
2.75	1.2582e-02	1.7813e-04 (1.42 %)	8.6265e-04 (6.86 %)	1.6312e-03 (13 %)
3.25	3.2693e-03	4.9119e-05 (1.5 %)	2.2475e-04 (6.87 %)	4.3985e-04 (13.5 %)
3.75	1.0795e-03	1.7736e-05 (1.64 %)	7.4556e-05 (6.91 %)	1.4523e-04 (13.5 %)
4.25	3.7171e-04	6.8724e-06 (1.85 %)	2.5865e-05 (6.96 %)	5.0009e-05 (13.5 %)
4.75	1.5255e-04	3.2360e-06 (2.12 %)	1.0733e-05 (7.04 %)	2.0523e-05 (13.5 %)
5.25	6.2374e-05	1.6397e-06 (2.63 %)	4.4940e-06 (7.2 %)	8.3916e-06 (13.5 %)
5.75	2.9112e-05	9.4173e-07 (3.23 %)	2.1681e-06 (7.45 %)	3.9166e-06 (13.5 %)
6.25	1.5003e-05	3.3433e-07 (2.23 %)	1.0605e-06 (7.07 %)	2.0185e-06 (13.5 %)
6.75	7.8205e-06	2.0614e-07 (2.64 %)	5.6366e-07 (7.21 %)	1.0521e-06 (13.5 %)
7.25	4.2017e-06	1.3091e-07 (3.12 %)	3.1078e-07 (7.4 %)	5.6528e-07 (13.5 %)
7.75	2.4949e-06	9.6381e-08 (3.86 %)	1.9313e-07 (7.74 %)	3.3566e-07 (13.5 %)
8.25	1.6075e-06	7.1426e-08 (4.44 %)	1.2935e-07 (8.05 %)	2.1627e-07 (13.5 %)
8.75	1.0706e-06	5.4812e-08 (5.12 %)	9.0343e-08 (8.44 %)	1.4403e-07 (13.5 %)
9.5	5.6961e-07	2.6021e-08 (4.57 %)	4.6229e-08 (8.12 %)	8.9770e-08 (15.8 %)
10.5	2.4205e-07	1.5826e-08 (6.54 %)	2.2674e-08 (9.37 %)	6.4535e-08 (26.7 %)
11.5	1.1202e-07	1.0366e-08 (9.25 %)	1.2803e-08 (11.4 %)	3.6831e-08 (32.9 %)
12.5	5.4660e-08	6.7961e-09 (12.4 %)	7.7222e-09 (14.1 %)	1.7971e-08 (32.9 %)
13.5	3.8893e-08	5.7416e-09 (14.8 %)	6.3066e-09 (16.2 %)	1.2787e-08 (32.9 %)
15	1.2194e-08	2.3056e-09 (18.9 %)	2.4464e-09 (20.1 %)	4.0091e-09 (32.9 %)
17	6.6950e-09	1.9334e-09 (28.9 %)	1.9848e-09 (29.6 %)	2.2012e-09 (32.9 %)

Table E.3: Neutral Pion Invariant Yield as a function of p_T in $\sqrt{s_{\text{NN}}} = 200$ GeV Au+Au Collisions (20-30 % Central).

p_T	$1/2\pi p_T N_{\text{eve}} \cdot d^2N/dp_T dy$	statistic error	p_T uncorrelated error	p_T correlated error
1.25	9.3124e-01	1.5545e-02 (1.67 %)	6.4375e-02 (6.91 %)	1.0310e-01 (11.1 %)
1.75	1.7126e-01	2.3899e-03 (1.4 %)	1.1734e-02 (6.85 %)	1.9755e-02 (11.5 %)
2.25	3.5071e-02	4.7218e-04 (1.35 %)	2.3996e-03 (6.84 %)	4.3319e-03 (12.4 %)
2.75	8.3272e-03	1.1237e-04 (1.35 %)	5.6980e-04 (6.84 %)	1.0795e-03 (13 %)
3.25	2.1964e-03	3.1836e-05 (1.45 %)	1.5074e-04 (6.86 %)	2.9550e-04 (13.5 %)
3.75	7.7022e-04	1.1993e-05 (1.56 %)	5.3042e-05 (6.89 %)	1.0362e-04 (13.5 %)
4.25	2.5106e-04	4.4899e-06 (1.79 %)	1.7430e-05 (6.94 %)	3.3776e-05 (13.5 %)
4.75	1.0915e-04	2.3124e-06 (2.12 %)	7.6785e-06 (7.03 %)	1.4685e-05 (13.5 %)
5.25	4.6000e-05	1.2236e-06 (2.66 %)	3.3195e-06 (7.22 %)	6.1886e-06 (13.5 %)
5.75	2.1495e-05	7.2565e-07 (3.38 %)	1.6142e-06 (7.51 %)	2.8918e-06 (13.5 %)
6.25	1.1097e-05	2.5805e-07 (2.33 %)	7.8789e-07 (7.1 %)	1.4930e-06 (13.5 %)
6.75	5.6873e-06	1.6401e-07 (2.88 %)	4.1527e-07 (7.3 %)	7.6514e-07 (13.5 %)
7.25	3.6492e-06	1.2218e-07 (3.35 %)	2.7360e-07 (7.5 %)	4.9095e-07 (13.5 %)
7.75	2.1195e-06	8.3428e-08 (3.94 %)	1.6485e-07 (7.78 %)	2.8515e-07 (13.5 %)
8.25	1.2430e-06	6.0655e-08 (4.88 %)	1.0311e-07 (8.3 %)	1.6723e-07 (13.5 %)
8.75	6.9400e-07	4.3274e-08 (6.24 %)	6.3561e-08 (9.16 %)	9.3368e-08 (13.5 %)
9.5	3.9219e-07	2.1031e-08 (5.36 %)	3.3682e-08 (8.59 %)	6.1808e-08 (15.8 %)
10.5	1.9124e-07	1.3664e-08 (7.14 %)	1.8742e-08 (9.8 %)	5.0987e-08 (26.7 %)
11.5	9.4865e-08	9.1483e-09 (9.64 %)	1.1144e-08 (11.7 %)	3.1190e-08 (32.9 %)
12.5	4.1622e-08	6.0341e-09 (14.5 %)	6.6488e-09 (16 %)	1.3685e-08 (32.9 %)
13.5	2.7216e-08	5.0482e-09 (18.5 %)	5.3682e-09 (19.7 %)	8.9481e-09 (32.9 %)
15	7.3302e-09	1.7784e-09 (24.3 %)	1.8451e-09 (25.2 %)	2.4101e-09 (32.9 %)
17	3.1546e-09	1.2882e-09 (40.8 %)	1.3055e-09 (41.4 %)	1.0372e-09 (32.9 %)

Table E.4: Neutral Pion Invariant Yield as a function of p_T in $\sqrt{s_{\text{NN}}} = 200$ GeV Au+Au Collisions (30-40 % Central).

p_T	$1/2\pi p_T N_{\text{eve}} \cdot d^2N/dp_T dy$	statistic error	p_T uncorrelated error	p_T correlated error
1.25	5.5352e-01	8.8923e-03 (1.61 %)	3.8181e-02 (6.9 %)	6.1279e-02 (11.1 %)
1.75	1.0200e-01	1.3822e-03 (1.36 %)	6.9806e-03 (6.84 %)	1.1766e-02 (11.5 %)
2.25	2.1895e-02	2.8418e-04 (1.3 %)	1.4960e-03 (6.83 %)	2.7044e-03 (12.4 %)
2.75	5.3576e-03	7.0562e-05 (1.32 %)	3.6626e-04 (6.84 %)	6.9455e-04 (13 %)
3.25	1.5457e-03	2.1208e-05 (1.37 %)	1.0583e-04 (6.85 %)	2.0795e-04 (13.5 %)
3.75	4.9805e-04	7.6737e-06 (1.54 %)	3.4280e-05 (6.88 %)	6.7006e-05 (13.5 %)
4.25	1.8232e-04	3.2840e-06 (1.8 %)	1.2663e-05 (6.95 %)	2.4528e-05 (13.5 %)
4.75	7.2716e-05	1.6345e-06 (2.25 %)	5.1445e-06 (7.07 %)	9.7830e-06 (13.5 %)
5.25	3.2158e-05	9.2915e-07 (2.89 %)	2.3488e-06 (7.3 %)	4.3265e-06 (13.5 %)
5.75	1.6670e-05	5.9573e-07 (3.57 %)	1.2670e-06 (7.6 %)	2.2427e-06 (13.5 %)
6.25	7.2796e-06	1.9284e-07 (2.65 %)	5.2502e-07 (7.21 %)	9.7936e-07 (13.5 %)
6.75	4.1670e-06	1.2981e-07 (3.12 %)	3.0820e-07 (7.4 %)	5.6061e-07 (13.5 %)
7.25	2.3069e-06	8.8086e-08 (3.82 %)	1.7806e-07 (7.72 %)	3.1036e-07 (13.5 %)
7.75	1.3043e-06	6.3236e-08 (4.85 %)	1.0795e-07 (8.28 %)	1.7547e-07 (13.5 %)
8.25	9.0141e-07	4.9008e-08 (5.44 %)	7.7835e-08 (8.63 %)	1.2127e-07 (13.5 %)
8.75	5.6604e-07	3.7253e-08 (6.58 %)	5.3194e-08 (9.4 %)	7.6153e-08 (13.5 %)
9.5	2.5220e-07	1.6859e-08 (6.68 %)	2.3884e-08 (9.47 %)	3.9747e-08 (15.8 %)
10.5	1.0097e-07	9.6721e-09 (9.58 %)	1.1808e-08 (11.7 %)	2.6921e-08 (26.7 %)
11.5	6.4036e-08	7.3947e-09 (11.5 %)	8.5519e-09 (13.4 %)	2.1054e-08 (32.9 %)
12.5	3.0648e-08	5.1407e-09 (16.8 %)	5.5366e-09 (18.1 %)	1.0077e-08 (32.9 %)
13.5	1.3790e-08	3.3460e-09 (24.3 %)	3.4715e-09 (25.2 %)	4.5339e-09 (32.9 %)
15	7.6868e-09	1.8123e-09 (23.6 %)	1.8842e-09 (24.5 %)	2.5273e-09 (32.9 %)

Table E.5: Neutral Pion Invariant Yield as a function of p_T in $\sqrt{s_{\text{NN}}} = 200$ GeV Au+Au Collisions (40-50 % Central).

p_T	$1/2\pi p_T N_{\text{eve}} \cdot d^2N/dp_T dy$	statistic error	p_T uncorrelated error	p_T correlated error
1.25	3.1837e-01	4.9340e-03 (1.55 %)	2.1920e-02 (6.88 %)	3.5246e-02 (11.1 %)
1.75	5.7470e-02	7.4832e-04 (1.3 %)	3.9272e-03 (6.83 %)	6.6294e-03 (11.5 %)
2.25	1.2075e-02	1.5034e-04 (1.25 %)	8.2387e-04 (6.82 %)	1.4915e-03 (12.4 %)
2.75	2.9901e-03	3.7968e-05 (1.27 %)	2.0414e-04 (6.83 %)	3.8763e-04 (13 %)
3.25	8.8318e-04	1.2178e-05 (1.38 %)	6.0484e-05 (6.85 %)	1.1882e-04 (13.5 %)
3.75	2.8959e-04	4.6061e-06 (1.59 %)	1.9965e-05 (6.89 %)	3.8960e-05 (13.5 %)
4.25	1.1167e-04	2.1840e-06 (1.96 %)	7.8030e-06 (6.99 %)	1.5024e-05 (13.5 %)
4.75	4.8223e-05	1.2043e-06 (2.5 %)	3.4518e-06 (7.16 %)	6.4878e-06 (13.5 %)
5.25	2.1343e-05	7.0489e-07 (3.3 %)	1.5958e-06 (7.48 %)	2.8714e-06 (13.5 %)
5.75	9.5276e-06	4.0434e-07 (4.24 %)	7.5630e-07 (7.94 %)	1.2818e-06 (13.5 %)
6.25	4.4937e-06	1.4075e-07 (3.13 %)	3.3269e-07 (7.4 %)	6.0456e-07 (13.5 %)
6.75	2.5294e-06	9.6755e-08 (3.83 %)	1.9533e-07 (7.72 %)	3.4030e-07 (13.5 %)
7.25	1.4456e-06	6.8072e-08 (4.71 %)	1.1848e-07 (8.2 %)	1.9449e-07 (13.5 %)
7.75	8.3064e-07	4.9813e-08 (6 %)	7.4741e-08 (9 %)	1.1175e-07 (13.5 %)
8.25	5.8699e-07	3.9145e-08 (6.67 %)	5.5523e-08 (9.46 %)	7.8971e-08 (13.5 %)
8.75	3.1744e-07	2.8008e-08 (8.82 %)	3.5184e-08 (11.1 %)	4.2707e-08 (13.5 %)
9.5	1.6883e-07	1.3215e-08 (7.83 %)	1.7404e-08 (10.3 %)	2.6608e-08 (15.8 %)
10.5	7.6276e-08	8.3549e-09 (11 %)	9.7972e-09 (12.8 %)	2.0336e-08 (26.7 %)
11.5	3.7643e-08	5.7363e-09 (15.2 %)	6.2675e-09 (16.6 %)	1.2377e-08 (32.9 %)
12.5	2.4804e-08	4.5661e-09 (18.4 %)	4.8598e-09 (19.6 %)	8.1554e-09 (32.9 %)
13.5	8.0415e-09	2.5436e-09 (31.6 %)	2.6002e-09 (32.3 %)	2.6439e-09 (32.9 %)

Table E.6: Neutral Pion Invariant Yield as a function of p_T in $\sqrt{s_{\text{NN}}} = 200$ GeV Au+Au Collisions (50-60 % Central).

p_T	$1/2\pi p_T N_{\text{eve}} \cdot d^2N/dp_T dy$	statistic error	p_T uncorrelated error	p_T correlated error
1.25	1.6692e-01	2.4230e-03 (1.45 %)	1.1456e-02 (6.86 %)	1.8479e-02 (11.1 %)
1.75	2.9148e-02	3.5544e-04 (1.22 %)	1.9874e-03 (6.82 %)	3.3623e-03 (11.5 %)
2.25	6.1090e-03	7.1982e-05 (1.18 %)	4.1608e-04 (6.81 %)	7.5456e-04 (12.4 %)
2.75	1.5651e-03	1.9494e-05 (1.25 %)	1.0678e-04 (6.82 %)	2.0290e-04 (13 %)
3.25	4.6610e-04	6.6136e-06 (1.42 %)	3.1959e-05 (6.86 %)	6.2707e-05 (13.5 %)
3.75	1.5535e-04	2.7102e-06 (1.74 %)	1.0768e-05 (6.93 %)	2.0900e-05 (13.5 %)
4.25	5.8851e-05	1.3746e-06 (2.34 %)	4.1803e-06 (7.1 %)	7.9176e-06 (13.5 %)
4.75	2.4709e-05	7.6782e-07 (3.11 %)	1.8267e-06 (7.39 %)	3.3243e-06 (13.5 %)
5.25	1.1341e-05	4.5629e-07 (4.02 %)	8.8714e-07 (7.82 %)	1.5258e-06 (13.5 %)
5.75	5.9365e-06	3.1023e-07 (5.23 %)	5.0481e-07 (8.5 %)	7.9867e-07 (13.5 %)
6.25	2.5818e-06	1.0060e-07 (3.9 %)	2.0029e-07 (7.76 %)	3.4735e-07 (13.5 %)
6.75	1.4184e-06	6.9527e-08 (4.9 %)	1.1784e-07 (8.31 %)	1.9082e-07 (13.5 %)
7.25	8.4022e-07	5.0048e-08 (5.96 %)	7.5377e-08 (8.97 %)	1.1304e-07 (13.5 %)
7.75	4.3311e-07	3.4858e-08 (8.05 %)	4.5379e-08 (10.5 %)	5.8269e-08 (13.5 %)
8.25	2.5970e-07	2.5690e-08 (9.89 %)	3.1040e-08 (12 %)	3.4939e-08 (13.5 %)
8.75	1.8469e-07	2.1141e-08 (11.4 %)	2.4504e-08 (13.3 %)	2.4848e-08 (13.5 %)
9.5	8.4647e-08	9.2833e-09 (11 %)	1.0882e-08 (12.9 %)	1.3340e-08 (15.8 %)
10.5	2.7424e-08	5.3903e-09 (19.7 %)	5.6956e-09 (20.8 %)	7.3118e-09 (26.7 %)
11.5	2.5779e-08	4.6324e-09 (18 %)	4.9446e-09 (19.2 %)	8.4756e-09 (32.9 %)
12.5	1.1231e-08	3.0023e-09 (26.7 %)	3.0954e-09 (27.6 %)	3.6926e-09 (32.9 %)
13.5	8.7235e-09	2.6309e-09 (30.2 %)	2.6952e-09 (30.9 %)	2.8682e-09 (32.9 %)

Table E.7: Neutral Pion Invariant Yield as a function of p_T in $\sqrt{s_{\text{NN}}} = 200$ GeV Au+Au Collisions (60-70 % Central).

p_T	$1/2\pi p_T N_{\text{eve}} \cdot d^2N/dp_T dy$	statistic error	p_T uncorrelated error	p_T correlated error
1.25	7.6615e-02	1.0265e-03 (1.34 %)	5.2410e-03 (6.84 %)	8.4819e-03 (11.1 %)
1.75	1.3115e-02	1.5058e-04 (1.15 %)	8.9257e-04 (6.81 %)	1.5128e-03 (11.5 %)
2.25	2.8174e-03	3.2646e-05 (1.16 %)	1.9180e-04 (6.81 %)	3.4799e-04 (12.4 %)
2.75	7.6110e-04	9.9626e-06 (1.31 %)	5.2019e-05 (6.83 %)	9.8668e-05 (13 %)
3.25	2.1660e-04	3.5371e-06 (1.63 %)	1.4954e-05 (6.9 %)	2.9140e-05 (13.5 %)
3.75	7.4875e-05	1.6458e-06 (2.2 %)	5.2855e-06 (7.06 %)	1.0073e-05 (13.5 %)
4.25	2.9205e-05	8.7061e-07 (2.98 %)	2.1438e-06 (7.34 %)	3.9291e-06 (13.5 %)
4.75	1.1685e-05	4.8906e-07 (4.19 %)	9.2389e-07 (7.91 %)	1.5720e-06 (13.5 %)
5.25	5.3910e-06	3.0323e-07 (5.62 %)	4.7194e-07 (8.75 %)	7.2529e-07 (13.5 %)
5.75	2.6851e-06	2.0235e-07 (7.54 %)	2.7091e-07 (10.1 %)	3.6125e-07 (13.5 %)
6.25	1.0052e-06	7.2726e-08 (7.24 %)	9.9176e-08 (9.87 %)	1.3523e-07 (13.5 %)
6.75	5.7148e-07	5.0013e-08 (8.75 %)	6.3015e-08 (11 %)	7.6885e-08 (13.5 %)
7.25	3.7291e-07	3.1875e-08 (8.55 %)	4.0519e-08 (10.9 %)	5.0170e-08 (13.5 %)
7.75	2.1795e-07	2.4421e-08 (11.2 %)	2.8463e-08 (13.1 %)	2.9323e-08 (13.5 %)
8.25	1.3194e-07	1.7660e-08 (13.4 %)	1.9754e-08 (15 %)	1.7751e-08 (13.5 %)
8.75	7.7041e-08	1.3035e-08 (16.9 %)	1.4023e-08 (18.2 %)	1.0365e-08 (13.5 %)
9.5	3.4130e-08	5.7721e-09 (16.9 %)	6.2096e-09 (18.2 %)	5.3789e-09 (15.8 %)
10.5	1.3201e-08	3.4093e-09 (25.8 %)	3.5224e-09 (26.7 %)	3.5195e-09 (26.7 %)
11.5	9.7485e-09	2.8147e-09 (28.9 %)	2.8897e-09 (29.6 %)	3.2052e-09 (32.9 %)

Table E.8: Neutral Pion Invariant Yield as a function of p_T in $\sqrt{s_{\text{NN}}} = 200$ GeV Au+Au Collisions (70-80 % Central).

p_T	$1/2\pi p_T N_{\text{eve}} \cdot d^2N/dp_T dy$	statistic error	p_T uncorrelated error	p_T correlated error
1.25	3.0490e-02	4.1175e-04 (1.35 %)	2.0864e-03 (6.84 %)	3.3755e-03 (11.1 %)
1.75	5.2307e-03	6.1257e-05 (1.17 %)	3.5619e-04 (6.81 %)	6.0337e-04 (11.5 %)
2.25	1.1379e-03	1.3860e-05 (1.22 %)	7.7581e-05 (6.82 %)	1.4055e-04 (12.4 %)
2.75	2.9771e-04	4.4293e-06 (1.49 %)	2.0456e-05 (6.87 %)	3.8595e-05 (13 %)
3.25	8.7624e-05	1.7555e-06 (2 %)	6.1345e-06 (7 %)	1.1789e-05 (13.5 %)
3.75	2.8283e-05	8.3358e-07 (2.95 %)	2.0723e-06 (7.33 %)	3.8050e-06 (13.5 %)
4.25	1.2017e-05	4.6614e-07 (3.88 %)	9.3119e-07 (7.75 %)	1.6167e-06 (13.5 %)
4.75	4.6356e-06	2.6791e-07 (5.78 %)	4.1046e-07 (8.85 %)	6.2366e-07 (13.5 %)
5.25	1.9448e-06	1.7325e-07 (8.91 %)	2.1688e-07 (11.2 %)	2.6164e-07 (13.5 %)
5.75	1.1500e-06	1.1166e-07 (9.71 %)	1.3572e-07 (11.8 %)	1.5471e-07 (13.5 %)
6.25	4.5536e-07	3.3849e-08 (7.43 %)	4.5595e-08 (10 %)	6.1263e-08 (13.5 %)
6.75	2.9271e-07	2.5871e-08 (8.84 %)	3.2479e-08 (11.1 %)	3.9380e-08 (13.5 %)
7.25	1.4350e-07	1.7310e-08 (12.1 %)	1.9807e-08 (13.8 %)	1.9306e-08 (13.5 %)
7.75	7.8964e-08	1.2347e-08 (15.6 %)	1.3435e-08 (17 %)	1.0624e-08 (13.5 %)
8.25	7.1930e-08	1.1386e-08 (15.8 %)	1.2366e-08 (17.2 %)	9.6772e-09 (13.5 %)
8.75	3.3553e-08	7.5070e-09 (22.4 %)	7.8372e-09 (23.4 %)	4.5141e-09 (13.5 %)
9.5	1.8740e-08	3.7492e-09 (20 %)	3.9544e-09 (21.1 %)	2.9533e-09 (15.8 %)
10.5	6.7851e-09	2.1459e-09 (31.6 %)	2.1937e-09 (32.3 %)	1.8090e-09 (26.7 %)
11.5	1.8467e-09	1.0663e-09 (57.7 %)	1.0735e-09 (58.1 %)	6.0718e-10 (32.9 %)

Table E.9: Neutral Pion Invariant Yield as a function of p_T in $\sqrt{s_{\text{NN}}} = 200$ GeV Au+Au Collisions (80-92 % Central).

p_T	$1/2\pi p_T N_{\text{eve}} \cdot d^2N/dp_T dy$	statistic error	p_T uncorrelated error	p_T correlated error
1.25	9.1877e-01	9.2075e-03 (1 %)	6.2317e-02 (6.78 %)	1.0172e-01 (11.1 %)
1.75	1.6729e-01	1.4276e-03 (0.853 %)	1.1313e-02 (6.76 %)	1.9298e-02 (11.5 %)
2.25	3.5445e-02	2.9257e-04 (0.825 %)	2.3957e-03 (6.76 %)	4.3781e-03 (12.4 %)
2.75	7.8642e-03	6.4589e-05 (0.821 %)	5.3148e-04 (6.76 %)	1.0195e-03 (13 %)
3.25	2.0789e-03	1.8144e-05 (0.873 %)	1.4063e-04 (6.76 %)	2.7969e-04 (13.5 %)
3.75	6.5378e-04	5.9942e-06 (0.917 %)	4.4265e-05 (6.77 %)	8.7958e-05 (13.5 %)
4.25	2.2286e-04	2.2030e-06 (0.989 %)	1.5111e-05 (6.78 %)	2.9983e-05 (13.5 %)
4.75	9.1835e-05	1.0156e-06 (1.11 %)	6.2436e-06 (6.8 %)	1.2355e-05 (13.5 %)
5.25	3.8082e-05	4.8723e-07 (1.28 %)	2.6006e-06 (6.83 %)	5.1233e-06 (13.5 %)
5.75	1.7819e-05	2.7658e-07 (1.55 %)	1.2269e-06 (6.89 %)	2.3974e-06 (13.5 %)
6.25	9.0581e-06	9.8827e-08 (1.09 %)	6.1562e-07 (6.8 %)	1.2186e-06 (13.5 %)
6.75	4.9628e-06	6.1983e-08 (1.25 %)	3.3864e-07 (6.82 %)	6.6768e-07 (13.5 %)
7.25	2.8102e-06	4.0224e-08 (1.43 %)	1.9276e-07 (6.86 %)	3.7807e-07 (13.5 %)
7.75	1.6385e-06	2.7764e-08 (1.69 %)	1.1336e-07 (6.92 %)	2.2043e-07 (13.5 %)
8.25	1.0016e-06	1.9884e-08 (1.99 %)	7.0071e-08 (7 %)	1.3475e-07 (13.5 %)
8.75	6.1256e-07	1.4406e-08 (2.35 %)	4.3544e-08 (7.11 %)	8.2411e-08 (13.5 %)
9.5	3.1952e-07	6.6634e-09 (2.09 %)	2.2446e-08 (7.02 %)	5.0355e-08 (15.8 %)
10.5	1.4783e-07	4.1524e-09 (2.81 %)	1.0751e-08 (7.27 %)	3.9415e-08 (26.7 %)
11.5	7.3244e-08	2.7337e-09 (3.73 %)	5.6226e-09 (7.68 %)	2.4081e-08 (32.9 %)
12.5	3.6624e-08	1.8949e-09 (5.17 %)	3.1026e-09 (8.47 %)	1.2041e-08 (32.9 %)
13.5	1.9433e-08	1.3509e-09 (6.95 %)	1.8774e-09 (9.66 %)	6.3893e-09 (32.9 %)
15	8.4594e-09	6.4070e-10 (7.57 %)	8.5588e-10 (10.1 %)	2.7813e-09 (32.9 %)
17	3.2511e-09	4.4990e-10 (13.8 %)	4.9998e-10 (15.4 %)	1.0689e-09 (32.9 %)
19	1.1435e-09	3.4482e-10 (30.2 %)	3.5325e-10 (30.9 %)	3.7595e-10 (32.9 %)

Table E.10: Neutral Pion Invariant Yield as a function of p_T in $\sqrt{s_{\text{NN}}} = 200$ GeV Au+Au Collisions (Minimum Bias).

E.2 Neutral Pion Nuclear Modification Factor (R_{AA}) in $\sqrt{s_{NN}} = 200$ GeV Au+Au Collisions

p_T	R_{AA}	p_T uncorrelated error	p_T correlated error	global scaling error
1.25	3.8832e-01	3.2330e-02 (8.33 %)	4.8574e-02 (12.5 %)	5.3536e-02 (13.8 %)
1.75	4.3102e-01	3.4983e-02 (8.12 %)	5.5587e-02 (12.9 %)	5.9423e-02 (13.8 %)
2.25	4.3471e-01	3.8391e-02 (8.83 %)	6.0691e-02 (14 %)	5.9932e-02 (13.8 %)
2.75	3.2445e-01	2.8746e-02 (8.86 %)	5.9640e-02 (18.4 %)	4.4731e-02 (13.8 %)
3.25	2.5797e-01	2.1796e-02 (8.45 %)	3.9590e-02 (15.3 %)	3.5566e-02 (13.8 %)
3.75	2.2814e-01	1.8297e-02 (8.02 %)	3.4467e-02 (15.1 %)	3.1453e-02 (13.8 %)
4.25	2.0799e-01	1.6837e-02 (8.09 %)	3.1316e-02 (15.1 %)	2.8675e-02 (13.8 %)
4.75	2.0990e-01	1.7003e-02 (8.1 %)	3.1602e-02 (15.1 %)	2.8938e-02 (13.8 %)
5.25	1.8056e-01	1.4855e-02 (8.23 %)	2.7225e-02 (15.1 %)	2.4893e-02 (13.8 %)
5.75	1.8819e-01	1.6059e-02 (8.53 %)	2.8443e-02 (15.1 %)	2.5946e-02 (13.8 %)
6.25	1.9554e-01	1.5701e-02 (8.03 %)	2.9640e-02 (15.2 %)	2.6959e-02 (13.8 %)
6.75	2.0839e-01	1.7048e-02 (8.18 %)	3.1692e-02 (15.2 %)	2.8731e-02 (13.8 %)
7.25	2.0084e-01	1.6771e-02 (8.35 %)	3.0653e-02 (15.3 %)	2.7689e-02 (13.8 %)
7.75	1.9051e-01	1.6554e-02 (8.69 %)	2.9187e-02 (15.3 %)	2.6265e-02 (13.8 %)
8.25	1.8800e-01	1.6917e-02 (9 %)	2.8916e-02 (15.4 %)	2.5919e-02 (13.8 %)
8.75	2.0149e-01	1.8680e-02 (9.27 %)	3.1116e-02 (15.4 %)	2.7778e-02 (13.8 %)
9.5	2.1360e-01	1.9423e-02 (9.09 %)	3.7601e-02 (17.6 %)	2.9449e-02 (13.8 %)
10.5	2.2373e-01	2.2443e-02 (10 %)	6.2345e-02 (27.9 %)	3.0845e-02 (13.8 %)
11.5	2.2475e-01	2.5290e-02 (11.3 %)	7.6245e-02 (33.9 %)	3.0986e-02 (13.8 %)
12.5	2.1867e-01	2.9432e-02 (13.5 %)	7.4319e-02 (34 %)	3.0147e-02 (13.8 %)
13.5	1.7313e-01	3.0569e-02 (17.7 %)	5.8947e-02 (34 %)	2.3869e-02 (13.8 %)
15	2.5131e-01	4.1545e-02 (16.5 %)	8.5796e-02 (34.1 %)	3.4647e-02 (13.8 %)
17	2.5008e-01	7.1014e-02 (28.4 %)	8.5669e-02 (34.3 %)	3.4477e-02 (13.8 %)
19	2.9961e-01	1.5277e-01 (51 %)	1.0298e-01 (34.4 %)	4.1306e-02 (13.8 %)

Table E.11: Neutral Pion R_{AA} as a function of p_T in $\sqrt{s_{NN}} = 200$ GeV Au+Au Collisions (0-10 % Central).

p_T	R _{AA}	p_T uncorrelated error	p_T correlated error	global scaling error
1.25	4.4469e-01	3.6681e-02 (8.25 %)	5.5625e-02 (12.5 %)	6.1445e-02 (13.8 %)
1.75	4.6429e-01	3.7383e-02 (8.05 %)	5.9878e-02 (12.9 %)	6.4155e-02 (13.8 %)
2.25	4.6994e-01	4.1201e-02 (8.77 %)	6.5609e-02 (14 %)	6.4935e-02 (13.8 %)
2.75	4.0564e-01	3.5678e-02 (8.8 %)	7.4562e-02 (18.4 %)	5.6050e-02 (13.8 %)
3.25	3.3982e-01	2.8409e-02 (8.36 %)	5.2151e-02 (15.3 %)	4.6955e-02 (13.8 %)
3.75	3.1807e-01	2.5132e-02 (7.9 %)	4.8053e-02 (15.1 %)	4.3950e-02 (13.8 %)
4.25	2.7609e-01	2.1917e-02 (7.94 %)	4.1567e-02 (15.1 %)	3.8149e-02 (13.8 %)
4.75	2.7201e-01	2.1717e-02 (7.98 %)	4.0954e-02 (15.1 %)	3.7586e-02 (13.8 %)
5.25	2.7309e-01	2.2080e-02 (8.09 %)	4.1177e-02 (15.1 %)	3.7734e-02 (13.8 %)
5.75	2.4306e-01	2.0259e-02 (8.33 %)	3.6736e-02 (15.1 %)	3.3586e-02 (13.8 %)
6.25	2.4711e-01	1.9669e-02 (7.96 %)	3.7457e-02 (15.2 %)	3.4146e-02 (13.8 %)
6.75	2.6103e-01	2.1189e-02 (8.12 %)	3.9697e-02 (15.2 %)	3.6069e-02 (13.8 %)
7.25	2.6990e-01	2.2411e-02 (8.3 %)	4.1192e-02 (15.3 %)	3.7294e-02 (13.8 %)
7.75	2.8633e-01	2.4370e-02 (8.51 %)	4.3866e-02 (15.3 %)	3.9564e-02 (13.8 %)
8.25	2.7631e-01	2.4474e-02 (8.86 %)	4.2498e-02 (15.4 %)	3.8180e-02 (13.8 %)
8.75	2.6672e-01	2.4855e-02 (9.32 %)	4.1190e-02 (15.4 %)	3.6854e-02 (13.8 %)
9.5	2.5434e-01	2.3676e-02 (9.31 %)	4.4772e-02 (17.6 %)	3.5144e-02 (13.8 %)
10.5	2.9054e-01	2.9595e-02 (10.2 %)	8.0962e-02 (27.9 %)	4.0147e-02 (13.8 %)
11.5	2.7202e-01	3.2134e-02 (11.8 %)	9.2282e-02 (33.9 %)	3.7587e-02 (13.8 %)
12.5	2.9629e-01	4.0919e-02 (13.8 %)	1.0070e-01 (34 %)	4.0941e-02 (13.8 %)
13.5	2.6339e-01	4.6677e-02 (17.7 %)	8.9678e-02 (34 %)	3.6394e-02 (13.8 %)
15	3.8294e-01	6.3348e-02 (16.5 %)	1.3073e-01 (34.1 %)	5.2913e-02 (13.8 %)
17	2.0670e-01	7.5723e-02 (36.6 %)	7.0811e-02 (34.3 %)	2.8562e-02 (13.8 %)
19	5.3740e-01	2.4625e-01 (45.8 %)	1.8471e-01 (34.4 %)	7.4257e-02 (13.8 %)

Table E.12: Neutral Pion R_{AA} as a function of p_T in $\sqrt{s_{NN}} = 200$ GeV Au+Au Collisions (10-20 % Central).

p_T	R _{AA}	p_T uncorrelated error	p_T correlated error	global scaling error
1.25	4.7405e-01	3.8990e-02 (8.22 %)	5.9298e-02 (12.5 %)	6.8092e-02 (14.4 %)
1.75	5.2420e-01	4.2107e-02 (8.03 %)	6.7604e-02 (12.9 %)	7.5295e-02 (14.4 %)
2.25	5.3575e-01	4.6848e-02 (8.74 %)	7.4796e-02 (14 %)	7.6954e-02 (14.4 %)
2.75	4.6195e-01	4.0525e-02 (8.77 %)	8.4913e-02 (18.4 %)	6.6353e-02 (14.4 %)
3.25	4.0001e-01	3.3292e-02 (8.32 %)	6.1388e-02 (15.3 %)	5.7457e-02 (14.4 %)
3.75	3.8665e-01	3.0414e-02 (7.87 %)	5.8414e-02 (15.1 %)	5.5539e-02 (14.4 %)
4.25	3.5478e-01	2.8050e-02 (7.91 %)	5.3415e-02 (15.1 %)	5.0960e-02 (14.4 %)
4.75	3.5649e-01	2.8189e-02 (7.91 %)	5.3672e-02 (15.1 %)	5.1206e-02 (14.4 %)
5.25	3.2929e-01	2.6445e-02 (8.03 %)	4.9652e-02 (15.1 %)	4.7299e-02 (14.4 %)
5.75	3.2137e-01	2.6510e-02 (8.25 %)	4.8570e-02 (15.1 %)	4.6160e-02 (14.4 %)
6.25	3.2619e-01	2.5886e-02 (7.94 %)	4.9443e-02 (15.2 %)	4.6853e-02 (14.4 %)
6.75	3.1732e-01	2.5718e-02 (8.1 %)	4.8256e-02 (15.2 %)	4.5579e-02 (14.4 %)
7.25	3.0460e-01	2.5375e-02 (8.33 %)	4.6489e-02 (15.3 %)	4.3753e-02 (14.4 %)
7.75	3.1056e-01	2.7027e-02 (8.7 %)	4.7578e-02 (15.3 %)	4.4608e-02 (14.4 %)
8.25	3.3239e-01	3.0065e-02 (9.04 %)	5.1123e-02 (15.4 %)	4.7744e-02 (14.4 %)
8.75	3.5664e-01	3.3768e-02 (9.47 %)	5.5077e-02 (15.4 %)	5.1228e-02 (14.4 %)
9.5	3.6936e-01	3.4503e-02 (9.34 %)	6.5019e-02 (17.6 %)	5.3054e-02 (14.4 %)
10.5	3.5342e-01	3.7454e-02 (10.6 %)	9.8483e-02 (27.9 %)	5.0765e-02 (14.4 %)
11.5	3.4202e-01	4.3056e-02 (12.6 %)	1.1603e-01 (33.9 %)	4.9127e-02 (14.4 %)
12.5	3.2812e-01	4.9847e-02 (15.2 %)	1.1152e-01 (34 %)	4.7131e-02 (14.4 %)
13.5	4.3572e-01	7.5154e-02 (17.2 %)	1.4835e-01 (34 %)	6.2586e-02 (14.4 %)
15	3.2145e-01	6.7592e-02 (21 %)	1.0974e-01 (34.1 %)	4.6172e-02 (14.4 %)
17	4.8660e-01	1.4801e-01 (30.4 %)	1.6670e-01 (34.3 %)	6.9895e-02 (14.4 %)

Table E.13: Neutral Pion R_{AA} as a function of p_T in $\sqrt{s_{NN}} = 200$ GeV Au+Au Collisions (20-30 % Central).

p_T	R _{AA}	p_T uncorrelated error	p_T correlated error	global scaling error
1.25	5.2403e-01	4.3046e-02 (8.21 %)	6.5550e-02 (12.5 %)	7.4074e-02 (14.1 %)
1.75	5.8484e-01	4.6911e-02 (8.02 %)	7.5424e-02 (12.9 %)	8.2669e-02 (14.1 %)
2.25	5.7023e-01	4.9816e-02 (8.74 %)	7.9610e-02 (14 %)	8.0605e-02 (14.1 %)
2.75	5.2025e-01	4.5585e-02 (8.76 %)	9.5631e-02 (18.4 %)	7.3540e-02 (14.1 %)
3.25	4.5731e-01	3.8019e-02 (8.31 %)	7.0182e-02 (15.3 %)	6.4643e-02 (14.1 %)
3.75	4.6946e-01	3.6845e-02 (7.85 %)	7.0925e-02 (15.1 %)	6.6361e-02 (14.1 %)
4.25	4.0776e-01	3.2182e-02 (7.89 %)	6.1392e-02 (15.1 %)	5.7638e-02 (14.1 %)
4.75	4.3408e-01	3.4320e-02 (7.91 %)	6.5353e-02 (15.1 %)	6.1358e-02 (14.1 %)
5.25	4.1325e-01	3.3231e-02 (8.04 %)	6.2312e-02 (15.1 %)	5.8415e-02 (14.1 %)
5.75	4.0379e-01	3.3536e-02 (8.31 %)	6.1028e-02 (15.1 %)	5.7077e-02 (14.1 %)
6.25	4.1058e-01	3.2697e-02 (7.96 %)	6.2234e-02 (15.2 %)	5.8037e-02 (14.1 %)
6.75	3.9269e-01	3.2156e-02 (8.19 %)	5.9719e-02 (15.2 %)	5.5508e-02 (14.1 %)
7.25	4.5019e-01	3.7907e-02 (8.42 %)	6.8709e-02 (15.3 %)	6.3637e-02 (14.1 %)
7.75	4.4896e-01	3.9218e-02 (8.74 %)	6.8781e-02 (15.3 %)	6.3463e-02 (14.1 %)
8.25	4.3738e-01	4.0533e-02 (9.27 %)	6.7271e-02 (15.4 %)	6.1826e-02 (14.1 %)
8.75	3.9343e-01	3.9796e-02 (10.1 %)	6.0757e-02 (15.4 %)	5.5613e-02 (14.1 %)
9.5	4.3276e-01	4.2214e-02 (9.75 %)	7.6180e-02 (17.6 %)	6.1173e-02 (14.1 %)
10.5	4.7517e-01	5.2184e-02 (11 %)	1.3241e-01 (27.9 %)	6.7167e-02 (14.1 %)
11.5	4.9289e-01	6.3474e-02 (12.9 %)	1.6721e-01 (33.9 %)	6.9672e-02 (14.1 %)
12.5	4.2518e-01	7.1951e-02 (16.9 %)	1.4450e-01 (34 %)	6.0102e-02 (14.1 %)
13.5	5.1885e-01	1.0679e-01 (20.6 %)	1.7666e-01 (34 %)	7.3342e-02 (14.1 %)
15	3.2884e-01	8.5323e-02 (25.9 %)	1.1226e-01 (34.1 %)	4.6483e-02 (14.1 %)
17	3.9017e-01	1.6363e-01 (41.9 %)	1.3366e-01 (34.3 %)	5.5153e-02 (14.1 %)

Table E.14: Neutral Pion R_{AA} as a function of p_T in $\sqrt{s_{NN}} = 200$ GeV Au+Au Collisions (30-40 % Central).

p_T	R _{AA}	p_T uncorrelated error	p_T correlated error	global scaling error
1.25	5.6959e-01	4.6717e-02 (8.2 %)	7.1248e-02 (12.5 %)	8.5207e-02 (15 %)
1.75	6.3698e-01	5.1049e-02 (8.01 %)	8.2149e-02 (12.9 %)	9.5288e-02 (15 %)
2.25	6.5100e-01	5.6824e-02 (8.73 %)	9.0886e-02 (14 %)	9.7384e-02 (15 %)
2.75	6.1209e-01	5.3602e-02 (8.76 %)	1.1251e-01 (18.4 %)	9.1565e-02 (15 %)
3.25	5.8850e-01	4.8848e-02 (8.3 %)	9.0315e-02 (15.3 %)	8.8035e-02 (15 %)
3.75	5.5514e-01	4.3551e-02 (7.85 %)	8.3867e-02 (15.1 %)	8.3044e-02 (15 %)
4.25	5.4149e-01	4.2753e-02 (7.9 %)	8.1527e-02 (15.1 %)	8.1004e-02 (15 %)
4.75	5.2881e-01	4.1999e-02 (7.94 %)	7.9617e-02 (15.1 %)	7.9107e-02 (15 %)
5.25	5.2832e-01	4.2899e-02 (8.12 %)	7.9661e-02 (15.1 %)	7.9032e-02 (15 %)
5.75	5.7264e-01	4.8031e-02 (8.39 %)	8.6547e-02 (15.1 %)	8.5663e-02 (15 %)
6.25	4.9251e-01	3.9717e-02 (8.06 %)	7.4654e-02 (15.2 %)	7.3676e-02 (15 %)
6.75	5.2614e-01	4.3528e-02 (8.27 %)	8.0014e-02 (15.2 %)	7.8707e-02 (15 %)
7.25	5.2042e-01	4.4849e-02 (8.62 %)	7.9427e-02 (15.3 %)	7.7851e-02 (15 %)
7.75	5.0522e-01	4.6392e-02 (9.18 %)	7.7400e-02 (15.3 %)	7.5578e-02 (15 %)
8.25	5.8002e-01	5.5521e-02 (9.57 %)	8.9210e-02 (15.4 %)	8.6767e-02 (15 %)
8.75	5.8680e-01	6.0627e-02 (10.3 %)	9.0619e-02 (15.4 %)	8.7781e-02 (15 %)
9.5	5.0891e-01	5.3636e-02 (10.5 %)	8.9585e-02 (17.6 %)	7.6130e-02 (15 %)
10.5	4.5879e-01	5.8271e-02 (12.7 %)	1.2784e-01 (27.9 %)	6.8631e-02 (15 %)
11.5	6.0843e-01	8.7367e-02 (14.4 %)	2.0640e-01 (33.9 %)	9.1016e-02 (15 %)
12.5	5.7252e-01	1.0826e-01 (18.9 %)	1.9458e-01 (34 %)	8.5645e-02 (15 %)
13.5	4.8075e-01	1.2428e-01 (25.9 %)	1.6369e-01 (34 %)	7.1917e-02 (15 %)
15	6.3059e-01	1.5959e-01 (25.3 %)	2.1528e-01 (34.1 %)	9.4332e-02 (15 %)

Table E.15: Neutral Pion R_{AA} as a function of p_T in $\sqrt{s_{NN}} = 200$ GeV Au+Au Collisions (40-50 % Central).

p_T	R _{AA}	p_T uncorrelated error	p_T correlated error	global scaling error
1.25	6.4619e-01	5.2929e-02 (8.19 %)	8.0831e-02 (12.5 %)	1.2218e-01 (18.9 %)
1.75	7.0789e-01	5.6670e-02 (8.01 %)	9.1294e-02 (12.9 %)	1.3384e-01 (18.9 %)
2.25	7.0815e-01	6.1759e-02 (8.72 %)	9.8866e-02 (14 %)	1.3389e-01 (18.9 %)
2.75	6.7381e-01	5.8960e-02 (8.75 %)	1.2386e-01 (18.4 %)	1.2740e-01 (18.9 %)
3.25	6.6325e-01	5.5060e-02 (8.3 %)	1.0179e-01 (15.3 %)	1.2540e-01 (18.9 %)
3.75	6.3665e-01	5.0010e-02 (7.86 %)	9.6183e-02 (15.1 %)	1.2037e-01 (18.9 %)
4.25	6.5420e-01	5.1892e-02 (7.93 %)	9.8496e-02 (15.1 %)	1.2369e-01 (18.9 %)
4.75	6.9172e-01	5.5450e-02 (8.02 %)	1.0414e-01 (15.1 %)	1.3078e-01 (18.9 %)
5.25	6.9158e-01	5.7236e-02 (8.28 %)	1.0428e-01 (15.1 %)	1.3076e-01 (18.9 %)
5.75	6.4557e-01	5.6128e-02 (8.69 %)	9.7569e-02 (15.1 %)	1.2206e-01 (18.9 %)
6.25	5.9967e-01	4.9386e-02 (8.24 %)	9.0896e-02 (15.2 %)	1.1338e-01 (18.9 %)
6.75	6.2994e-01	5.3958e-02 (8.57 %)	9.5798e-02 (15.2 %)	1.1910e-01 (18.9 %)
7.25	6.4327e-01	5.8201e-02 (9.05 %)	9.8177e-02 (15.3 %)	1.2163e-01 (18.9 %)
7.75	6.3464e-01	6.2431e-02 (9.84 %)	9.7226e-02 (15.3 %)	1.1999e-01 (18.9 %)
8.25	7.4498e-01	7.6896e-02 (10.3 %)	1.1458e-01 (15.4 %)	1.4086e-01 (18.9 %)
8.75	6.4908e-01	7.7151e-02 (11.9 %)	1.0024e-01 (15.4 %)	1.2272e-01 (18.9 %)
9.5	6.7197e-01	7.5923e-02 (11.3 %)	1.1829e-01 (17.6 %)	1.2705e-01 (18.9 %)
10.5	6.8359e-01	9.4112e-02 (13.8 %)	1.9049e-01 (27.9 %)	1.2925e-01 (18.9 %)
11.5	7.0544e-01	1.2321e-01 (17.5 %)	2.3932e-01 (33.9 %)	1.3338e-01 (18.9 %)
12.5	9.1393e-01	1.8620e-01 (20.4 %)	3.1061e-01 (34 %)	1.7280e-01 (18.9 %)
13.5	5.5296e-01	1.8173e-01 (32.9 %)	1.8827e-01 (34 %)	1.0455e-01 (18.9 %)

Table E.16: Neutral Pion R_{AA} as a function of p_T in $\sqrt{s_{NN}} = 200$ GeV Au+Au Collisions (50-60 % Central).

p_T	R _{AA}	p_T uncorrelated error	p_T correlated error	global scaling error
1.25	7.2242e-01	5.9043e-02 (8.17 %)	9.0365e-02 (12.5 %)	2.0499e-01 (28.4 %)
1.75	7.6558e-01	6.1189e-02 (7.99 %)	9.8735e-02 (12.9 %)	2.1724e-01 (28.4 %)
2.25	7.6394e-01	6.6553e-02 (8.71 %)	1.0665e-01 (14 %)	2.1678e-01 (28.4 %)
2.75	7.5205e-01	6.5780e-02 (8.75 %)	1.3824e-01 (18.4 %)	2.1340e-01 (28.4 %)
3.25	7.4639e-01	6.2012e-02 (8.31 %)	1.1455e-01 (15.3 %)	2.1180e-01 (28.4 %)
3.75	7.2828e-01	5.7444e-02 (7.89 %)	1.1002e-01 (15.1 %)	2.0666e-01 (28.4 %)
4.25	7.3515e-01	5.9064e-02 (8.03 %)	1.1068e-01 (15.1 %)	2.0861e-01 (28.4 %)
4.75	7.5576e-01	6.2176e-02 (8.23 %)	1.1379e-01 (15.1 %)	2.1446e-01 (28.4 %)
5.25	7.8364e-01	6.7307e-02 (8.59 %)	1.1816e-01 (15.1 %)	2.2237e-01 (28.4 %)
5.75	8.5772e-01	7.9027e-02 (9.21 %)	1.2963e-01 (15.1 %)	2.4339e-01 (28.4 %)
6.25	7.3467e-01	6.2855e-02 (8.56 %)	1.1136e-01 (15.2 %)	2.0847e-01 (28.4 %)
6.75	7.5323e-01	6.8526e-02 (9.1 %)	1.1455e-01 (15.2 %)	2.1374e-01 (28.4 %)
7.25	7.9723e-01	7.7773e-02 (9.76 %)	1.2167e-01 (15.3 %)	2.2622e-01 (28.4 %)
7.75	7.0562e-01	7.9075e-02 (11.2 %)	1.0810e-01 (15.3 %)	2.0023e-01 (28.4 %)
8.25	7.0282e-01	8.8880e-02 (12.6 %)	1.0810e-01 (15.4 %)	1.9943e-01 (28.4 %)
8.75	8.0527e-01	1.1229e-01 (13.9 %)	1.2436e-01 (15.4 %)	2.2851e-01 (28.4 %)
9.5	7.1839e-01	9.8152e-02 (13.7 %)	1.2646e-01 (17.6 %)	2.0385e-01 (28.4 %)
10.5	5.2409e-01	1.1190e-01 (21.4 %)	1.4604e-01 (27.9 %)	1.4871e-01 (28.4 %)
11.5	1.0301e+00	2.0493e-01 (19.9 %)	3.4947e-01 (33.9 %)	2.9231e-01 (28.4 %)
12.5	8.8239e-01	2.4814e-01 (28.1 %)	2.9989e-01 (34 %)	2.5039e-01 (28.4 %)
13.5	1.2791e+00	4.0228e-01 (31.5 %)	4.3551e-01 (34 %)	3.6296e-01 (28.4 %)

Table E.17: Neutral Pion R_{AA} as a function of p_T in $\sqrt{s_{NN}} = 200$ GeV Au+Au Collisions (60-70 % Central).

p_T	R _{AA}	p_T uncorrelated error	p_T correlated error	global scaling error
1.25	7.5161e-01	6.1285e-02 (8.15 %)	9.4017e-02 (12.5 %)	2.6481e-01 (35.2 %)
1.75	7.8079e-01	6.2322e-02 (7.98 %)	1.0070e-01 (12.9 %)	2.7509e-01 (35.2 %)
2.25	7.9860e-01	6.9551e-02 (8.71 %)	1.1149e-01 (14 %)	2.8137e-01 (35.2 %)
2.75	8.2897e-01	7.2585e-02 (8.76 %)	1.5238e-01 (18.4 %)	2.9207e-01 (35.2 %)
3.25	7.8619e-01	6.5627e-02 (8.35 %)	1.2065e-01 (15.3 %)	2.7699e-01 (35.2 %)
3.75	7.9561e-01	6.3651e-02 (8 %)	1.2020e-01 (15.1 %)	2.8031e-01 (35.2 %)
4.25	8.2692e-01	6.8180e-02 (8.25 %)	1.2450e-01 (15.1 %)	2.9135e-01 (35.2 %)
4.75	8.1009e-01	7.0409e-02 (8.69 %)	1.2196e-01 (15.1 %)	2.8541e-01 (35.2 %)
5.25	8.4433e-01	7.9754e-02 (9.45 %)	1.2731e-01 (15.1 %)	2.9748e-01 (35.2 %)
5.75	8.7937e-01	9.4044e-02 (10.7 %)	1.3291e-01 (15.1 %)	3.0982e-01 (35.2 %)
6.25	6.4834e-01	6.8110e-02 (10.5 %)	9.8274e-02 (15.2 %)	2.2843e-01 (35.2 %)
6.75	6.8790e-01	8.0024e-02 (11.6 %)	1.0461e-01 (15.2 %)	2.4237e-01 (35.2 %)
7.25	8.0202e-01	9.2406e-02 (11.5 %)	1.2241e-01 (15.3 %)	2.8257e-01 (35.2 %)
7.75	8.0486e-01	1.0987e-01 (13.7 %)	1.2330e-01 (15.3 %)	2.8357e-01 (35.2 %)
8.25	8.0937e-01	1.2570e-01 (15.5 %)	1.2448e-01 (15.4 %)	2.8516e-01 (35.2 %)
8.75	7.6139e-01	1.4239e-01 (18.7 %)	1.1758e-01 (15.4 %)	2.6826e-01 (35.2 %)
9.5	6.5657e-01	1.2325e-01 (18.8 %)	1.1558e-01 (17.6 %)	2.3132e-01 (35.2 %)
10.5	5.7180e-01	1.5519e-01 (27.1 %)	1.5934e-01 (27.9 %)	2.0146e-01 (35.2 %)
11.5	8.8300e-01	2.6586e-01 (30.1 %)	2.9955e-01 (33.9 %)	3.1110e-01 (35.2 %)

Table E.18: Neutral Pion R_{AA} as a function of p_T in $\sqrt{s_{NN}} = 200$ GeV Au+Au Collisions (70-80 % Central).

p_T	R _{AA}	p_T uncorrelated error	p_T correlated error	global scaling error
1.25	7.4779e-01	6.0986e-02 (8.16 %)	9.3539e-02 (12.5 %)	1.9697e-01 (26.3 %)
1.75	7.7852e-01	6.2166e-02 (7.99 %)	1.0040e-01 (12.9 %)	2.0507e-01 (26.3 %)
2.25	8.0635e-01	7.0292e-02 (8.72 %)	1.1257e-01 (14 %)	2.1240e-01 (26.3 %)
2.75	8.1064e-01	7.1211e-02 (8.78 %)	1.4901e-01 (18.4 %)	2.1353e-01 (26.3 %)
3.25	7.9513e-01	6.7012e-02 (8.43 %)	1.2203e-01 (15.3 %)	2.0944e-01 (26.3 %)
3.75	7.5132e-01	6.1891e-02 (8.24 %)	1.1351e-01 (15.1 %)	1.9790e-01 (26.3 %)
4.25	8.5063e-01	7.3244e-02 (8.61 %)	1.2807e-01 (15.1 %)	2.2406e-01 (26.3 %)
4.75	8.0346e-01	7.6824e-02 (9.56 %)	1.2097e-01 (15.1 %)	2.1164e-01 (26.3 %)
5.25	7.6147e-01	8.9111e-02 (11.7 %)	1.1482e-01 (15.1 %)	2.0058e-01 (26.3 %)
5.75	9.4151e-01	1.1603e-01 (12.3 %)	1.4230e-01 (15.1 %)	2.4800e-01 (26.3 %)
6.25	7.3427e-01	7.8148e-02 (10.6 %)	1.1130e-01 (15.2 %)	1.9341e-01 (26.3 %)
6.75	8.8086e-01	1.0305e-01 (11.7 %)	1.3396e-01 (15.2 %)	2.3203e-01 (26.3 %)
7.25	7.7157e-01	1.1053e-01 (14.3 %)	1.1776e-01 (15.3 %)	2.0324e-01 (26.3 %)
7.75	7.2900e-01	1.2737e-01 (17.5 %)	1.1168e-01 (15.3 %)	1.9203e-01 (26.3 %)
8.25	1.1031e+00	1.9504e-01 (17.7 %)	1.6966e-01 (15.4 %)	2.9057e-01 (26.3 %)
8.75	8.2901e-01	1.9688e-01 (23.7 %)	1.2802e-01 (15.4 %)	2.1837e-01 (26.3 %)
9.5	9.0124e-01	1.9469e-01 (21.6 %)	1.5865e-01 (17.6 %)	2.3739e-01 (26.3 %)
10.5	7.3477e-01	2.4033e-01 (32.7 %)	2.0475e-01 (27.9 %)	1.9354e-01 (26.3 %)
11.5	4.1819e-01	2.4408e-01 (58.4 %)	1.4187e-01 (33.9 %)	1.1015e-01 (26.3 %)

Table E.19: Neutral Pion R_{AA} as a function of p_T in $\sqrt{s_{NN}} = 200$ GeV Au+Au Collisions (80-92 % Central).

p_T	R _{AA}	p_T uncorrelated error	p_T correlated error	global scaling error
1.25	4.4039e-01	3.5694e-02 (8.11 %)	5.5087e-02 (12.5 %)	6.0889e-02 (13.8 %)
1.75	4.8663e-01	3.8662e-02 (7.94 %)	6.2759e-02 (12.9 %)	6.7282e-02 (13.8 %)
2.25	4.9090e-01	4.2566e-02 (8.67 %)	6.8534e-02 (14 %)	6.7872e-02 (13.8 %)
2.75	4.1850e-01	3.6395e-02 (8.7 %)	7.6928e-02 (18.4 %)	5.7863e-02 (13.8 %)
3.25	3.6869e-01	3.0353e-02 (8.23 %)	5.6582e-02 (15.3 %)	5.0976e-02 (13.8 %)
3.75	3.3943e-01	2.6295e-02 (7.75 %)	5.1280e-02 (15.1 %)	4.6931e-02 (13.8 %)
4.25	3.0832e-01	2.3896e-02 (7.75 %)	4.6420e-02 (15.1 %)	4.2629e-02 (13.8 %)
4.75	3.1108e-01	2.3945e-02 (7.7 %)	4.6836e-02 (15.1 %)	4.3011e-02 (13.8 %)
5.25	2.9141e-01	2.2426e-02 (7.7 %)	4.3940e-02 (15.1 %)	4.0291e-02 (13.8 %)
5.75	2.8513e-01	2.2085e-02 (7.75 %)	4.3094e-02 (15.1 %)	3.9423e-02 (13.8 %)
6.25	2.8546e-01	2.1965e-02 (7.69 %)	4.3270e-02 (15.2 %)	3.9469e-02 (13.8 %)
6.75	2.9188e-01	2.2665e-02 (7.77 %)	4.4389e-02 (15.2 %)	4.0356e-02 (13.8 %)
7.25	2.9530e-01	2.3202e-02 (7.86 %)	4.5069e-02 (15.3 %)	4.0829e-02 (13.8 %)
7.75	2.9563e-01	2.3591e-02 (7.98 %)	4.5290e-02 (15.3 %)	4.0874e-02 (13.8 %)
8.25	3.0020e-01	2.4390e-02 (8.12 %)	4.6173e-02 (15.4 %)	4.1507e-02 (13.8 %)
8.75	2.9579e-01	2.4564e-02 (8.3 %)	4.5679e-02 (15.4 %)	4.0897e-02 (13.8 %)
9.5	3.0032e-01	2.5260e-02 (8.41 %)	5.2866e-02 (17.6 %)	4.1523e-02 (13.8 %)
10.5	3.1288e-01	2.7535e-02 (8.8 %)	8.7186e-02 (27.9 %)	4.3260e-02 (13.8 %)
11.5	3.2415e-01	3.0196e-02 (9.32 %)	1.0997e-01 (33.9 %)	4.4818e-02 (13.8 %)
12.5	3.1867e-01	3.2336e-02 (10.1 %)	1.0831e-01 (34 %)	4.4060e-02 (13.8 %)
13.5	3.1557e-01	3.5689e-02 (11.3 %)	1.0745e-01 (34 %)	4.3632e-02 (13.8 %)
15	3.2325e-01	3.8519e-02 (11.9 %)	1.1036e-01 (34.1 %)	4.4693e-02 (13.8 %)
17	3.4252e-01	5.7599e-02 (16.8 %)	1.1734e-01 (34.3 %)	4.7357e-02 (13.8 %)
19	2.9667e-01	9.4151e-02 (31.7 %)	1.0197e-01 (34.4 %)	4.1018e-02 (13.8 %)

Table E.20: Neutral Pion R_{AA} as a function of p_T in $\sqrt{s_{NN}} = 200$ GeV Au+Au Collisions (Minimum Bias).

Appendix F

Direct Photon Data Tables

F.1 Direct Photon Excess Double Ratio in $\sqrt{s_{\text{NN}}} = 200 \text{ GeV}$ Au+Au Collisions

p_T	ratio	statistic error	p_T uncorrelated error	p_T correlated error
1.25	9.7978e-01	2.2244e-02 (2.27 %)	7.3584e-02 (7.51 %)	1.1855e-01 (12.1 %)
1.75	9.4810e-01	1.9152e-02 (2.02 %)	7.0524e-02 (7.44 %)	1.1293e-01 (11.9 %)
2.25	8.9953e-01	1.8295e-02 (2.03 %)	6.6945e-02 (7.44 %)	1.0464e-01 (11.6 %)
2.75	1.1322e+00	2.3421e-02 (2.07 %)	8.4367e-02 (7.45 %)	1.2963e-01 (11.4 %)
3.25	1.4328e+00	3.2715e-02 (2.28 %)	1.0767e-01 (7.51 %)	1.6020e-01 (11.2 %)
3.75	1.4435e+00	3.7100e-02 (2.57 %)	1.0979e-01 (7.61 %)	1.5885e-01 (11 %)
4.25	1.5178e+00	4.4581e-02 (2.94 %)	1.1743e-01 (7.74 %)	1.6307e-01 (10.7 %)
4.75	1.6574e+00	4.7636e-02 (2.87 %)	1.2782e-01 (7.71 %)	1.7527e-01 (10.6 %)
5.25	2.1104e+00	6.9804e-02 (3.31 %)	1.6635e-01 (7.88 %)	2.1796e-01 (10.3 %)
5.75	2.1554e+00	8.7333e-02 (4.05 %)	1.7716e-01 (8.22 %)	2.1926e-01 (10.2 %)
6.25	2.3596e+00	6.7787e-02 (2.87 %)	1.8175e-01 (7.7 %)	2.3505e-01 (9.96 %)
6.75	2.3855e+00	7.8725e-02 (3.3 %)	1.8761e-01 (7.86 %)	2.3580e-01 (9.88 %)
7.25	2.7133e+00	1.0117e-01 (3.73 %)	2.1832e-01 (8.05 %)	2.6824e-01 (9.89 %)
7.75	3.0228e+00	1.3707e-01 (4.53 %)	2.5519e-01 (8.44 %)	3.1119e-01 (10.3 %)
8.25	3.0569e+00	1.6088e-01 (5.26 %)	2.7025e-01 (8.84 %)	3.4922e-01 (11.4 %)
8.75	3.1980e+00	1.8717e-01 (5.85 %)	2.9396e-01 (9.19 %)	4.4299e-01 (13.9 %)
9.5	3.2237e+00	1.6341e-01 (5.07 %)	2.7986e-01 (8.68 %)	6.5552e-01 (20.3 %)
10.5	3.2801e+00	2.2721e-01 (6.93 %)	3.2275e-01 (9.84 %)	7.0662e-01 (21.5 %)
11.5	3.8193e+00	3.4162e-01 (8.94 %)	4.3253e-01 (11.3 %)	8.1779e-01 (21.4 %)
13	4.4918e+00	4.4572e-01 (9.92 %)	5.4256e-01 (12.1 %)	9.5364e-01 (21.2 %)
15	3.5045e+00	5.5336e-01 (15.8 %)	6.0062e-01 (17.1 %)	7.7952e-01 (22.2 %)
18	3.3955e+00	8.3553e-01 (24.6 %)	8.6453e-01 (25.5 %)	7.4115e-01 (21.8 %)

Table F.1: Direct Photon Excess Ratio as a function of p_T in $\sqrt{s_{\text{NN}}} = 200 \text{ GeV}$ Au+Au Collisions (0-10 % Central).

p_T	ratio	statistic error	p_T uncorrelated error	p_T correlated error
1.25	9.3859e-01	1.8158e-02 (1.93 %)	6.9603e-02 (7.42 %)	1.1357e-01 (12.1 %)
1.75	9.8608e-01	1.6711e-02 (1.69 %)	7.2544e-02 (7.36 %)	1.1746e-01 (11.9 %)
2.25	9.9305e-01	1.6584e-02 (1.67 %)	7.3000e-02 (7.35 %)	1.1552e-01 (11.6 %)
2.75	1.0470e+00	1.8089e-02 (1.73 %)	7.7103e-02 (7.36 %)	1.1987e-01 (11.4 %)
3.25	1.2332e+00	2.6371e-02 (2.14 %)	9.2140e-02 (7.47 %)	1.3788e-01 (11.2 %)
3.75	1.3306e+00	2.8776e-02 (2.16 %)	9.9502e-02 (7.48 %)	1.4642e-01 (11 %)
4.25	1.4521e+00	3.7105e-02 (2.56 %)	1.1036e-01 (7.6 %)	1.5602e-01 (10.7 %)
4.75	1.5109e+00	3.8443e-02 (2.54 %)	1.1476e-01 (7.6 %)	1.5977e-01 (10.6 %)
5.25	1.6143e+00	4.7623e-02 (2.95 %)	1.2492e-01 (7.74 %)	1.6670e-01 (10.3 %)
5.75	1.9688e+00	7.1930e-02 (3.65 %)	1.5811e-01 (8.03 %)	2.0027e-01 (10.2 %)
6.25	2.0401e+00	5.6233e-02 (2.76 %)	1.5624e-01 (7.66 %)	2.0318e-01 (9.96 %)
6.75	2.2707e+00	7.3713e-02 (3.25 %)	1.7806e-01 (7.84 %)	2.2444e-01 (9.88 %)
7.25	2.2309e+00	8.4978e-02 (3.81 %)	1.8024e-01 (8.08 %)	2.2039e-01 (9.88 %)
7.75	2.2721e+00	9.9964e-02 (4.4 %)	1.8997e-01 (8.36 %)	2.3354e-01 (10.3 %)
8.25	2.5092e+00	1.3138e-01 (5.24 %)	2.2122e-01 (8.82 %)	2.8624e-01 (11.4 %)
8.75	2.9178e+00	1.8067e-01 (6.19 %)	2.7450e-01 (9.41 %)	4.0390e-01 (13.8 %)
9.5	3.1142e+00	1.7860e-01 (5.74 %)	2.8293e-01 (9.09 %)	6.3313e-01 (20.3 %)
10.5	2.6381e+00	2.0342e-01 (7.71 %)	2.7386e-01 (10.4 %)	5.6524e-01 (21.4 %)
11.5	3.2166e+00	3.3250e-01 (10.3 %)	3.9995e-01 (12.4 %)	6.8517e-01 (21.3 %)
13	4.0042e+00	4.1913e-01 (10.5 %)	5.0108e-01 (12.5 %)	8.4650e-01 (21.1 %)
15	2.8178e+00	4.5921e-01 (16.3 %)	4.9491e-01 (17.6 %)	6.1602e-01 (21.9 %)
18	3.4097e+00	9.8474e-01 (28.9 %)	1.0097e+00 (29.6 %)	7.4519e-01 (21.9 %)

Table F.2: Direct Photon Excess Ratio as a function of p_T in $\sqrt{s_{NN}} = 200$ GeV Au+Au Collisions (10-20 % Central).

p_T	ratio	statistic error	p_T uncorrelated error	p_T correlated error
1.25	9.9875e-01	1.8140e-02 (1.82 %)	7.3765e-02 (7.39 %)	1.2085e-01 (12.1 %)
1.75	9.7895e-01	1.5636e-02 (1.6 %)	7.1805e-02 (7.33 %)	1.1661e-01 (11.9 %)
2.25	9.8854e-01	1.5195e-02 (1.54 %)	7.2382e-02 (7.32 %)	1.1499e-01 (11.6 %)
2.75	1.1230e+00	1.8070e-02 (1.61 %)	8.2397e-02 (7.34 %)	1.2858e-01 (11.4 %)
3.25	1.2052e+00	2.4824e-02 (2.06 %)	8.9776e-02 (7.45 %)	1.3474e-01 (11.2 %)
3.75	1.2638e+00	2.5972e-02 (2.06 %)	9.4123e-02 (7.45 %)	1.3907e-01 (11 %)
4.25	1.3327e+00	3.4713e-02 (2.6 %)	1.0151e-01 (7.62 %)	1.4319e-01 (10.7 %)
4.75	1.4440e+00	3.2889e-02 (2.28 %)	1.0817e-01 (7.51 %)	1.5227e-01 (10.6 %)
5.25	1.6218e+00	4.5972e-02 (2.83 %)	1.2480e-01 (7.7 %)	1.6749e-01 (10.3 %)
5.75	1.7408e+00	6.1159e-02 (3.51 %)	1.3870e-01 (7.97 %)	1.7707e-01 (10.2 %)
6.25	1.8608e+00	5.2413e-02 (2.82 %)	1.4291e-01 (7.68 %)	1.8532e-01 (9.96 %)
6.75	2.1033e+00	7.1636e-02 (3.41 %)	1.6635e-01 (7.91 %)	2.0789e-01 (9.88 %)
7.25	2.2816e+00	9.3757e-02 (4.11 %)	1.8772e-01 (8.23 %)	2.2548e-01 (9.88 %)
7.75	2.2484e+00	1.1533e-01 (5.13 %)	1.9716e-01 (8.77 %)	2.3117e-01 (10.3 %)
8.25	2.3749e+00	1.4099e-01 (5.94 %)	2.1967e-01 (9.25 %)	2.7090e-01 (11.4 %)
8.75	2.1284e+00	1.5105e-01 (7.1 %)	2.1305e-01 (10 %)	2.9364e-01 (13.8 %)
9.5	2.3359e+00	1.4635e-01 (6.26 %)	2.1969e-01 (9.4 %)	4.7274e-01 (20.2 %)
10.5	2.9361e+00	2.5002e-01 (8.52 %)	3.2324e-01 (11 %)	6.3156e-01 (21.5 %)
11.5	3.1164e+00	3.6720e-01 (11.8 %)	4.2567e-01 (13.7 %)	6.6374e-01 (21.3 %)
13	2.5749e+00	3.1845e-01 (12.4 %)	3.6219e-01 (14.1 %)	5.3192e-01 (20.7 %)
15	3.8594e+00	8.3665e-01 (21.7 %)	8.7595e-01 (22.7 %)	8.6594e-01 (22.4 %)
18	3.7687e+00	1.1742e+00 (31.2 %)	1.2004e+00 (31.9 %)	8.3212e-01 (22.1 %)

Table F.3: Direct Photon Excess Ratio as a function of p_T in $\sqrt{s_{NN}} = 200$ GeV Au+Au Collisions (20-30 % Central).

p_T	ratio	statistic error	p_T uncorrelated error	p_T correlated error
1.25	1.0187e+00	1.7909e-02 (1.76 %)	7.5096e-02 (7.37 %)	1.2327e-01 (12.1 %)
1.75	9.6975e-01	1.4604e-02 (1.51 %)	7.0943e-02 (7.32 %)	1.1551e-01 (11.9 %)
2.25	1.0416e+00	1.5385e-02 (1.48 %)	7.6135e-02 (7.31 %)	1.2116e-01 (11.6 %)
2.75	1.1797e+00	1.8264e-02 (1.55 %)	8.6404e-02 (7.32 %)	1.3507e-01 (11.4 %)
3.25	1.2858e+00	2.2390e-02 (1.74 %)	9.4730e-02 (7.37 %)	1.4375e-01 (11.2 %)
3.75	1.2464e+00	2.6185e-02 (2.1 %)	9.2984e-02 (7.46 %)	1.3715e-01 (11 %)
4.25	1.4405e+00	3.9712e-02 (2.76 %)	1.1049e-01 (7.67 %)	1.5477e-01 (10.7 %)
4.75	1.4341e+00	3.3189e-02 (2.31 %)	1.0786e-01 (7.52 %)	1.5165e-01 (10.6 %)
5.25	1.5586e+00	4.5529e-02 (2.92 %)	1.2043e-01 (7.73 %)	1.6094e-01 (10.3 %)
5.75	1.7239e+00	6.4045e-02 (3.72 %)	1.3891e-01 (8.06 %)	1.7534e-01 (10.2 %)
6.25	1.7385e+00	5.3667e-02 (3.09 %)	1.3528e-01 (7.78 %)	1.7309e-01 (9.96 %)
6.75	1.8850e+00	7.3387e-02 (3.89 %)	1.5320e-01 (8.13 %)	1.8621e-01 (9.88 %)
7.25	1.6195e+00	7.6702e-02 (4.74 %)	1.3839e-01 (8.55 %)	1.5971e-01 (9.86 %)
7.75	1.9878e+00	1.0932e-01 (5.5 %)	1.7857e-01 (8.98 %)	2.0412e-01 (10.3 %)
8.25	1.9262e+00	1.3290e-01 (6.9 %)	1.9033e-01 (9.88 %)	2.1913e-01 (11.4 %)
8.75	2.2603e+00	1.9321e-01 (8.55 %)	2.5060e-01 (11.1 %)	3.1191e-01 (13.8 %)
9.5	2.1806e+00	1.6400e-01 (7.52 %)	2.2402e-01 (10.3 %)	4.4031e-01 (20.2 %)
10.5	2.5165e+00	2.4337e-01 (9.67 %)	2.9956e-01 (11.9 %)	5.3844e-01 (21.4 %)
11.5	2.3195e+00	3.0526e-01 (13.2 %)	3.4376e-01 (14.8 %)	4.8724e-01 (21 %)
13	2.2549e+00	3.3569e-01 (14.9 %)	3.6743e-01 (16.3 %)	4.6054e-01 (20.4 %)
15	3.9590e+00	1.0948e+00 (27.7 %)	1.1268e+00 (28.5 %)	8.8878e-01 (22.4 %)
18	4.0233e+00	1.7728e+00 (44.1 %)	1.7928e+00 (44.6 %)	8.9189e-01 (22.2 %)

Table F.4: Direct Photon Excess Ratio as a function of p_T in $\sqrt{s_{NN}} = 200$ GeV Au+Au Collisions (30-40 % Central).

p_T	ratio	statistic error	p_T uncorrelated error	p_T correlated error
1.25	1.0147e+00	1.7202e-02 (1.7 %)	7.4652e-02 (7.36 %)	1.2278e-01 (12.1 %)
1.75	9.8690e-01	1.4527e-02 (1.47 %)	7.2129e-02 (7.31 %)	1.1755e-01 (11.9 %)
2.25	1.0168e+00	1.4920e-02 (1.47 %)	7.4307e-02 (7.31 %)	1.1828e-01 (11.6 %)
2.75	1.0729e+00	1.7056e-02 (1.59 %)	7.8680e-02 (7.33 %)	1.2285e-01 (11.4 %)
3.25	1.1844e+00	2.0968e-02 (1.77 %)	8.7342e-02 (7.37 %)	1.3242e-01 (11.2 %)
3.75	1.2645e+00	2.9100e-02 (2.3 %)	9.5083e-02 (7.52 %)	1.3915e-01 (11 %)
4.25	1.2338e+00	3.9132e-02 (3.17 %)	9.6593e-02 (7.83 %)	1.3256e-01 (10.7 %)
4.75	1.3737e+00	3.4299e-02 (2.5 %)	1.0412e-01 (7.58 %)	1.4526e-01 (10.6 %)
5.25	1.4742e+00	4.7504e-02 (3.22 %)	1.1567e-01 (7.85 %)	1.5223e-01 (10.3 %)
5.75	1.4039e+00	5.6750e-02 (4.04 %)	1.1530e-01 (8.21 %)	1.4276e-01 (10.2 %)
6.25	1.5945e+00	5.8579e-02 (3.67 %)	1.2807e-01 (8.03 %)	1.5874e-01 (9.96 %)
6.75	1.7141e+00	7.6236e-02 (4.45 %)	1.4408e-01 (8.41 %)	1.6929e-01 (9.88 %)
7.25	1.6795e+00	9.3939e-02 (5.59 %)	1.5201e-01 (9.05 %)	1.6570e-01 (9.87 %)
7.75	1.8784e+00	1.3045e-01 (6.94 %)	1.8658e-01 (9.93 %)	1.9285e-01 (10.3 %)
8.25	1.5630e+00	1.3026e-01 (8.33 %)	1.7069e-01 (10.9 %)	1.7739e-01 (11.3 %)
8.75	1.5163e+00	1.5481e-01 (10.2 %)	1.8785e-01 (12.4 %)	2.0795e-01 (13.7 %)
9.5	2.0442e+00	1.9388e-01 (9.48 %)	2.4087e-01 (11.8 %)	4.1237e-01 (20.2 %)
10.5	2.1256e+00	2.8957e-01 (13.6 %)	3.2465e-01 (15.3 %)	4.5252e-01 (21.3 %)
11.5	1.7996e+00	3.0331e-01 (16.9 %)	3.2655e-01 (18.1 %)	3.7293e-01 (20.7 %)
13	2.7499e+00	4.8467e-01 (17.6 %)	5.1877e-01 (18.9 %)	5.7029e-01 (20.7 %)
15	2.1974e+00	6.3708e-01 (29 %)	6.5235e-01 (29.7 %)	4.6848e-01 (21.3 %)
18	3.8830e+00	1.8421e+00 (47.4 %)	1.8600e+00 (47.9 %)	8.5906e-01 (22.1 %)

Table F.5: Direct Photon Excess Ratio as a function of p_T in $\sqrt{s_{NN}} = 200$ GeV Au+Au Collisions (40-50 % Central).

p_T	ratio	statistic error	p_T uncorrelated error	p_T correlated error
1.25	1.0144e+00	1.6591e-02 (1.64 %)	7.4489e-02 (7.34 %)	1.2274e-01 (12.1 %)
1.75	9.7996e-01	1.3978e-02 (1.43 %)	7.1534e-02 (7.3 %)	1.1673e-01 (11.9 %)
2.25	1.0147e+00	1.4596e-02 (1.44 %)	7.4090e-02 (7.3 %)	1.1803e-01 (11.6 %)
2.75	1.1099e+00	1.7605e-02 (1.59 %)	8.1384e-02 (7.33 %)	1.2708e-01 (11.4 %)
3.25	1.1576e+00	2.2790e-02 (1.97 %)	8.5950e-02 (7.42 %)	1.2943e-01 (11.2 %)
3.75	1.2097e+00	3.2754e-02 (2.71 %)	9.2581e-02 (7.65 %)	1.3311e-01 (11 %)
4.25	1.2113e+00	4.6802e-02 (3.86 %)	9.8526e-02 (8.13 %)	1.3014e-01 (10.7 %)
4.75	1.2220e+00	3.4629e-02 (2.83 %)	9.4055e-02 (7.7 %)	1.2921e-01 (10.6 %)
5.25	1.3023e+00	4.9071e-02 (3.77 %)	1.0529e-01 (8.09 %)	1.3448e-01 (10.3 %)
5.75	1.3909e+00	6.8103e-02 (4.9 %)	1.2052e-01 (8.67 %)	1.4144e-01 (10.2 %)
6.25	1.6216e+00	7.2564e-02 (4.47 %)	1.3669e-01 (8.43 %)	1.6146e-01 (9.96 %)
6.75	1.5479e+00	8.7966e-02 (5.68 %)	1.4114e-01 (9.12 %)	1.5285e-01 (9.87 %)
7.25	1.5398e+00	1.0997e-01 (7.14 %)	1.5522e-01 (10.1 %)	1.5188e-01 (9.86 %)
7.75	1.7235e+00	1.5293e-01 (8.87 %)	1.9585e-01 (11.4 %)	1.7688e-01 (10.3 %)
8.25	1.5173e+00	1.5724e-01 (10.4 %)	1.9024e-01 (12.5 %)	1.7222e-01 (11.3 %)
8.75	1.8532e+00	2.3892e-01 (12.9 %)	2.7228e-01 (14.7 %)	2.5521e-01 (13.8 %)
9.5	1.7717e+00	2.0960e-01 (11.8 %)	2.4328e-01 (13.7 %)	3.5636e-01 (20.1 %)
10.5	2.0349e+00	3.2330e-01 (15.9 %)	3.5248e-01 (17.3 %)	4.3289e-01 (21.3 %)
11.5	1.7924e+00	3.9693e-01 (22.1 %)	4.1485e-01 (23.1 %)	3.7184e-01 (20.7 %)
13	1.7650e+00	3.9580e-01 (22.4 %)	4.1209e-01 (23.3 %)	3.5355e-01 (20 %)
15	7.8509e+00	4.2586e+00 (54.2 %)	4.2934e+00 (54.7 %)	1.8202e+00 (23.2 %)
18	2.4046e+00	1.1827e+00 (49.2 %)	1.1924e+00 (49.6 %)	5.0665e-01 (21.1 %)

Table F.6: Direct Photon Excess Ratio as a function of p_T in $\sqrt{s_{NN}} = 200$ GeV Au+Au Collisions (50-60 % Central).

p_T	ratio	statistic error	p_T uncorrelated error	p_T correlated error
1.25	9.6927e-01	1.4941e-02 (1.54 %)	7.0979e-02 (7.32 %)	1.1728e-01 (12.1 %)
1.75	9.8870e-01	1.3371e-02 (1.35 %)	7.2032e-02 (7.29 %)	1.1777e-01 (11.9 %)
2.25	1.0461e+00	1.4663e-02 (1.4 %)	7.6312e-02 (7.29 %)	1.2169e-01 (11.6 %)
2.75	1.1205e+00	1.9112e-02 (1.71 %)	8.2457e-02 (7.36 %)	1.2829e-01 (11.4 %)
3.25	1.1289e+00	2.6623e-02 (2.36 %)	8.5089e-02 (7.54 %)	1.2622e-01 (11.2 %)
3.75	1.1877e+00	4.1038e-02 (3.46 %)	9.4407e-02 (7.95 %)	1.3069e-01 (11 %)
4.25	1.2006e+00	6.1647e-02 (5.13 %)	1.0576e-01 (8.81 %)	1.2899e-01 (10.7 %)
4.75	1.2385e+00	4.4287e-02 (3.58 %)	9.9078e-02 (8 %)	1.3096e-01 (10.6 %)
5.25	1.2302e+00	5.8055e-02 (4.72 %)	1.0541e-01 (8.57 %)	1.2701e-01 (10.3 %)
5.75	1.1705e+00	7.2303e-02 (6.18 %)	1.1056e-01 (9.45 %)	1.1898e-01 (10.2 %)
6.25	1.4498e+00	8.4726e-02 (5.84 %)	1.3376e-01 (9.23 %)	1.4428e-01 (9.95 %)
6.75	1.4884e+00	1.1121e-01 (7.47 %)	1.5370e-01 (10.3 %)	1.4690e-01 (9.87 %)
7.25	1.2901e+00	1.2375e-01 (9.59 %)	1.5397e-01 (11.9 %)	1.2701e-01 (9.85 %)
7.75	1.6286e+00	1.9837e-01 (12.2 %)	2.2954e-01 (14.1 %)	1.6695e-01 (10.3 %)
8.25	1.5829e+00	2.3918e-01 (15.1 %)	2.6397e-01 (16.7 %)	1.7960e-01 (11.3 %)
8.75	1.5747e+00	2.7465e-01 (17.4 %)	2.9606e-01 (18.8 %)	2.1601e-01 (13.7 %)
9.5	1.9708e+00	3.1560e-01 (16 %)	3.4429e-01 (17.5 %)	3.9698e-01 (20.1 %)
10.5	2.3079e+00	6.0851e-01 (26.4 %)	6.2913e-01 (27.3 %)	4.9245e-01 (21.3 %)
11.5	1.5035e+00	4.1263e-01 (27.4 %)	4.2450e-01 (28.2 %)	3.0720e-01 (20.4 %)
13	1.3395e+00	4.0069e-01 (29.9 %)	4.0938e-01 (30.6 %)	2.5857e-01 (19.3 %)
15	1.2855e+00	7.6404e-01 (59.4 %)	7.6770e-01 (59.7 %)	2.4999e-01 (19.4 %)

Table F.7: Direct Photon Excess Ratio as a function of p_T in $\sqrt{s_{NN}} = 200$ GeV Au+Au Collisions (60-70 % Central).

p_T	ratio	statistic error	p_T uncorrelated error	p_T correlated error
1.25	9.6557e-01	1.3936e-02 (1.44 %)	7.0515e-02 (7.3 %)	1.1683e-01 (12.1 %)
1.75	1.0629e+00	1.3888e-02 (1.31 %)	7.7347e-02 (7.28 %)	1.2660e-01 (11.9 %)
2.25	1.0367e+00	1.5494e-02 (1.49 %)	7.5815e-02 (7.31 %)	1.2059e-01 (11.6 %)
2.75	1.0019e+00	2.0818e-02 (2.08 %)	7.4686e-02 (7.45 %)	1.1472e-01 (11.4 %)
3.25	1.1040e+00	3.4884e-02 (3.16 %)	8.6388e-02 (7.83 %)	1.2343e-01 (11.2 %)
3.75	1.1434e+00	5.5657e-02 (4.87 %)	9.8983e-02 (8.66 %)	1.2582e-01 (11 %)
4.25	1.2727e+00	8.8911e-02 (6.99 %)	1.2730e-01 (10 %)	1.3675e-01 (10.7 %)
4.75	1.2189e+00	5.9960e-02 (4.92 %)	1.0585e-01 (8.68 %)	1.2889e-01 (10.6 %)
5.25	1.2123e+00	8.1128e-02 (6.69 %)	1.1876e-01 (9.8 %)	1.2519e-01 (10.3 %)
5.75	1.0865e+00	9.9120e-02 (9.12 %)	1.2592e-01 (11.6 %)	1.1047e-01 (10.2 %)
6.25	1.6721e+00	1.6406e-01 (9.81 %)	2.0295e-01 (12.1 %)	1.6653e-01 (9.96 %)
6.75	1.8875e+00	2.2408e-01 (11.9 %)	2.6146e-01 (13.9 %)	1.8656e-01 (9.88 %)
7.25	1.3954e+00	1.9524e-01 (14 %)	2.1902e-01 (15.7 %)	1.3762e-01 (9.86 %)
7.75	1.2741e+00	2.3688e-01 (18.6 %)	2.5349e-01 (19.9 %)	1.3047e-01 (10.2 %)
8.25	1.2991e+00	2.9282e-01 (22.5 %)	3.0680e-01 (23.6 %)	1.4724e-01 (11.3 %)
8.75	1.2968e+00	3.6836e-01 (28.4 %)	3.7940e-01 (29.3 %)	1.7760e-01 (13.7 %)
9.5	1.8922e+00	4.8406e-01 (25.6 %)	5.0181e-01 (26.5 %)	3.8171e-01 (20.2 %)
10.5	2.4834e+00	8.9694e-01 (36.1 %)	9.1343e-01 (36.8 %)	5.3254e-01 (21.4 %)
11.5	1.1691e+00	5.6720e-01 (48.5 %)	5.7231e-01 (49 %)	2.3514e-01 (20.1 %)
13	2.4821e+00	1.2423e+00 (50 %)	1.2534e+00 (50.5 %)	5.1285e-01 (20.7 %)

Table F.8: Direct Photon Excess Ratio as a function of p_T in $\sqrt{s_{NN}} = 200$ GeV Au+Au Collisions (70-80 % Central).

p_T	ratio	statistic error	p_T uncorrelated error	p_T correlated error
1.25	9.7218e-01	1.4202e-02 (1.46 %)	7.1031e-02 (7.31 %)	1.1763e-01 (12.1 %)
1.75	1.1720e+00	1.5952e-02 (1.36 %)	8.5403e-02 (7.29 %)	1.3960e-01 (11.9 %)
2.25	1.0350e+00	1.7798e-02 (1.72 %)	7.6204e-02 (7.36 %)	1.2040e-01 (11.6 %)
2.75	1.0813e+00	2.8023e-02 (2.59 %)	8.2327e-02 (7.61 %)	1.2381e-01 (11.4 %)
3.25	1.1718e+00	4.8015e-02 (4.1 %)	9.6655e-02 (8.25 %)	1.3101e-01 (11.2 %)
3.75	1.3614e+00	8.6079e-02 (6.32 %)	1.3003e-01 (9.55 %)	1.4981e-01 (11 %)
4.25	1.1904e+00	1.1356e-01 (9.54 %)	1.4197e-01 (11.9 %)	1.2790e-01 (10.7 %)
4.75	1.3054e+00	8.7655e-02 (6.72 %)	1.2810e-01 (9.81 %)	1.3804e-01 (10.6 %)
5.25	1.3263e+00	1.3522e-01 (10.2 %)	1.6519e-01 (12.5 %)	1.3695e-01 (10.3 %)
5.75	1.1192e+00	1.3191e-01 (11.8 %)	1.5427e-01 (13.8 %)	1.1378e-01 (10.2 %)
6.25	1.3560e+00	1.6275e-01 (12 %)	1.8937e-01 (14 %)	1.3497e-01 (9.95 %)
6.75	1.2500e+00	1.8503e-01 (14.8 %)	2.0534e-01 (16.4 %)	1.2332e-01 (9.87 %)
7.25	1.1873e+00	2.4463e-01 (20.6 %)	2.5875e-01 (21.8 %)	1.1690e-01 (9.85 %)
7.75	1.4943e+00	3.7580e-01 (25.1 %)	3.9045e-01 (26.1 %)	1.5317e-01 (10.3 %)
8.25	7.4877e-01	2.3950e-01 (32 %)	2.4510e-01 (32.7 %)	8.3746e-02 (11.2 %)
8.75	9.9476e-01	4.0414e-01 (40.6 %)	4.1002e-01 (41.2 %)	1.3513e-01 (13.6 %)
9.5	1.1535e+00	4.0070e-01 (34.7 %)	4.0846e-01 (35.4 %)	2.2872e-01 (19.8 %)
10.5	1.5758e+00	7.7615e-01 (49.3 %)	7.8357e-01 (49.7 %)	3.3166e-01 (21 %)

Table F.9: Direct Photon Excess Ratio as a function of p_T in $\sqrt{s_{NN}} = 200$ GeV Au+Au Collisions (80-92 % Central).

p_T	ratio	statistic error	p_T uncorrelated error	p_T correlated error
1.25	1.0190e+00	1.1799e-02 (1.16 %)	7.3896e-02 (7.25 %)	1.2330e-01 (12.1 %)
1.75	1.0102e+00	1.0724e-02 (1.06 %)	7.3111e-02 (7.24 %)	1.2033e-01 (11.9 %)
2.25	1.0121e+00	1.0578e-02 (1.05 %)	7.3225e-02 (7.23 %)	1.1774e-01 (11.6 %)
2.75	1.1353e+00	1.1840e-02 (1.04 %)	8.2136e-02 (7.23 %)	1.2999e-01 (11.4 %)
3.25	1.2684e+00	1.6733e-02 (1.32 %)	9.2333e-02 (7.28 %)	1.4181e-01 (11.2 %)
3.75	1.3734e+00	1.6792e-02 (1.22 %)	9.9741e-02 (7.26 %)	1.5113e-01 (11 %)
4.25	1.4270e+00	1.9171e-02 (1.34 %)	1.0392e-01 (7.28 %)	1.5332e-01 (10.7 %)
4.75	1.4847e+00	1.8831e-02 (1.27 %)	1.0791e-01 (7.27 %)	1.5701e-01 (10.6 %)
5.25	1.6766e+00	2.4156e-02 (1.44 %)	1.2235e-01 (7.3 %)	1.7314e-01 (10.3 %)
5.75	1.8274e+00	3.1296e-02 (1.71 %)	1.3437e-01 (7.35 %)	1.8587e-01 (10.2 %)
6.25	1.9351e+00	2.6658e-02 (1.38 %)	1.4081e-01 (7.28 %)	1.9272e-01 (9.96 %)
6.75	2.1074e+00	3.3691e-02 (1.6 %)	1.5413e-01 (7.31 %)	2.0827e-01 (9.88 %)
7.25	2.1447e+00	3.9975e-02 (1.86 %)	1.5794e-01 (7.36 %)	2.1186e-01 (9.88 %)
7.75	2.3168e+00	5.1340e-02 (2.22 %)	1.7258e-01 (7.45 %)	2.3819e-01 (10.3 %)
8.25	2.3210e+00	6.0811e-02 (2.62 %)	1.7541e-01 (7.56 %)	2.6461e-01 (11.4 %)
8.75	2.5202e+00	7.7921e-02 (3.09 %)	1.9452e-01 (7.72 %)	3.4831e-01 (13.8 %)
9.5	2.6770e+00	7.3512e-02 (2.75 %)	2.0201e-01 (7.55 %)	5.4291e-01 (20.3 %)
10.5	2.7604e+00	1.0160e-01 (3.68 %)	2.1737e-01 (7.87 %)	5.9236e-01 (21.5 %)
11.5	2.9165e+00	1.4074e-01 (4.83 %)	2.4524e-01 (8.41 %)	6.1912e-01 (21.2 %)
13	3.2371e+00	1.6583e-01 (5.12 %)	2.7531e-01 (8.5 %)	6.7744e-01 (20.9 %)
15	3.3395e+00	2.9280e-01 (8.77 %)	3.6743e-01 (11 %)	7.4093e-01 (22.2 %)
18	3.3821e+00	4.5082e-01 (13.3 %)	5.0223e-01 (14.8 %)	7.3886e-01 (21.8 %)

Table F.10: Direct Photon Excess Ratio as a function of p_T in $\sqrt{s_{NN}} = 200$ GeV Au+Au Collisions (Minimum Bias).

F.2 Direct Photon Invariant Yield in $\sqrt{s_{\text{NN}}} = 200$ GeV Au+Au Collisions

p_T	$1/2\pi p_T N_{\text{eve}} \cdot d^2N/dp_T dy$	statistic error	p_T uncorrelated error	p_T correlated error
1.25	3.2752e-01			
1.75	4.1786e-02			
2.25	5.5879e-03			
2.75	9.6075e-04	1.6617e-04 (17.3 %)	5.6005e-04 (58.3 %)	1.4074e-03 (146 %)
3.25	6.8639e-04	4.1775e-05 (6.09 %)	1.2567e-04 (18.3 %)	3.6488e-04 (53.2 %)
3.75	2.2313e-04	1.5625e-05 (7 %)	4.0738e-05 (18.3 %)	1.1509e-04 (51.6 %)
4.25	9.5832e-05	6.8475e-06 (7.15 %)	1.5496e-05 (16.2 %)	4.3295e-05 (45.2 %)
4.75	5.0280e-05	2.4316e-06 (4.84 %)	6.2825e-06 (12.5 %)	1.8990e-05 (37.8 %)
5.25	3.2222e-05	1.1125e-06 (3.45 %)	2.5271e-06 (7.84 %)	8.6247e-06 (26.8 %)
5.75	1.6944e-05	6.8855e-07 (4.06 %)	1.3401e-06 (7.91 %)	4.3342e-06 (25.6 %)
6.25	1.0540e-05	3.3193e-07 (3.15 %)	7.0054e-07 (6.65 %)	2.3953e-06 (22.7 %)
6.75	6.0288e-06	2.2392e-07 (3.71 %)	4.1225e-07 (6.84 %)	1.3255e-06 (22 %)
7.25	4.1024e-06	1.5646e-07 (3.81 %)	2.5030e-07 (6.1 %)	7.9212e-07 (19.3 %)
7.75	2.6464e-06	1.1346e-07 (4.29 %)	1.5763e-07 (5.96 %)	4.6854e-07 (17.7 %)
8.25	1.6063e-06	8.2553e-08 (5.14 %)	1.0515e-07 (6.55 %)	2.7769e-07 (17.3 %)
8.75	1.1480e-06	6.5518e-08 (5.71 %)	7.8858e-08 (6.87 %)	1.9510e-07 (17 %)
9.5	6.2811e-07	3.1818e-08 (5.07 %)	3.9524e-08 (6.29 %)	1.1240e-07 (17.9 %)
10.5	3.0284e-07	2.0597e-08 (6.8 %)	2.3276e-08 (7.69 %)	5.3688e-08 (17.7 %)
11.5	1.8142e-07	1.4323e-08 (7.89 %)	1.5317e-08 (8.44 %)	2.8900e-08 (15.9 %)
13	7.4378e-08	5.6757e-09 (7.63 %)	5.9766e-09 (8.04 %)	1.0772e-08 (14.5 %)
15	2.1204e-08	2.9567e-09 (13.9 %)	3.0207e-09 (14.2 %)	3.3803e-09 (15.9 %)
18	4.7533e-09	8.8580e-10 (18.6 %)	8.9623e-10 (18.9 %)	7.5023e-10 (15.8 %)

Table F.11: Direct Photon Invariant Yield as a function of p_T in $\sqrt{s_{\text{NN}}} = 200$ GeV Au+Au Collisions (0-10 % Central). For points with no errors given, data value represents 90 % confidence level upper limit.

p_T	$1/2\pi p_T N_{\text{eve}} \cdot d^2N/dp_T dy$	statistic error	p_T uncorrelated error	p_T correlated error
1.25	1.9529e-01			
1.75	3.5846e-02			
2.25	6.9556e-03			
2.75	2.7916e-04	1.1306e-04 (40.5 %)	4.5014e-04 (161 %)	1.0954e-03 (392 %)
3.25	3.2077e-04	3.6771e-05 (11.5 %)	1.0813e-04 (33.7 %)	2.8339e-04 (88.3 %)
3.75	1.4281e-04	1.1583e-05 (8.11 %)	3.4129e-05 (23.9 %)	9.2946e-05 (65.1 %)
4.25	6.8242e-05	5.2336e-06 (7.67 %)	1.2447e-05 (18.2 %)	3.4110e-05 (50 %)
4.75	3.1823e-05	1.7853e-06 (5.61 %)	5.0046e-06 (15.7 %)	1.4358e-05 (45.1 %)
5.25	1.6893e-05	9.1652e-07 (5.43 %)	2.2693e-06 (13.4 %)	6.5131e-06 (38.6 %)
5.75	1.1484e-05	5.1782e-07 (4.51 %)	1.0524e-06 (9.16 %)	3.2373e-06 (28.2 %)
6.25	6.3751e-06	2.5307e-07 (3.97 %)	5.3865e-07 (8.45 %)	1.6655e-06 (26.1 %)
6.75	4.3320e-06	1.8078e-07 (4.17 %)	3.2383e-07 (7.48 %)	9.9386e-07 (22.9 %)
7.25	2.4777e-06	1.2875e-07 (5.2 %)	2.0347e-07 (8.21 %)	5.5862e-07 (22.5 %)
7.75	1.5644e-06	9.5055e-08 (6.08 %)	1.3521e-07 (8.64 %)	3.4077e-07 (21.8 %)
8.25	1.0835e-06	7.1063e-08 (6.56 %)	9.1039e-08 (8.4 %)	2.1431e-07 (19.8 %)
8.75	8.2936e-07	5.6071e-08 (6.76 %)	6.6292e-08 (7.99 %)	1.4926e-07 (18 %)
9.5	4.4487e-07	2.6560e-08 (5.97 %)	3.1690e-08 (7.12 %)	8.1598e-08 (18.3 %)
10.5	1.7674e-07	1.6827e-08 (9.52 %)	1.8740e-08 (10.6 %)	3.7311e-08 (21.1 %)
11.5	1.0798e-07	1.1457e-08 (10.6 %)	1.2083e-08 (11.2 %)	1.9064e-08 (17.7 %)
13	5.6325e-08	4.9856e-09 (8.85 %)	5.2217e-09 (9.27 %)	8.5669e-09 (15.2 %)
15	1.4674e-08	2.5980e-09 (17.7 %)	2.6533e-09 (18.1 %)	2.7025e-09 (18.4 %)
18	3.4885e-09	7.5386e-10 (21.6 %)	7.6046e-10 (21.8 %)	5.5015e-10 (15.8 %)

Table F.12: Direct Photon Invariant Yield as a function of p_T in $\sqrt{s_{\text{NN}}} = 200$ GeV Au+Au Collisions (10-20 % Central). For points with no errors given, data value represents 90 % confidence level upper limit.

p_T	$1/2\pi p_T N_{\text{eve}} \cdot d^2N/dp_T dy$	statistic error	p_T uncorrelated error	p_T correlated error
1.25	1.7774e-01			
1.75	2.4457e-02			
2.25	4.8350e-03			
2.75	5.1639e-04	7.6600e-05 (14.8 %)	3.1821e-04 (61.6 %)	8.0879e-04 (157 %)
3.25	2.1509e-04	2.7986e-05 (13 %)	8.2309e-05 (38.3 %)	2.1256e-04 (98.8 %)
3.75	9.2275e-05	9.0255e-06 (9.78 %)	2.7430e-05 (29.7 %)	7.2489e-05 (78.6 %)
4.25	4.0369e-05	4.3358e-06 (10.7 %)	1.0006e-05 (24.8 %)	2.5694e-05 (63.6 %)
4.75	2.1866e-05	1.2871e-06 (5.89 %)	3.9312e-06 (18 %)	1.1033e-05 (50.5 %)
5.25	1.2577e-05	6.7124e-07 (5.34 %)	1.6689e-06 (13.3 %)	4.8092e-06 (38.2 %)
5.75	7.0908e-06	4.0709e-07 (5.74 %)	8.3416e-07 (11.8 %)	2.3556e-06 (33.2 %)
6.25	4.2541e-06	2.1114e-07 (4.96 %)	4.3337e-07 (10.2 %)	1.2413e-06 (29.2 %)
6.75	2.7925e-06	1.4380e-07 (5.15 %)	2.4381e-07 (8.73 %)	6.8989e-07 (24.7 %)
7.25	1.7786e-06	1.0246e-07 (5.76 %)	1.4969e-07 (8.42 %)	3.9296e-07 (22.1 %)
7.75	1.0170e-06	7.4854e-08 (7.36 %)	9.8235e-08 (9.66 %)	2.2379e-07 (22 %)
8.25	7.2531e-07	5.8704e-08 (8.09 %)	7.1813e-08 (9.9 %)	1.5029e-07 (20.7 %)
8.75	3.9859e-07	4.4881e-08 (11.3 %)	5.2346e-08 (13.1 %)	9.4571e-08 (23.7 %)
9.5	2.4928e-07	2.2233e-08 (8.92 %)	2.6407e-08 (10.6 %)	5.9319e-08 (23.8 %)
10.5	1.5517e-07	1.4786e-08 (9.53 %)	1.6083e-08 (10.4 %)	2.9900e-08 (19.3 %)
11.5	7.9152e-08	9.8392e-09 (12.4 %)	1.0264e-08 (13 %)	1.4306e-08 (18.1 %)
13	2.3278e-08	3.6521e-09 (15.7 %)	3.7954e-09 (16.3 %)	4.7467e-09 (20.4 %)
15	1.1829e-08	2.1160e-09 (17.9 %)	2.1400e-09 (18.1 %)	1.8015e-09 (15.2 %)
18	2.6502e-09	6.2431e-10 (23.6 %)	6.2822e-10 (23.7 %)	3.9856e-10 (15 %)

Table F.13: Direct Photon Invariant Yield as a function of p_T in $\sqrt{s_{\text{NN}}} = 200$ GeV Au+Au Collisions (20-30 % Central). For points with no errors given, data value represents 90 % confidence level upper limit.

p_T	$1/2\pi p_T N_{\text{eve}} \cdot d^2N/dp_T dy$	statistic error	p_T uncorrelated error	p_T correlated error
1.25	8.9151e-03	8.7874e-03 (98.6 %)	3.5947e-02 (403 %)	8.4165e-02 (944 %)
1.75	1.5649e-02			
2.25	5.4438e-04	2.1054e-04 (38.7 %)	9.8276e-04 (181 %)	2.3776e-03 (437 %)
2.75	4.9791e-04	4.9562e-05 (9.95 %)	2.1028e-04 (42.2 %)	5.5126e-04 (111 %)
3.25	2.0628e-04	1.5434e-05 (7.48 %)	5.5697e-05 (27 %)	1.5324e-04 (74.3 %)
3.75	6.2717e-05	6.9736e-06 (11.1 %)	2.0083e-05 (32 %)	5.2233e-05 (83.3 %)
4.25	3.6728e-05	3.4108e-06 (9.29 %)	7.1057e-06 (19.3 %)	1.8724e-05 (51 %)
4.75	1.5658e-05	9.6419e-07 (6.16 %)	2.8622e-06 (18.3 %)	7.9818e-06 (51 %)
5.25	8.4449e-06	5.2579e-07 (6.23 %)	1.2530e-06 (14.8 %)	3.4810e-06 (41.2 %)
5.75	5.1847e-06	3.2824e-07 (6.33 %)	6.3540e-07 (12.3 %)	1.7482e-06 (33.7 %)
6.25	2.7361e-06	1.7391e-07 (6.36 %)	3.3069e-07 (12.1 %)	8.7907e-07 (32.1 %)
6.75	1.6516e-06	1.1740e-07 (7.11 %)	1.8483e-07 (11.2 %)	4.6289e-07 (28 %)
7.25	7.5696e-07	8.8159e-08 (11.6 %)	1.2702e-07 (16.8 %)	2.5927e-07 (34.3 %)
7.75	6.9324e-07	6.6217e-08 (9.55 %)	8.5220e-08 (12.3 %)	1.7349e-07 (25 %)
8.25	3.8309e-07	4.8396e-08 (12.6 %)	5.7607e-08 (15 %)	9.9145e-08 (25.9 %)
8.75	2.9259e-07	3.6753e-08 (12.6 %)	4.0872e-08 (14 %)	6.5037e-08 (22.2 %)
9.5	1.5374e-07	1.8035e-08 (11.7 %)	2.0524e-08 (13.3 %)	3.9641e-08 (25.8 %)
10.5	9.7343e-08	1.2401e-08 (12.7 %)	1.3316e-08 (13.7 %)	2.1518e-08 (22.1 %)
11.5	4.2374e-08	8.0570e-09 (19 %)	8.3796e-09 (19.8 %)	9.9736e-09 (23.5 %)
13	1.3827e-08	2.9928e-09 (21.6 %)	3.0832e-09 (22.3 %)	3.2225e-09 (23.3 %)
15	7.4562e-09	1.6609e-09 (22.3 %)	1.6725e-09 (22.4 %)	1.1202e-09 (15 %)
18	1.3824e-09	4.4164e-10 (31.9 %)	4.4299e-10 (32 %)	2.0165e-10 (14.6 %)

Table F.14: Direct Photon Invariant Yield as a function of p_T in $\sqrt{s_{\text{NN}}} = 200$ GeV Au+Au Collisions (30-40 % Central). For points with no errors given, data value represents 90 % confidence level upper limit.

p_T	$1/2\pi p_T N_{\text{eve}} \cdot d^2N/dp_T dy$	statistic error	p_T uncorrelated error	p_T correlated error
1.25	4.2812e-03	5.1847e-03 (121 %)	2.1916e-02 (512 %)	5.1318e-02 (1.2e+03 %)
1.75	1.0265e-02			
2.25	1.4313e-04	1.3810e-04 (96.5 %)	6.3763e-04 (445 %)	1.5220e-03 (1.06e+03 %)
2.75	1.3922e-04	3.5410e-05 (25.4 %)	1.4450e-04 (104 %)	3.5720e-04 (257 %)
3.25	9.3927e-05	1.1264e-05 (12 %)	3.9225e-05 (41.8 %)	1.0205e-04 (109 %)
3.75	4.2733e-05	5.1006e-06 (11.9 %)	1.3005e-05 (30.4 %)	3.3493e-05 (78.4 %)
4.25	1.4016e-05	2.7100e-06 (19.3 %)	5.1947e-06 (37.1 %)	1.2000e-05 (85.6 %)
4.75	8.9032e-06	6.9336e-07 (7.79 %)	1.9047e-06 (21.4 %)	5.1018e-06 (57.3 %)
5.25	4.9700e-06	4.0355e-07 (8.12 %)	8.8218e-07 (17.8 %)	2.3093e-06 (46.5 %)
5.75	2.2242e-06	2.6652e-07 (12 %)	4.8911e-07 (22 %)	1.1416e-06 (51.3 %)
6.25	1.4323e-06	1.3199e-07 (9.22 %)	2.2417e-07 (15.7 %)	5.3285e-07 (37.2 %)
6.75	9.6756e-07	9.5323e-08 (9.85 %)	1.3993e-07 (14.5 %)	3.1057e-07 (32.1 %)
7.25	5.2010e-07	6.7882e-08 (13.1 %)	8.8983e-08 (17.1 %)	1.6725e-07 (32.2 %)
7.75	3.7586e-07	4.9922e-08 (13.3 %)	5.9546e-08 (15.8 %)	1.0096e-07 (26.9 %)
8.25	1.6733e-07	3.8504e-08 (23 %)	4.4300e-08 (26.5 %)	6.0933e-08 (36.4 %)
8.75	9.6879e-08	2.9433e-08 (30.4 %)	3.2459e-08 (33.5 %)	3.9857e-08 (41.1 %)
9.5	8.6676e-08	1.3972e-08 (16.1 %)	1.5278e-08 (17.6 %)	2.4358e-08 (28.1 %)
10.5	3.7810e-08	8.3859e-09 (22.2 %)	8.7371e-09 (23.1 %)	1.0172e-08 (26.9 %)
11.5	1.7176e-08	6.0551e-09 (35.3 %)	6.2318e-09 (36.3 %)	5.7875e-09 (33.7 %)
13	1.2255e-08	2.5467e-09 (20.8 %)	2.5951e-09 (21.2 %)	2.3579e-09 (19.2 %)
15	3.1374e-09	1.3197e-09 (42.1 %)	1.3297e-09 (42.4 %)	7.3639e-10 (23.5 %)
18	1.2681e-09	4.2669e-10 (33.6 %)	4.2794e-10 (33.7 %)	1.8804e-10 (14.8 %)

Table F.15: Direct Photon Invariant Yield as a function of p_T in $\sqrt{s_{\text{NN}}} = 200$ GeV Au+Au Collisions (40-50 % Central). For points with no errors given, data value represents 90 % confidence level upper limit.

p_T	$1/2\pi p_T N_{\text{eve}} \cdot d^2N/dp_T dy$	statistic error	p_T uncorrelated error	p_T correlated error
1.25	2.3413e-03	2.8014e-03 (120 %)	1.2248e-02 (523 %)	2.8731e-02 (1.23e+03 %)
1.75	5.5741e-03			
2.25	6.9663e-05	7.6699e-05 (110 %)	3.5625e-04 (511 %)	8.4961e-04 (1.22e+03 %)
2.75	1.2022e-04	2.0837e-05 (17.3 %)	8.3050e-05 (69.1 %)	2.0907e-04 (174 %)
3.25	4.7691e-05	7.7256e-06 (16.2 %)	2.3586e-05 (49.5 %)	5.9668e-05 (125 %)
3.75	2.0266e-05	3.6630e-06 (18.1 %)	8.0235e-06 (39.6 %)	1.9420e-05 (95.8 %)
4.25	7.7440e-06	2.0480e-06 (26.4 %)	3.3941e-06 (43.8 %)	7.2420e-06 (93.5 %)
4.75	3.4822e-06	5.1358e-07 (14.7 %)	1.2676e-06 (36.4 %)	3.0829e-06 (88.5 %)
5.25	2.0800e-06	3.0613e-07 (14.7 %)	5.9487e-07 (28.6 %)	1.3799e-06 (66.3 %)
5.75	1.2161e-06	1.8560e-07 (15.3 %)	2.9678e-07 (24.4 %)	6.4055e-07 (52.7 %)
6.25	9.1379e-07	1.0072e-07 (11 %)	1.4972e-07 (16.4 %)	3.2961e-07 (36.1 %)
6.75	4.4538e-07	7.0284e-08 (15.8 %)	9.2948e-08 (20.9 %)	1.7173e-07 (38.6 %)
7.25	2.5601e-07	5.1885e-08 (20.3 %)	6.2777e-08 (24.5 %)	9.6796e-08 (37.8 %)
7.75	1.9490e-07	3.8720e-08 (19.9 %)	4.3683e-08 (22.4 %)	5.9322e-08 (30.4 %)
8.25	9.8986e-08	3.0466e-08 (30.8 %)	3.3560e-08 (33.9 %)	3.8442e-08 (38.8 %)
8.75	8.8764e-08	2.2638e-08 (25.5 %)	2.3935e-08 (27 %)	2.5201e-08 (28.4 %)
9.5	4.2370e-08	1.0858e-08 (25.6 %)	1.1574e-08 (27.3 %)	1.4956e-08 (35.3 %)
10.5	2.5947e-08	7.1659e-09 (27.6 %)	7.3934e-09 (28.5 %)	7.4216e-09 (28.6 %)
11.5	9.8876e-09	4.5987e-09 (46.5 %)	4.6780e-09 (47.3 %)	3.3616e-09 (34 %)
13	3.8898e-09	1.8644e-09 (47.9 %)	1.8930e-09 (48.7 %)	1.2930e-09 (33.2 %)
15	3.6846e-09	1.0499e-09 (28.5 %)	1.0521e-09 (28.6 %)	4.5763e-10 (12.4 %)
18	5.9286e-10	3.4260e-10 (57.8 %)	3.4354e-10 (57.9 %)	1.2140e-10 (20.5 %)

Table F.16: Direct Photon Invariant Yield as a function of p_T in $\sqrt{s_{\text{NN}}} = 200$ GeV Au+Au Collisions (50-60 % Central). For points with no errors given, data value represents 90 % confidence level upper limit.

p_T	$1/2\pi p_T N_{\text{eve}} \cdot d^2N/dp_T dy$	statistic error	p_T uncorrelated error	p_T correlated error
1.25	1.8067e-02			
1.75	2.9638e-03			
2.25	1.1132e-04	3.8892e-05 (34.9 %)	1.8115e-04 (163 %)	4.3926e-04 (395 %)
2.75	6.9262e-05	1.2352e-05 (17.8 %)	4.4051e-05 (63.6 %)	1.1058e-04 (160 %)
3.25	2.0695e-05	5.0970e-06 (24.6 %)	1.2861e-05 (62.1 %)	3.1128e-05 (150 %)
3.75	9.8015e-06	2.5839e-06 (26.4 %)	4.6383e-06 (47.3 %)	1.0357e-05 (106 %)
4.25	3.9437e-06	1.4776e-06 (37.5 %)	2.0708e-06 (52.5 %)	3.8599e-06 (97.9 %)
4.75	1.9547e-06	3.4377e-07 (17.6 %)	6.9654e-07 (35.6 %)	1.6259e-06 (83.2 %)
5.25	8.5852e-07	2.0938e-07 (24.4 %)	3.4598e-07 (40.3 %)	7.1775e-07 (83.6 %)
5.75	3.3706e-07	1.4412e-07 (42.8 %)	2.0475e-07 (60.7 %)	3.5920e-07 (107 %)
6.25	3.8745e-07	7.4162e-08 (19.1 %)	9.8097e-08 (25.3 %)	1.7681e-07 (45.6 %)
6.75	2.2715e-07	5.2311e-08 (23 %)	6.2749e-08 (27.6 %)	9.5257e-08 (41.9 %)
7.25	8.1546e-08	3.8405e-08 (47.1 %)	4.3596e-08 (53.5 %)	5.0309e-08 (61.7 %)
7.75	9.0076e-08	2.7623e-08 (30.7 %)	2.9615e-08 (32.9 %)	3.0167e-08 (33.5 %)
8.25	5.0331e-08	2.0405e-08 (40.5 %)	2.1376e-08 (42.5 %)	1.7855e-08 (35.5 %)
8.75	3.5485e-08	1.6787e-08 (47.3 %)	1.7384e-08 (49 %)	1.3414e-08 (37.8 %)
9.5	2.7265e-08	7.9228e-09 (29.1 %)	8.1905e-09 (30 %)	8.0700e-09 (29.6 %)
10.5	1.2031e-08	4.5191e-09 (37.6 %)	4.5702e-09 (38 %)	2.9205e-09 (24.3 %)
11.5	4.3906e-09	3.6696e-09 (83.6 %)	3.7158e-09 (84.6 %)	2.1629e-09 (49.3 %)
13	1.0868e-09	1.3828e-09 (127 %)	1.3970e-09 (129 %)	7.1623e-10 (65.9 %)
15	2.0725e-10	5.9564e-10 (287 %)	5.9706e-10 (288 %)	1.5578e-10 (75.2 %)

Table F.17: Direct Photon Invariant Yield as a function of p_T in $\sqrt{s_{\text{NN}}} = 200$ GeV Au+Au Collisions (60-70 % Central). For points with no errors given, data value represents 90 % confidence level upper limit.

p_T	$1/2\pi p_T N_{\text{eve}} \cdot d^2N/dp_T dy$	statistic error	p_T uncorrelated error	p_T correlated error
1.25	8.1247e-03			
1.75	3.6431e-04	8.4902e-05 (23.3 %)	4.3336e-04 (119 %)	1.0515e-03 (289 %)
2.25	4.1194e-05	2.0065e-05 (48.7 %)	8.4695e-05 (206 %)	2.0328e-04 (493 %)
2.75	5.4088e-07	7.4381e-06 (1.38e+03 %)	2.1964e-05 (4.06e+03 %)	5.0694e-05 (9.37e+03 %)
3.25	7.8169e-06	3.2688e-06 (41.8 %)	6.4188e-06 (82.1 %)	1.4365e-05 (184 %)
3.75	3.5975e-06	1.7441e-06 (48.5 %)	2.5398e-06 (70.6 %)	4.8474e-06 (135 %)
4.25	2.5696e-06	1.0036e-06 (39.1 %)	1.2225e-06 (47.6 %)	1.9287e-06 (75.1 %)
4.75	8.1365e-07	2.1721e-07 (26.7 %)	3.5010e-07 (43 %)	7.2925e-07 (89.6 %)
5.25	3.6151e-07	1.3637e-07 (37.7 %)	1.8543e-07 (51.3 %)	3.2432e-07 (89.7 %)
5.75	7.4378e-08	9.2046e-08 (124 %)	1.1155e-07 (150 %)	1.4863e-07 (200 %)
6.25	2.1668e-07	4.7754e-08 (22 %)	5.3619e-08 (24.7 %)	7.4121e-08 (34.2 %)
6.75	1.5976e-07	3.4675e-08 (21.7 %)	3.7315e-08 (23.4 %)	4.4729e-08 (28 %)
7.25	4.7429e-08	2.5031e-08 (52.8 %)	2.6555e-08 (56 %)	2.2741e-08 (47.9 %)
7.75	1.8991e-08	1.8398e-08 (96.9 %)	1.9083e-08 (100 %)	1.2228e-08 (64.4 %)
8.25	1.2612e-08	1.3776e-08 (109 %)	1.4113e-08 (112 %)	7.6540e-09 (60.7 %)
8.75	7.3467e-09	1.0182e-08 (139 %)	1.0338e-08 (141 %)	4.8250e-09 (65.7 %)
9.5	9.7030e-09	4.8555e-09 (50 %)	4.9215e-09 (50.7 %)	3.0687e-09 (31.6 %)
10.5	6.3074e-09	3.1115e-09 (49.3 %)	3.1282e-09 (49.6 %)	1.4192e-09 (22.5 %)
11.5	5.3530e-10	2.1352e-09 (399 %)	2.1454e-09 (401 %)	7.2645e-10 (136 %)
13	1.2792e-09	8.5190e-10 (66.6 %)	8.5402e-10 (66.8 %)	2.7129e-10 (21.2 %)

Table F.18: Direct Photon Invariant Yield as a function of p_T in $\sqrt{s_{\text{NN}}} = 200$ GeV Au+Au Collisions (70-80 % Central). For points with no errors given, data value represents 90 % confidence level upper limit.

p_T	$1/2\pi p_T N_{\text{eve}} \cdot d^2N/dp_T dy$	statistic error	p_T uncorrelated error	p_T correlated error
1.25	3.3574e-03			
1.75	3.9736e-04	3.6634e-05 (9.22 %)	1.7423e-04 (43.8 %)	4.4435e-04 (112 %)
2.25	1.5871e-05	9.6522e-06 (60.8 %)	3.4574e-05 (218 %)	8.1949e-05 (516 %)
2.75	8.9856e-06	3.8243e-06 (42.6 %)	8.9665e-06 (99.8 %)	2.0772e-05 (231 %)
3.25	5.2479e-06	1.7901e-06 (34.1 %)	2.8768e-06 (54.8 %)	6.0755e-06 (116 %)
3.75	3.4787e-06	9.5277e-07 (27.4 %)	1.1921e-06 (34.3 %)	2.1065e-06 (60.6 %)
4.25	7.6219e-07	5.6428e-07 (74 %)	6.3689e-07 (83.6 %)	7.8145e-07 (103 %)
4.75	4.5988e-07	1.2146e-07 (26.4 %)	1.6504e-07 (35.9 %)	3.1045e-07 (67.5 %)
5.25	2.0413e-07	7.5956e-08 (37.2 %)	8.9030e-08 (43.6 %)	1.2719e-07 (62.3 %)
5.75	4.4691e-08	5.2363e-08 (117 %)	5.9151e-08 (132 %)	6.6076e-08 (148 %)
6.25	5.2939e-08	2.6077e-08 (49.3 %)	2.8313e-08 (53.5 %)	2.9026e-08 (54.8 %)
6.75	2.3472e-08	1.9696e-08 (83.9 %)	2.0872e-08 (88.9 %)	1.6911e-08 (72 %)
7.25	8.8007e-09	1.3454e-08 (153 %)	1.3885e-08 (158 %)	7.9487e-09 (90.3 %)
7.75	1.2634e-08	9.9092e-09 (78.4 %)	1.0088e-08 (79.8 %)	5.0456e-09 (39.9 %)
8.25	6.5506e-09			
8.75	7.8461e-09			
9.5	9.3399e-10	2.9209e-09 (313 %)	2.9521e-09 (316 %)	1.4056e-09 (150 %)
10.5	1.2819e-09	1.7326e-09 (135 %)	1.7396e-09 (136 %)	5.8364e-10 (45.5 %)

Table F.19: Direct Photon Invariant Yield as a function of p_T in $\sqrt{s_{\text{NN}}} = 200$ GeV Au+Au Collisions (80-92 % Central). For points with no errors given, data value represents 90 % confidence level upper limit.

p_T	$1/2\pi p_T N_{\text{eve}} \cdot d^2N/dp_T dy$	statistic error	p_T uncorrelated error	p_T correlated error
1.25	8.9152e-03	6.1069e-03 (68.5 %)	3.4926e-02 (392 %)	8.3044e-02 (931 %)
1.75	7.2305e-04	8.7711e-04 (121 %)	5.2564e-03 (727 %)	1.2495e-02 (1.73e+03 %)
2.25	1.5992e-04	1.6233e-04 (102 %)	9.7923e-04 (612 %)	2.3552e-03 (1.47e+03 %)
2.75	3.6043e-04	3.3895e-05 (9.4 %)	1.9887e-04 (55.2 %)	5.1653e-04 (143 %)
3.25	1.7341e-04	1.1762e-05 (6.78 %)	4.9278e-05 (28.4 %)	1.3581e-04 (78.3 %)
3.75	7.5068e-05	3.3207e-06 (4.42 %)	1.5338e-05 (20.4 %)	4.4284e-05 (59 %)
4.25	3.1073e-05	1.3597e-06 (4.38 %)	5.6043e-06 (18 %)	1.6225e-05 (52.2 %)
4.75	1.4672e-05	4.7467e-07 (3.24 %)	2.3173e-06 (15.8 %)	6.8813e-06 (46.9 %)
5.25	8.4507e-06	2.2738e-07 (2.69 %)	9.7367e-07 (11.5 %)	3.0512e-06 (36.1 %)
5.75	4.9014e-06	1.2837e-07 (2.62 %)	4.7108e-07 (9.61 %)	1.5182e-06 (31 %)
6.25	2.8214e-06	6.4411e-08 (2.28 %)	2.4101e-07 (8.54 %)	7.8338e-07 (27.8 %)
6.75	1.7989e-06	4.2990e-08 (2.39 %)	1.3348e-07 (7.42 %)	4.4346e-07 (24.7 %)
7.25	1.0744e-06	2.9802e-08 (2.77 %)	7.8819e-08 (7.34 %)	2.5167e-07 (23.4 %)
7.75	7.1256e-07	2.1626e-08 (3.03 %)	4.7662e-08 (6.69 %)	1.5253e-07 (21.4 %)
8.25	4.3914e-07	1.5889e-08 (3.62 %)	3.0408e-08 (6.92 %)	9.2835e-08 (21.1 %)
8.75	3.1071e-07	1.2203e-08 (3.93 %)	2.0208e-08 (6.5 %)	6.2439e-08 (20.1 %)
9.5	1.7749e-07	5.9001e-09 (3.32 %)	1.0207e-08 (5.75 %)	3.6791e-08 (20.7 %)
10.5	8.7139e-08	3.7898e-09 (4.35 %)	5.3902e-09 (6.19 %)	1.7662e-08 (20.3 %)
11.5	4.7401e-08	2.5741e-09 (5.43 %)	3.1917e-09 (6.73 %)	8.9911e-09 (19 %)
13	1.9947e-08	1.0279e-09 (5.15 %)	1.2279e-09 (6.16 %)	3.4058e-09 (17.1 %)
15	6.7888e-09	5.4865e-10 (8.08 %)	5.8672e-10 (8.64 %)	1.1144e-09 (16.4 %)
18	1.5564e-09	1.6362e-10 (10.5 %)	1.6969e-10 (10.9 %)	2.4669e-10 (15.9 %)

Table F.20: Direct Photon Invariant Yield as a function of p_T in $\sqrt{s_{\text{NN}}} = 200$ GeV Au+Au Collisions (Minimum Bias). For points with no errors given, data value represents 90 % confidence level upper limit.

F.3 Direct Photon Nuclear Modification Factor (R_{AA}) in $\sqrt{s_{NN}} = 200$ GeV Au+Au Collisions

p_T	R_{AA}	p_T uncorrelated error	p_T correlated error	global scaling error
5.25	1.1624e+00	9.1227e-02 (7.85 %)	4.8493e-01 (41.7 %)	1.6025e-01 (13.8 %)
5.75	1.0870e+00	8.5972e-02 (7.91 %)	4.2033e-01 (38.7 %)	1.4986e-01 (13.8 %)
6.25	1.1490e+00	7.6406e-02 (6.65 %)	3.7976e-01 (33.1 %)	1.5841e-01 (13.8 %)
6.75	1.0744e+00	7.3535e-02 (6.84 %)	3.4184e-01 (31.8 %)	1.4812e-01 (13.8 %)
7.25	1.1561e+00	7.0620e-02 (6.11 %)	3.2139e-01 (27.8 %)	1.5939e-01 (13.8 %)
7.75	1.1458e+00	6.8307e-02 (5.96 %)	2.9758e-01 (26 %)	1.5797e-01 (13.8 %)
8.25	1.0419e+00	6.8223e-02 (6.55 %)	2.6002e-01 (25 %)	1.4364e-01 (13.8 %)
8.75	1.0908e+00	7.4937e-02 (6.87 %)	2.7003e-01 (24.8 %)	1.5038e-01 (13.8 %)
9.5	1.0201e+00	6.4210e-02 (6.29 %)	2.5178e-01 (24.7 %)	1.4063e-01 (13.8 %)
10.5	9.4810e-01	7.2970e-02 (7.7 %)	2.2897e-01 (24.2 %)	1.3071e-01 (13.8 %)
11.5	1.0356e+00	8.7650e-02 (8.46 %)	2.3382e-01 (22.6 %)	1.4278e-01 (13.8 %)
13	9.6039e-01	7.7476e-02 (8.07 %)	2.0726e-01 (21.6 %)	1.3240e-01 (13.8 %)
15	7.1767e-01	1.0230e-01 (14.3 %)	1.5709e-01 (21.9 %)	9.8942e-02 (13.8 %)
18	5.6037e-01	1.0578e-01 (18.9 %)	1.2202e-01 (21.8 %)	7.7257e-02 (13.8 %)

Table F.21: Direct Photon R_{AA} as a function of p_T in $\sqrt{s_{NN}} = 200$ GeV Au+Au Collisions (0-10 % Central).

p_T	R_{AA}	p_T uncorrelated error	p_T correlated error	global scaling error
5.25	9.6610e-01	1.2982e-01 (13.4 %)	4.8407e-01 (50.1 %)	1.3349e-01 (13.8 %)
5.75	1.1680e+00	1.0703e-01 (9.16 %)	4.7238e-01 (40.4 %)	1.6139e-01 (13.8 %)
6.25	1.1017e+00	9.3121e-02 (8.45 %)	3.9085e-01 (35.5 %)	1.5224e-01 (13.8 %)
6.75	1.2239e+00	9.1561e-02 (7.48 %)	3.9759e-01 (32.5 %)	1.6911e-01 (13.8 %)
7.25	1.1070e+00	9.0965e-02 (8.22 %)	3.3362e-01 (30.1 %)	1.5296e-01 (13.8 %)
7.75	1.0739e+00	9.2846e-02 (8.65 %)	3.1040e-01 (28.9 %)	1.4838e-01 (13.8 %)
8.25	1.1142e+00	9.3631e-02 (8.4 %)	2.9797e-01 (26.7 %)	1.5395e-01 (13.8 %)
8.75	1.2493e+00	9.9868e-02 (7.99 %)	3.1800e-01 (25.5 %)	1.7263e-01 (13.8 %)
9.5	1.1454e+00	8.1611e-02 (7.13 %)	2.8645e-01 (25 %)	1.5827e-01 (13.8 %)
10.5	8.7722e-01	9.3078e-02 (10.6 %)	2.3450e-01 (26.7 %)	1.2121e-01 (13.8 %)
11.5	9.7725e-01	1.0950e-01 (11.2 %)	2.3284e-01 (23.8 %)	1.3503e-01 (13.8 %)
13	1.1530e+00	1.0721e-01 (9.3 %)	2.5454e-01 (22.1 %)	1.5932e-01 (13.8 %)
15	7.8740e-01	1.4243e-01 (18.1 %)	1.8702e-01 (23.8 %)	1.0880e-01 (13.8 %)
18	6.5201e-01	1.4225e-01 (21.8 %)	1.4191e-01 (21.8 %)	9.0093e-02 (13.8 %)

Table F.22: Direct Photon R_{AA} as a function of p_T in $\sqrt{s_{NN}} = 200$ GeV Au+Au Collisions (10-20 % Central).

p_T	R _{AA}	p_T uncorrelated error	p_T correlated error	global scaling error
5.25	1.1598e+00	1.5393e-01 (13.3 %)	5.7827e-01 (49.9 %)	1.6659e-01 (14.4 %)
5.75	1.1628e+00	1.3679e-01 (11.8 %)	5.1276e-01 (44.1 %)	1.6702e-01 (14.4 %)
6.25	1.1854e+00	1.2078e-01 (10.2 %)	4.4785e-01 (37.8 %)	1.7027e-01 (14.4 %)
6.75	1.2721e+00	1.1112e-01 (8.74 %)	4.2937e-01 (33.8 %)	1.8272e-01 (14.4 %)
7.25	1.2812e+00	1.0790e-01 (8.42 %)	3.8182e-01 (29.8 %)	1.8403e-01 (14.4 %)
7.75	1.1256e+00	1.0876e-01 (9.66 %)	3.2724e-01 (29.1 %)	1.6168e-01 (14.4 %)
8.25	1.2026e+00	1.1908e-01 (9.9 %)	3.3006e-01 (27.4 %)	1.7273e-01 (14.4 %)
8.75	9.6809e-01	1.2714e-01 (13.1 %)	2.8831e-01 (29.8 %)	1.3906e-01 (14.4 %)
9.5	1.0348e+00	1.0964e-01 (10.6 %)	3.0263e-01 (29.2 %)	1.4864e-01 (14.4 %)
10.5	1.2417e+00	1.2881e-01 (10.4 %)	3.1421e-01 (25.3 %)	1.7836e-01 (14.4 %)
11.5	1.1550e+00	1.4993e-01 (13 %)	2.7880e-01 (24.1 %)	1.6590e-01 (14.4 %)
13	7.6832e-01	1.2539e-01 (16.3 %)	1.9914e-01 (25.9 %)	1.1036e-01 (14.4 %)
15	1.0234e+00	1.8521e-01 (18.1 %)	2.1877e-01 (21.4 %)	1.4700e-01 (14.4 %)
18	7.9863e-01	1.8945e-01 (23.7 %)	1.6964e-01 (21.2 %)	1.1471e-01 (14.4 %)

Table F.23: Direct Photon R_{AA} as a function of p_T in $\sqrt{s_{NN}} = 200$ GeV Au+Au Collisions (20-30 % Central).

p_T	R _{AA}	p_T uncorrelated error	p_T correlated error	global scaling error
5.25	1.3252e+00	1.9666e-01 (14.8 %)	6.9151e-01 (52.2 %)	1.8732e-01 (14.1 %)
5.75	1.4468e+00	1.7732e-01 (12.3 %)	6.4346e-01 (44.5 %)	2.0452e-01 (14.1 %)
6.25	1.2974e+00	1.5683e-01 (12.1 %)	5.2030e-01 (40.1 %)	1.8339e-01 (14.1 %)
6.75	1.2803e+00	1.4333e-01 (11.2 %)	4.6418e-01 (36.3 %)	1.8098e-01 (14.1 %)
7.25	9.2793e-01	1.5573e-01 (16.8 %)	3.6805e-01 (39.7 %)	1.3117e-01 (14.1 %)
7.75	1.3057e+00	1.6054e-01 (12.3 %)	4.1025e-01 (31.4 %)	1.8456e-01 (14.1 %)
8.25	1.0808e+00	1.6254e-01 (15 %)	3.4073e-01 (31.5 %)	1.5278e-01 (14.1 %)
8.75	1.2093e+00	1.6893e-01 (14 %)	3.4589e-01 (28.6 %)	1.7094e-01 (14.1 %)
9.5	1.0861e+00	1.4500e-01 (13.4 %)	3.3542e-01 (30.9 %)	1.5352e-01 (14.1 %)
10.5	1.3256e+00	1.8142e-01 (13.7 %)	3.6488e-01 (27.5 %)	1.8739e-01 (14.1 %)
11.5	1.0522e+00	2.0817e-01 (19.8 %)	2.9946e-01 (28.5 %)	1.4873e-01 (14.1 %)
13	7.7663e-01	1.7326e-01 (22.3 %)	2.1955e-01 (28.3 %)	1.0978e-01 (14.1 %)
15	1.0978e+00	2.4630e-01 (22.4 %)	2.3306e-01 (21.2 %)	1.5517e-01 (14.1 %)
18	7.0889e-01	2.2726e-01 (32.1 %)	1.4832e-01 (20.9 %)	1.0021e-01 (14.1 %)

Table F.24: Direct Photon R_{AA} as a function of p_T in $\sqrt{s_{NN}} = 200$ GeV Au+Au Collisions (30-40 % Central).

p_T	R _{AA}	p_T uncorrelated error	p_T correlated error	global scaling error
5.25	1.4261e+00	2.5318e-01 (17.8 %)	8.0461e-01 (56.4 %)	2.1334e-01 (15 %)
5.75	1.1350e+00	2.4960e-01 (22 %)	6.6913e-01 (59 %)	1.6979e-01 (15 %)
6.25	1.2420e+00	1.9440e-01 (15.7 %)	5.4984e-01 (44.3 %)	1.8579e-01 (15 %)
6.75	1.3716e+00	1.9840e-01 (14.5 %)	5.4160e-01 (39.5 %)	2.0518e-01 (15 %)
7.25	1.1659e+00	1.9950e-01 (17.1 %)	4.4151e-01 (37.9 %)	1.7441e-01 (15 %)
7.75	1.2945e+00	2.0511e-01 (15.8 %)	4.2592e-01 (32.9 %)	1.9365e-01 (15 %)
8.25	8.6334e-01	2.2857e-01 (26.5 %)	3.5069e-01 (40.6 %)	1.2915e-01 (15 %)
8.75	7.3223e-01	2.4533e-01 (33.5 %)	3.2882e-01 (44.9 %)	1.0954e-01 (15 %)
9.5	1.1197e+00	1.9737e-01 (17.6 %)	3.6777e-01 (32.8 %)	1.6750e-01 (15 %)
10.5	9.4159e-01	2.1762e-01 (23.1 %)	2.9667e-01 (31.5 %)	1.4086e-01 (15 %)
11.5	7.7992e-01	2.8301e-01 (36.3 %)	2.9092e-01 (37.3 %)	1.1667e-01 (15 %)
13	1.2587e+00	2.6669e-01 (21.2 %)	3.1498e-01 (25 %)	1.8829e-01 (15 %)
15	8.4468e-01	3.5801e-01 (42.4 %)	2.3529e-01 (27.9 %)	1.2636e-01 (15 %)
18	1.1892e+00	4.0145e-01 (33.8 %)	2.5083e-01 (21.1 %)	1.7790e-01 (15 %)

Table F.25: Direct Photon R_{AA} as a function of p_T in $\sqrt{s_{NN}} = 200$ GeV Au+Au Collisions (40-50 % Central).

p_T	R_{AA}	p_T uncorrelated error	p_T correlated error	global scaling error
5.25	1.1772e+00	3.3671e-01 (28.6 %)	8.6714e-01 (73.7 %)	2.2259e-01 (18.9 %)
5.75	1.2241e+00	2.9872e-01 (24.4 %)	7.3600e-01 (60.1 %)	2.3144e-01 (18.9 %)
6.25	1.5629e+00	2.5609e-01 (16.4 %)	6.7712e-01 (43.3 %)	2.9549e-01 (18.9 %)
6.75	1.2453e+00	2.5991e-01 (20.9 %)	5.5909e-01 (44.9 %)	2.3545e-01 (18.9 %)
7.25	1.1320e+00	2.7759e-01 (24.5 %)	4.8418e-01 (42.8 %)	2.1402e-01 (18.9 %)
7.75	1.3240e+00	2.9677e-01 (22.4 %)	4.7506e-01 (35.9 %)	2.5033e-01 (18.9 %)
8.25	1.0073e+00	3.4153e-01 (33.9 %)	4.3119e-01 (42.8 %)	1.9046e-01 (18.9 %)
8.75	1.3233e+00	3.5682e-01 (27 %)	4.4484e-01 (33.6 %)	2.5020e-01 (18.9 %)
9.5	1.0796e+00	2.9492e-01 (27.3 %)	4.2298e-01 (39.2 %)	2.0412e-01 (18.9 %)
10.5	1.2745e+00	3.6320e-01 (28.5 %)	4.2022e-01 (33 %)	2.4098e-01 (18.9 %)
11.5	8.8556e-01	4.1901e-01 (47.3 %)	3.3275e-01 (37.6 %)	1.6744e-01 (18.9 %)
13	7.8803e-01	3.8355e-01 (48.7 %)	2.9071e-01 (36.9 %)	1.4900e-01 (18.9 %)
15	1.9567e+00	5.5876e-01 (28.6 %)	3.8105e-01 (19.5 %)	3.6995e-01 (18.9 %)
18	1.0966e+00	6.3551e-01 (58 %)	2.7836e-01 (25.4 %)	2.0734e-01 (18.9 %)

Table F.26: Direct Photon R_{AA} as a function of p_T in $\sqrt{s_{NN}} = 200$ GeV Au+Au Collisions (50-60 % Central).

p_T	R_{AA}	p_T uncorrelated error	p_T correlated error	global scaling error
5.25	1.0361e+00	4.1757e-01 (40.3 %)	9.2752e-01 (89.5 %)	2.9401e-01 (28.4 %)
5.75	7.2343e-01	4.3945e-01 (60.7 %)	7.9899e-01 (110 %)	2.0528e-01 (28.4 %)
6.25	1.4130e+00	3.5777e-01 (25.3 %)	7.2857e-01 (51.6 %)	4.0096e-01 (28.4 %)
6.75	1.3543e+00	3.7413e-01 (27.6 %)	6.4773e-01 (47.8 %)	3.8428e-01 (28.4 %)
7.25	7.6884e-01	4.1105e-01 (53.5 %)	4.9862e-01 (64.9 %)	2.1817e-01 (28.4 %)
7.75	1.3048e+00	4.2901e-01 (32.9 %)	5.0242e-01 (38.5 %)	3.7026e-01 (28.4 %)
8.25	1.0922e+00	4.6385e-01 (42.5 %)	4.3448e-01 (39.8 %)	3.0992e-01 (28.4 %)
8.75	1.1280e+00	5.5262e-01 (49 %)	4.7230e-01 (41.9 %)	3.2009e-01 (28.4 %)
9.5	1.4814e+00	4.4502e-01 (30 %)	5.0565e-01 (34.1 %)	4.2037e-01 (28.4 %)
10.5	1.2602e+00	4.7871e-01 (38 %)	3.6916e-01 (29.3 %)	3.5759e-01 (28.4 %)
11.5	8.3851e-01	7.0965e-01 (84.6 %)	4.3430e-01 (51.8 %)	2.3794e-01 (28.4 %)
13	4.6951e-01	6.0351e-01 (129 %)	3.1839e-01 (67.8 %)	1.3323e-01 (28.4 %)
15	2.3468e-01	6.7608e-01 (288 %)	1.7987e-01 (76.6 %)	6.6594e-02 (28.4 %)

Table F.27: Direct Photon R_{AA} as a function of p_T in $\sqrt{s_{NN}} = 200$ GeV Au+Au Collisions (60-70 % Central).

p_T	R_{AA}	p_T uncorrelated error	p_T correlated error	global scaling error
5.25	9.8894e-01	5.0727e-01 (51.3 %)	9.4197e-01 (95.3 %)	3.4843e-01 (35.2 %)
5.75	3.6184e-01	5.4269e-01 (150 %)	7.3066e-01 (202 %)	1.2749e-01 (35.2 %)
6.25	1.7912e+00	4.4326e-01 (24.7 %)	7.4848e-01 (41.8 %)	6.3108e-01 (35.2 %)
6.75	2.1591e+00	5.0432e-01 (23.4 %)	7.8229e-01 (36.2 %)	7.6069e-01 (35.2 %)
7.25	1.0136e+00	5.6751e-01 (56 %)	5.2657e-01 (52 %)	3.5712e-01 (35.2 %)
7.75	6.2355e-01	6.2658e-01 (100 %)	4.1860e-01 (67.1 %)	2.1969e-01 (35.2 %)
8.25	6.2032e-01	6.9419e-01 (112 %)	3.9269e-01 (63.3 %)	2.1855e-01 (35.2 %)
8.75	5.2937e-01	7.4489e-01 (141 %)	3.6049e-01 (68.1 %)	1.8651e-01 (35.2 %)
9.5	1.1950e+00	6.0611e-01 (50.7 %)	4.2907e-01 (35.9 %)	4.2102e-01 (35.2 %)
10.5	1.4975e+00	7.4269e-01 (49.6 %)	4.1694e-01 (27.8 %)	5.2759e-01 (35.2 %)
11.5	2.3173e-01	9.2873e-01 (401 %)	3.1665e-01 (137 %)	8.1643e-02 (35.2 %)
13	1.2526e+00	8.3629e-01 (66.8 %)	3.3277e-01 (26.6 %)	4.4132e-01 (35.2 %)

Table F.28: Direct Photon R_{AA} as a function of p_T in $\sqrt{s_{NN}} = 200$ GeV Au+Au Collisions (70-80 % Central).

p_T	R _{AA}	p_T uncorrelated error	p_T correlated error	global scaling error
5.25	1.3961e+00	6.0889e-01 (43.6 %)	9.7789e-01 (70 %)	3.6774e-01 (26.3 %)
5.75	5.4355e-01	7.1941e-01 (132 %)	8.1895e-01 (151 %)	1.4317e-01 (26.3 %)
6.25	1.0940e+00	5.8513e-01 (53.5 %)	6.5480e-01 (59.9 %)	2.8818e-01 (26.3 %)
6.75	7.9301e-01	7.0517e-01 (88.9 %)	5.9975e-01 (75.6 %)	2.0888e-01 (26.3 %)
7.25	4.7019e-01	7.4182e-01 (158 %)	4.3496e-01 (92.5 %)	1.2385e-01 (26.3 %)
7.75	1.0371e+00	8.2808e-01 (79.8 %)	4.5866e-01 (44.2 %)	2.7318e-01 (26.3 %)
8.25	-7.2293e-01	-1.1254e+00 (156 %)	-4.1981e-01 (58.1 %)	-1.9043e-01 (26.3 %)
8.75	-1.0364e-02	-1.0587e+00 (1.02e+04 %)	-3.4093e-01 (3.29e+03 %)	-2.7300e-03 (26.3 %)
9.5	2.8757e-01	9.0891e-01 (316 %)	4.3553e-01 (151 %)	7.5747e-02 (26.3 %)
10.5	7.6087e-01	1.0325e+00 (136 %)	3.6820e-01 (48.4 %)	2.0042e-01 (26.3 %)

Table F.29: Direct Photon R_{AA} as a function of p_T in $\sqrt{s_{NN}} = 200$ GeV Au+Au Collisions (80-92 % Central).

p_T	R _{AA}	p_T uncorrelated error	p_T correlated error	global scaling error
5.25	1.1295e+00	1.3019e-01 (11.5 %)	5.4495e-01 (48.2 %)	1.5617e-01 (13.8 %)
5.75	1.1651e+00	1.1198e-01 (9.61 %)	4.9435e-01 (42.4 %)	1.6108e-01 (13.8 %)
6.25	1.1396e+00	9.7377e-02 (8.55 %)	4.1822e-01 (36.7 %)	1.5756e-01 (13.8 %)
6.75	1.1878e+00	8.8204e-02 (7.43 %)	4.0046e-01 (33.7 %)	1.6422e-01 (13.8 %)
7.25	1.1219e+00	8.2368e-02 (7.34 %)	3.4555e-01 (30.8 %)	1.5511e-01 (13.8 %)
7.75	1.1431e+00	7.6512e-02 (6.69 %)	3.2719e-01 (28.6 %)	1.5805e-01 (13.8 %)
8.25	1.0554e+00	7.3096e-02 (6.93 %)	2.9303e-01 (27.8 %)	1.4592e-01 (13.8 %)
8.75	1.0939e+00	7.1152e-02 (6.5 %)	2.9511e-01 (27 %)	1.5124e-01 (13.8 %)
9.5	1.0681e+00	6.1446e-02 (5.75 %)	2.8632e-01 (26.8 %)	1.4767e-01 (13.8 %)
10.5	1.0108e+00	6.2658e-02 (6.2 %)	2.6355e-01 (26.1 %)	1.3976e-01 (13.8 %)
11.5	1.0026e+00	6.7768e-02 (6.76 %)	2.4879e-01 (24.8 %)	1.3862e-01 (13.8 %)
13	9.5432e-01	5.9138e-02 (6.2 %)	2.2330e-01 (23.4 %)	1.3195e-01 (13.8 %)
15	8.5136e-01	7.3698e-02 (8.66 %)	1.8932e-01 (22.2 %)	1.1771e-01 (13.8 %)
18	6.7985e-01	7.4378e-02 (10.9 %)	1.4836e-01 (21.8 %)	9.3998e-02 (13.8 %)

Table F.30: Direct Photon R_{AA} as a function of p_T in $\sqrt{s_{NN}} = 200$ GeV Au+Au Collisions (Minimum Bias).

Appendix G

Summary of Systematic Error

G.1 Factorized systematic error on π^0 invariant yield

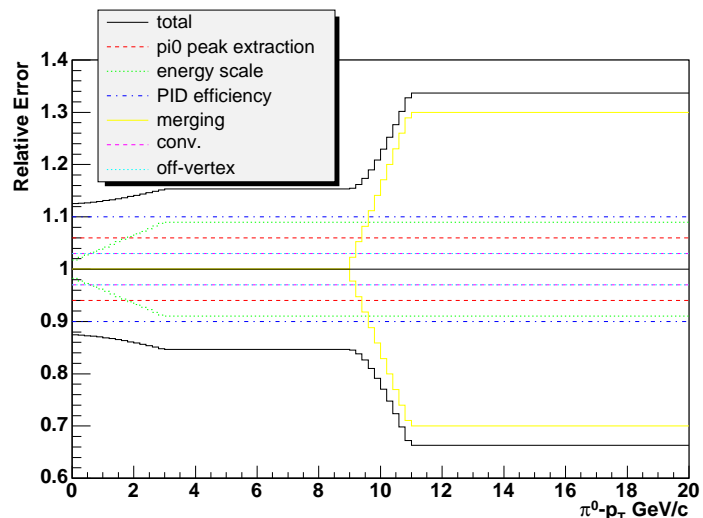


Figure G.1: Factorized relative systematic error on π^0 invariant yield as a function of π^0 - p_T .

G.2 Factorized systematic error on direct photon excess ratio

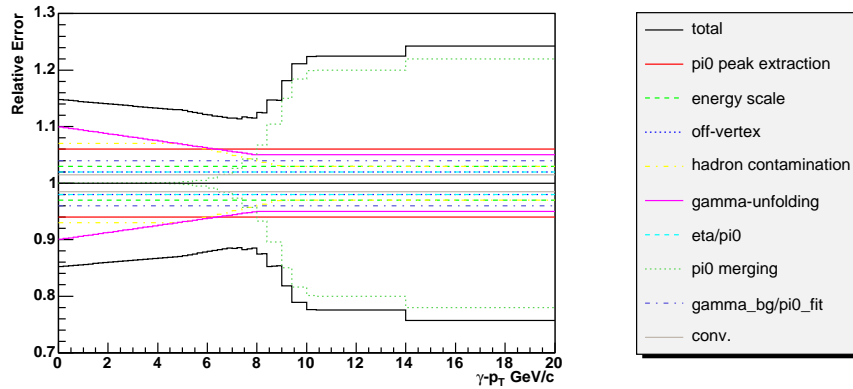


Figure G.2: Factorized relative systematic error on direct photon excess ratio as a function of $\gamma\text{-}p_T$.

G.3 Factorized systematic error on direct photon invariant yield

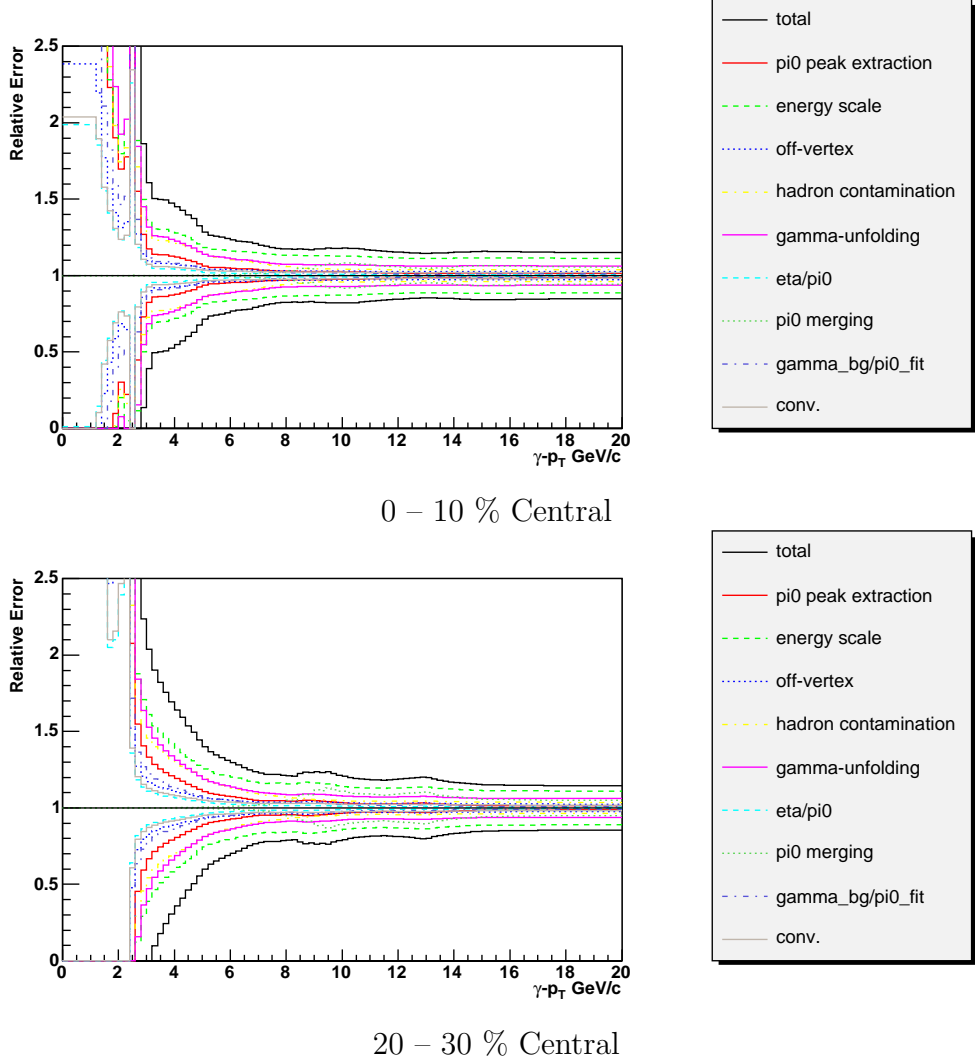


Figure G.3: Factorized relative systematic error on direct photon invariant yield as a function of $\gamma\text{-}p_T$. Since the factorized systematic errors are weighted analytically as described at Sec. 5.6.3, the systematic error on the yield fluctuates due to the statistic fluctuation.

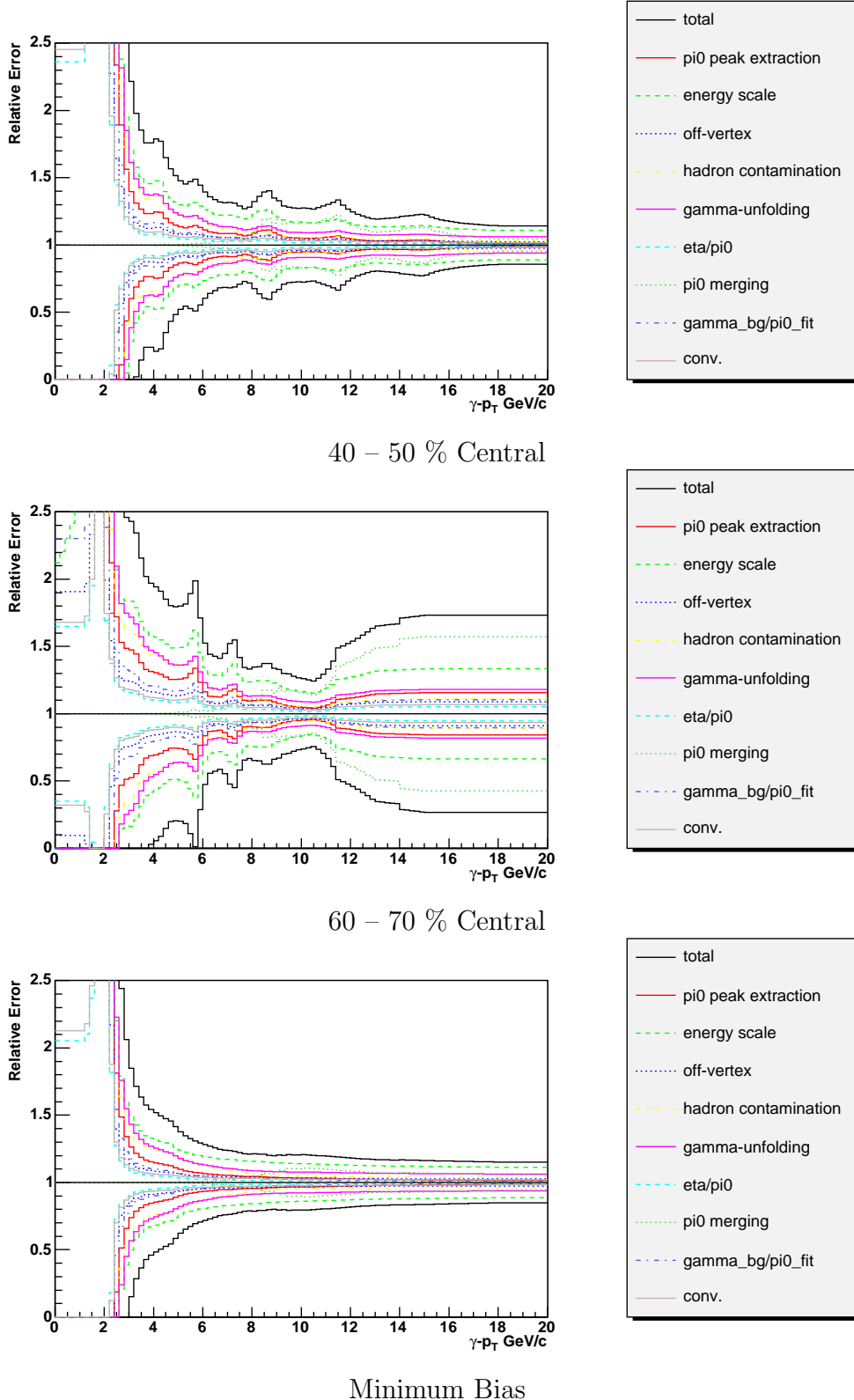


Figure G.4: Factorized relative systematic error on direct photon invariant yield as a function of $\gamma\text{-}p_{\text{T}}$. Since the factorized systematic errors are weighted analytically as described at Sec. 5.6.3, the systematic error on the yield fluctuates due to the statistic fluctuation.

Appendix H

$\gamma\gamma$ Invariant Mass Distribution

Here some samples of invariant mass spectrum of $\gamma\gamma$ are shown.

H.1 Central 0-10 %

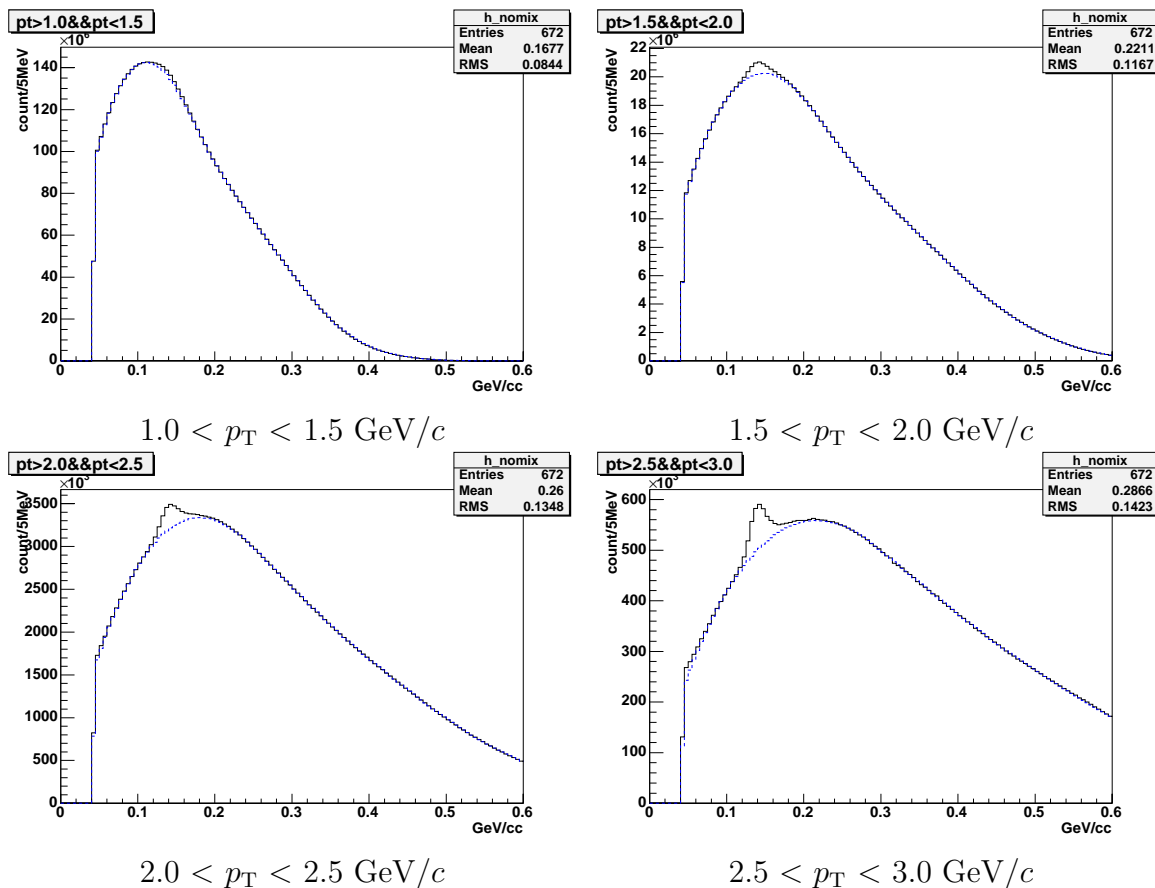


Figure H.1: $\gamma\gamma$ invariant mass spectra in 0-10 % central ($1.0 < p_T < 3.0 \text{ GeV}/c$). Dashed blue line is estimated combinatorial background by event mixing method.

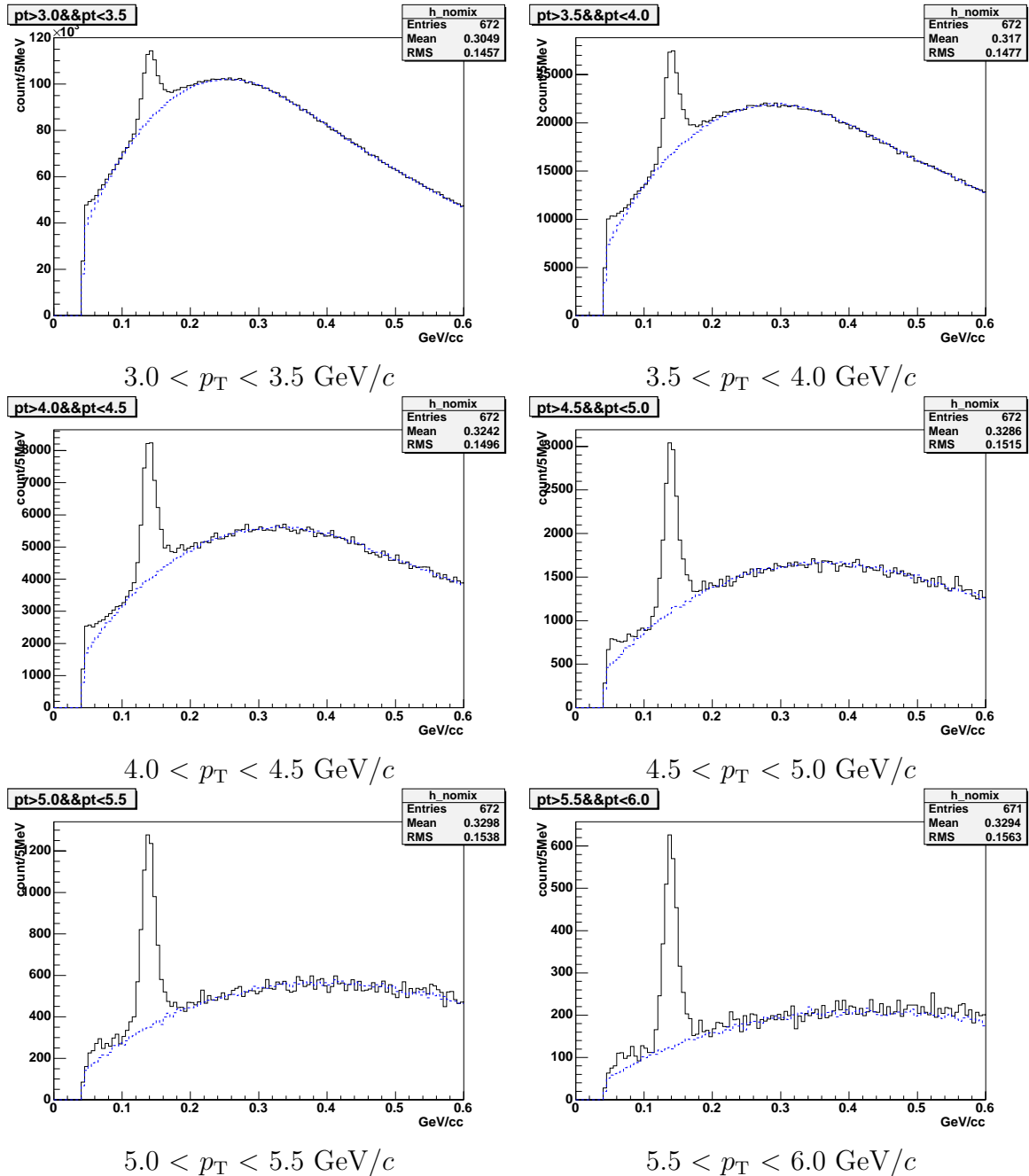


Figure H.2: $\gamma\gamma$ invariant mass spectra in 0-10 % central ($3.0 < p_T < 6.0$ GeV/ c). Dashed blue line is estimated combinatorial background by event mixing method.

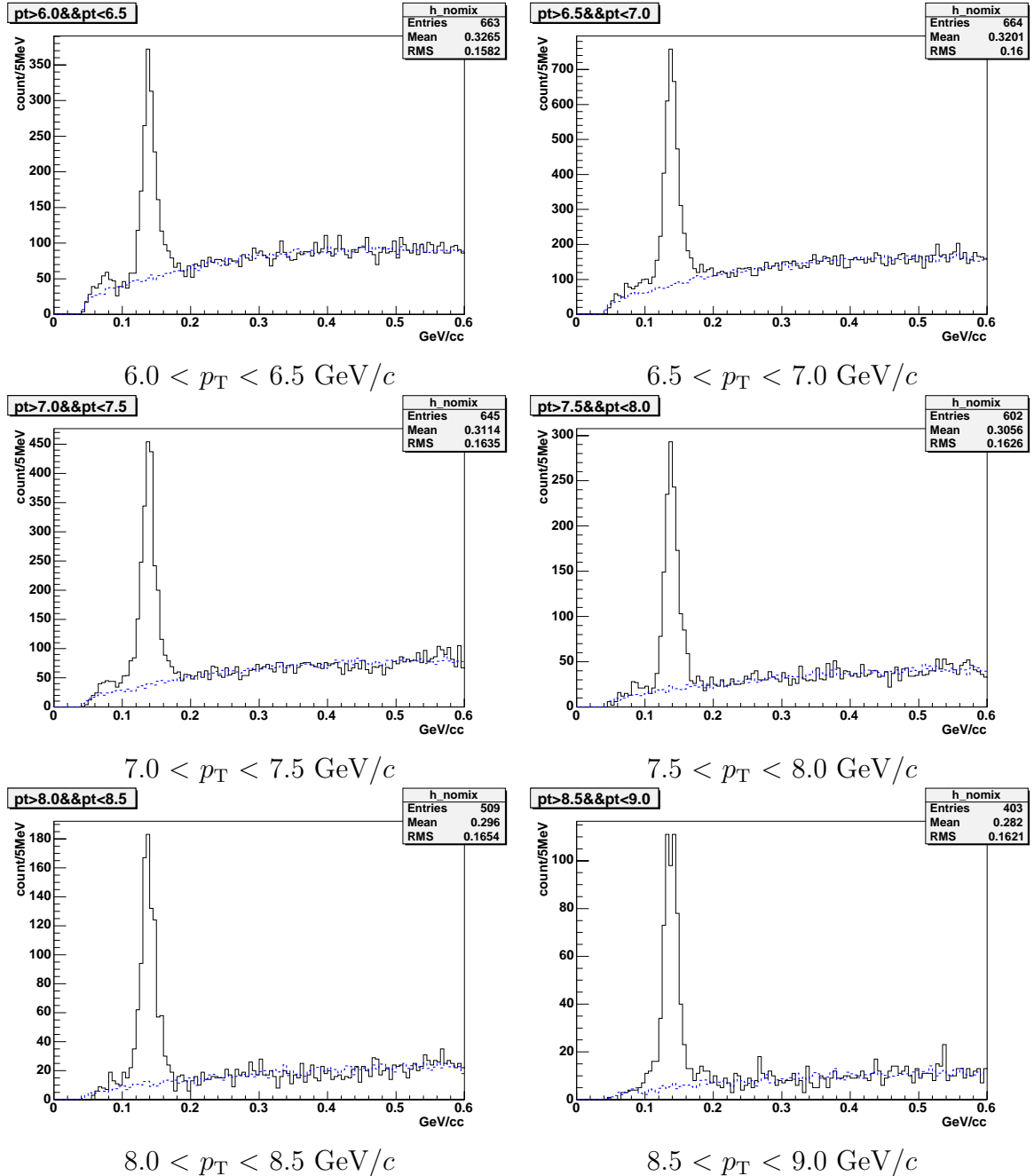


Figure H.3: $\gamma\gamma$ invariant mass spectra in 0-10 % central ($6.0 < p_T < 9.0 \text{ GeV}/c$). Dashed blue line is estimated combinatorial background by event mixing method.

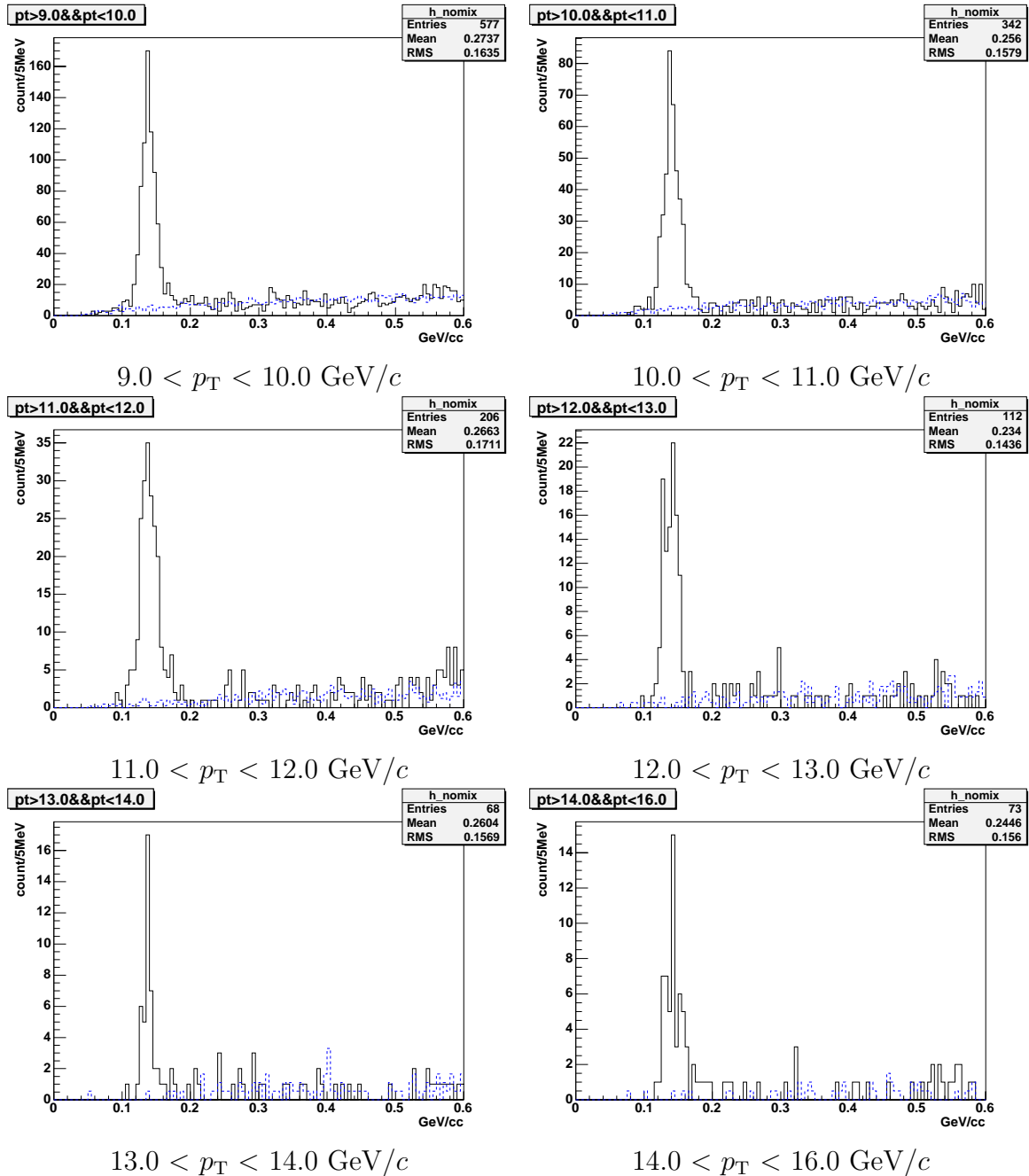
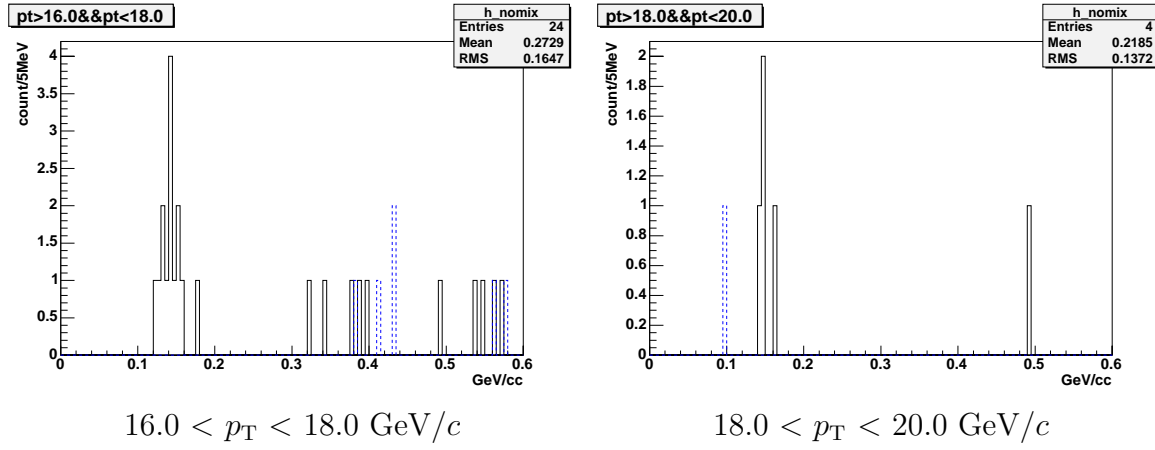
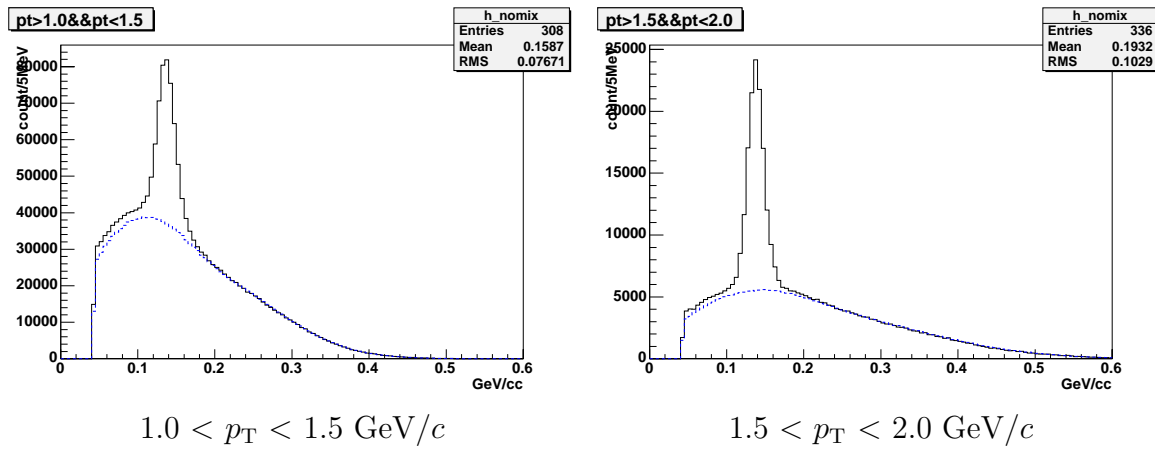


Figure H.4: $\gamma\gamma$ invariant mass spectra in 0-10 % central ($9.0 < p_T < 16.0 \text{ GeV}/c$). Dashed blue line is estimated combinatorial background by event mixing method.



H.2 Central 80-92 %



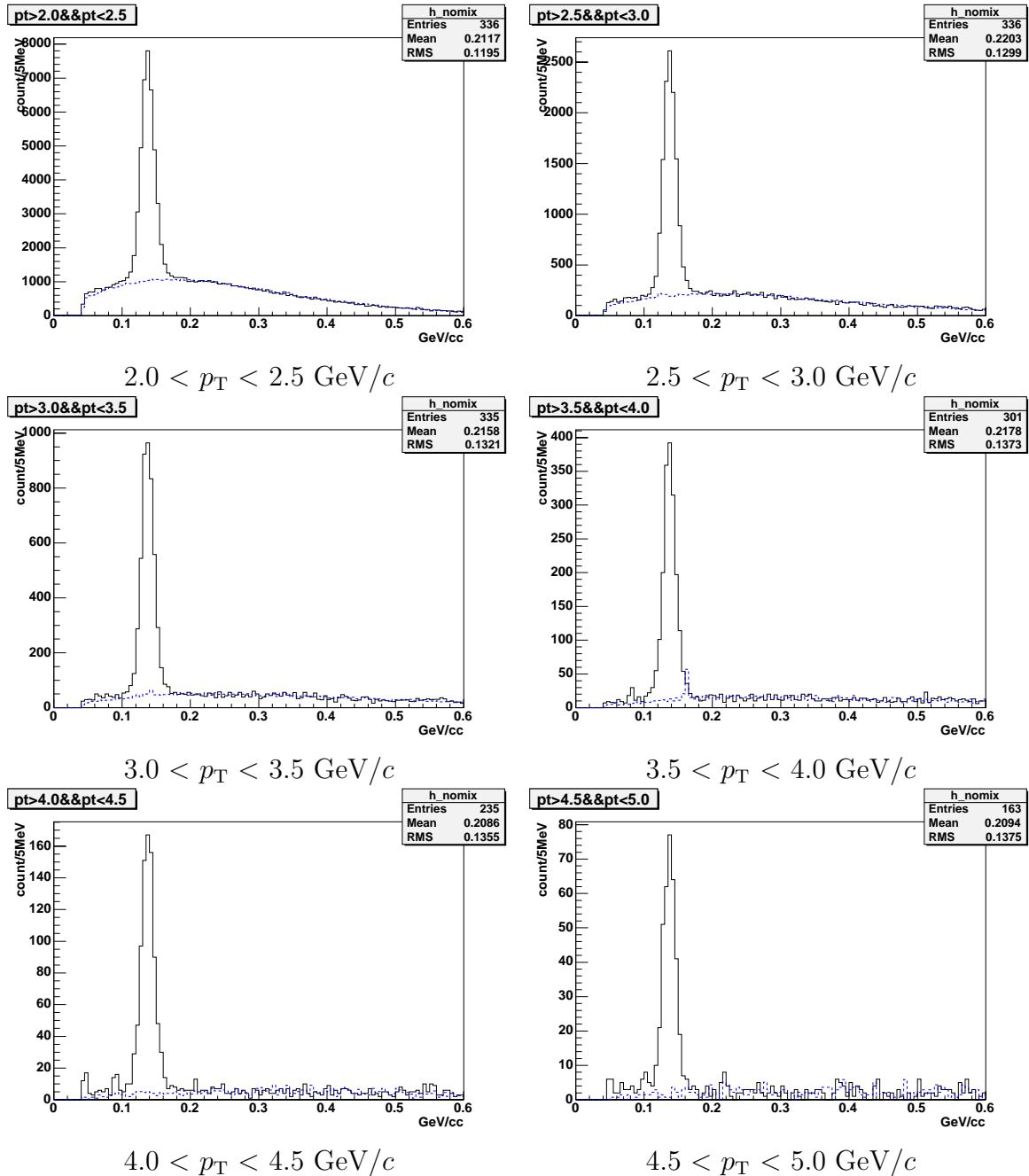


Figure H.7: $\gamma\gamma$ invariant mass spectra in 80-92 % central ($2.0 < p_T < 5.0$ GeV/ c). Dashed blue line is estimated combinatorial background by event mixing method.

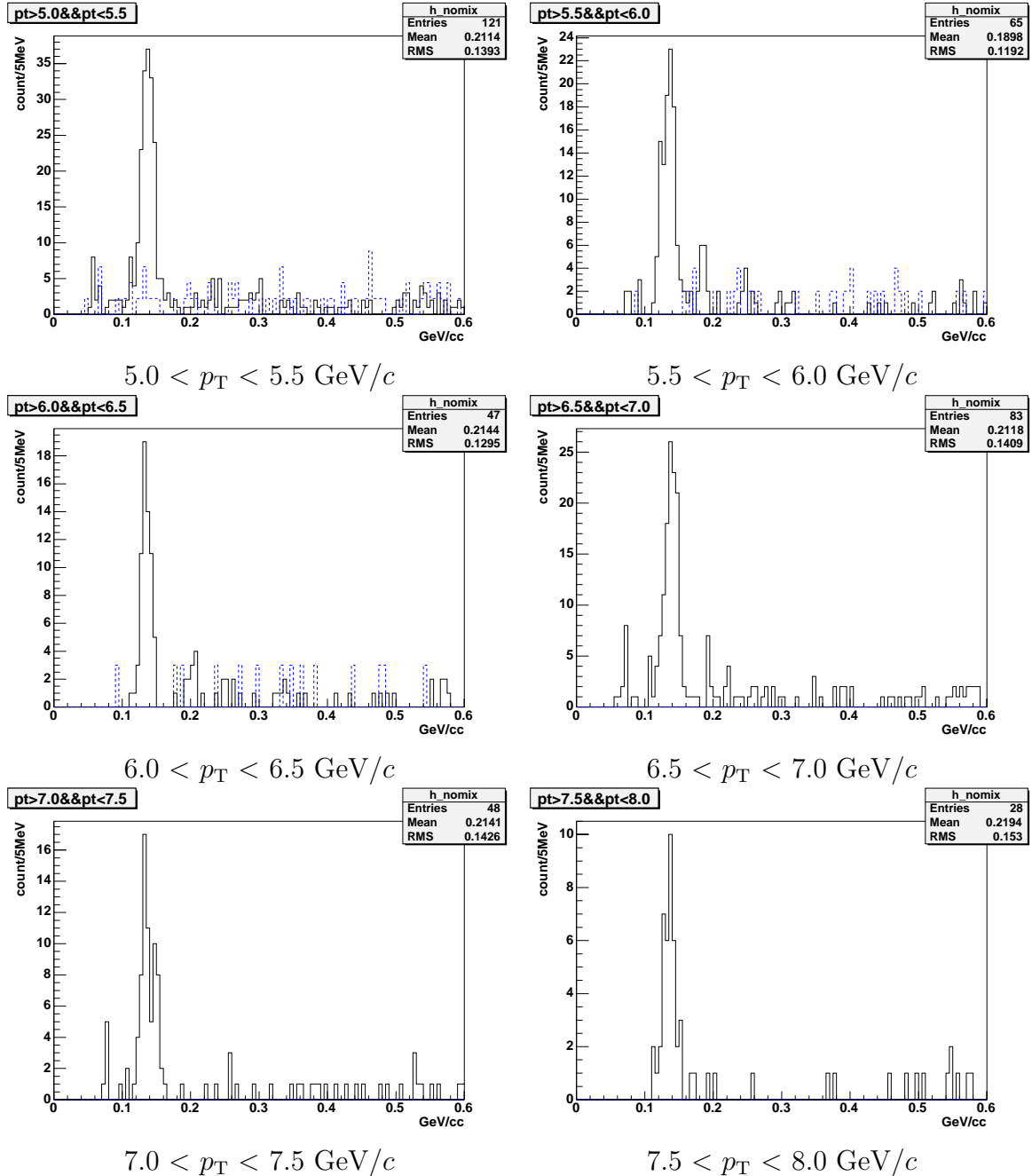


Figure H.8: $\gamma\gamma$ invariant mass spectra in 80-92 % central ($5.0 < p_T < 8.0 \text{ GeV}/c$). Dashed blue line is estimated combinatorial background by event mixing method.

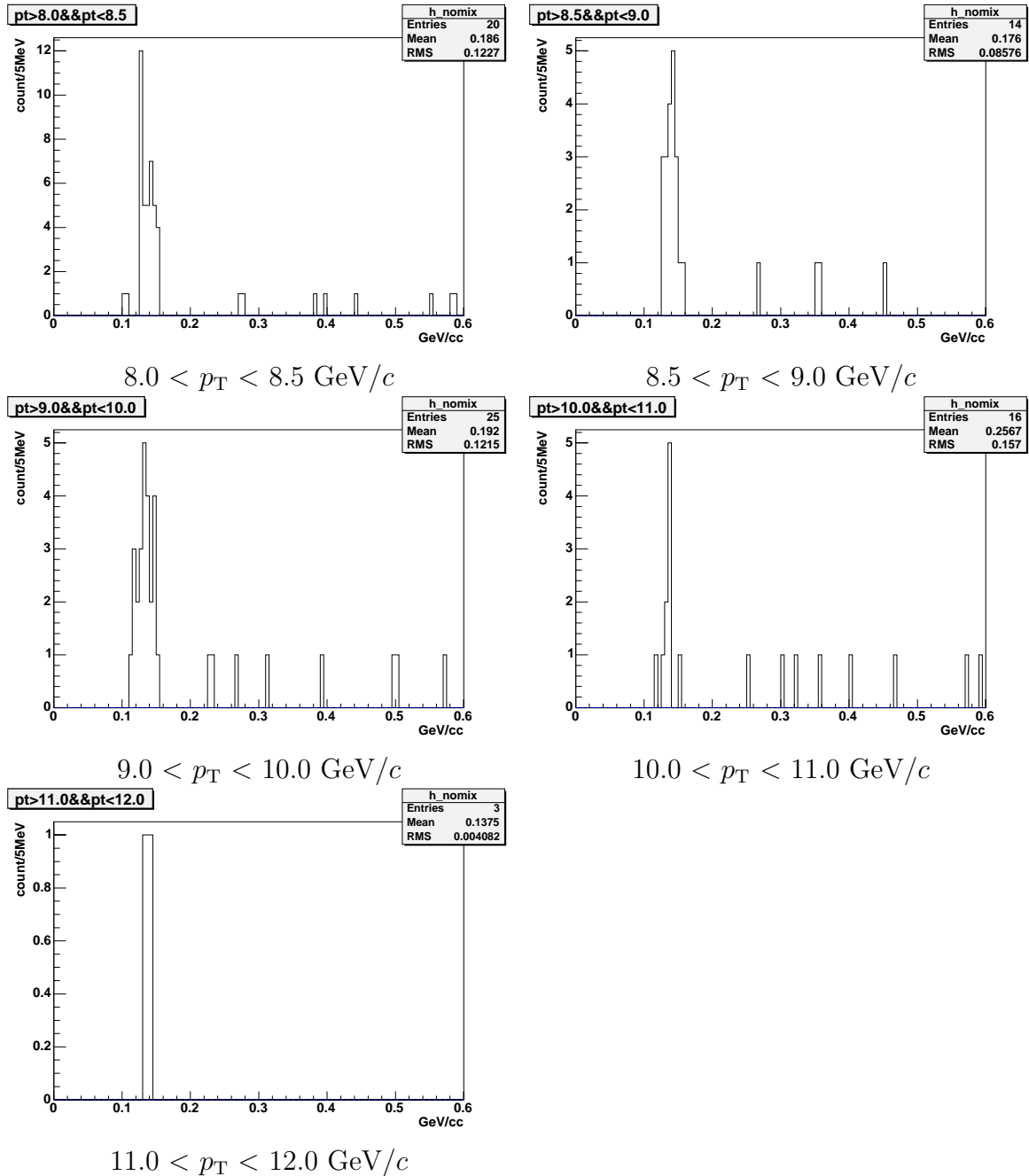


Figure H.9: $\gamma\gamma$ invariant mass spectra in 80-92 % central ($8.0 < p_T < 12.0 \text{ GeV}/c$). Dashed blue line is estimated combinatorial background by event mixing method.

Appendix I

Information of the analysis

I.1 List of Analyzed Runs

Followings are run list of good run which are used for analysis (Total 650 runs).

108368	108768	108772	108908	108928	108943	109187	109189	109191	109192	109196	109204
109214	109217	109220	109228	109240	109242	109246	109247	109252	109291	109293	109297
109355	109361	109363	109366	109422	109424	109426	109470	109477	109479	109482	109549
109550	109569	109573	109576	109587	109593	109654	109655	109656	109657	109659	109660
109664	109672	109675	109677	109679	109684	109690	109691	109693	109699	109763	109764
109765	109767	109769	109820	109821	109822	111396	111402	111406	111413	111421	111423
111425	111436	111467	111468	111485	111494	111495	111497	111498	111500	111502	111528
111530	111531	111532	111538	111539	111544	111555	111556	111558	111559	111560	111583
111592	111593	111603	111604	111687	111688	111695	111697	111699	111701	111705	111711
111714	111716	111743	111824	111830	111831	111838	111893	111894	111895	111951	111953
111955	111957	111959	111964	111966	111982	111984	111985	112057	112059	112061	112064
112066	112075	112122	112124	112128	112184	112186	112232	112233	112234	112283	112284
112286	112287	112288	112318	112320	112323	112403	112411	112475	112476	112479	112480
112482	112483	112492	112493	112504	112506	112507	112509	112511	112657	112660	112661
112664	112666	113106	113107	113108	113194	113198	113201	113202	113204	113232	113284
113286	113288	113290	113464	113466	113468	113528	113529	113530	113559	113562	113564
113570	113573	113574	113575	113580	113688	113689	113690	113691	113695	113696	113703
113706	113716	113838	113839	113840	113842	113851	113852	113854	113871	113873	113875
113877	113879	113880	113902	113904	113975	113979	113982	113983	113986	114001	114066
114069	114074	114075	114076	114089	114102	114143	114144	114145	114147	114271	114278
114280	114287	114295	114296	114329	114330	114332	114334	114399	114401	114405	114406
114414	114432	114467	114468	114471	114594	114602	114614	114616	114618	114681	114689
114802	114805	114808	114836	114837	114884	114887	114901	114927	114929	114936	114965
114967	114970	114971	114972	114993	114994	114997	115031	115050	115069	115070	115077
115087	115179	115180	115182	115185	115191	115205	115227	115237	115345	115347	115350
115358	115361	115366	116061	116085	116087	116160	116161	116163	116167	116169	116178
116184	116186	116192	116228	116229	116236	116237	116313	116315	116317	116321	116338
116341	116353	116359	116419	116421	116423	116425	116427	116468	116472	116533	116534
116539	116544	116546	116547	116551	116566	116571	116572	116574	116609	116617	116620
116636	116637	116642	116646	116657	116659	116660	116662	116690	116701	116702	116706

Table I.1: List of runs used in the analysis of Au+Au data (part1).

116707	116708	116742	116743	116746	116747	116749	116776	116777	116831	116833	116838
116842	116913	116917	116921	116927	116929	116933	117119	117120	117122	117128	117225
117226	117253	117255	117256	117258	117290	117291	117295	117297	117303	117311	117327
117328	117427	117428	117429	117430	117431	117433	117435	117441	117443	117447	117455
117457	117543	117544	117546	117547	117574	117575	117576	117579	117581	117583	117586
117590	117592	117602	117604	117606	117607	117609	117613	117684	117685	117686	117694
117716	117725	117759	117760	117764	117766	117768	117770	117772	117776	117779	117781
117821	117823	117825	117826	117827	117847	117848	117849	117851	117852	117921	117922
117925	117927	118019	118024	118028	118038	118042	118211	118252	118254	118301	118304
118308	118312	118314	118321	118435	118438	118440	118446	118457	118458	118462	118464
118468	118469	118674	118676	118751	118754	118767	118770	118777	118779	118870	118901
118903	118911	118912	118929	118932	118933	118934	119100	119106	119108	119129	119133
119134	119138	119139	119140	119141	119143	119264	119267	119268	119269	119314	119326
119327	119329	119380	119381	119386	119387	119417	119420	119421	119428	119433	119440
119448	119451	119452	119550	119618	119621	119684	119687	119688	119690	119691	119763
119768	119917	119919	119921	119925	119926	119928	119969	120039	120045	120048	120057
120058	120059	120060	120061	120062	120063	120064	120078	120079	120081	120082	120194
120199	120200	120214	120234	120237	120238	120240	120246	120261	120269	120274	120278
120279	120285	120286	120394	120396	120397	120404	120405	120406	120407	120408	120410
120411	120416	120419	120420	120422	120426	120427	120428	120478	120479	120480	120483
120489	120495	120496	120497	120499	121220	121224	121233	121237	121266	121271	121275
121287	121288	121289	121291	121292	121293	121294	121295	121296	121343	121344	121347
121401	121404	121406	121408	121449	121458	121463	121465	121510	121511	121513	121523
121526	121531	121534	121543	121544	121545	121548	121554	122041	122213	122214	122215
122220	122223										

Table I.2: List of runs used in the analysis of Au+Au data (part2).

I.2 Excluded EMCal Modules

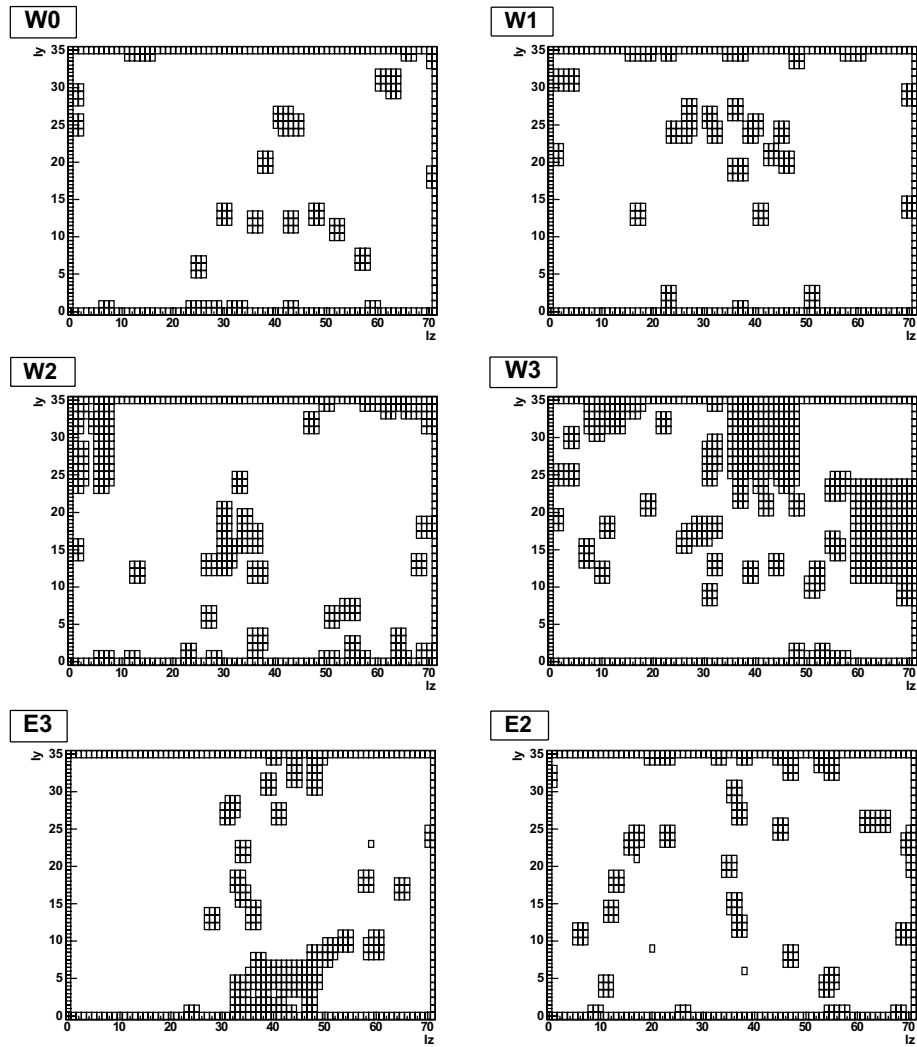


Figure I.1: Modules flagged as bad for the analysis of the Au+Au data (boxes). The regions excluded on the edge of the calorimeter sectors are also shown.

Bibliography

- [1] S. Abachi et al. “The Isolated Photon Cross Section in the Central and Forward Rapidity Regions in p-pbar Collisions at $\text{sqrt}(s) = 1.8 \text{ TeV}$ ”. *Phys. Rev. Lett.*, **77**:5011–5015. (1996).
- [2] F. Abe et al. “Transverse-momentum distributions of charged particles produced in p \bar{p} interaction at $\sqrt{s} = 630$ and 1800 GeV”. *Phys. Rev. Lett.*, **61**:1819–1822. (1988).
- [3] F. Abe et al. “Precision Measurement of the Prompt Photon Cross Section in p \bar{p} Collisions at $\sqrt{s}=1.8 \text{ TeV}$ ”. *Phys. Rev. Lett.*, **74**:1891–1893. (1995).
- [4] K. Abe et al. “Production of π^+ , K^+ , K^0 , K^{*0} , ϕ , p and Λ^0 in hadronic Z^0 decays”. *Phys. Rev.*, **D59**:052001. (1999).
- [5] B. I. Abelev et al. “Transverse momentum and centrality dependence of high-pT non-photonic electron suppression in Au+Au collisions at $\sqrt{s_{\text{NN}}} = 200 \text{ GeV}$ ”. nucl-ex/0607012, (2006).
- [6] P. Abreu et al. “Measurement of the gluon fragmentation function and a comparison of the scaling violation in gluon and quark jets”. *Eur. Phys. J.*, **C13**:573–589. (2000).
- [7] K. H. Ackermann et al. “STAR detector overview”. *Nucl. Instrum. Meth.*, **A499**:624–632. (2003).
- [8] D. Acosta et al. “Measurement of Prompt Charm Meson Production Cross Sections in p \bar{p} Collisions at $\sqrt{s} = 1.96 \text{ TeV}$ ”. *Phys. Rev. Lett.*, **91**:241804. (2003).
- [9] M. Adamczyk et al. “The BRAHMS experiment at RHIC”. *Nucl. Instrum. Meth.*, **A499**:437–468. (2003).
- [10] J. Adams et al. “ ρ^0 Production and Possible Modification in Au+Au and p+p Collisions at $\sqrt{s_{\text{NN}}} = 200 \text{ GeV}$ ”. *Phys. Rev. Lett.*, **92**:092301. (2004).
- [11] A. Adare et al. “Energy Loss and Flow of Heavy Quarks in Au+Au Collisions at $\sqrt{s_{\text{NN}}} = 200 \text{ GeV}$ ”. nucl-ex/0611018, (2006).
- [12] K. Adcox et al. “Measurement of the mid-rapidity transverse energy distribution from $\sqrt{s_{\text{NN}}} = 130 \text{ GeV}$ Au + Au collisions at RHIC”. *Phys. Rev. Lett.*, **87**:052301. (2001).

- [13] K. Adcox et al. “Measurement of single electrons and implications for charm production in Au+Au collisions at $\sqrt{s_{NN}} = 130$ GeV”. *Phys. Rev. Lett.*, **88**:192303. (2002).
- [14] K. Adcox et al. “Suppression of hadrons with large transverse momentum in central Au + Au collisions at $\sqrt{s_{NN}} = 130$ GeV”. *Phys. Rev. Lett.*, **88**:022301. (2002).
- [15] K. Adcox et al. “PHENIX central arm tracking detectors”. *Nucl. Instrum. Meth.*, **A499**:489–507. (2003).
- [16] K. Adcox et al. “PHENIX detector overview”. *Nucl. Instrum. Meth.*, **A499**:469–479. (2003).
- [17] A. Adil and I. Vitev. “Collisional dissociation of heavy mesons in dense QCD matter”. hep-ph/0611109, (2006).
- [18] C. Adler et al. “The RHIC zero-degree calorimeters”. *Nucl. Instrum. Meth.*, **A499**:433–436. (2003).
- [19] S. S. Adler et al. “Centrality Dependence of π^0 and η Production at Large Transverse Momentum in $\sqrt{s_{NN}} = 200$ GeV d+Au Collisions”. nucl-ex/0610036.
- [20] S. S. Adler et al. “Absence of suppression in particle production at large transverse momentum in $\sqrt{s_{NN}} = 200$ GeV d + Au collisions”. *Phys. Rev. Lett.*, **91**:072303. (2003).
- [21] S. S. Adler et al. “Absence of suppression in particle production at large transverse momentum in $\sqrt{s_{NN}} = 200$ GeV d + Au collisions”. *Phys. Rev. Lett.*, **91**:072303. (2003).
- [22] S. S. Adler et al. “Elliptic Flow of Identified Hadrons in Au+Au Collisions at $\sqrt{s_{NN}} = 200$ GeV”. *Phys. Rev. Lett.*, **91**:182301. (2003).
- [23] S. S. Adler et al. “Mid-rapidity neutral pion production in proton proton collisions at $\sqrt{s} = 200$ GeV”. *Phys. Rev. Lett.*, **91**:241803. (2003).
- [24] S. S. Adler et al. “PHENIX on-line and off-line computing”. *Nucl. Instrum. Meth.*, **A499**:593–602. (2003).
- [25] S. S. Adler et al. “PHENIX on-line systems”. *Nucl. Instrum. Meth.*, **A499**:560–592. (2003).
- [26] S. S. Adler et al. “PHENIX online systems”. *Nucl. Instrum. Meth.*, **A499**:560–592. (2003).
- [27] S. S. Adler et al. “Suppressed pi0 production at large transverse momentum in central Au + Au collisions at $\sqrt{s_{NN}} = 200$ GeV”. *Phys. Rev. Lett.*, **91**:072301. (2003).
- [28] S. S. Adler et al. “High-p(T) charged hadron suppression in Au + Au collisions at $\sqrt{s_{NN}} = 200$ GeV”. *Phys. Rev.*, **C69**:034910. (2004).

- [29] S. S. Adler et al. “Identified charged particle spectra and yields in Au + Au collisions at $\sqrt{s_{NN}} = 200$ GeV”. *Phys. Rev.*, **C69**:034909. (2004).
- [30] S. S. Adler et al. “Centrality Dependence of Charm Production from Single Electrons in Au+Au Collisions at $\sqrt{s_{NN}} = 200$ GeV”. *Phys. Rev. Lett.*, **94**:082301. (2005).
- [31] S. S. Adler et al. “Centrality Dependence of Direct Photon Production in $\sqrt{s_{NN}} = 200$ GeV Au+Au Collisions”. *Phys. Rev. Lett.*, **94**:232301. (2005).
- [32] S. S. Adler et al. “Measurement of Single Electron Event Anisotropy in Au+Au Collisions at $\sqrt{s_{NN}} = 200$ GeV”. *Phys. Rev.*, **C72**:024901. (2005).
- [33] S. S. Adler et al. “Systematic Studies of the Centrality and $\sqrt{s_{NN}}$ Dependence of $dE_T/d\eta$ and $dN_{ch}/d\eta$ in Heavy Ion Collisions at Mid-rapidity”. *Phys. Rev.*, **C71**:034908. (2005).
- [34] S. S. Adler et al. “Common suppression pattern of high pT eta and pi0 in Au+Au at $\sqrt{s_{NN}} = 200$ GeV”. *Phys. Rev. Lett.*, **96**:202301. (2006).
- [35] S. S. Adler et al. “Jet Properties from Dihadron Correlations in p+p Collisions at $\sqrt{s}=200$ GeV”. *Phys. Rev.*, **D74**:072002. (2006).
- [36] S. S. Adler et al. “Measurement of identified pi0 and inclusive photon v2 and implication to the direct photon production in $\sqrt{s_{NN}} = 200$ GeV Au+Au collisions”. *Phys. Rev. Lett.*, **96**:202302. (2006).
- [37] S. S. Adler et al. “Single Electrons from Heavy Flavor Decays in p+p Collisions at $\sqrt{s} = 200$ GeV”. *Phys. Rev. Lett.*, **96**:032001. (2006).
- [38] S. S. Adler et al. “High transverse momentum eta meson production in p+p, d+Au and Au+Au collisions at $\sqrt{s_{NN}} = 200$ GeV”. *Phys. Rev.*, **C75**:024909. (2007).
- [39] S. S. Adler et al. “Measurement of direct photon production in p + p collisions at $\sqrt{s} = 200$ GeV”. *Phys. Rev. Lett.*, **98**:012002. (2007).
- [40] M. M. Aggarwal et al. “Centrality Dependence of Neutral Pion Production in 158 A GeV Pb + Pb Collisions”. *Phys. Rev. Lett.*, **81**:4087–4091. (1998).
- [41] M. M. Aggarwal et al. “Direct photon production in 158 AGeV Pb-208 + Pb-208 collisions”. nucl-ex/0006007, (2000).
- [42] M. M. Aggarwal et al. “Observation of direct photons in central 158 AGeV Pb-208 + Pb-208 collisions”. *Phys. Rev. Lett.*, **85**:3595–3599. (2000).
- [43] M. M. Aggarwal et al. “Transverse mass distributions of neutral pions from 208-Pb induced reactions at 158 AGeV”. *Eur. Phys. J.*, **C23**:225–236. (2002).
- [44] L. Ahle et al. “Global transverse energy distributions in Si+Al, Au at 14.6A GeV/c and Au+Au at 11.6A GeV/c”. *Phys. Lett. B*, **332**:258. (1994).

- [45] S. Aid et al. “A Measurement and QCD Analysis of the Proton Structure Function $F_2(x, Q^2)$ at HERA”. *Nucl. Phys.*, **B470**:3–40. (1996).
- [46] H. Aihara et al. “Charged-Hadron Inclusive Cross Sections and Fractions in e+e- Annihilation at $\sqrt{s} = 29$ GeV”. *Phys. Rev. Lett.*, **61**:1263–1266. (1988).
- [47] T. Akesson et al. “Inclusive photon production in pA and AA collisions at 200A GeV”. *Z. Phys.*, **C46**:369–375. (1990).
- [48] Y. Akiba et al. “Ring imaging Cherenkov detector of PHENIX experiment at RHIC”. *Nucl. Instrum. Meth.*, **A433**:143–148. (1999).
- [49] H. Akikawa et al. “PHENIX muon arms”. *Nucl. Instrum. Meth.*, **A499**:537–548. (2003).
- [50] J. Alam et al. “Photon interferometry and size of the hot zone in relativistic heavy ion collisions”. *Phys. Rev.*, **C67**:054902. (2003).
- [51] J. Alam, S. Sarkar, T. Hatsuda, T. K. Nayak, and B. Sinha. “Photons from Pb-Pb Collisions at CERN SPS”. *Phys. Rev.*, **C63**:021901. (2001).
- [52] C. Albajar et al. “Direct photon production at the CERN proton-antiproton collider”. *Phys. Lett.*, **B209**:385–396. (1988).
- [53] R. Alber et al. “Transverse momentum distributions of neutral pions from nuclear collisions at 200 AGeV”. *Eur. Phys. J.*, **C5**:255–267. (1998).
- [54] T. Alber et al. “Transverse Energy Production in b + Pb Collisions at 158 GeV per Nucleon”. *Phys. Rev. Lett.*, **75**:3814. (1995).
- [55] R. Albrecht et al. “Upper limit for thermal direct photon production in heavy-ion collisions at 60 and 200A GeV”. *Z. Phys.*, **C51**:1–10. (1991).
- [56] G. Alexander et al. “A comparison of b and uds quark jets to gluon jets”. *Z. Phys.*, **C69**:543–560. (1996).
- [57] J. Alitti et al. “A measurement of single and double prompt photon production at the CERN pp> collider”. *Phys. Lett.*, **B288**:386–394. (1992).
- [58] M. Allen et al. “PHENIX inner detectors”. *Nucl. Instrum. Meth.*, **A499**:549–559. (2003).
- [59] B. Alper et al. “Production spectra of π^\pm , K^\pm , p^\pm at large angles in proton-proton collisions in the CERN intersecting storage rings”. *Nucl. Phys.*, **B100**:237–290. (1975).
- [60] E. Anassontzis et al. “High-pT direct photon production in pp collisions”. *Z. Phys.*, **C13**:277–289. (1982).
- [61] A. L. S. Angelis et al. “A measurement of the transverse momenta of partons, and of jet fragmentation as a function of \sqrt{s} in p-p collisions”. *Phys. Lett.*, **B97**:163–168. (1980).

- [62] A. L. S. Angelis et al. “Large transverse momentum pi0 production in alpha+alpha, d+d and p+p collisions at the CERN ISR”. *Phys. Lett.*, **B185**:213–217. (1987).
- [63] A. L. S. Angelis et al. “Direct photon production at the CERN ISR”. *Nucl. Phys.*, **B327**:541–568. (1989).
- [64] L. Apanasevich et al. “Measurement of direct photon production at Tevatron fixed target energies”. *Phys. Rev.*, **D70**:092009. (2004).
- [65] L. Aphecetche et al. “PHENIX calorimeter”. *Nucl. Instrum. Meth.*, **A499**:521–536. (2003).
- [66] H. Appelshäuser et al. “Spectator Nucleons in Pb+Pb Collisions at 158 A·GeV”. *Eur. Phys. J.*, **A2**:383–390. (1998).
- [67] F. Arleo. “Hard pion and prompt photon at RHIC, from single to double inclusive production”. *JHEP*, **0609**:015. (2006).
- [68] N. Armesto, C. A. Salgado, and U. A. Wiedemann. “Low-pT Collective Flow Induces High-pT Jet Quenching”. *Phys. Rev.*, **D72**:064910. (2005).
- [69] M. Arneodo et al. “The structure function ratios F_2^C/F_2^D and F_2^C/F_2^D at small x”. *Nucl. Phys.*, **B441**:12–30. (1995).
- [70] P. Arnold, G. D. Moore, and L. G. Yaffe. “Photon Emission from Ultrarelativistic Plasmas”. *JHEP*, **0111**:057. (2001).
- [71] P. Arnold, G. D. Moore, and L. G. Yaffe. “Photon and Gluon Emission in Relativistic Plasmas”. *JHEP*, **0206**:030. (2002).
- [72] P. Arnold, G. D. Moore, and L. G. Yaffe. “Photon emission from quark gluon plasma: Complete leading order results”. *JHEP*, **12**:009. (2001).
- [73] S. H. Aronson et al. “PHENIX magnet system”. *Nucl. Instrum. Meth.*, **A499**:480–488. (2003).
- [74] J. J. Aubert et al. “Experimental Observation of a Heavy Particle J ”. *Phys. Rev. Lett.*, **33**:1404–1406. (1974).
- [75] J. J. Aubert et al. “THE RATIO OF THE NUCLEON STRUCTURE FUNCTIONS $F_2(N)$ FOR IRON AND DEUTERIUM”. *Phys. Lett.*, **B123**:275. (1983).
- [76] J. E. Augustin et al. “Discovery of a Narrow Resonance in e+e- Annihilation”. *Phys. Rev. Lett.*, **33**:1406–1408. (1974).
- [77] P. Aurenche et al. “Prompt photon production at large pT in QCD beyond the leading order”. *Phys. Lett.*, **B140**:87–92. (1984).

- [78] P. Aurenche et al. “Prompt photon production at large pT scheme invariant QCD predictions and comparison with experiment”. *Nucl. Phys.*, **B297**:661–696. (1988).
- [79] P. Aurenche et al. “A critical phenomenological study of inclusive photon production in hadronic collisions”. *Eur. Phys. J.*, **C9**:107–119. (1999).
- [80] F. Aversa, P. Chiappetta, M. Greco, and J. P. Guillet. “QCD CORRECTIONS TO PARTON-PARTON SCATTERING PROCESSES”. *Nucl. Phys.*, **B327**:105. (1989).
- [81] T. C. Awes et al. “A simple method of shower localization and identification in laterally segmented calorimeters”. *Nucl. Instrum. Meth.*, **A311**:122–129. (1992).
- [82] T. C. Awes et al. “High energy beam test of the PHENIX lead-scintillator EM calorimeter”. nucl-ex/0202009, (2002).
- [83] B. B. Back et al. “Energy Dependence of Particle Multiplicities in Central Au+Au Collisions”. *Phys. Rev. Lett.*, **88**:022302. (2002).
- [84] B. B. Back et al. “The PHOBOS detector at RHIC”. *Nucl. Instrum. Meth.*, **A499**:603–623. (2003).
- [85] B. B. Back et al. “The PHOBOS perspective on discoveries at RHIC”. *Nucl. Phys.*, **A757**:28–101. (2005).
- [86] J. Badier et al. “Shashlik calorimeter Beam-test results”. *Nucl. Instrum. Meth.*, **A348**:74–86. (1994).
- [87] H. Baer et al. “calculation of the direct photon plus jet cross section in the next-to-leading-logarithm approximation”. *Phys. Lett.*, **B234**:127–131. (1990).
- [88] H. Baer et al. “Next-to-leading-logarithm calculation of direct photon production”. *Phys. Rev.*, **D42**:61–71. (1990).
- [89] R. Baier, Y. L. Dokshitzer, A. H. Mueller, S. Peigne, and D. Schiff. “Radiative energy loss and p(T)-broadening of high energy partons in nuclei”. *Nucl. Phys.*, **B484**:265–282. (1997).
- [90] R. Baier, Y. L. Dokshitzer, A. H. Mueller, S. Peigne, and D. Schiff. “Radiative energy loss of high energy quarks and gluons in a finite-volume quark-gluon plasma”. *Nucl. Phys.*, **B483**:291–320. (1997).
- [91] R. Baier, Y. L. Dokshitzer, A. H. Mueller, and D. Schiff. “Radiative energy loss of high energy partons traversing an expanding QCD plasma”. *Phys. Rev.*, **C58**:1706–1713. (1998).
- [92] R. Baier, Y. L. Dokshitzer, S. Peigne, and D. Schiff. “Induced gluon radiation in a QCD medium”. *Phys. Lett.*, **B345**:277–286. (1995).

- [93] R. Baier, D. Schiff, and B. G. Zakharov. “ENERGY LOSS IN PERTURBATIVE QCD”. *Ann. Rev. Nucl. Part. Sci.*, **50**:37–69. (2000).
- [94] G. Ballocchi et al. “Direct photon cross sections in proton-proton and antiproton-proton interactions at $\sqrt{s} = 24.3$ GeV”. *Phys. Lett.*, **B436**:222–230. (1998).
- [95] G. G. Barnafoldi, P. Levai, G. Papp, G. I. Fai, and Y. Zhang. “High p_T Pion Production in Heavy-Ion Collisions at RHIC Energies”. *nucl-th/0212111*, (2002).
- [96] S. A. Bass, M. Gyulassy, H. Stoecker, and W. Greiner. “Signatures of Quark-Gluon-Plasma formation in high energy heavy-ion collisions: A critical review”. *J. Phys. G*, **25**:R1. (1999).
- [97] S. Bathe and H. Büsching. “Parameterization of the final Run3 π^0 cross section in p+p”. PHENIX Internal Analysis Note 472, (2005).
- [98] R. Baur et al. “Search for direct photons from S-Au collisions at 200 GeV/nucleon”. *Z. Phys.*, **C71**:571–577. (1996).
- [99] G. Baym. “RHIC performance”. *Nucl. Phys.*, **B698**:23. (2002).
- [100] A. Bazilevsky et al. “Charge particle multiplicity and transverse energy measurements in Au—Au collisions in PHENIX at RHIC”. *Nucl. Phys.*, **A715**:486–489. (2003).
- [101] A. V. Bazilevsky, V. I. Kochetkov, V. K. Semenov, S. White, and E. P. Kistenev. “Electron/hadron separation in the electromagnetic calorimeter of the PHENIX setup”. *Instrum. Exp. Tech.*, **42**:167–173. (1999).
- [102] J. D. Bjorken. “Energy Loss Of Energetic Partons In Quark - Gluon Plasma: Possible Extinction Of High P(T) Jets In Hadron - Hadron Collisions.”. FERMILAB-PUB-82-059-THY, (1982).
- [103] J. D. Bjorken. “HIGHLY RELATIVISTIC NUCLEUS-NUCLEUS COLLISIONS: THE CENTRAL RAPIDITY REGION”. *Phys. Rev.*, **D27**:140–151. (1983).
- [104] M. Bonesini et al. “Production of high transverse momentum prompt photons and neutral pions in proton-proton interactions at 280 GeV/c”. *Z. Phys.*, **C38**:371–382. (1988).
- [105] L. Bourhis, M. Fontannaz, and J. Guillet. “Quark and gluon fragmentation functions into photons”. *Eur. Phys. J.*, **C2**:529–537. (1998).
- [106] R. Brandelik et al. “Charged pion, kaon and nucleon production by e^+e^- annihilation for c.m. energies between 3.6 and 5.2 GeV”. *Nucl. Phys.*, **B148**:189–227. (1979).
- [107] R. Brun and F. Carminati. “GEANT, Detector Description and Simulation Tool”. CERN Program Library Long Writeup W5013, (1993).
- [108] D. Buskulic et al. “Measurement of α_s from scaling violations in fragmentation functions in e^+e^- annihilation”. *Phys. Lett.*, **B357**:487–499. (1995).

- [109] M. Cacciari. “Rise and Fall of the Bottom Quark Production Excess”. hep-ph/0407187, (2004).
- [110] G. F. Chapline, M. H. Johnson, E. Teller, and M. S. Weiss. “Highly Excited Nuclear Matter”. *Phys. Rev.*, **D8**:4302–4308. (1973).
- [111] J. C. Collins and M. J. Perry. “Superdense Matter: neutrons or asymptotically Free Quarks”. *Phys. Rev. Lett.*, **34**:1353. (1975).
- [112] J. W. Cronin et al. “PRODUCTION OF HADRONS WITH LARGE TRANSVERSE MOMENTUM AT 200 GeV, 300-GeV, AND 400-GeV”. *Phys. Rev.*, **D11**:3105. (1975).
- [113] P. Darriulat et al. “Structure of final states with a high transverse momentum π^0 in proton-proton collisions”. *Nucl. Phys.*, **B107**:429–456. (1976).
- [114] G. David et al. “The calibration and monitoring system for the PHENIX lead-scintillator electromagnetic calorimeter”. *IEEE Trans. Nucl. Sci.*, **45**:705–706. (1998).
- [115] G. David et al. “The PHENIX lead-scintillator electromagnetic calorimeter: Test beam and construction experience”. *IEEE Trans. Nucl. Sci.*, **45**:692–697. (1998).
- [116] C. De Jager, H. De Vries, and C. De Vries. “Nuclear charge- and magnetization-density-distribution parameters from elastic electron scattering”. *Atomic Data and Nuclear Data Tables*, **14**:479–508. (1974).
- [117] D. d’Enterria. “Indications of suppressed high pT hadron production in nucleus-nucleus collisions at CERN-SPS”. *Phys. Lett.*, **B576**:32–43. (2004).
- [118] D. d’Enterria. “Photon Conversions in the Central Arms for Runs 1-3”. PHENIX Internal Analysis Note 322, (2004).
- [119] D. d’Enterria, T. C. Awes, G. David, S. Mioduszewski, C. Klein-Bösing, and K. Reygers. “Suppressed π^0 Production at Large Transverse Momentum in Central Au+Au Collisions at $\sqrt{s_{NN}} = 200$ GeV”. PHENIX Internal Analysis Note 170, (2003).
- [120] M. Derrick et al. “Measurement of the Proton Structure Function F_2 at low x and low Q_2 at HERA”. *Z. Phys.*, **C69**:607–620. (1996).
- [121] M. Djordjevic. “Collisional Energy Loss in a Finite Size QCD Matter”. *Phys. Rev.*, **C74**:064907. (2006).
- [122] M. Djordjevic, M. Gyulassy, R. Vogt, and S. Wicks. “Influence of Bottom Quark Jet Quenching on Single Electron Tomography of Au+Au”. *Phys. Lett.*, **B632**:81–86. (2006).
- [123] Y. L. Dokshitzer and D. E. Kharzeev. “Heavy quark colorimetry of QCD matter”. *Phys. Lett.*, **B519**:199–206. (2001).

- [124] A. Dumitru, L. Frankfurt, L. Gerland, H. Stocker, and M. Strikman. “Nuclear broadening effects on hard prompt photons at CERN- SPS and BNL-RHIC energies”. *Phys. Rev.*, **C64**:054909. (2001).
- [125] A. K. Dutt-Mazumder, J. Alam, P. Roy, and B. Sinha. “Stopping power of hot QCD plasma”. *Phys. Rev.*, **D71**:094016. (2005).
- [126] M. S. Emery et al. “A multichannel ADC for use in the PHENIX detector”. *IEEE Trans. Nucl. Sci.*, **44**:374–378. (1997).
- [127] K. J. Eskola, H. Honkanen, C. A. Salgado, and U. A. Wiedemann. “The Fragility of High-pT Hadron Spectra as a Hard Probe”. *Nucl. Phys.*, **A747**:511–529. (2005).
- [128] C. W. Fabjan and F. Gianotti. “Calorimetry for particle physics”. *Rev. Of Mod. Phys.*, **75**:1243. (2003).
- [129] E. L. Feinberg. “Direct Production Of Photons And Dileptons In Thermodynamical Models Of Multiple Hadron Production”. *Nuovo Cim.*, **A34**:391. (1976).
- [130] R. J. Fries, B. Muller, and D. K. Srivastava. “Centrality Dependence of Direct Photons in Au+Au Collisions at $\sqrt{s_{NN}} = 200$ GeV”. *Phys. Rev.*, **C72**:041902. (2005).
- [131] R. J. Fries, B. Muller, and D. K. Srivastava. “High energy photons from passage of jets through quark gluon plasma”. *Phys. Rev. Lett.*, **90**:132301. (2003).
- [132] C. Gale and J. I. Kapusta. “Vector dominance model at finite temperature”. *Nucl. Phys.*, **B357**:65–89. (1991).
- [133] K. Gallmeister, C. Greiner, and Z. Xu. “Quenching of high p(T) hadron spectra by hadronic interactions in heavy ion collisions at RHIC”. *Phys. Rev.*, **C67**:044905. (2003).
- [134] K. Gallmeister, B. Kampfer, and O. P. Pavlenko. “A unique large thermal source of real and virtual photons in the reactions Pb(158 AGeV) + Pb, Au”. *Phys. Rev.*, **C62**:057901. (2000).
- [135] R. J. Glauber and G. Matthiae. “High-energy scattering of protons by nuclei”. *Nucl. Phys.*, **B21**:135–157. (1970).
- [136] M. Gluck, E. Reya, and A. Vogt. “Dynamical parton distributions of the proton and small-x physics”. *Z. Phys.*, **C67**:433–447. (1995).
- [137] M. Gluck, E. Reya, and A. Vogt. “Parton fragmentation into photons beyond the leading order”. *Phys. Rev.*, **D51**:1427. (1995).
- [138] L. E. Gordon and W. Vogelsang. “Polarized and unpolarized prompt photon production beyond the leading order”. *Phys. Rev.*, **D48**:3136–3159. (1993).
- [139] L. E. Gordon and W. Vogelsang. “Polarized and unpolarized isolated prompt photon production beyond the leading order”. *Phys. Rev.*, **D50**:1901–1916. (1994).

- [140] D. J. Gross and F. Wilczek. “Ultraviolet Behavior of Non-Abelian Gauge Theories”. *Phys. Rev. Lett.*, **30**:1343. (1973).
- [141] X. Guo and X.-N. Wang. “Multiple Scattering, Parton Energy Loss and Modified Fragmentation Functions in Deeply Inelastic eA Scattering”. *Phys. Rev. Lett.*, **85**:3591–3594. (2000).
- [142] M. Gyulassy, P. Levai, and I. Vitev. “Jet quenching in thin quark-gluon plasmas I: formalizm”. *Nucl. Phys.*, **B571**:197–233. (2000).
- [143] M. Gyulassy, P. Levai, and I. Vitev. “Non-Abelian energy loss at finite opacity”. *Phys. Rev. Lett.*, **85**:5535–5538. (2000).
- [144] M. Gyulassy, P. Levai, and I. Vitev. “Reaction operator approach to non-Abelian energy loss”. *Nucl. Phys.*, **B594**:371–419. (2001).
- [145] M. Gyulassy, P. Levai, and I. Vitev. “Jet Tomography of Au+Au Reactions Including Multi-gluon Fluctuations”. *Phys. Lett.*, **B538**:282–288. (2002).
- [146] M. Gyulassy. “The QGP discovered at RHIC”. nucl-th/0403032, (2004).
- [147] M. Gyulassy and L. McLerran. “New Forms of QCD Matter Discovered at RHIC”. nucl-th/0405013, (2004).
- [148] M. Gyulassy and M. Plumer. “JET QUENCHING IN DENSE MATTER”. *Phys. Lett.*, **B243**:432–438. (1990).
- [149] M. Gyulassy, I. Vitev, X.-N. Wang, and B.-W. Zhang. “Jet Quenching and Radiative Energy Loss in Dense Nuclear Matter”. nucl-th/0302077, (2003).
- [150] M. Gyulassy and X.-N. Wang. “Multiple collisions and induced gluon Bremsstrahlung in QCD”. *Nucl. Phys.*, **B420**:583–614. (1994).
- [151] D. T. Haar. *Collected Papers of L.D. Landau*. Gordon and Breach, (1965).
- [152] T. Hachiya et al. “Study of the BBC trigger efficiency based on simulations for run-2 analysis”. PHENIX Internal Analysis Note 107, (2002).
- [153] R. Hagedorn. “MULTIPLICITIES, P(T) DISTRIBUTIONS AND THE EXPECTED HADRON → QUARK - GLUON PHASE TRANSITION”. *Riv.Nuovo Cim.*, **6N10**:1–50. (1984).
- [154] H. Hahn et al. “The RHIC design overview”. *Nucl. Instrum. Meth.*, **A499**:245–263. (2003).
- [155] F. Halzen and H. C. Liu. “Experimental signatures of phase transition to quark matter in high-energy collisions of nuclei”. *Phys. Rev.*, **D25**:1842. (1982).

- [156] H. Hees, V. Greco, and R. Rapp. “Heavy-quark probes of the quark-gluon plasma and interpretation of recent data taken at the BNL Relativistic Heavy Ion Collider”. *Phys. Rev.*, **C73**:034913. (2006).
- [157] T. Hirano and Y. Nara. “Hydrodynamical afterburner for the Color Glass Condensate and the parton energy loss”. *Nucl. Phys.*, **A743**:305. (2004).
- [158] T. Hirano and K. Tsuda. “Collective flow and two-pion correlations from a relativistic hydrodynamic model with early chemical freeze-out”. *Phys. Rev.*, **C66**:054905. (2002).
- [159] T. Hirano. “Hydrodynamic models”. *J. Phys.*, **G30**:S845–S852. (2004).
- [160] P. Huovinen, P. F. Kolbb, U. Heinz, P. V. Ruuskanend, and S. A. Voloshin. “Radial and elliptic flow at RHIC: further predictions”. *Phys. Lett.*, **B503**:58–64. (2001).
- [161] P. Huovinen, P. V. Ruuskanen, and S. S. Rasanen. “Photon emission in heavy ion collisions at the CERN SPS”. *Phys. Lett.*, **B535**:109–116. (2002).
- [162] D. Ivanishchev et al. “Hadron decay of omega and Ks - mesons in Run5 p+p”. PHENIX Internal Analysis Note 535, (2006).
- [163] B. Jager, A. Schafer, M. Stratmann, and W. Vogelsang. “Next-to-leading order QCD corrections to high-pT pion production in longitudinally polarized pp collisions”. *Phys. Rev.*, **D67**:054005. (2003).
- [164] S. Jeon, J. Jalilian-Marian, and I. Sarcevic. “The Origin of Large-p_T π^0 Suppression at RHIC”. *Nucl. Phys.*, **B562**:45–50. (2003).
- [165] S. Jeon and G. D. Moore. “Energy Loss of Leading Partons in a Thermal QCD Medium”. *Phys. Rev.*, **C71**:034901. (2005).
- [166] J. I. Kapusta, P. Lichard, and D. Seibert. “High-energy photons from quark - gluon plasma versus hot hadronic gas”. *Phys. Rev.*, **D44**:2774–2788. (1991).
- [167] F. Karsch, E. Laermann, and A. Peikert. “The pressure in 2, 2+1 and 3 flavour QCD”. *Phys. Lett.*, **B478**:447–455. (2000).
- [168] F. Karsch. “Lattice QCD at high temperature and density”. *Lect. Notes Phys.*, **583**:209–249. (2002).
- [169] S. Kelly, D. Morrison, J. Nagle, and K. Reygers. “Calculation of the Number of Participating Nucleons for Centrality Classes Defined with the ZDC and BBC”. PHENIX Internal Analysis Note 33, (2000).
- [170] D. Kharzeev, E. Levin, and L. McLerran. “Parton saturation and N(part) scaling of semi-hard processes in QCD”. *Phys. Lett.*, **B561**:93–101. (2003).
- [171] K. Kleinknecht. *Detektoren für Teilchenstrahlung*. Teubner, (1992).

- [172] B. A. Kniehl, G. Kramer, and B. Potter. “Testing the universality of fragmentation functions”. *Nucl. Phys.*, **B597**:337–369. (2001).
- [173] P. F. Kolb. “Expansion rates at RHIC”. *Heavy Ion Phys.*, **21**:243–248. (2004).
- [174] P. F. Kolb and R. Rapp. “Transverse flow and hadrochemistry in Au+Au collisions at $\sqrt{s_{NN}} = 200$ GeV”. *Phys. Rev.*, **C67**:044903. (2003).
- [175] S. Kretzer. “Fragmentation functions from flavor-inclusive and flavor-tagged e+e- annihilations”. *Phys. Rev.*, **D62**:054001. (2000).
- [176] A. Krzywicki, J. Engels, B. Petersson, and U. Sukhatme. “Does a nucleus act like a gluon filter?”. *Phys. Lett.*, **B85**:407–412. (1979).
- [177] T. D. Lee. “Abnormal nuclear states and vacuum excitation”. *Rev. Mod. Phys.*, **47**:267–275. (1975).
- [178] T. D. Lee and G. C. Wick. “Vacuum stability and vacuum excitation in a spin-0 field theory”. *Phys. Rev.*, **D9**:2291–2316. (1974).
- [179] M. Lev and B. Petersson. “Nuclear effects at large transverse momentum in a QCD parton model”. *Z. Phys.*, **C21**. (1983).
- [180] C. D. Marzo et al. “Measurement of direct photon production at large transverse momentum in $\pi^- p$, $\pi^+ p$, and pp collisions at 300 GeV/c”. *Phys. Rev.*, **D36**:8–15. (1987).
- [181] T. Matsubara. “A New Approach to Quantum-Statistical Mechanics”. *Prog. Theor. Phys.*, **14**:351–378. (1955).
- [182] L. McLerran and T. Toimela. “Photon and dilepton emission from the quark-gluon plasma: Some general considerations”. *Phys. Rev.*, **D31**:545–563. (1985).
- [183] A. B. Migdal. “Bremsstrahlung and Pair Production in Condensed Matter at High Energies”. *Phys. Rev.*, **103**(6):1811. (1956).
- [184] A. Milov et al. “Hadron decay of omega meson in Run4 Au+Au”. PHENIX Internal Analysis Note 537, (2006).
- [185] J. T. Mitchell et al. “Event reconstruction in the PHENIX central arm spectrometers”. *Nucl. Instrum. Meth.*, **A482**:491–512. (2002).
- [186] B. Muller. “Phenomenology of Jet Quenching in Heavy Ion Collisions”. *Phys. Rev.*, **C67**:061901. (2003).
- [187] M. G. Mustafa. “Energy Loss of Charm Quarks in the Quark-Gluon Plasma: Collisional vs Radiative”. *Phys. Rev.*, **C72**:014905. (2005).
- [188] J. Nagle et al. “Minimum Bias Trigger Selection and Centrality Note”. PHENIX Internal Analysis Note 113, (2002).

- [189] M. D. Negra et al. “Observation of jet structure in high pT events at the ISR and the importance of parton transverse momentum”. *Nucl. Phys.*, **B127**:1–42. (1977).
- [190] A. Oskarsson et al. “Construction and performance of the PHENIX pad chambers”. *Nucl. Instrum. Meth.*, **A497**:263–293. (2003).
- [191] T. Peitzmann and M. H. Thoma. “Direct photons from relativistic heavy-ion collisions”. *Phys. Rept.*, **364**:175–246. (2002).
- [192] J. Pumplin et al. “New generation of parton distributions with uncertainties from global QCD analysis”. *JHEP*, **07**:012. (2002).
- [193] J. W. Qiu and G. Sterman. “Power corrections in hadronic scattering (I). Leading $1/Q^2$ corrections to the Drell-Yan cross section”. *Nucl. Phys.*, **B353**:105–136. (1991).
- [194] J. W. Qiu and G. Sterman. “Power corrections in hadronic scattering (II). Factorization”. *Nucl. Phys.*, **B353**:137–164. (1991).
- [195] R. Rapp. “Thermal photons in strong interactions”. *Mod. Phys. Lett.*, **A19**:1717–1732. (2004).
- [196] K. Reygers. “Glauber Monte-Carlo Calculation for Au+Au Collisions at $\sqrt{s_{NN}} = 200 \text{ GeV}$ ”. PHENIX Internal Analysis Note 169, (2003).
- [197] C. A. Salgado and U. A. Wiedemann. “Calculating Quenching Weights”. *Phys. Rev.*, **D68**:014008. (2003).
- [198] P. Shukla. “Glauber model for heavy ion collisions from low energies to high energies”. nucl-th/0112039, (2001).
- [199] E. V. Shuryak. “Quark-gluon plasma and hadronic production of leptons, photons and psions”. *Phys. Lett.*, **B78**:150–153. (1978).
- [200] E. V. Shuryak. “QUANTUM CHROMODYNAMICS AND THE THEORY OF SUPERDENSE MATTER”. *Phys. Rept.*, **61**:177–180. (1980).
- [201] T. Sjostrand, L. Lonnblad, S. Mrenna, and P. Skands. “PYTHIA 6.3 Physics and Manual”. hep-ph/0308153, (2003).
- [202] J. Slivova. *Azimuthal Correlations of High-pt Pions in 158 AGeV/c Pb-Au Collisions measured by the CERES/NA45 Experiment*. PhD thesis, Charles University, (2003).
- [203] G. Sozzi et al. “Direct photon production in $p\bar{p}$ and pp interactions at $\sqrt{s} = 24.3 \text{ GeV}$ ”. *Phys. Lett.*, **B317**:243–249. (1993).
- [204] D. K. Srivastava. “Intensity interferometry of thermal photons from relativistic heavy-ion collisions”. *Phys. Rev.*, **C71**:034905. (2005).

- [205] D. K. Srivastava. “Parton distributions: a new global analysis”. *Eur. Phys. J.*, **C4**:463–496. (1998).
- [206] D. K. Srivastava and B. Sinha. “Radiation of single photons from $Pb + Pb$ collisions at the CERN SPS and quark hadron phase transition”. *Phys. Rev.*, **C64**:034902. (2001).
- [207] F. D. Steffen and M. H. Thoma. “Hard thermal photon production in relativistic heavy ion collisions”. *Phys. Lett.*, **B510**:98–106. (2001).
- [208] M. J. Tannenbaum. “Fits to data with Correlated Systematic Errors”. PHENIX Internal Analysis Note 563, (2007).
- [209] E. Tarkovsky. “The HERA-B electromagnetic calorimeter”. *Nucl. Instrum. Meth.*, **A379**:515–517. (1996).
- [210] D. Teaney, J. Lauret, and E. V. Shuryak. “A Hydrodynamic Description of Heavy Ion Collisions at the SPS and RHIC”. *nucl-th/0110037*, (2001).
- [211] S. Turbide, C. Gale, S. Jeon, and G. D. Moore. “Energy Loss of Leading Hadrons and Direct Photon production in Evolving Quark-Gluon Plasma”. *Phys. Rev.*, **C72**:014906. (2005).
- [212] S. Turbide, R. Rapp, and C. Gale. “Hadronic production of thermal photons”. *Phys. Rev.*, **C69**:014903. (2004).
- [213] S. Turbide, R. Rapp, and C. Gale. “Photon production in relativistic nuclear collisions at SPS and RHIC energies”. *Int.J.Mod.Phys.*, **A19**:5351–5358. (2004).
- [214] I. Vitev. “Testing the theory of QGP-induced energy loss at RHIC and the LHC”. *Phys. Lett.*, **B639**:38–45. (2006).
- [215] I. Vitev and M. Gyulassy. “High-p(T) tomography of $d + Au$ and $Au + Au$ at SPS, RHIC, and LHC”. *Phys. Rev. Lett.*, **89**:252301. (2002).
- [216] W. Vogelsang and M. R. Whalley. “A compilation of data on single and double prompt photon production in hadron - hadron interactions”. *J. Phys. G*, **23**:7A–1. (1997).
- [217] E. Wang and X.-N. Wang. “Interplay of soft and hard processes and hadron pT spectra in pA and AA collisions”. *Phys. Rev.*, **C64**:034901. (2001).
- [218] E. Wang and X.-N. Wang. “Parton Energy Loss with Detailed Balance”. *Phys. Rev. Lett.*, **87**:142301. (2001).
- [219] E. Wang and X.-N. Wang. “Jet tomography of dense and nuclear matter”. *Phys. Rev. Lett.*, **89**:162301. (2002).
- [220] X.-N. Wang. “Medium-induced parton energy loss in $\gamma +$ jet events of high-energy heavy-ion collisions”. *Phys. Rev.*, **C55**:3047–3061. (1997).

- [221] X.-N. Wang. “Effect of jet quenching on high p(T) hadron spectra in high-energy nuclear collisions”. *Phys. Rev.*, **C58**:2321. (1998).
- [222] X.-N. Wang. “Where Is the Jet Quenching in Pb+Pb Collisions at 158A GeV?”. *Phys. Rev. Lett.*, **81**:2655. (1998).
- [223] X.-N. Wang. “Probe initial parton density and formation time via jet quenching”. *Nucl. Phys.*, **A715**:775–778. (2003).
- [224] X.-N. Wang. “Why the observed jet quenching at RHIC is due to parton energy loss”. *Phys. Lett.*, **B579**:299–308. (2004).
- [225] X.-N. Wang. “Discovery of jet quenching and beyond”. *Nucl. Phys.*, **A750**:98–120. (2005).
- [226] X.-N. Wang and X. Guo. “Multiple parton scattering in nuclei: parton energy loss”. *Nucl. Phys.*, **A696**:788–832. (2001).
- [227] X.-N. Wang and M. Gyulassy. “HIJING: A Monte Carlo model for multiple jet production in p p, p A and A A collisions”. *Phys. Rev.*, **D44**:3501–3516. (1991).
- [228] X.-N. Wang and M. Gyulassy. “Gluon shadowing and jet quenching in A + A collisions at $\sqrt{s} = 200\text{GeV}$ ”. *Phys. Rev. Lett.*, **68**:1480–1483. (1992).
- [229] X.-N. Wang, M. Gyulassy, and M. Plümer. “Landau-Pomeranchuk-Migdal effect in QCD and radiative energy loss in a quark-gluon plasma”. *Phys. Rev.*, **D51**:3436–3446. (1995).
- [230] X.-N. Wang, Z. Huang, and I. Sarcevic. “Jet Quenching in the Direction Opposite to a Tagged Photon in High-Energy Heavy-Ion Collisions”. *Phys. Rev. Lett.*, **77**:231. (1996).
- [231] H. A. Weldon. “Simple rules for discontinuities in finite-temperature field theory”. *Phys. Rev.*, **D28**:2007–2015. (1983).
- [232] L. W. Whitlow et al. “Precise measurements of the proton and deuteron structure functions from a global analysis of the SLAC deep inelastic electron scattering cross sections”. *Phys. Lett.*, **B282**:475–482. (1992).
- [233] S. Wicks, W. Horowitz, M. Djordjevic, and M. Gyulassy. “Elastic, Inelastic, and Path Length Fluctuations in Jet Tomography”. *Nucl. Phys.*, **A784**:426–442. (2006).
- [234] U. A. Wiedemann. “Gluon radiation off hard quarks in a nuclear environment: opacity expansion”. *Nucl. Phys.*, **B588**:303–344. (2000).
- [235] U. A. Wiedemann. “Transverse dynamics of hard partons in nuclear media and the QCD dipole”. *Nucl. Phys.*, **B582**:409–450. (2000).
- [236] C.-Y. Wong. *Introduction to High-Energy Heavy-Ion Collisions*. World Scientific, Singapore, (1994).

- [237] W. M. Yao et al. “Review of Particle Physics”. *Journal of Physics*, **33**:278–298. (2006).
- [238] B. G. Zakharov. “Induced photon emission from quark jets in ultrarelativistic heavy-ion collisions”. *JETP Lett.*, **80**:1–6. (2004).
- [239] B.-W. Zhang and X.-N. Wang. “Multiple parton scattering in nuclei: beyond helicity amplitude approximation”. *Nucl. Phys.*, **A720**:429–451. (2003).
- [240] H. Zhang, J. Owens, E. Wang, and X.-N. Wang. “Dihadron Tomography of High-Energy Nuclear Collisions in NLO pQCD”. nucl-th/0701045, (2007).